



**Prifysgol Abertawe
Swansea University**

Active vibration control of a flexible robot
link using piezoelectric actuators

Darren Williams

Supervised by:

Dr Hamed Haddad Khodaparast and Dr Shakir Jiffri

Submitted to Swansea University in fulfilment of the requirements for the degree of

Doctor of Philosophy in

Aerospace Engineering

Swansea University

May 2022

Abstract

Nuisance vibrations are a concern throughout the engineering realm, and many researchers are dedicated to finding a solution to attenuate them. This research primarily focusses upon the suppression of vibrations in a robot system, with the control system being designed so that it is both affordable and lightweight. Such constraints aim to provide a solution that may be utilised in a variety of applications. The utilisation of piezoelectric elements as both actuators and sensors provides several advantages in that they are lightweight, easily integrated into an existing system and have a good force to weight ratio when used as actuators. To read and control these elements a single board computer was employed, in acknowledgement of the constraining parameters of the design. The amalgamation of vibration control and robotics has lent to the research being conducted with separate objectives set, isolating certain elements of the overall system design for validation. Ultimately, these separate investigations progress to the integration of the robot and control systems prior to further research concerning nonlinear vibrations, dynamic control and the discrete-time domain modelling of the system.

This research first investigates the viability of the chosen components as a vibration attenuation solution. In addition, analytical models of the system have been created, for two types of sensors to determine the most effective; an inertial measurement unit and a collocated pair of piezoelectric sensors. These models are based on Euler-Bernoulli beam theory and aim to validate the control theory through a comparison of the experimental data. These experiments isolate the vibration problem from a robot system through the investigation of the control of a long slender beam envisioned as a robot manipulator link, but excited using a shaker platform in a sinusoidal manner. An observation of the theory related to the voltage produced by the piezoelectric elements, suggests that even with the application of only proportional control by the system, the controlled output would have components indicative of both proportional and derivative control. This observation and the underlying theory are further analysed within this research.

The next objectives are to compare the performance of the control system developed in this research which utilises a Raspberry Pi 3B+ [1] with one that employs a dSPACE MicroLabBox [2], and to determine the suitability of the former for use with robot systems. With the former ensuring that the constraints placed on the design, those which influenced the selection of the components, does not conclude to the dSPACE MicroLabBox system being overtly preferable. The latter investigates both the impact of the system's inclusion on the functionality of the system and the system's performance with respect to the intended application. The KUKA LBR iiwa 7 R800 [3] robot manipulator is utilised to satisfy this objective, wherein the link is mounted on the end effector of the manipulator acting as an eighth link. The final investigation in this research pertains to the attenuation of nonlinear vibrations experienced by a robot manipulator link. Additional components were added to the link to induce a geometric nonlinearity in the system. An analytical model of the amended system was created to validate the theory through comparison with experimental results. The control system was employed for multiple cases to ascertain the level of its performance with regards to the suppression of nonlinear vibrations.

Declarations and Statements

This work has not previously been accepted in substance for any degree and is not being concurrently submitted in candidature for any degree.

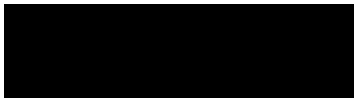
Signed:



Date: 04/05/2022

This thesis is the result of my own investigations, except where otherwise stated. Other sources are acknowledged by footnotes giving explicit references. A bibliography is appended.

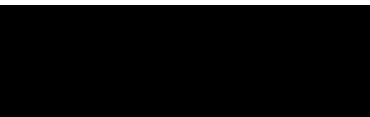
Signed:



Date: 04/05/2022

I hereby give consent for my thesis, if accepted, to be available for photocopying and for inter-library loan, and for the title and summary to be made available to outside organisations.

Signed:



Date: 04/05/2022

Acknowledgements

Here I would like to express my gratitude to those whom have helped in this endeavour and have seen me through many joys and tribulations.

Firstly, I would like to thank my supervisors Dr Hamed Haddad Khodaparast and Dr Shakir Jiffri, who have helped me with every hurdle, and listened to every problem answering with patience and kindness. They have not only helped me unendingly in this academic endeavour, but also with respect to my career. I also wish to express my gratitude to Professor Chenguang Yang who was initially part of my supervisory team and played a major role in my understanding of robotics.

I would also like to thank numerous members of academic staff, fellow postgraduate students and technicians. Swansea University is an excellent place to study and the level of support from everyone at the institution is to be revered. From using equipment for the first time, to asking how it works for the hundredth time, the level of patience within this academic community is unfathomable. I apologise to all those whom I have not named, however I would like to explicitly thank Javad Taghipour for his collaboration within this research.

My gratitude is also expressed to the Engineering and Physical Sciences Research Council (Doctoral Training Partnership) for funding this research.

On a more personal note I wish to thank my parents and sisters who have supported me throughout my life and are always only a request for assistance away. Between them they have read almost as many words as I have written during this research, have assisted in the creation of several ‘contraptions’ for this research, and have even accepted these contraptions as part of the furniture during the Covid-19 pandemic. I also wish to thank my Nan who has listened to every conundrum, and has revelled in the triumphs, I hope Bampi would be proud.

I also express my gratitude to my friends, who have understood when this research has taken a priority and have shown boundless patience and support. Lastly, but certainly not least, I wish to thank my fiancée whom has seen me through many a disheartenment and celebration during this time, reminding me that sometimes the best way forward is to take a step back and relax. Here’s to the next chapter!

Contents

1	Introduction	1
1.1	Literature review	3
1.1.1	Passive vibration control	3
1.1.2	Active vibration control	6
1.1.3	PZT sensors and actuators	10
1.1.4	Single board computers (SBCs)	11
1.1.5	Modelling beams	14
1.1.6	Control schemes and hardware	17
1.1.7	The control of flexible robot links	18
1.1.8	Modelling robot manipulators	19
1.1.9	Nonlinear modelling and control	20
1.2	Problem definition	24
1.3	Suggested application	26
1.4	Outline of thesis	28
1.5	Outcomes of this research	29
2	Robot manipulator	30
2.1	A brief overview and history of robotics	30
2.2	Applications	36
2.3	KUKA LBR iiwa 7 R800	45
2.4	Analytical Model	47
2.5	Experimental validation	53
2.6	Summary	56
3	Model and validation of open loop systems	57
3.1	Robot links	57
3.2	Inertial measurement units (IMUs)	58
3.3	Piezoelectric sensors and actuators	63
3.4	System A: Robot link, IMUs and piezoelectric actuators	68
3.4.1	Analytical model	68

3.4.2	COMSOL model	73
3.4.3	Experimental validation	75
3.5	System B: Robot link, piezoelectric sensors and piezoelectric actuators .	87
3.5.1	Motivation behind altering the sensors	87
3.5.2	Analytical model	93
3.5.3	Experimental validation	100
3.6	Summary	105
4	Control theory and system	106
4.1	An overview of the control system design	106
4.2	Analytical models	108
4.2.1	Control system A	108
4.2.2	Control system B	110
4.3	Components	113
4.3.1	Single board computer	113
4.3.2	Actuators	117
4.3.3	High voltage drivers	119
4.3.4	Inertial measurement units	120
4.3.5	Analog to digital converter and piezoelectric sensors	124
4.4	Integration of components	129
4.4.1	Communication between Raspberry Pi 3 and IMUs	132
4.4.2	Communication between the RPi, ADC and PZT sensors	139
4.4.3	Communication between the RPi, HVDs and PZT actuators	146
4.5	dSPACE controller for validation of component selection	149
4.6	Health and safety considerations	153
4.7	Summary	159
5	Experimental results of the control systems and validation of the analytical models	160
5.1	Control System A	161
5.2	Control System B	174
5.3	A comparison of performance: dSPACE vs. Raspberry Pi 3 (Control System B)	181
5.4	Link mounted on robot manipulator (Control System B)	188
5.5	Summary	198
6	Control of a nonlinear response	199
6.1	A brief overview and history	200
6.2	Inducing a geometric nonlinearity	204

6.3	Application of control	218
6.4	Analytical model and optimisation	229
6.5	Analytical model validation	234
6.6	Summary	238
7	Optimal control of the system via the implementation of a more advanced control method	239
7.1	Modifications to analytical model	240
7.2	Overview of PID control and associated tuning methods	247
7.3	An investigation of PID tuning methods	250
7.4	The discrete-time Fourier transform	270
7.5	Summary	282
8	Conclusions	283

List of Figures

1.1.1	The road engine design of G.B. Selden patented in 1895 [11].	4
1.1.2	Illustration of the experimental set-up used in the research by dell’Isola et al [15].	5
1.1.3	Illustration of the experimental set-up used in the research by Bailey and Hubbard [25].	8
1.1.4	Contour plots of the controllability index with respect to size and placement of a PZT element on a cantilever beam for a) the first mode and b) the first two modes (Wang and Wang [36])	12
1.1.5	Results from the research by Iwaniec et al., a) through c) represent the acceleration in the time domain for the x, y and z axes, receptively, and d) through f) represent the same data in the frequency domain [42]. .	13
1.1.6	“Comparison of the model predictions and experimental measurements; (a) voltage FRF and (b) tip velocity FRF for 1 k Ω , (c) voltage FRF and (d) tip velocity FRF for 33 k Ω , (e) voltage FRF and (f) tip velocity FRF for 470 k Ω ” [54]	16
1.1.7	Illustration of D-H parameters assignment based on the KUKA LBR iiwa 7 R800 as in the research by [73].	20
1.3.1	Image of the PD6B-AW-ARM by PRODRONE [90].	27
2.1.1	Annual installations of industrial robots by customer industry worldwide (1000 units).	32
2.1.2	Annual installations of industrial robots by application (1000 units). .	32
2.1.3	Service robots for professional use, top seven based on unit sales (1000 units).	33
2.2.1	Image of the Harris T7 Multi-Mission Robotic System [110].	36
2.2.2	Image of the Canadarm2 and Dextre carrying the RapidScat instrument assembly [99].	37
2.2.3	An image of the Dextre robot, outlining its components [111].	38
2.2.4	Image of the da Vinci Surgical System [112].	38

2.2.5	CAD model of the Modular Prosthetic Limb highlighting the sensors included in the design [115].	39
2.2.6	Johnny Matheny testing the Modular Prosthetic Limb [116].	40
2.2.7	The Samsung Chef Bot making a salad on command [118].	41
2.2.8	KUKA iiwa in industry moving components whilst mounted on a movable platform [120].	41
2.2.9	Universal Robots' UR10 collaborative robot working in an automotive assembly line alongside people [122].	42
2.2.10	Images of Soft Robotic's mGrip modular end effector tool [124].	43
2.2.11	Images of 'the right trousers' by a collaboration of researchers.	44
2.3.1	Image of the KUKA LBR iiwa 7 R800 workspace and joint lengths.	46
2.4.1	Illustration of the right-hand coordinate system	47
2.4.2	Illustration of the analytical model of the manipulator including coordinate frames and orientation of the joints.	48
2.5.1	Cartesian coordinates of analytical model and the robot manipulator.	53
2.5.2	Joint velocities from analytical model and the robot manipulator for each joint (J1-J7).	55
3.2.1	Simplified illustration of a MEMS accelerometer.	58
3.2.2	Illustration of the Coriolis effect.	59
3.2.3	Simplified illustration of a MEMS gyroscope.	60
3.2.4	Illustration of the set-up to demonstrate the Hall effect.	61
3.2.5	Illustration of a Hall transducer.	62
3.2.6	Image of a MEMS magnetometer [138].	63
3.3.1	Illustration of dipoles in the PZT structure.	65
3.3.2	Illustration of the voltage output from the PZT sensors in relation to the direction of the transverse motion of the structure.	66
3.3.3	Illustration of the identification as to which PZT actuator should be employed for a particular direction of the transverse motion.	67
3.4.1	Visualisation of the analytical model for control system A.	69
3.4.2	Image of the three dimensional finite element model including the mesh used.	73
3.4.3	Mesh convergence study.	74
3.4.4	Illustration of the experimental set-up for the validation of the analytical model.	75
3.4.5	Dimensions of the KUKA manipulator's media flange [142].	76
3.4.6	Exploded view of the clamp assembly design.	76

3.4.7	Dimensions of part A of the clamp assembly, from the front view and plan view.	77
3.4.8	Dimensions of part B of the clamp assembly, from the front view and side view.	78
3.4.9	Dimensions of the bracket, from the front, side and plan view.	79
3.4.10	Trend of the percentage decrease of the amplitude of the link's response achieved by the actuator against the start position of the actuator along the length of the beam.	80
3.4.11	Experimental set-up for open loop validation.	82
3.4.12	FRF base excitation input, tip acceleration output, no piezoelectric patches.	84
3.4.13	FRF base excitation input, tip acceleration output, two piezoelectric patches.	85
3.4.14	FRF base excitation input, voltage output, two piezoelectric patches.	86
3.5.1	Comparison between sinusoidal and circular motion of the manipulator's end effector against the frequency obtained for the excitation of the link.	88
3.5.2	An illustration of the sinusoidal and circular motions of the robot manipulator's end effector.	89
3.5.3	Comparison between sinusoidal and circular motion of the manipulator's end effector against time for the excitation of the link.	89
3.5.4	Illustration of the PZT actuator highlighting the difference between the active and overall dimensions.	90
3.5.5	FRFs of the second link with the additional mass of an IMU and a magnet.	91
3.5.6	Tip mass influence on natural frequency of link B.	93
3.5.7	Illustration of the analytical model.	94
3.5.8	Circuit diagram of the PZT sensors.	97
3.5.9	Illustration of the experimental set-up used to validate the analytical model of link B.	101
3.5.10	FRFs of tip displacement divided by base displacement for the open loop system.	102
3.5.11	FRFs of voltage output from PZT sensors divided by base displacement for the open loop system.	103
4.2.1	Illustration of the proportional control system.	110
4.3.1	Board diagram of the Raspberry Pi 3 and the corresponding GPIO pinout diagram.	117
4.3.2	Image of the PZT actuator employed in this research.	118
4.3.3	DRV2700EVM-HV500 board diagram.	119

4.3.4	An image of the MPU9250 and its pinouts.	123
4.3.5	Illustration of SAR ADC operation.	124
4.3.6	Illustration of SAR ADC logic.	125
4.3.7	MCP3008 pin diagram.	127
4.3.8	MCP3008 functional block diagram.	128
4.4.1	Visualisation of the physical connections within control system A. . . .	130
4.4.2	Visualisation of the physical connections within control system B. . . .	131
4.4.3	Visualisation of I ² C protocol.	132
4.4.4	Visualisation of data manipulation.	136
4.4.5	Visualisation of data check and manipulation.	137
4.4.6	An illustration of the connections between the PZT sensors and PZT actuators, including the circuit diagram.	139
4.4.7	Manipulation of voltage by the circuits and the Raspberry Pi.	141
4.4.8	Circuit diagram of a potential divider circuit.	142
4.4.9	Visualisation of general SPI protocol.	143
4.4.10	Visualisation of the MCP3008 SPI protocol.	145
4.4.11	Illustration of PWM method.	147
4.4.12	Relationship between the input and output voltage of the HVDs. . . .	147
4.4.13	Flow diagram illustrating the connection between the SBC, a HVD and a PZT actuator.	148
4.5.1	Image of dSPACE MicroLabBox.	149
4.5.2	Image of the connection ports on the top side of the dSPACE Micro- LabBox, highlighting those related to the connections of the control system.	152
4.6.1	Circuit enclosure design.	157
4.6.2	Exploded view of circuit enclosure design.	158
4.6.3	Circuit diagram of the circuit used to prevent accidental contact with high voltage source.	158
4.6.4	Image of the circuit enclosure.	159
5.1.1	Illustration of the experimental set-up used to validate the closed loop analytical model of control system A.	162
5.1.2	Image of the experimental set-up used to validate the closed loop ana- lytical model of control system A.	163
5.1.3	Results of control system A; open loop, closed loop and closed loop with phase correction.	165
5.1.4	Experimental results in the time domain showing the influence of the phase correction on the voltage application.	167

5.1.5	Analytical results in the time domain showing the influence of the phase correction on the voltage application.	168
5.1.6	Analytical time delay results comparing uncontrolled and controlled tip displacement with varying time delay on the controlled results.	169
5.1.7	Comparison between analytical and experimental results.	171
5.1.8	Results in the time domain with and without control (base excitation frequency: 15.8 Hz).	172
5.2.1	Illustration of the experimental set-up used to validate the closed loop analytical model of control system B.	174
5.2.2	Image of the experimental set-up used to validate the closed loop analytical model of control system B.	175
5.2.3	Percentage decrease attained by the RPi for a range of gain values ($K_p = 0$ to 1040).	176
5.2.4	FRF of tip displacement divided by base displacement for multiple gains for the experimental (solid lines) and analytical (dashed lines) results.	177
5.2.5	FRF of voltage output from PZT sensors divided by base displacement for multiple gains for the experimental (solid lines) and analytical (dashed lines) results.	179
5.2.6	Proportionality between tip displacement and voltage output from piezoelectric sensors for varying gains.	180
5.3.1	Example of the signals from the dSPACE governing the shaker and RPi outputs.	182
5.3.2	Example of the signals from the dSPACE governing the change of gain value at each cycle.	183
5.3.3	Comparison of the settling time achieved with increasing proportional gain between the dSPACE and Raspberry Pi 3 systems.	184
5.3.4	Experimental results of the dSPACE and RPi control systems for two gain values.	185
5.3.5	Comparison between the FRFs of the RPi and dSPACE control systems for different cases of gains.	186
5.3.6	Comparison of the percentage decrease of tip displacement achieved with increasing proportional gain between the dSPACE and Raspberry Pi 3 systems.	187
5.4.1	The relationship between centripetal acceleration of the end effector against the frequency for a range of maximum joint velocities.	189
5.4.2	The relationship between the radius of the motion of the end effector against the frequency for a selected range of maximum joint velocities.	189

5.4.3	An illustration of the connections between the PZT sensors and PZT actuators, including the circuit diagram (repeated).	191
5.4.4	Experimental set-up of the link mounted upon the robot manipulator.	191
5.4.5	Settling time against proportional gain (K_p) for joint one of the KUKA manipulator moving 10° at 100% velocity.	193
5.4.6	Percentage decrease of voltage from sensors when excited at the natural frequency, when mounted on the KUKA manipulator.	194
5.4.7	Relationship between radius of the end effector motion and velocity of the robot manipulator, and the excitation frequency produced.	195
5.4.8	A comparison between the predicted frequencies obtained from interpolating data, and the experimental frequencies attained.	196
5.4.9	The response of the system against the frequency of excitation for three cases of K_p , for the experimental results (solid lines) and the analytical results (dashed lines).	196
5.4.10	A comparison of the calculated end effector position from the analytical model and the end effector position retrieved from the experimental studies.	197
6.1.1	Relationship between the static deflection of a system due to increasing levels of force for five different definitions of the stiffness term.	203
6.2.1	Image of an initial set-up used in the nonlinear experiments (see ‘Case 2’ in Table 6.2.1).	205
6.2.2	The change in the natural frequency of the system in relation to an increase in the magnitude of force for multiple cases wherein the structure is altered.	205
6.2.3	Image of the improved set-up used in the nonlinear experiments.	208
6.2.4	Image of the spring configuration utilised in the nonlinear experiments.	209
6.2.5	Illustration of the connections between the components and devices used throughout the nonlinear experiments.	210
6.2.6	An illustration of the nonlinear experimental set-up, including the circuitry of the employed control system.	211
6.2.7	Response of the structure under increasing forces, sweeping upwards through frequencies surrounding the first natural frequency.	212
6.2.8	Response of the structure under increasing forces, sweeping upwards through frequencies surrounding the second natural frequency.	214
6.2.9	Results pertaining to the first natural frequency of the structure for five different excitation force magnitudes, sweeping both up and down the frequency range.	215

6.2.10	Results pertaining to the second natural frequency of the structure for five different excitation force magnitudes, sweeping both up and down the frequency range.	216
6.3.1	An illustration of the circuit used in the nonlinear experiments.	219
6.3.2	An illustration of the boundary conditions for the linear and nonlinear investigations.	219
6.3.3	Controlled response of the structure excited at 3 N of force sweeping upwards through the frequency range surrounding the first natural frequency for varying gain values.	220
6.3.4	The voltage output from the PZT sensors divided by the magnitude of the force excitation (3 N) for multiple proportional gain values.	221
6.3.5	Controlled response of the structure excited at 5 N of force sweeping upwards through the frequency range surrounding the first natural frequency for varying gain values.	222
6.3.6	The voltage output from the PZT sensors divided by the magnitude of the force excitation (5 N) for multiple proportional gain values.	222
6.3.7	Controlled response of the structure excited at 7 N of force sweeping upwards through the frequency range surrounding the first natural frequency for varying gain values.	223
6.3.8	The voltage output from the PZT sensors divided by the magnitude of the force excitation (7 N) for multiple proportional gain values.	223
6.3.9	The response of the structure for an excitation force of 3 N, sweeping both upwards and downwards in frequency for selected cases of proportional gain values.	224
6.3.10	The response of the structure for an excitation force of 5 N, sweeping both upwards and downwards in frequency for selected cases of proportional gain values.	225
6.3.11	The response of the structure for an excitation force of 7 N, sweeping both upwards and downwards in frequency for selected cases of proportional gain values.	226
6.3.12	The response of the structure where the base excitation was swept upwards through the first and second natural frequencies at a force level of 3 N for three magnitudes of control gain.	227
6.3.13	The response of the structure where the base excitation was swept upwards through the first and second natural frequencies at a force level of 5 N for three magnitudes of control gain.	227

6.3.14	The response of the structure where the base excitation was swept upwards through the first and second natural frequencies at a force level of 7 N for three magnitudes of control gain.	228
6.4.1	An illustration of the nonlinear analytical model.	229
6.5.1	A comparison between the experimental data obtained across the first and second natural frequencies experimentally, and the data simulated by the analytical model at a force level of 5 N with a) no control applied, and b) control applied.	236
6.5.2	A comparison between the experimental data obtained across the first and second natural frequencies experimentally, and the data simulated by the analytical model at a force level of 7 N with a) no control applied, and b) control applied.	237
7.1.1	The response of the system (tip displacement divided by the base displacement) for varying values of integral gain ($K_p = K_d = 0$).	243
7.1.2	An illustration of the block diagram of the closed loop system, highlighting the control block.	245
7.1.3	A comparison between the experimental (solid lines), analytical model (dashed lines), and transfer function model (dotted lines) results concerning a) the tip displacement, and b) the voltage output from the sensors.	246
7.2.1	The results published by Tan et al. [180] showing the responses of the system for a) nominal model and b) delay increases by 20%.	249
7.3.1	The value of the ITAE for the case of the parametric sweep of the proportional gain (K_p), with the integral and derivative gains set to zero ($K_d = K_i = 0$)	252
7.3.2	The value of the ITAE for the case of a) the parametric sweep of the integral gain when $K_p = 2860$, b) the parametric sweep of the derivative gain when $K_p = 2860$, c) the parametric sweep of the derivative gain when $K_p = 2860$ and $K_i = -23745$, and d) the parametric sweep of the integral gain when $K_p = 2860$ and $K_d = 120$	253
7.3.3	The value of the ITAE for the case of a) the parametric sweep of the proportional and integral gains ($K_d = 0$), and b) the parametric sweep of the proportional and derivative gains ($K_i = 0$).	256
7.3.4	The response of the system subjected to a unit impulse with the application of the values from the parametric sweep, the optimisation and the Z-N method for a) P, b) PI, c) PD, and d) PID control.	258

7.3.5	The response of the system subjected to a unit impulse with the application of the values from the optimisation for the four cases of control P, PI, PD and PID, alongside the case where no control was applied.	259
7.3.6	The response of the system subjected to a harmonic disturbance with the application of the values from the parametric sweep, ITAE method and the Z-N method compared with the case where no control was applied for a) P, b) PI, c) PD, and d) PID control.	260
7.3.7	The voltage applied to the PZT actuators when utilising P control with the gain value obtained from the optimisation in the case of a harmonic disturbance of the frequencies a) 2 Hz, b) 2.5 Hz, c) 3 Hz, and 10 Hz.	264
7.3.8	The response of the system when utilising P control with the gain value obtained from the optimisation in the case of a harmonic disturbance of the frequencies a) 2 Hz, b) 2.5 Hz, c) 3 Hz, and 10 Hz.	265
7.3.9	The response of the system subjected to a harmonic disturbance with the application of the control values from the parametric sweep, ITAE method and the Z-N method with the voltage limit removed. These cases were compared with the case where no control was applied for a) P, b) PI, c) PD, and d) PID control.	267
7.4.1	A simplified version of the block diagram of the system.	270
7.4.2	The transient response of the link for both the CTDM and the DTDM.	271
7.4.3	ITAE values across a parametric sweep of the proportional gain for the CTDM, the DTDM and the DTDM where the integral was performed using the sampling interval of the CTDM.	273
7.4.4	ITAE values normalised to unity across a parametric sweep of the proportional gain for the CTDM, the DTDM and the DTDM where the integral was performed using the sampling interval of the CTDM.	274
7.4.5	ITAE values normalised to unity across a parametric sweep of the derivative gain whilst holding the proportional gain constant ($K_p = 2860$) for the CTDM, the DTDM and the DTDM where the integral was performed using the sampling interval of the CTDM.	275
7.4.6	The transient response of the system as a result of a unit impulse disturbance for both the CTDM and the DTDM, where the control gain values were obtained through optimisation for use within a) P, b) PI, c) PD, and d) PID control.	276
7.4.7	The transient response of the system as a result of a unit impulse disturbance for both the CTDM and the DTDM using P control for a) $K_p = 100$, b) $K_p = 1000$, c) $K_p = 10000$ and d) $K_p = 100000$	277

7.4.8	The transient response of the system as a result of a unit impulse disturbance for both the CTDM and the DTDM using PI control ($K_p = 2860$) for a) $K_i = -100$, b) $K_i = -1000$, c) $K_i = -10000$ and d) $K_i = -25000$	279
7.4.9	The transient response of the system as a result of a unit impulse disturbance for both the CTDM and the DTDM using PD control ($K_p = 2860$) for a) $K_d = 100$, b) $K_d = 1000$, c) $K_d = 10000$, and d) $K_d = 100000$	280
7.4.10	A comparison between the experimental (solid lines), the CTDM (dashed lines), and the DTDM (dotted lines) results.	281

List of Tables

2.1.1	Time-line of the milestones surrounding industrial robotic manipulators.	34
2.1.2	Time-line of the milestones surrounding industrial robotic manipulators (continued).	35
2.3.1	Labels of dimensions shown in Figure 2.3.1 outlining the KUKA LBR iiwa 7 R800 workspace.	46
2.4.1	D-H parameters, range of motion (ROM) and maximum joint velocities (MJV) used in the analytical model.	49
3.3.1	Actions on the PZT element and the resultant polarity of the voltage output with respect to the poling voltage.	65
3.4.1	Geometric, mechanical and electric properties of link A and piezoelectric patches.	80
3.5.1	Geometric, mechanical and electric properties of link B and piezoelectric patches.	90
3.5.2	Nomenclature repeated for convenience.	95
4.3.1	SBC specification comparison.	114
4.3.2	SBC specification comparison (continued).	115
4.3.3	Specifications of the selected piezoelectric actuator.	118
4.3.4	HVD board switch positions for each maximum voltage selection.	120
4.3.5	Comparison between potential IMUs based upon their specifications.	122
4.3.6	MCP3008 specifications.	127
4.4.1	List of writing registers associated with the IMUs' sensors.	134
4.4.2	List of reading registers associated with the IMUs' sensors.	136
4.4.3	List of sensitivity factors associated with the gyroscope.	138
4.4.4	List of sensitivity factors associated with the accelerometer.	138
4.4.5	MCP3008 clock timing parameters.	144
4.4.6	MCP3008 configuration bits.	146
4.5.1	Comparison between the RPi and the dSPACE MicroLabBox.	150
4.6.1	Risk assessment of experiments.	154
4.6.2	Risk assessment of experiments (continued).	155

6.1.1	A brief history of dynamics that includes some of the major milestones and notable works leading to current research on nonlinear dynamics. . .	201
6.2.1	Alterations made to the experimental set-up, leading to the suppression of its softening aspects.	206
6.2.2	Geometric, mechanical and electric properties of link B and piezoelectric patches.	210
6.4.1	Nomenclature used in the nonlinear analytical model (with some variables repeated for convenience).	230
6.5.1	Values of the unknown parameters obtained through optimisation. . .	234
7.3.1	The Ziegler-Nichols tuning method parameters for four control types (P, PI, PD and PID).	250
7.3.2	Gain values obtained based on the parametric sweeps, alongside the corresponding ITAE value for each of the investigations.	254
7.3.3	Gain values obtained based on the parametric sweeps, the optimisation and the Z-N tuning method, alongside the corresponding ITAE value for each of the control schemes (P, PI, PD and PID).	257
7.3.4	The percentage decrease of the response amplitude based on the uncontrolled response amplitude when the voltage limit is imposed.	262
7.3.5	The percentage decrease of the response amplitude based on the uncontrolled response amplitude when the voltage limit is not imposed. . . .	266
7.3.6	The natural frequencies of the link for the cases where P, PI, PD and PID were employed, for the three methods of obtaining the optimal gains both with and without the voltage limitation.	266

Abbreviations

AC	Alternating Current
ACLD	Active Constrained Layer Damping
ADC	Analog to Digital Converter
AI	Artificial Intelligence
AVC	Active Vibration Control
BCM	Broadcom
C-C	Cohen-Coon
CLK	Clock
CNC	Computer Numerical Control
\overline{CS}	Chip Select
CSA	Control System A
CSB	Control System B
CTDM	Continuous-Time Domain Model
DAC	Digital to Analog Converter
DAQ	Data Acquisition
DC	Direct Current
D-H	Denavit-Hartenberg
DOF	Degrees Of Freedom
DTDM	Discrete-Time Domain Model
DTFT	Discrete-Time Fourier Transform
EBT	Euler-Bernoulli Beam Theory
EDSM	Equivalent Dynamic Stiffness Damping
EVM	Evaluation Module
FEM	Finite Element Modelling
FES	Functional Electrical Stimulation
FFT	Fast Fourier Transform
FK	Forward Kinematics
FRF	Frequency Response Function
G-P	Gain-Phase
GPIO	General Purpose Input/Output
GPR	Gaussian Progress Regression
GUI	Graphics User Interface
HVD	High Voltage Driver
HWRC	Half Wave Rectifier Circuit

I ² C	Inter-Integrated Circuit
IAE	Integral of the Absolute Error
IK	Inverse Kinematics
IMU	Inertial Measurement Unit
IoT	Internet of Things
ISE	Integral of the Square Error
ITAE	Integral of the Time-weighted Absolute Error
LDS	Laser Displacement Sensor
LDR	Light Dependent Resistor
LQG	Linear Quadratic Gaussian
LQR	Linear Quadratic Regulator
LSB	Least Significant Bit
MCXA	Modified Complex Averaging
MEMS	Microelectromechanical Systems
MF	Media Flange
MISO	Master Input Slave Output
MJV	Maximum Joint Velocities
MOSI	Master Output Slave Input
MPL	Modular Prosthetic Limb
MSB	Most Significant Bit
MSMA	Magnetic Shape Memory Alloys
P	Proportional (control)
PI	Proportional-Integral (control)
PID	Proportional-Integral-Derivative (control)
PC	Personal Computer
PD	Proportional-Derivative (control)
PDC	Potential Divider Circuit
PEM	Piezoelectromechanical
PID	Proportional Integral Derivative
PPF	Positive Position Feedback
PZT	Lead Zirconate Titanate
RAM	Random Access Memory
ROM	Read Only Memory
RPi	Raspberry Pi Model 3 B+
SAR	Successive-approximation
SBC	Single Board Computer

SCL	Serial Clock
SDA	Serial Data
SHM	Structural Health Monitoring
SMA	Shape Memory Alloy
SMC	Sliding Mode Control
SOC	Splice On Connector
SPI	Serial Peripheral Interface
SSA	Self-Sensing Actuator
TBT	Timoshenko Beam Theory
UART	Universal Asynchronous Receiver-Transmitter
WOVL	WithOut Voltage Limit
WVL	With Voltage Limit
Z-N	Ziegler-Nichols

Nomenclature

a	D-H parameter
a_c	Centripetal acceleration
A	Cross-sectional area (of both the link and PZT elements)
A_{lk}	Cross-sectional area (of the link)
A_{pa}	Cross-sectional area (of PZT actuators)
A_{ps}	Cross-sectional area (of PZT sensors)
B	Magnetic field (vector component with subscript denoting direction)
\bar{B}	Magnetic field (vector)
c	A constant of the Lyapunov function
c_a	Viscous air damping coefficient
C	Damping term
C_{ps}	Capacitance of PZT sensors
d	D-H parameter
D_{OUT}	Serial data out
E	Young's modulus (of both the link and PZT elements)
E_{lk}	Young's modulus (of the link)
E_{out}	End effector coordinate output
E_{pa}	Young's modulus (of PZT actuators)
E_{P_0}	Error of system (in terms of the generalised coordinate)
E_{ps}	Young's modulus (of PZT sensors)
$E_{V_{ps}}$	Error of the system (in terms of the voltage output from the PZT sensors)
\bar{E}	Electric field
E_{Hall}	Hall electric field
f	Frequency
$func$	Arbitrary function
F_i	The i^{th} coordinate frame
F	Force with subscripts denoting the direction (x , y , and z)
g_0	Magnitude of the base displacement (CSB)
G	Transfer function (subscripts denote variants)
h	Thickness (of both the link and PZT elements)
h_{lk}	Thickness (of the link)
h_{pa}	Thickness (of PZT actuators)
h_{ps}	Thickness (of PZT sensors)
H	Heaviside function

i	General index number (unless otherwise stated)
i_{ps}	Current from PZT sensors
I	Second moment of area (of both the link and PZT elements)
I_{lk}	Second moment of area (of the link)
I_{pa}	Second moment of area (of PZT actuators)
I_{ps}	Second moment of area (of PZT sensors)
IMG	Imaginary component of PZT sensor voltage
j	$\sqrt{-1}$
k_l	Linear spring stiffness
k_n	Nonlinear spring stiffness
k_s	Stiffness of the stinger
K	Stiffness term
K_{cr}	Critical gain
K_d	Derivative gain value
K_i	Integral gain value
K_p	Proportional gain value
$l_{spring,0}$	Relaxed spring length
$l_{spring,ext}$	Extended spring length
L	Length (of both the link and PZT elements)
L_{lk}	Length (of the link)
L_{pa}	Length (of PZT actuators)
L_{ps}	Length (of PZT sensors)
L_{pa}^Ψ	Active length (of PZT actuators)
L_{ps}^Ψ	Active length (of PZT sensors)
M	Mass term
M_{FT}	Mass of force transducer
M_{IMU}	Mass of IMU
M_{TM}	Mass of tip mass
n	Mode number
N_f	Number of frequency points in optimisation process
O	Objective function
P	Generalised coordinate
q_0	Magnitude of charge
$Q_{n,i}$	The complex amplitude of the i^{th} harmonic of the generalised coordinate
r	Radius of robot end effector motion

R_1	Resistor across PZT sensors (part of HWRC)
R_2	Resistor in the PDC
R_3	Resistor in the PDC
R_{lps}	Resistive load across PZT sensors (internal resistance)
RE	Real component of the PZT sensor voltage
s	$j\omega$ (continuous-time domain) $\frac{2(z-1)}{T_t(z+1)}$ (discrete-time domain)
S	Sensitivity matrix
sig	Closed loop control signal (CSA)
t	Time
t_{HI}	Time that the signal is held high
t_{LO}	Time that the signal is held low
t_{SUCS}	Time delay in starting communication and the clock line's first rise
T	Transformation matrix
T_{cr}	Critical period
T_t	Sampling interval
u_1	Weighting of the natural frequency in the objective function
u_2	Weighting of the damping ratio in the objective function
u_{RE}	Weighting applied to the stiffness term of the link structure
u_{IMG}	Weighting applied to the damping term of the link structure
\vec{v}	Velocity of charge (vector component with subscript denoting direction)
$\vec{v}_{i,max}$	Maximum joint velocity of i^{th} joint
\bar{v}	Velocity of charge (vector)
V_{DAC}	Voltage output from the digital to analog converter
V_{GND}	Voltage ground
V_{Hall}	Hall voltage
V_{in}	Voltage input to a device
$V_{in,pa}$	Amplitude of voltage applied to PZT actuators
V_{pa}	Voltage to the PZT actuators
V_{ps}	Voltage from PZT sensors
V_{REF}	Reference voltage
$w(y, t)$	Transverse motion of the link structure
$w_b(y, t)$	Applied base excitation to the link structure
$w_{rel}(y, t)$	Relative transverse motion of the link structure
W	Width (of both the link and PZT elements)

W_{Hall}	Width (of the Hall sensor)
W_{lk}	Width (of the link)
W_{pa}	Width (of PZT actuators)
W_{ps}	Width (of PZT sensors)
W_{pa}^{Ψ}	Active width (of PZT actuators)
W_{ps}^{Ψ}	Active width (of PZT sensors)
$x(t)$	Base excitation displacement (CSA)
x_0	Magnitude of the base displacement (CSA)
y_1	Start of piezo actuators (CSA)/PZT sensors (CSB)
y_2	End of piezo actuators (CSA)/PZT sensors (CSB)
y_3	Start of PZT actuator (CSB)
y_4	End of PZT actuator (CSB)
y_{IMU}	IMU position along the length of the link
y_{LDS}	Distance along the length of the link at which the LDS is positioned
z	$j\omega$ (discrete-time domain)
α	D-H parameter
α_{NL}	A factor of nonlinear restoring force
α_V	Ratio between displacement of link and voltage from PZT sensors
β_n	Weighted frequency of the n^{th} mode
γ_n	Magnitude of the eigenfunction for the n^{th} mode
Γ	Rotation about world frame axes of robot manipulator
δ	Dirac delta function
Δf	Frequency interval
$\bar{\epsilon}_{33}$	Dielectric permittivity coefficient
ζ	Damping ratio
ϑ_{pa}	Piezoelectric coupling term of the PZT actuators
ϑ_{ps}	Piezoelectric coupling term of the PZT sensors
θ_{pa}	Piezoelectric coupling coefficient of the PZT actuators (after Galerkin decomposition)
θ_{ps}	Piezoelectric coupling coefficient of the PZT sensors (after Galerkin decomposition)
$\dot{\Theta}$	Angular velocity
κ_{nps}	Modal coupling term of the PZT sensors for the n^{th} mode
Λ_i	Angle of a joint at some step i in a series
REF	Control reference signal

ρ	Density (of both the link and PZT elements)
ρ_{lk}	Density (of the link)
ρ_{ps}	Density (of PZT sensors)
ρ_{pa}	Density (of PZT actuators)
σ_n	Dimensionless ratio of the n^{th} mode
Υ	Coefficient of proportional damping
ϕ	Mode shape
Φ_i	Joint angle of i^{th} joint (radians) (D-H parameter)
Ψ_i	Joint angle of i^{th} joint (degrees) (sensitivity matrix parameter)
ω	Angular frequency
ω_n	Natural angular frequency
ω_p	Excitation frequency in the frequency domain
Ω_F	Frequency of the force applied to the link
Ω_v	Frequency of voltage applied to PZT actuators
Ω_x	Frequency of excitation applied to the link
ϖ	Coefficient of proportional damping

Chapter 1

Introduction

Vibrations are commonplace throughout engineering, from small intricate structures such as microelectromechanical systems (MEMS) to large structures such as buildings and bridges. In some situations vibrations are useful and are even induced, however, more often than not those non-induced vibrations can be categorised as a nuisance. Unwanted vibrations can cause a multitude of problems of varying degree, from making a journey uncomfortable (i.e. a car driving over a rough road) to damaging the structural integrity (possibly leading to the collapse) of a building or bridge. An example of this is the resonant structural response of the Millennium Bridge in London [4] which led to the structure swaying from side to side as pedestrians walked across it. A considerable amount of research has been conducted to offer a solution to the attenuation of unwanted vibrations [5, 6], especially for systems used by the general public (i.e. shock absorbing suspension systems in cars).

Robot systems are becoming increasingly popular, and their range of applications wider with new technology and market demand being used by both industries and the general public. This rising field of engineering is not immune from the same vibration problems that plague other areas of engineering. In addition, another commonality lies in the endeavours of robotics to produce lighter, less expensive robots with an equivalent or ideally a higher performance level than pre-existing models. The lower the cost of a design the higher the profit, and the lighter the product the easier it is to transport and/or mount on surfaces. Industrial applications of robotics often includes the implementation of robot manipulators (arms) within a production line. Sometimes these manipulators remain fixed in one place, and in others they are to move along a production line or warehouse as part of an automated process. The latter case often requires a specialist moving platform, and even in the former case the manipulators will require additional equipment for transport/installation.

Acknowledging both of these engineering issues/desires (vibration and weight reduc-

tion) and the rising popularity of robotics this research aims to explore current works seeking a solution to the issue or fulfilling the desire. By doing so a potential research gap may be identified, defining a specific problem that requires a solution. A literature review of existing research pertaining to the fields in question has been conducted and the findings presented in this chapter. Following this a specific problem has been defined based on the potential contribution to the fields of robotics and vibration control that may be yielded from this research. A suggested application is proposed in order to further highlight the solution's potential within engineering, before an overview of how this research has been conducted and is presented in this text.

1.1 Literature review

Active vibration control using smart materials has increasing prevalence in research as a solution for unwanted vibrations experienced in mechanical devices and structures [7]. From large structures to small intricate designs unwanted vibrations many cause a multitude of issues, including: inaccuracies in movements, discomfort to the user(s) and the degradation of a structure. Reducing the magnitude of these vibrations and therefore limiting their negative impact consequently becomes an important aspect of a design. Relevant research to that of this thesis has been reviewed, and is presented here segmented based upon the main topic(s) of the research in a manner that befits the topics addressed or considered in this thesis.

The first two topics to be addressed involve passive and active vibration control, particularly concerning the relevant advantages and disadvantages in relation to this research. Following this, research relating to PZT elements is reviewed, then research which employs single board computers (SBCs), modelling techniques for beam type structures are then investigated before works that pertain to the control of flexible robot links. The last two topics of interest involve the modelling of robot manipulators and research that relates to nonlinear vibrations including modelling and control.

1.1.1 Passive vibration control

Passive vibration control does not utilise an external power source to attenuate vibrations, instead it utilises structures, devices or materials to dissipate the energy from the vibrations. This form of vibration control has issues when considering the changes in the host structure's vibrations in terms of the frequency (when the frequency is far from the control system's inherent resonance) or direction of the motion [8]. However, the advantages of this type of control lie in its independence from an external power source and controllers that are employed in active vibration control systems, omitting these, the control system is often less expensive [9]. One of the earliest forms of suspension, the Leaf-Spring, was used in stage coaches to reduce vibrations experienced by the driver/passengers [10], which is a form of passive vibration control. Due to the limitation of the technologies at that time these suspension devices were constructed from wrought iron. To obtain the correct combination of both compliance and strength the sections were layered to form a curved structure. Two of these curved structures were mounted back to back to create an elliptical shape in an effort to increase the overall compliance of the system. The device was then mounted between the chassis and the wheels of the vehicle to absorb the vibrations produced from the wheels moving over an uneven surface. A patent held by G.B. Selden approved in 1895 shows these

leaf springs as part of an 'Improved Road-Engine' design, denoted as 'E' in Figure 1.1.1 [11].

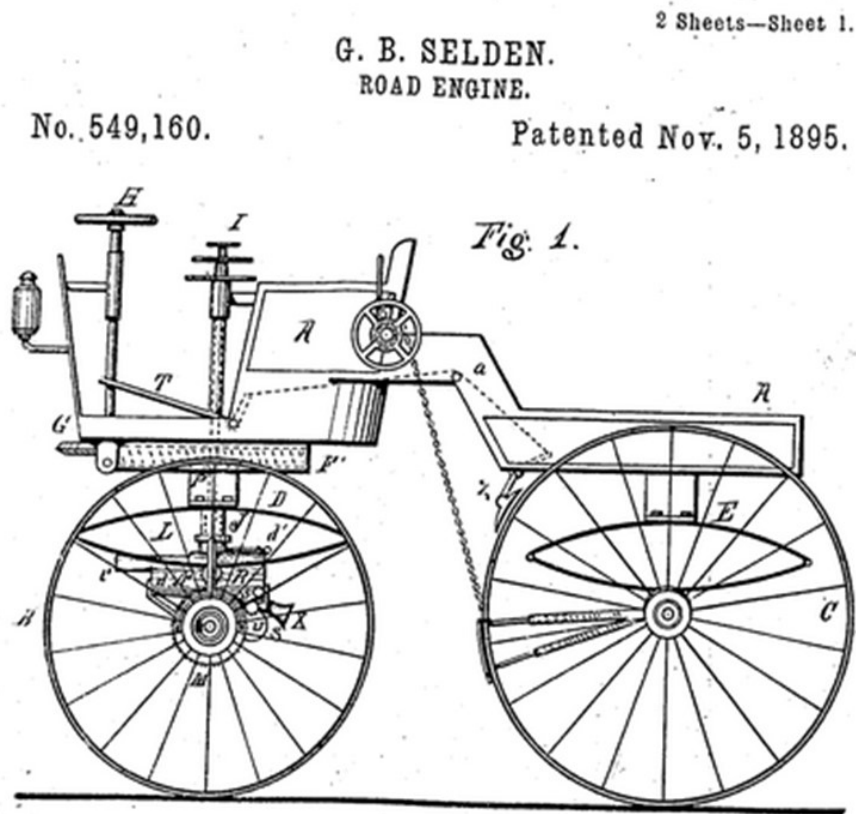


Figure 1.1.1: The road engine design of G.B. Selden patented in 1895 [11].

One of the first and more prevalent pieces of research focussing on Lead Zirconate Titanate (PZT) elements and their use in intelligent structures was that by Crawley and de Luis [12]. This research considered the PZT elements both surface mounted and embedded actuators on/within a cantilever host beam. This research does not investigate the use of these PZT elements as part of a control system, but focusses on the impact of their inclusion on the dynamics of the structure. It also observes the displacement produced through the application of voltage to the PZT elements resulting in a strain on the host beam. An analytical model was developed for both of these cases based on Euler-Bernoulli beam theory (EBT), to provide a method of accurately predicting such intelligent structures, with the results from the model compared to those obtained experimentally. Crawley and de Luis proved that a good level of excitation could be yielded from PZT elements, whilst their inclusion within the structure has limited effects on the dynamic properties. It may be concluded from the PZT elements' excitation capabilities, they had the potential to counteract unwanted excitations. This research provided a good foundation for related research which expanded on the concept

of intelligent structures, with an impressive number of citations.

The authors (as part of a team) then published further research investigating the utilisation of PZT elements to facilitate energy dissipation from a structure [13]. The strain from the mechanical structure is converted from mechanical to electrical energy by the PZT element, and this electrical energy is dissipated through a resistor. This in turn leads to the suppression of the vibration in the structure, this type of control system is considered to be passive. There is no feedback system, and the properties or parameters of the materials/components are not adjusted in relation to the magnitude of the vibrations experienced, as with the Leaf-Spring design. Further research on this concept that employs PZT elements was conducted by Hagood and von Flotow [14] with the intention to negate the disadvantage of requiring a power supply as experienced by other control systems. dell’Isola et al. expanded on this idea through research which explores the performance of distributed electric networks and piezoelectric elements in terms of attenuating the vibrations experience by a beam, with a set-up as shown in Figure 1.1.2 [15]. This research utilised both resistors (R) and inductors (L) connected in parallel to piezoelectric elements which were distributed across a beam structure to create what is referred to as a piezoelectromechanical (PEM) structure.

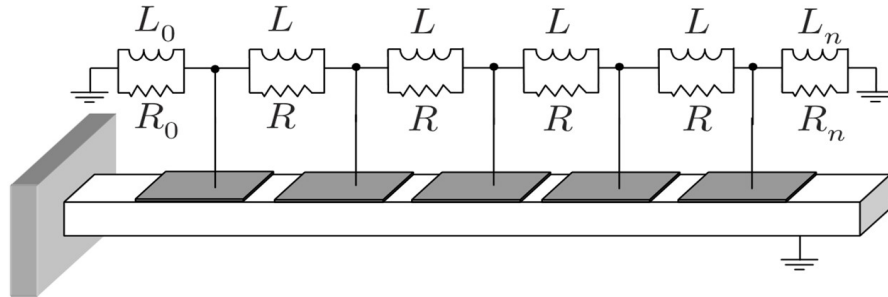


Figure 1.1.2: Illustration of the experimental set-up used in the research by dell’Isola et al [15].

The distribution of the PZT elements and electronic components was utilised in an effort to “prove the technical feasibility of PEM structures and the effectiveness of the underlying concept of distributed control in reducing tuning inductances without affecting damping performance”. In other words this research aims to address the main issues that arise with passive damping systems that include PZT elements. Whilst using a resistor in parallel allows for the control of a wide range of frequencies and its implementation requires only the addition of the components to the system, the performance of this system is limited. To improve the performance an inductor may be introduced into the circuit, also in parallel with the resistor and the PZT element. However, to obtain the advantage of better performance there is a requirement that the electric circuit be ‘tuned’ so that its natural frequency is in line with that of the

structure, which in turn requires a very large value of inductance. The higher the level of inductance, the larger the parasitic dissipation experienced which affects the optimal design of the system. Aside from this issue, the necessity for tuning the system greatly reduces the frequency range in which the system is effective. The approach used by dell'Isola et al. did find advantages in the distributed system in that the lumped electric network led to a reduction of the optimal value of inductance, and that this value decreased with the increasing number of PZT elements. In addition, the distributed manner also allowed for a reduction of the vibrations in first, second and third modes, leading to a solution for multi-modal damping.

1.1.2 Active vibration control

In contrast to passive vibration control, active vibration control (AVC) utilises electrically powered sensors, actuators and controllers to form a closed loop system. Whilst the findings by dell'Isola et al. [15] showed that passive control using PZT elements was promising solution for attenuating vibrations with no power source, the limitations of such a system were a concern for this research. The main aim of this research was to control vibrations of unknown frequencies as experienced by a robot manipulator link, as well as investigating the control system's performance when the link is subject to nonlinear vibrations. Hence, employing AVC was considered as a more suitable choice as there are less limitations in terms of the frequency range and performance. The requirement of a power source was not deemed a disadvantage in this research as the main application is on a system which itself requires a power source. An array of research has been published that investigates the use of PZT elements in AVC systems, focussing on different types of structures and utilising a variety of components and control theories to control the PZT actuators [16, 17, 18]. Which structural type/components/control theory used in the research is dependent on the particular problem to be addressed.

Shell structures are used across multiple fields of engineering, and may be defined as structures that are curved with one dimension (i.e. their thickness) smaller than the others [19]. Research by Sun et al. [20] focussed on the AVC of conical shells, to prevent user discomfort and/or false instrument readings in such applications as rocket construction or the nuclear industry. Several PZT elements of varying sizes were surface mounted onto an aluminium conical shell, and were assigned to be an excitation source, a sensor, or an actuator. Aside from the novel implementation of the PZT elements coupled with the commonly used structure, this research also sought to provide a better solution with regards to the control theory used. A combination of fuzzy and sliding mode control was employed in an attempt to overcome their disadvantages as individual theories and build on their advantages simultaneously. Fuzzy logic control (or just

fuzzy control) was first introduced in a proposal by Zadeh [21], but its concept had been studied a lot sooner, known as ‘infinite-valued logic’ from the 1920s [22]. It’s concept is somewhat of an opposition to Boolean logic in which the values returned by a logic statement are either entirely true or entirely false (0 or 1), in fuzzy logic a ‘degree of truth’ is used where the statement could return any value between 0 and 1. A higher value in this logic system represents the closer the statement is to the truth. The advantage of fuzzy logic control is that an accurate mathematical model is not required, however it can yield poor dynamic responses. Sliding mode control may be defined as a type of control that has a number of feedback laws and a switching function, which adjusts the output depending on the current system behaviour. A disadvantage of this type of control is chattering, where the oscillations have a finite frequency and amplitude. The combination of these two control systems were proven experimentally to be a robust and effective solution for vibration suppression in a conical shell structure, balancing out the advantages and disadvantages of the individual systems.

Other research which considers shell structures includes that by Ray and Reddy [23], which focussed on the vibration suppression of a fluid conveying cylindrical shell structure. Here the PZT elements were laminated in the shell structure to produce a active constrained layer damping (ACLD). This research utilised a velocity feedback control law, to control the PZT elements, the novelty of this research lies in the observation of the hydro-elastic behaviour of the structure which was modelled using three-dimensional finite elements. It differed from existing finite element models of such intelligent structures as it included the implementation of separate first order shear deformation theories for the laminated shell. Research by Qiu et al. [24] considered a different structure to shells; a cantilever plate. The choice of this structure was based on the specific application of the flexible appendages of spacecraft, where components such as solar panels and satellites dishes may be modelled as cantilever plates. The optimal placement of the PZT elements as well as their performance was observed in this work, and as with the research conducted by Sun et al. [20] the work combines two control theories for the advantageous result (positive position feedback (PPF) and proportional-derivative (PD) control).

A highly revered piece of research by Bailey and Hubbard [25] also focusses on the aerospace applications of PZT elements used in an AVC system. In this instance the structure was developed throughout the paper in terms of size and complexity, until a scale model of a flexible satellite was created. The structure had four perpendicular arms which extended from a central hub, so that each of these arms could be modelled as cantilever beams, hence Euler-Bernoulli beam theory could be used to produce an analytical model. The control algorithms used in this research were designed based on Lyapunov’s second method, which makes use of the Lyapunov function that is analogous

to the potential function used in classical dynamics which observes the potential energy of a system [26]. In this work the Lyapunov function was found with the intention of minimising the time rate of change of the function at each point in time. In other terms this function can be considered to be a method of measuring either how far the beam is from equilibrium or the amount of energy in the system.

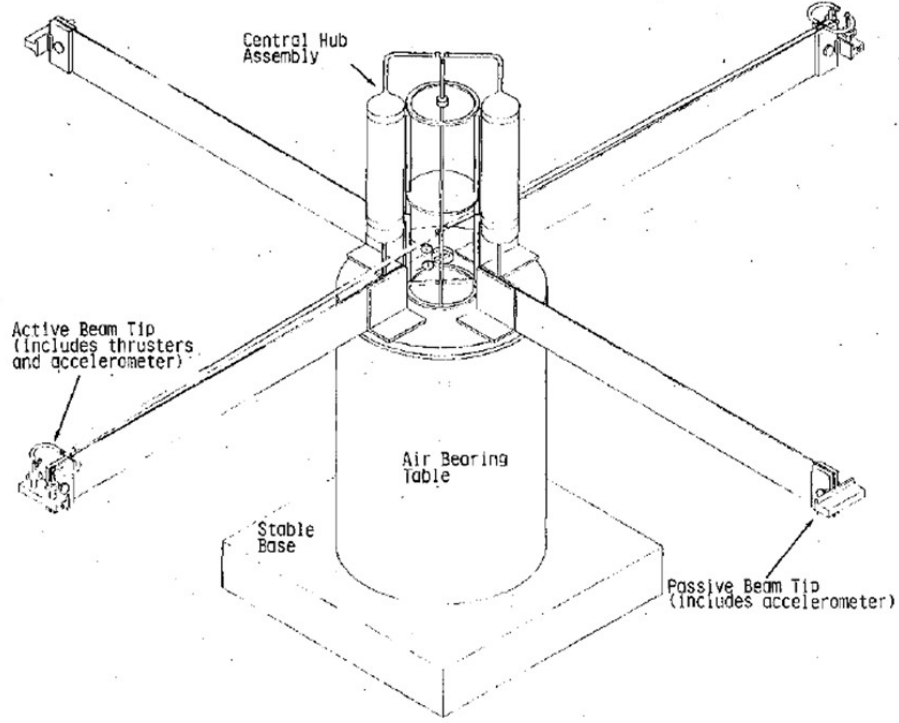


Figure 1.1.3: Illustration of the experimental set-up used in the research by Bailey and Hubbard [25].

$$V = -sgn \left(c \cdot \frac{\partial^2 w}{\partial t \partial x} \Big|_L \right) \cdot V_{max} \quad (1.1)$$

The experimental set-up used by Bailey and Hubbard is illustrated in Figure 1.1.3, and highlights the components of the satellite. An accelerometer is placed on each of the arms to measure the motion at the tips, a PZT layer of distributed elements is bonded to each arm as an actuator. Equation 1.1 is that used in the research to calculate the voltage to be applied to the PZT actuators (V). $sgn()$ represents the sign function and c is a constant to ensure to ensure that the bending moment produced by the PZT elements opposes the angular velocity experienced at the tip of the arms. The partial differential $\frac{\partial^2 w}{\partial t \partial x} \Big|_L$ represents this angular velocity, measured at the tip position (L), and V_{max} is the maximum voltage which may be safely applied to the PZT element(s). As with most control laws this one has its advantages and disadvantages. As the input

to the control law is the angular velocity at the tips of the arms, and every mode has angular motion at the tip, the control law should, theoretically, work with all modes. Only one sensor is required in this system, as the control law only requires the angular velocity at one point along the beam. The main disadvantage of the control law is that when the argument to the $sgn()$ function is zero it becomes nonlinear and discontinuous, which leads to problems and the inability to find solutions. To overcome this, Bailey and Hubbard sought to replace the function with a continuous one that would provide a better approximation. In addition there would also be an issue in that the angular tip velocity would not be “readily available”. To overcome this the accelerometer may be used to predict the linear velocity of the tip, but this prediction is only accurate if the vibration is only associated with one mode. Hence, the first mode was selected for use as it is easily isolated. Two additional algorithms were included in this research to verify the performance of the Lyapunov control law, the first being “constant-gain negative velocity feedback” and the second being “constant-amplitude negative velocity feedback”.

$$V(t) = -sgn \left(f \cdot c \cdot \frac{\partial w}{\partial t} \Big|_L \right) \cdot V_{max} \quad (1.2)$$

$$V(t) = -k \left(f \cdot c \cdot \frac{\partial w}{\partial t} \Big|_L \right), |V(t)| \leq V_{max} \quad (1.3)$$

$$V(t) = -k(t) \left(f \cdot c \cdot \frac{\partial w}{\partial t} \Big|_L \right), |V(t)| \leq V_{max} \quad (1.4)$$

Equation 1.2 is the Lyapunov control law used in [25], which is effectively Equation 1.1 written in terms of the tip’s linear velocity. Equation 1.3 and Equation 1.4 show the constant-gain and constant-amplitude control laws, respectively, both with negative velocity feedback. The performance of the latter two control laws was observed through experimental results, and both were found to adequately suppress the vibrations experienced in the satellite arms. At $V_{max} = 200$ V rms the constant-gain control law was found to have an average loss factor of 0.007, and for the same maximum voltage the constant-amplitude control law had a damping loss factor of 0.04. The settling time of the satellite arm without control was shown to be significantly over 50 seconds (around 60 seconds may be assumed from the results), the constant-gain control law reduced this to 50 seconds, and the constant-amplitude control law reduced this further to 15 seconds. Both of these control laws utilised a maximum voltage of $V_{max} = 200$ V rms. Thus, also proving that with some compromises within the control law, an accelerometer may be used as an input. Beneficial not only for the requirement for only one sensor, but also that the accelerometer readings are independent of the dynamic parameters

that may change with the application of control. Other work which utilises accelerometers as sensors includes that by Gatti et al. [27], which investigated the performance of a collocated accelerometer/PZT actuator combination on a simply supported beam. However, as highlighted in Bailey and Hubbard’s work the compromises made to the control law impose restrictions on the number of modes that may be controlled. Thus further research in AVC seeks to find a solution through the implication of alternate sensors, each with their own merits and flaws as with accelerometers.

1.1.3 PZT sensors and actuators

One of the more prevalent sensor options used in the research of AVC using PZT elements as actuators, is using additional elements as sensors. As previously mentioned, research by Sun et al. employed PZT sensors to provide an input into the chosen control law [20]. PZT elements have the potential for use in other structural shapes such as a plate as demonstrated by Wang et al. [28], or a beam as by Waghulde et al. [29]. Another possibility for the use of PZT elements in AVC was explored by Dosch et al. [30], where the authors utilised a single PZT element as both a sensor and an actuator. The research focussed on the control of a cantilever beam via both strain rate and position feedback control, judging the performance of the control system on the settling time from an initial displacement. The authors concluded that the reductions were “comparable to similar vibration suppression schemes using a separate piezoelectric sensors and actuator”.

A few drawbacks of the implementation of one self-sensing PZT element were noted by Liseli et al. [31]. A voltage based self-sensing actuator (SSA) requires a reference capacitance, which should be equal to the capacitance of the PZT element at all times. However, the PZT element’s capacitance is highly influenced by the pre-load and the control input voltage. In certain (more extreme) conditions the capacitance and/or general performance in terms of sensing/actuation are negatively affected [32, 33]. Hence, to ensure a good level of performance from a voltage based SSA “tedious continual tuning” must be performed on the reference capacitance. The disadvantage of a charge based SSA lies in the PZT elements’ transitional behaviour; following its instantaneous deformation due to an applied electric field, should this electric field be maintained the element will continue to deform due to the creep effect. As a result (even with a small deformation), the element will continue to produce strain-induced charges, which will increase the difference in capacitance between the element and the reference capacitance. As previous mentioned, for a sufficient level of control performance to be attained, these two capacitance values must be equal.

Research by Kumar and Narayanan [34] not only investigates the use in PZT ele-

ments as a collocated sensor/actuator pair for the AVC of a flexible beam, but also investigates the optimal placement of these elements along the length of the beam from a finite element model of the structure. The authors utilised a linear quadratic regulator (LQR) controller within the model, and based the optimal placement on the performance of the LQR controller. Another research piece by Bruch et al. [35] concerns the optimal placement of PZT actuators, with the objective of the shape control of a beam. Interestingly, the authors investigated the performance of a single and a collocated pair of PZT actuators. The conclusion attained from this research was that whilst a single actuator is sufficient for simpler cases, more complicated cases render the solitary actuator virtually redundant. The optimal placement and size of two collocated actuators was also investigated by Wang and Wang [36], where the authors employed EBT with modifications to include the PZT elements as part of the host structure. A controllability index was defined which measures the input energy required to achieve a desired structural control by the PZT elements.

Selected results from the research by Wang and Wang are included as Figure 1.1.4 which contains two plots for an analytical model of a cantilever beam for a) the first mode and b) the first two modes. The x-axis denotes the placement of the PZT element along the beam (from the clamped end of the beam to the centre of the PZT element), and the y-axis denotes the size of the PZT element (width and thickness remain constant). The authors conclude (among other findings) that for the first mode the controllability index is at its highest value when the PZT elements span the full length of the beam (1.5 m). The authors then continue to conclude that for smaller sized PZT elements the optimal placement lies in the region nearest to the fixed end of the beam. Acknowledging the expense of PZT elements which is dependent on their size, it is possible to understand the reasoning behind the authors' investigation of different lengths of PZT elements. The investigation of the first and second modes in modal analysis led to the observation by the authors that the optimal size of the PZT elements would be 1.2 m in length. In addition, the optimal location for the PZT elements was found to be approximately 0.85 m from the fixed end of the beam, which lies between the maximum curvature locations of the first and second modes. Analysing Figure 1.1.4b it may be inferred that even with alternate lengths of the PZT element this optimal location region remains valid.

1.1.4 Single board computers (SBCs)

Many researchers have utilised single board computers (SBCs) as the processor within their control system design. The works of Chomette and Mamou-Mani [37], and Jossic et al. [38] both see the use of a SBC known as a BeagleBone Black as part of the AVC

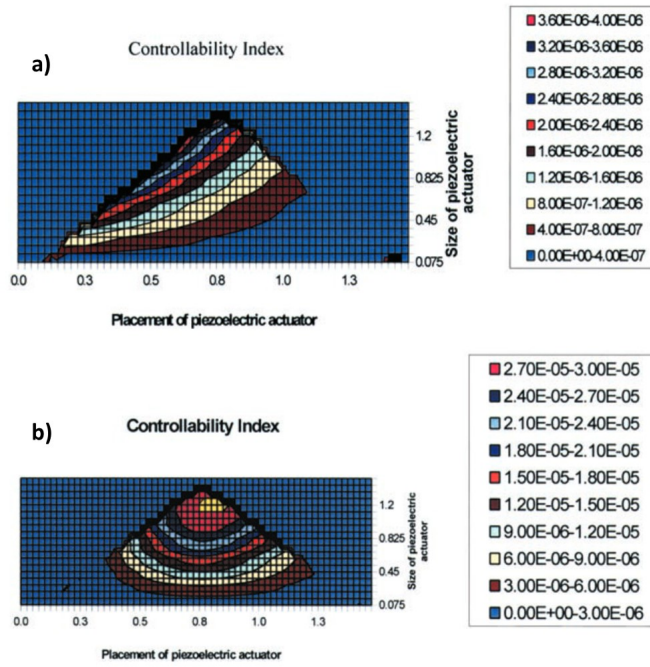


Figure 1.1.4: Contour plots of the controllability index with respect to size and placement of a PZT element on a cantilever beam for a) the first mode and b) the first two modes (Wang and Wang [36])

of Chinese gongs and a plate structure, respectively. Khan and Li [39] implemented an Arduino ATmega-2560 for the generation of signals for controlling the state of solenoid valves that in turn control soft robot chambers. A Raspberry Pi (RPi) 3 Model B was employed by Weber et al. [40] to control reaction wheels to stabilise the motion of a cable-driven parallel robot. This brand of SBC was utilised in the control estimation of a cantilever beam by Abdollahpouri et al. [41], wherein the authors described the SBC as “low-cost”. Continuing with this SBC option, it was utilised by Iwaniec et al. [42] to develop a vibration spectrum analyser. It would be pertinent to highlight that the sensor used as an input in this work is a digital 3-axis accelerometer (ADXL345), which communicates with the SBC via an I²C protocol. The authors highlighted that there are limitations with respect to the maximum frequency that can be analysed, stating that for their chosen components the “output data rate of acceleration measurement should not exceed 800 Hz”. The authors also recognised that due to the nature of a MEMS accelerometer calibration would be required due to the internal elements being able to freely move which would require an offset to be included in order to obtain a relatively accurate measurement of acceleration. The research concludes that the designed analyser is capable of operating in real-time, producing an analysis of the vibration signal in both time and frequency domains. This is evidenced by the results published by the authors included here as Figure 1.1.5. Figures 1.1.5a through 1.1.5c contain

the acceleration data obtained from the accelerometer in the time domain, and Figures 1.1.5d through 1.1.5f represent these accelerations in the frequency domain. From the results and the authors' conclusion it may be assumed that the Raspberry Pi/ADXL345 combination would have a sufficient level of performance as a data acquisition system and spectrum analyser.

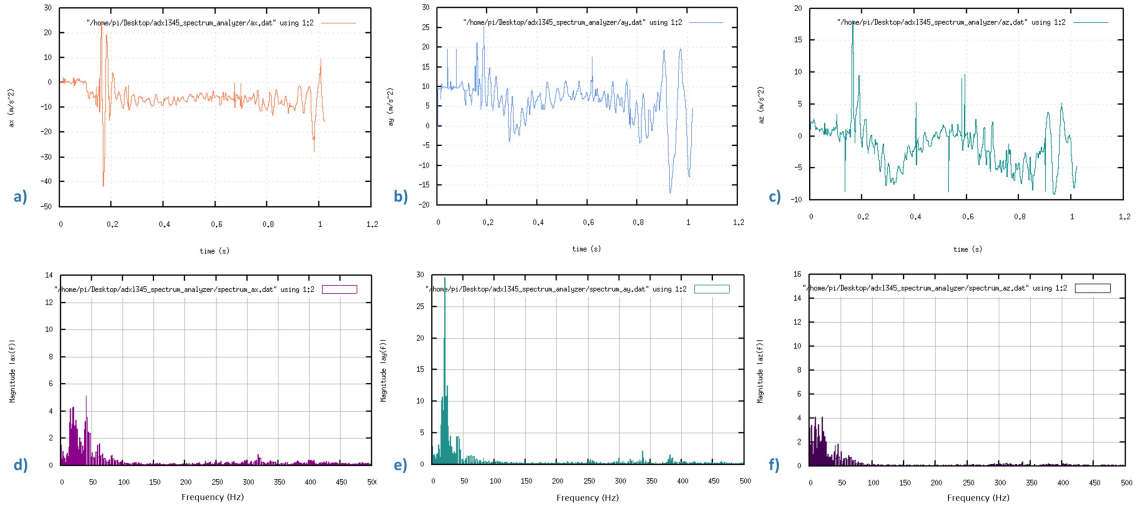


Figure 1.1.5: Results from the research by Iwaniec et al., a) through c) represent the acceleration in the time domain for the x, y and z axes, respectively, and d) through f) represent the same data in the frequency domain [42].

The RPi is able to communicate with a wide array of peripheral devices including via I²C, SPI, WiFi and Bluetooth (note other models may vary). Whilst the SBC is capable of an analog output through the use of pulse width modulation (PWM) it has no on board analog to digital converter (ADC). Hence in order to communicate with analog output devices an external ADC or an interface board must be employed. The latter was implemented in a system developed by Jindarat and Wuttidittachotti [43] wherein an Arduino UNO was used to interpret the signals from analog sensors. The system the authors developed assisted chicken farmers through the monitoring of the conditions in and around the chicken coop/barn. The RPi was identified as the most apt option for this research due its ability to communicate with a database server to send information to the farmer's smart phone. The Arduino UNO board communicated with the RPi via universal asynchronous receiver/transmitter (UART) communication, sending information based on the analog signals from a light dependent resistor (LDR) and an air quality detection sensor. The authors concluded not only that the system is effective, but is an innovation for chicken farming and alters a farm's status from "traditional" to a "smart/intelligent farm". Mahmud et al. [44] favoured the alternate to an interface board, an ADC, and the topic is of more relevance for this research. The authors used a combination of PZT elements, an ADC (MCP3008), and

a RPi for structural health monitoring (SHM) utilising the internet of things (IoT) to send the information to the end user. Two PZT elements were employed, one as an actuator/sensor and the other as solely a sensor placed on either end of an aluminium sheet that was envisioned as the structure of concern. The ADC interpreted the analog signals from the PZT elements, sending a digital communication via SPI to the RPi. The authors combined two SHM techniques; ‘pitch-catch’ and ‘pulse-echo’, and for both techniques the delay time is obtained as a measurement of the structure’s health. Where a delay time over the ‘healthy threshold’ (pitch-catch) or under (pulse-echo) implies damage is present in the structure. The results from the research proved that the system was capable of identifying structural damage. On a more pertinent note, the threshold of the delay time was one millisecond, hence it may be inferred that the component combination achieves a relatively high sampling rate.

1.1.5 Modelling beams

This research focusses on the vibration attenuation of a robot link, with its dimensions resembling a beam, hence it is poignant to consider other research which focusses on the modelling of a beam. The two main contenders for beam modelling that appear frequently in research are the Timoshenko (TBT) and Euler-Bernoulli beam theories (EBT). The latter having been first enunciated around 1750 [45], and the former in 1921 [46]. EBT may be considered a special case of TBT as both theorems may be utilised to predict the transverse motions of a beam, but EBT does not take into account the shear forces acting upon the beam. The article by Elishakoff [47] claims that “The use of the Google Scholar produces about 78,000 hits on the term “Timoshenko beam.””. This has continued to increase and is around 93000 ‘hits’ at the time of writing (February 2021), inferring that it is a very popular theory for beam modelling. A similar search in the same search engine for ‘Euler Bernoulli Beam’ yields around 88000 results at the time of writing. A question may then be posed; what determines this preference between the two methods of modelling within the research of beams? Concisely, EBT is best suited to “long” beams that are flexure-dominated, opposingly TBT applies for “short” beams that are shear-dominated. This was acknowledged by Beck and de Silva Jr. [48] in a piece of research in which the authors hypothesised that for a beam of “mid-length” both EBT and TBT should produce equivalent predictions. The research culminated in the authors acknowledging that for a “mid-length” beam EBT and TBT are equivalent. However, from their results it was recognised that uncertainty in the elastic modulus results in a higher level of propagation for TBT in comparison with EBT. In addition, for EBT an uncertainty in the height of the beam leads to a larger propagation of the displacement response for EBT than TBT.

Whilst this research does yield results of importance, admittedly the conclusion does not entirely answer the question. Conversely, another question may be posed; what defines a beam as “long” or “short”, hence making it more prone to either shear or flexural deformation? Inman and Singh [49] define a beam as suitable for modelling using EBT depending upon the ratio between its length (L) and width (W)/thickness (h). A length/width or length/thickness ratio greater or equal to ten ($L/W \geq 10$ or $L/h \geq 10$) is deemed suitable or “long”. At these ratios the shear deformation of the beam may be considered negligible in comparison to the traverse motion of the beam, hence the appropriateness of EBT. The work by Aldraihem et al. [50] further supports the use of EBT, through a comparison of the use of EBT and TBT to model intelligent beam structures. The authors acknowledged that TBT was “superior” in the prediction of a beam’s response, but also acknowledged that the two models converge for long slender beams. From the results of this research this convergence occurs when the length to thickness L/h or length to width ratio L/W is greater than eighty. As previously mentioned EBT could be considered as a special case of TBT, omitting the influences of shear forces where TBT does not. The inference being that TBT is suitable for the majority of beams, but the acquisition of the solutions to the model are based on equations of a higher complexity. This level of complexity is heightened with the inclusion of surface bonded PZT actuators, and so a multitude of research has been conducted involving EBT for beam structures of this nature.

With PZT elements having numerous applications, the focus of the research involving them and an Euler-Bernoulli Beam (EBB) varies. Afshari and Inman [51] utilised EBT in their research on the SHM of a beam utilising a PZT element as an actuator. Research on the AVC of a “smart piezo cantilever beam” was conducted by Kumar et al. [52], where the authors successfully utilised a PID controller to reduce the settling time of an EBB employing PZT sensors and actuators. EBT was implemented in the research by Su and Zu [53], to model a beam that was part of a bi-directional piezoelectric energy harvester. The authors successfully validated the EBT model through a comparison with experimental results.

Another investigation utilising EBT was conducted by Erturk and Inman [54], as with the previously cited work, the authors sought to model and validate an EBB structure that included PZT elements. This research also concerned energy harvesting and the classical EBT theory was coupled with the electric equations of the PZT elements to create an electro-mechanically coupled model of the structure. Figure 1.1.6 contains a set of results from this research, comparing the analytical model with the experimental results obtained. The results on the left hand side (or left column) of Figure 1.1.6 show the voltage frequency response functions (FRFs), and those on the right the tip velocity FRFs, each row of the FRFs contain the results for a different resistive load (R_l) across

the PZT elements. Referring to these results, particularly when the resistive load is set to $1\text{ k}\Omega$, the analytical model is highly representative of the experimental results in terms of the amplitude and damping of both the voltage output from the PZT element and the tip velocity of the structure. Additionally the analytical model is a very close match with the experimental results when $R_l = 33\text{ k}\Omega$, as is the case of $R_l = 470\text{ k}\Omega$. The authors acknowledge that there is change in the resonant frequency of the structure in the latter case, yet the model is still able to predict the experimental results successfully. The results published in this research infer that the EBT is suitable for use on beam structures that include PZT elements (provided that either L/h or L/W are greater than 10).

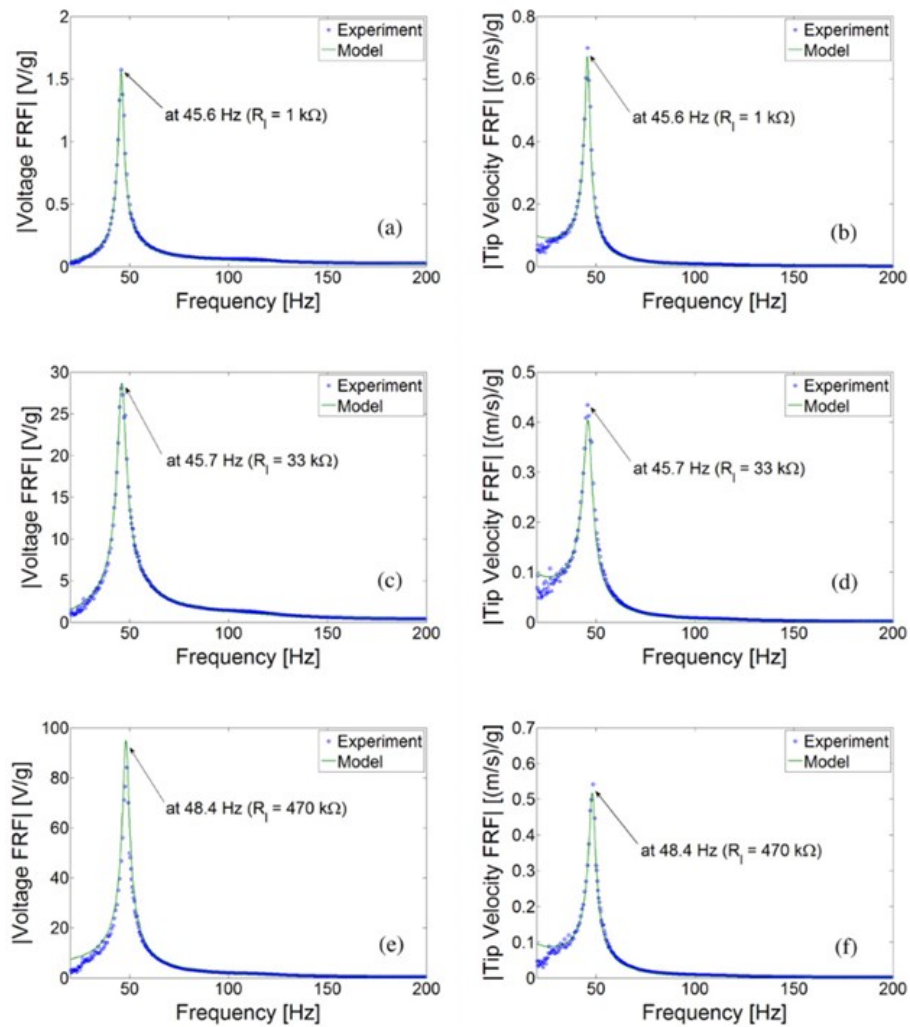


Figure 1.1.6: “Comparison of the model predictions and experimental measurements; (a) voltage FRF and (b) tip velocity FRF for $1\text{ k}\Omega$, (c) voltage FRF and (d) tip velocity FRF for $33\text{ k}\Omega$, (e) voltage FRF and (f) tip velocity FRF for $470\text{ k}\Omega$ ” [54]

1.1.6 Control schemes and hardware

Within the category of research that includes PZT elements, a multitude of these focus on AVC, and a variety of controller designs are employed. Each in turn has their advantages and disadvantages, but to remain relevant to this research those of most importance have been identified based on the performance of the control system and the components required. The latter holding the overall weight as the main point of interest, as this may severely limit the choice of components within a control system on the basis of the intended application. Research by Bailey and Hubbard [25] has been previously discussed, in which the control design was based on Lyapunov's second method. The physical control system includes a multitude of components, but the authors do not explicitly express the brand or model of these components. However a schematic of the equipment lists the parts as: a pre-amplifier, and integrator, a phase shifter, and audio amplifier and a step-up transistor. The system was monitored via a logarithmic plotter and the data was stored in a storage oscilloscope. Also previously mentioned was the successful outcome of the research, with the control system adequately suppressing the vibrations of the system. It may be inferred (from the amount of components mentioned) that the overall weight of the components employed is relatively larger than the weight of the structure itself. Other research by Dadfarnia et al. [55] also included a Lyapunov-based controller. Although this research only included numerical simulations, its mention is warranted given the relevancy; the system under consideration was a Cartesian robot modelled as a cantilever beam utilising a PZT element as an actuator.

A linear quadratic Gaussian (LQG) controller was employed to attenuate the vibrations of a composite beam in research by Han et al. [56], where PZT elements were used as sensors and actuators. The controller in this research was a personal computer (PC) fitted with a card to allow for analog to digital conversion (and visa versa) of signals. The results show that the controller was successful in the reduction of the settling time of the structure when placed under a prescribed initial displacement, especially with respect to the first mode where a reduction of nearly 50% was achieved. The second mode appeared to achieve a negligible reduction in the settling time, but a clear reduction in the amplitude of the response was present and reached a maximum reduction of approximately 50%. Alam et al. [57] also sought a solution for the AVC of beams with PZT elements as both actuators and sensors. As with the previous work a PC was used as a controller employing proportional integral derivative (PID) control, and the authors concluded that the results were effective. This conclusion was based on the application of the PID controller for three different beams; a) aluminium ($0.3 \times 0.003 \times 0.025$ m), b) aluminium ($0.18 \times 0.003 \times 0.027$ m) and c) composite ($0.5 \times 0.005 \times 0.03$ m), each subjected to an initial displacement of 0.025 m and released sharply.

A comparison of the damping factors of the open and closed loop response showed an increase when the control was applied: a) $\times 2$, b) $\times 1.56$, and c) $\times 1.82$. Research by Shan et al. [58] involves the use of positive position feedback (PPF) control with PZT actuators on a single link flexible manipulator. The authors did not differ from the other works just cited in that a PC was employed as a controller, they concluded that the proposed method was proven effective from the experimental results obtained.

1.1.7 The control of flexible robot links

There are multiple pieces that also investigate the control of flexible link manipulators utilising PZT elements, another of which is by Garcia-Perez et al. [59]. The authors investigated the vibration control and trajectory tracking of flexible link robots, involving an EBB envisioned as a robot link that was excited through a direct current (DC) motor. The control scheme employed in this work consisted of a combination of control theories, one for the position tracking of the flexible link and the other to attenuate the vibrations it experienced (PPF). The authors conclude that the system achieved “good dynamic performance” from the implementation of control with damping ratios being increased up to 300%. Shin et al. [60] carried out research on a flexible two-link manipulator with two joints driven by servo motors, where two collocated piezoelectric patches were bonded to each link for the purpose of control. This research also employed a combination of control schemes; sliding mode control (SMC) and constant amplitude control. Other notable works on the AVC of flexible manipulator links include [61], [62] and [63].

Other research focusses on components that are added to existing robot systems to assist in a task. For example, work by Nguyen et al. [64] posed that six degree of freedom robot manipulators are preferable over computer numerical control (CNC) machine tools due to their large work volume, low cost and versatility. However, the authors also identified a drawback in their utilisation in that industrial robots have a higher level of compliance. This compliance leads to a lower level of machining accuracy in high-force milling applications. In this research a Gaussian process regression (GPR) model was employed to predict and solve the LQR optimal control problem (which was pose dependent) to obtain the optimal gains for active vibration suppression with the experiments conducted on a KUKA KR500-3. The authors concluded that the method implemented successfully reduced the milling vibration amplitudes, and hence enhanced the milling accuracy. Sörnmo et al. [65] also aimed to improve the milling accuracy of an industrial robot through the use of a micro manipulator which included PZT actuators. The movements of these actuators were transferred to corresponding translational movements of the milling tool via a flexure mechanism.

The robot manipulator’s (REIS RV40) deviation from its intended path was detected by a tracking system, and the deviation was compensated by the designed micro controller. The control scheme utilised for this compensation was a PID controller. The authors concluded from the observation of the obtained experimental results that the method proposed provides a higher level of milling accuracy. Other notable works on the vibration suppression of industrial robot tools include [66], [67] and [68].

1.1.8 Modelling robot manipulators

Reviewing research on the vibration suppression within robot systems, provides an insight into the potential of robot manipulators in industrial practices. Their modelling provides a vital insight into their kinematics that may be utilised in the control of additional tools as required by their applications. To obtain adequate versatility robot manipulators with higher degrees of freedom (DOF) are preferable, but as a result their modelling becomes more complex, especially when considering their inverse kinematics (IK). The Denavit-Hartenberg (D-H) convention was first enunciated in 1955 [69], which standardised the coordinate frames for spacial linkages. A multitude of research on robot manipulators has utilised this convention for example: [70], [71] and [72]. The utilisation of this convention alongside homogeneous transformation matrices lends to an accurate prediction of the forward kinematics of a robot manipulator. Dependent on the number of DOFs of the manipulator a sufficient prediction of the inverse kinematics may be obtained, however for redundant manipulators additional modelling methods are required.

Work by Faria et al. [73], sought to model the inverse kinematics of a KUKA LBR iiwa 7 R800 manipulator. The analytical model of the robot manipulator was created using D-H parameters, and was simplified through the superimposition of a proceeding joint onto the next effectively envisioning two links lengths as one whilst maintaining the rotational components of both associated joints. The simplified model (omitting offsets) used in the research is shown as Figure 1.1.7, where it can be seen that the joints are combined and labelled as the base (b), the elbow (e), the wrist (w) and the flange (f). For the calculation of the IK, the authors introduced two additional parameters; the ‘Global Configuration’ (GC) and the arm angle (ψ). The former uniquely specifies the branch of the IK solutions for the GC manifold, and the latter indicates the elbow position within the redundancy circle. The authors concluded that the method reliably computes the “intervals of feasible elbow positions to avoid joint limits and singularities”, additionally noting that the method would be adequately suitable for real-time utilisation due to the time required for each operation being limited. Other researchers have also sought a solution to modelling the IK of redundant

manipulators, a space vector solution was proposed by Li et al. [74], the utilisation of a closed loop inverse kinematics (CLIK) algorithm was investigated by Wang et al. [75], and Bertram et al. [76] proposed a novel method based on the modification of the rapidly-exploring random trees (RRT) search algorithm.

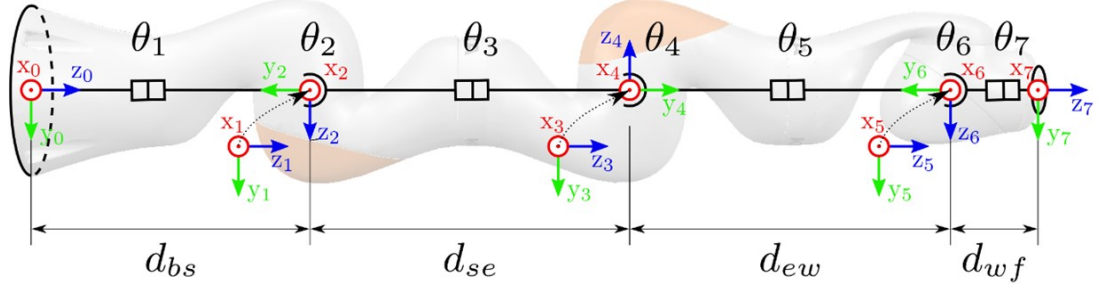


Figure 1.1.7: Illustration of D-H parameters assignment based on the KUKA LBR iiwa 7 R800 as in the research by [73].

1.1.9 Nonlinear modelling and control

Returning to the topic of AVC, it would be pertinent to investigate research concerning nonlinear vibrations of beams and research that includes the AVC of nonlinear vibrations. This is with the consideration that a designed control system may be tasked with the control of nonlinear vibrations in a system during its employment. Nonlinearity may be present in systems due to causes relating but not limited to the material properties, the geometry, or the external forces and constraints placed on a structure [77]. Research by Platanitis et al. [78] focussed on the AVC of a nonlinear wing section, aiming to control the pitch and plunge of the wing section through the adjustment of the deflection of leading and trailing edge control surfaces. An adaptive control scheme was employed to account for uncertainties present in the model leading to an inexact cancellation of the nonlinear parameters, through the augmentation of the feedback linearised system. This type of control scheme aims to produce an equivalent linear system based on the nonlinear system through the alteration of variables and a suitable feedback control signal [77]. The authors concluded that the predicted responses yielded through the implementation of this control scheme showed a good level of performance. However, they acknowledged that in practice this may be difficult to replicate due to the limitations involving hardware design. Whilst this particular piece of research does not pertain to beam structure per se, it does highlight some issues that may occur in the control of nonlinear vibrations i.e. the uncertainties that occur in the modelling of a nonlinear system.

Khorrami et al. [79] sought to reduce the vibrations experienced by a two link flexible

robot manipulator, utilising an adaptive nonlinear control (with PD inner-loop) scheme involving input preshaping. The alleviation of the nuisance vibrations was obtained through the alteration of the position and velocity of the joints. The authors identified that in order for the application of an input preshaping scheme to be effective the system needs to be both time-invariant and linear. This is not the case with a flexible two link manipulator as the vibrational frequencies are configuration dependent, additionally any significant payload variations would adjust these frequencies as well, and as such would not perform well on the proposed structure. Hence the authors’ implementation of the adaptive nonlinear control scheme, which “cancels out some of the nonlinearities” and reduces the latter of the aforementioned issues by self-tuning in the case of any payload or frequency variations. The authors concluded, after an analysis of both analytically and experimentally obtained results, that the designed control scheme was “quite effective” in the vibration suppression of the structure whilst handling a variety of payloads. Notably, the authors conducted a comparison between the control scheme of PD joint control, and feedback linearising control with a PD inner-loop. The latter of the two control schemes attenuated the amplitude of the acceleration experienced at the tip of the two joint manipulator more than the former by a factor of two. The authors then developed the control scheme further implementing adaptive input preshaping within the linearising control scheme, this inclusion yielded a settling time that was approximately six times lower than the non-adapting control scheme.

Some of the highly revered pieces of research in this area include those by Chen et al. [80] and Polycarpou and Ioannou [81]. The former introduced a fuzzy linear control design method for nonlinear systems as a solution for the setbacks that occur in the implementation of a feedback linearisation method. The latter developed a robust adaptive control design for nonlinear systems in which uncertainties lay in their parameters and unknown nonlinear functions. The research by Sun et al. [82] is of a higher similitude to this research as the authors investigated the AVC of a rotational flexible beam utilising PZT actuators. An enhanced PD feedback control scheme was employed, which included a nonlinear differentiator to improve the quality of the velocity signal input. Experiments were conducted which verified the effectiveness of the hybrid control scheme.

Linear control is a massively investigated topic, with relatively few questions remaining, the situation is the opposite for nonlinear control wherein a lot of questions remain unanswered. With a vast amount of information available for linear control schemes, many researchers find them (or an amended version as in [82]) suitable or, in some cases, even favourable for the control of nonlinear systems. Research by Schweickhardt and Allgöwer [83] corroborates this in the authors’ statement: “Linear controllers are favourable over nonlinear controllers because they put lower requirements on the

implementation”. In some cases, such as feedback linearisation, the design requires an accurate knowledge of the system parameters, and may also eliminate nonlinearities in the system that could be deemed useful. The authors investigated the implementation of linear control on a nonlinear system on the basis that a system may be more akin to a linear system, or to a nonlinear system or somewhere in between. This measure of a nonlinear system strays from the mathematical definition of linear and nonlinear, and defines the system based on aptly named “nonlinear measures”. These measures were first introduced by Desoer and Wang [84], and is based on some nonlinear system being represented by an equivalent linear model and an error system, and the gain in the error system is the nonlinear measure.

The conclusions of the research by Schweickhardt and Allgöwer suggest that the performance of linear control system is related to the nonlinear measure, in that a smaller error gain would result in a higher level of performance. It may be inferred that a linear control system employed on a system of a ‘weaker’ nonlinearity would have a higher level of performance than when said control system is applied to a system containing a higher level of nonlinearity. The difference between strong and weak nonlinearities was discussed by Rudenko and Hedberg [85], in which the authors highlighted that the assumptions and/or the linearisation of weakly nonlinear systems cannot be applied to strongly nonlinear systems:

1. “If the equation of state contains a singularity.”
2. “If the series diverges for strong disturbances.”
3. “If the linear term is absent, and higher nonlinearity dominates.”

Hence, an indication as to the degree of nonlinearity present in a system can be based on the the aptitude of the system to be represented through linearisation. The linearisation of a nonlinear system may be used to understand its behaviour, but is not without limitations. The approximation of the system via linearisation is within the vicinity of the operating point of the system, and as such can only predict the response of the system around this point [86]. Additionally, the complex nature of a nonlinear system in comparison to a linear one renders responses that are present only in nonlinear systems, for example limit cycles, chaos and mode coupled behaviour, and cannot be predicted by linear models. Thus, the prediction of nonlinear responses is a challenging task, and many researchers are devoted to attaining a solution. Harmin and Cooper [87] presented a method for the development of aeroelastic reduced order models (ROMs) for structures (in this case specifically those related to aerospace) that include geometric nonlinearities. The structure of focus in this research was a high altitude long endurance (HALE) wing, which (more often than not) have an aspect ratio resembling

a cantilever EBB. The nonlinear restoring forces in this case were obtained through regression analysis based on the static nonlinear force/displacement relationship that was obtained. The authors acknowledged that the method may be applied to other similar structures provided that the dynamic behaviour could be separated into a simple modal description.

Assumptions made in the linearisation of a nonlinear system to produce a model which can be updated to reflect the nonlinear system may yield a good representation of theoretical problems. However, for the most part experimental nonlinear systems may contain unknowns within their dynamics including noise, the estimation of unknown coordinates, and the error due to the disregard of higher harmonics in the system. Taghipour et al. [88] investigated a method of determining these parameters known as equivalent dynamic stiffness mapping (EDSM), or more precisely the sensitivity of this technique to the errors that are present in the modelling. To obtain the dynamics of the nonlinear systems considered the modified complex averaging technique (MCXA), finite element modelling (FEM) and arc-length continuation were employed. The systems of focus in this research were a discrete three DOF Duffing system and a cantilever beam where a nonlinear restoring force was applied to its free end. For the latter system the authors also employed an optimisation based framework, that was developed by them previously (see [89]). The results of this framework were compared with the results obtained through the employment of the EDSM technique. The authors concluded that the EDSM technique was sensitive to any inaccuracies, however the resultant response obtained from this technique could be utilised as the initial parameter estimate for the optimisation based framework. The framework sought to minimise the discrepancies between the measured/simulated data and the estimated nonlinear response, and it led to a more accurate representation of the response.

1.2 Problem definition

Upon review of existing research there are many published works concerning the topics of both robotics and vibration control, and indeed a combination of both. This research aims to build upon previous investigations after having identified a potential research gap in which a solution may make a good contribution to the field. Flexible manipulators and the reduction of their unwanted transverse vibrations, is a topic greatly analysed for the advantage of weight reduction in a robot system. As a manipulator link resembles a beam the solutions often extend to applications outside of the field of robotics including those relating to space, flight and building structures to name a few. The choice of components varies throughout the solutions posed by previous research, with PZT elements and MEMS sensors notably providing effective AVC solutions, both individually and in combination. Such components are frequently the choice of researchers due to their weight, inexpense and certain degree of novelty. However, a lot of research focusses on the control scheme justifiably seeking the optimum level of performance from the control system, especially with those seeking a solution to the AVC of nonlinear vibrations. Whilst there are some exceptions, many utilise PCs and other equipment which can limit the applications of a control system in certain situations. Therefore a requirement for a lightweight, inexpensive control system can be identified which can increase the variety of applications to which it may be applied.

An effective lightweight solution is especially relevant given the increasing popularity of UAVs and other unmanned vehicles, the designs of which are heavily dependent on weight. Hence, such an application is kept in mind throughout this research, principally during the design of the control system, but also during the experimental aspects as well. A suggested application for the solution produced by this research is discussed in greater detail in the following subsection. Whilst such control systems that are lightweight and inexpensive are advantageous, there are often compromises in terms of the effectiveness when implementing these constraints on the components. A system of inferior performance would not be as desirable, so it would be important to compare the designed controlled system's performance with that of a purpose-built system. Should there be little or at least an acceptable difference in the performance of the designed control system then it may be deemed as a suitable solution. A multitude of control schemes have been employed across existing research, with the vast majority proven effective. Whilst seeking the most effective scheme may be beneficial, one that requires high processing capacity, additional components or high levels of power would not be suitable in this case. Thus, the control scheme should be chosen based on the components used considering the processing capacity and inputs available.

Reviewing existing literature has also exposed the importance of analysing a control system's performance in a situation similar to its intended application. Some researchers have focussed their efforts on control systems and especially robot manipulator links on purpose built structures, which led to experimental results showing how effective the control system is. However, whilst these results provide a good indication of the performance of the control system they do not provide a clear insight into its influence on the functionality of an existing system. Other research employs the existing system as part of the AVC system, i.e. those which utilise a robot manipulator's joints to attenuate vibrations along a flexible link. Admittedly, in these cases the robot manipulator was the sole intended application. However, to improve viability for the solution produced by this research it would be pertinent not only to ensure that it does not negatively impact the functionality of the existing system but for the control system to function independently and be removable.

To further improve the variety of applicable situations for the solution, the AVC of nonlinear vibrations should be considered as this is also a highly prevalent topic in existing research. In addition, different applications may induce nonlinear responses of the structure in question, particularly if the existing structure is damaged or its boundary conditions/geometric features are inadvertently altered. A nonlinear control scheme is employed in a significant quantity of the current research, however such a solution is likely to incur a high processing penalty. An alternative, as used by other authors, is to utilise a linear control scheme for the AVC of a nonlinear response. This option is better suited to this research as the designed control scheme and system can be analysed for its effectiveness against unwanted nonlinear vibrations, without significant alterations to the design which may contradict the constraints placed on the component selection.

1.3 Suggested application

The driving factors for the control system design and subsequently its components are that it is lightweight and inexpensive. Whilst these factors may be desirable for a variety of applications, there are those in which they become more important. The least expensive solution to a problem can often drive the selection, especially when performance is not significantly compromised. This may be pertinent to companies ensuring a healthy profit margin, or to other applications in which the system may be subject to dangerous environments and may need to be replaced entirely somewhat regularly. The weight of a system is dependent on its application, but a lighter system is more often than not of greater desirability. This may be due to the transport of the system to the end user, or the surface/structure on which the user will mount/place the system, or may be because the system is intended for use on or in a vehicle.

Robot manipulators (explored further in the proceeding chapter) are produced in a variety of shapes, sizes and weights to suit their intended use. Some of the most common of the designs are relatively large and heavy as they are industrial robot manipulators intended to lift an/or utilise tools, components and parts during the manufacture of large items such as cars and aircraft. However, some of these manipulators are lighter and smaller for other more intricate tasks i.e. bomb disposal, circuit board creation and surgery. A bomb disposal robot could be considered to have two ‘parts’; a vehicular part for moving the robot from the operator’s safe distance to the device, and a manipulator to disarm the robot. The latter of these ‘parts’, the manipulator, needs to be light enough so that the vehicle is able to transport it, but strong enough for the tools and equipment required during the task to be supported and manipulated.

Whilst the weight of the manipulator in the application of bomb disposal has some importance in that it influences the design of the vehicular part, it is not as influential as in the case when the vehicle is to be airborne. Thus, leading to the proposed application of a search and rescue drone, with a structure not unlike PRODRONE’s PD6B-AW-ARM (as shown in Figure 1.3.1) [90]. It would be greatly advantageous for such a robot system to be airborne in environments that would lead to the necessity for search and rescue such as a collapsed structure. In such a scenario, the rubble is likely to be unstable, and the access inside the rubble is likely to be narrow. Flying a drone over the unstable structure rather than putting weight on the structure in the form of a rover type drone or even a person would be deemed a lot safer. However, some of the crevasses within the rubble may be too small for the drone to fly safely through, and so mounting a robot manipulator upon the drone can offer a greater level of exploration. Utilising a manipulator with long slender links will not only reduce the overall weight of the drone, but also allows for the end effector of the manipulator (potentially with a

camera mounted upon it) to fit into those small crevasses. Having more access to the collapsed structure, the search and rescue team will be able to visualise more of the environment identifying problem areas and any individuals that may be trapped.



Figure 1.3.1: Image of the PD6B-AW-ARM by PRODRONE [90].

Utilising long slender links may be advantageous for exploration purposes, but they are more susceptible to nuisance vibrations, especially when mounted on a drone. Thus, the employment of a vibration suppression system becomes necessary to ensure clear images of the rubble are obtained as well as preventing the manipulator from disrupting the parts of the rubble that may be precariously balanced. As with the manipulator this control system should be lightweight so that the drone is capable of flying with its additional mass on board. The cost of the control system should also be low, as even when flown by experienced operators the unstable nature of a collapsed building lends to it being highly dangerous environment. Part of or all of the drone system could be damaged and require replacement parts, hence the importance of keeping the total cost as low as possible. Another important consideration for this proposed application is that whilst a camera may be required in some circumstances, others may require alternate equipment such as an end effector tool to remove pieces of rubble or deliver medical supplies/rations to trapped individuals. As such, in some situations the control system may not be required, and if created to be part of the drone system will act as a redundant mass. Hence creating the control system to be independent and removable would be deemed advantageous, saving weight for alternate equipment.

1.4 Outline of thesis

Following the identification of a potential gap in research, and the proposal of potential application for the designed control system, robot manipulators are further investigated. A general outline and the current applications of robot manipulators is included, before identifying a particular model for use in testing the designed control system. Information on this selected manipulator has been obtained for the creation of an analytical model to predict its kinematics and is validated through experimental results. This research then turns its focus to the flexible link and the sensors and actuators of the control system, introduced simultaneously as these components are included in the developed analytical models. The first model is created with PZT elements as actuators, and inertial measurement units (IMUs) as sensors, whereas the second utilises PZT sensors in lieu of the IMUs. An investigation into the effectiveness of the IMUs as sensors was conducted prior to their exchange, hence the inclusion of the two control sensor options. In addition, the motivation behind the alteration of the control system components has been discussed. It was deemed more relevant to present the validation of the open loop analytical models of both control system options prior to presenting the closed loop results so that the text follows the development of the solution rather than the chronological order of the experiments.

Following the presentation and discussion of the validation of the open loop system, the control theory and system are discussed. This includes the analytical models of two control systems where ‘Control system A’ (CSA) utilises IMUs and ‘Control System B’ (CSB) employs PZT elements as sensors. The components and their integration for both control systems are discussed, prior to the introduction of a purpose-built control system used as a reference to observe the designed control system’s performance (CSB). Proceeding this four separate experimental investigations on the closed loop system are presented which concern the performance of the control system and the validation of the respective closed loop models. These four experiments consider the performance of control systems A and B, a comparison of control system B with the purpose built control system, and the instance where the flexible link is mounted on the robot manipulator. The latter also concerns the influence of the control system on the functionality of robot manipulator.

The induction of a nonlinear response of the structure is presented, including the amendments to the system in order to achieve this. CSB is then employed in the case where the response of the system is nonlinear, to ascertain its level of performance in such situations. Utilising the experimental results to update and hence validate the analytical model through optimisation. Following this, the analytical model of the system is modified to include dynamic control, namely proportional-integral-derivative

(PID) control and subsequently the derivatives thereof. This investigation is conducted utilising the model of the system to ascertain the optimum control gain values, and the resultant response when employing these values. The last investigation pertains to seeking a model of higher accuracy when used to represent a physical system, thus the model is represented in the discrete-time domain. Finally, the findings and contributions of this research are summarised and concluded, before the potential future work is discussed.

1.5 Outcomes of this research

The following are the journal papers that have been published from this research:

1. D Williams et al. “Active vibration control using piezoelectric actuators employing practical components”. *Journal of Vibration and Control* 25.21-22 (2019), pp. 2784-2798.
2. D Williams, H Haddad Khodaparast, and S Jiffri. “Active vibration control of an equipment mounting link for an exploration robot”. *Applied Mathematical Modelling* (2021).
3. D Williams et al. “Linear control of a Nonlinear Equipment Mounting Link”. *Vibration* 4(3) (2021), pp. 679-699.
4. D Williams et al. “PID tuning for a control system using PZT sensors”. *Journal of Vibration and Control* (Under preparation)

The following are the conference papers that have been published from this research:

1. Darren Williams, Hamed Haddad Khodaparast, and Chenyuang Yang. “Active vibration control of a flexible link robot with the use of piezoelectric actuators”. In: *MATEC Web of Conferences*. Vol. 148. EDP Sciences. 2018, p. 11005.
2. Darren Williams, Hamed Haddad Khodaparast, and Chenyuang Yang. “A practical approach of active vibration control with the use of piezoelectric actuators”. In: *Proceedings of ISMA2018 and USD2018*. ISMA and USD. 2018.

Chapter 2

Robot manipulator

A robot manipulator is a mechanism consisting of sequential links and joints, where the joints are controlled electronically to complete a task. The number of joints and links, as well as the joint type(s) (revolute, prismatic, cylindrical etc.) of a manipulator solely depend upon its design. Commonly referred to as robot arms they can move autonomously and/or with some human interaction or input. This chapter provides a brief history and overview of robot systems, with particular attention to robot manipulators, whilst investigating their current applications in a more general manner. From this the chapter proceeds to introduce a selection of robot manipulators used in a variety of applications, to further investigate the additional potential applications of the designed control system. The motivation behind the selection of the particular robot manipulator used within this research is explained, and its specifications and geometry is discussed. Furthermore this chapter contains the development of an analytical model of the robot manipulator, which is then experimentally validated before use in later experiments within this research.

2.1 A brief overview and history of robotics

The word ‘Robot’ and its subsequent modern definition is derived from the term ‘Robota’ which appears in multiple Slavic languages [91]. Robota had the original definition of “heavy monotonous work or slave labour (drudgery)”, a definition which was redefined through a play written by Karel Čapek. It was this 1921 play which introduced the modern definition of the term robot: “A machine capable of carrying out a complex series of actions automatically, especially one programmable by a computer.” [92]. Another author who was a poignant contribution to the history of robotics was Isaac Asimov, who envisioned robots as anthropomorphic mechanical creatures devoid of emotions, and produced the term ‘robotics’. Asimov also thought of these robots

as having a computer or a ‘brain’ which was programmed and was governed by three fundamental laws revolving around potential ethical issues [93]. A zeroeth law was later added by Asimov which incorporated humanity as a whole in addition to the existing laws surround the robot’s interactions with individuals [94]. The following are the four laws set out by Asimov:

0. “A robot may not injure humanity, or, through inaction, allow humanity to come to harm.”
1. “A robot may not injure a human being, or, through inaction, allow a human being to come to harm.”
2. “A robot must obey the orders given it by human beings except where such orders would conflict with the First Law.”
3. “A robot must protect its own existence as long as such protection does not conflict with the First or Second Laws.”

These rules are inclusive of robot manipulators, however, Stig Moberg generated an additional two laws intended for robot manipulators [95] (translated from Swedish). These additional laws state:

5. A robot must follow the trajectory specified by its master, as long as it does not conflict with the first three laws.
6. A robot must follow the velocity and acceleration specified by its master, as long as nothing stands in its way and it does not conflict with the other laws.

The history of robot manipulators intertwines with that of technological advancements in industry, where the first mass produced industrial robot manipulator was installed in a die-casting plant in 1961. The Unimate 1900 was conceived and produced by inventor George Devol and business man Joseph Engelberger [96]. Inclusive of this monumental milestone a brief time-line of robot manipulators can be found in Table 2.1.1 (and continued in Table 2.1.2. The last three years (2017-2019) have seen thousands of installations of industrial robot manipulators, Figure 2.1.1 shows these installations and provides an insight into the type of industries that use them [97]. It is clear to see that the top users of robots in the manufacture of their products are those that value and require accuracy and efficiency and/or the manipulation/transport of heavy or hazardous parts and materials i.e. the automotive and electrical/electronics industries. Figure 2.1.2 contains the annual installations of those industrial robots by their application within industry, further evidencing their type of usage within industry.

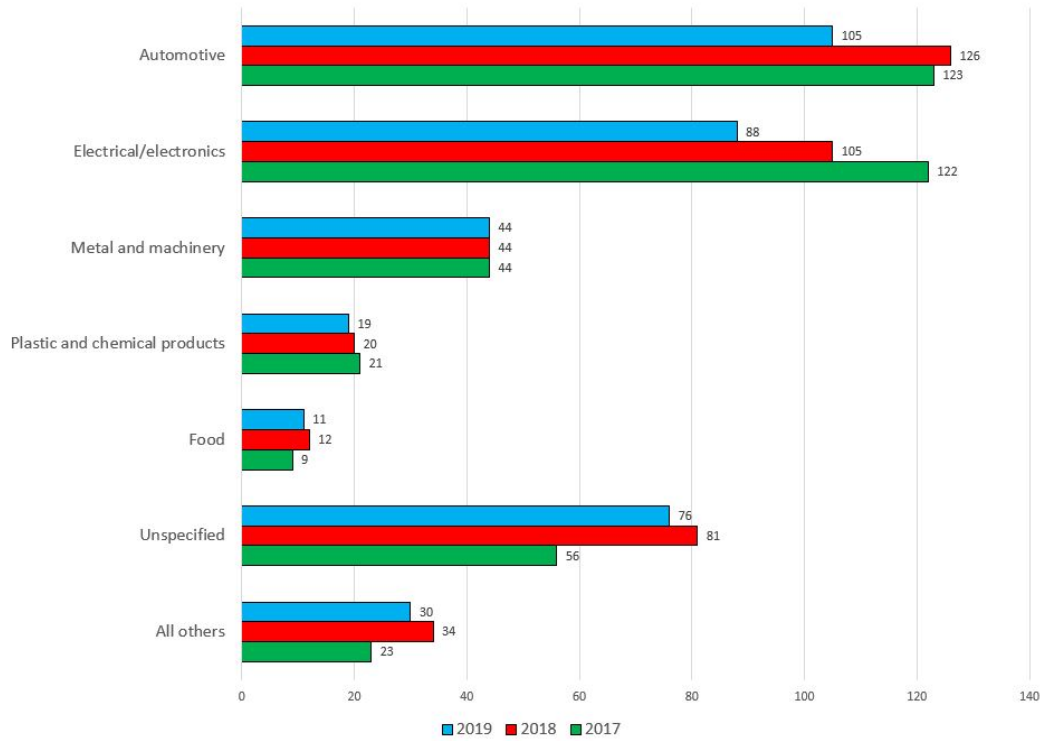


Figure 2.1.1: Annual installations of industrial robots by customer industry worldwide (1000 units).

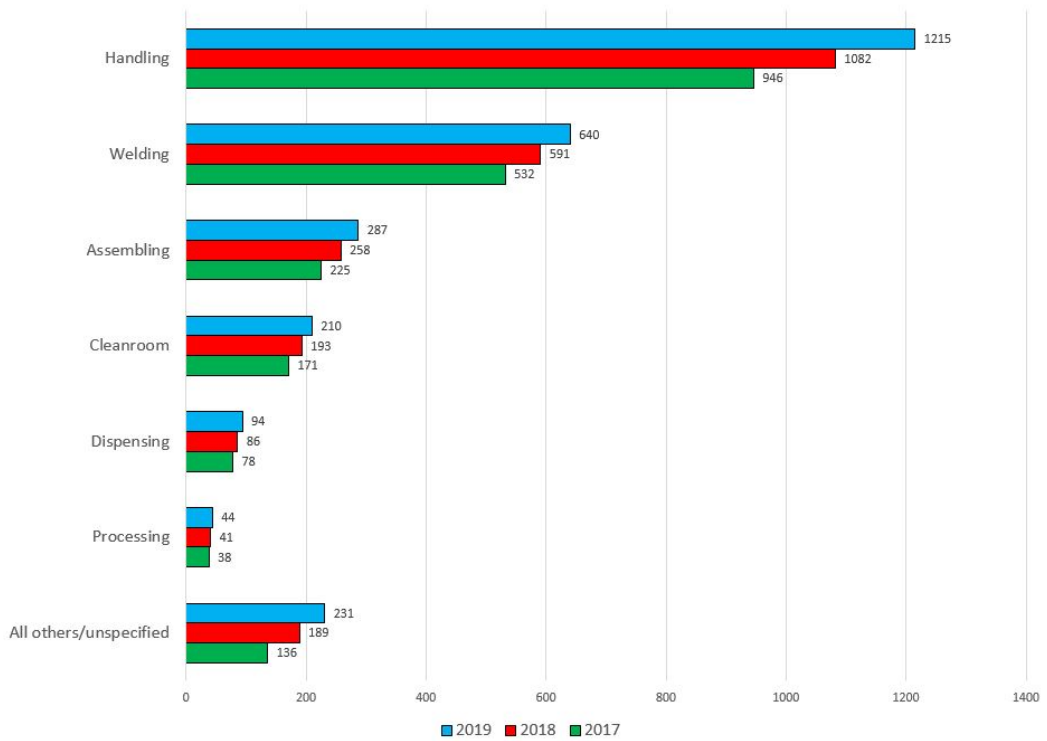


Figure 2.1.2: Annual installations of industrial robots by application (1000 units).

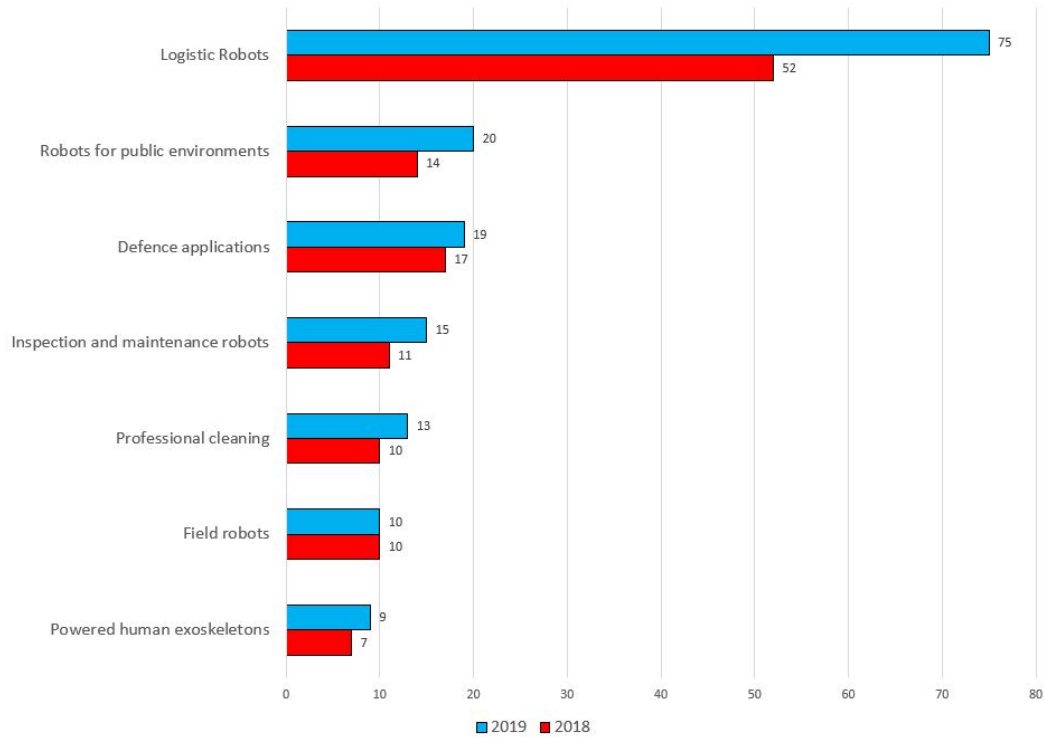


Figure 2.1.3: Service robots for professional use, top seven based on unit sales (1000 units).

The majority of the robots used in industry are robot manipulators (or robot arms) due to their dexterity and payload capacity. However, whilst other professional environments also employ robot manipulators, other types of robots are used to perform tasks. The data shown in Figure 2.1.3 contains the number of units sold for professional use organised by application, and is not limited to robot manipulators. However, analysing this data provides an insight into the potential applications of robotics, and highlights a market for the previously proposed application. In addition to the proposed application of the control system; a search and rescue drone. The designed control system has the potential for use in other markets such as inspection and maintenance, especially where this is to be carried out in dangerous environments.

1961	Unimate 1900 was installed in a die-casting plant for the removal of high temperature components from machines and welding. The commands for the robot were stored on a magnetic drum, and the manipulator would preform them step by step.
1963	The Rancho Arm was designed at the Rancho Los Amigos Hospital as a tool for the handicapped.
1965	The Orm (The Snake) was an air-powered robot arm which moved through the inflation of one or multiple rubber bladders positioned between seven metal disks.
1968	The Tentacle arm developed by Marvin Minsky in such a manner its movements were akin to that of an octopus. It was hydraulically powered and computer-controlled.
1969	The Stanford Arm invented by Victor Scheinman was the first computer-controlled, electrically powered robot arm.
1972	Bomb disposal robots were first conceived, at this time they were very primitive versions of what they are today. [98].
1974	The Silver Arm designed by David Silver which utilises pressure sensors for feedback in the assembly of small parts. The arm approximated the fine movements of human fingers.
1981	Takeo Kanade develops a prototype of the first direct drive (DD) robot arm. The arm has no external tendons or chains, driven instead by internally housed electric motors. The Canadarm manipulator was first tested in orbit [99].
1985	The Puma 560 was the first robot manipulator to assist in a surgical procedure; a brain biopsy [100].
1987	Mitsubishi Movemaster RM-501 Gripper was introduced. Small and commercially available this industrial robot was driven by electric motor, capable of moving 0.38 m/s and was accurate to 0.0005 m.
2000	The United Nations approximates that there are 742500 industrial robots in use worldwide [101]. The da Vinci Surgical system was approved by the food and drug administration (FDA), making it the first robot system to be approved for surgical procedures [102].
2003	KUKA produces a 6-axis robot amusement ride [103]
2006	KUKA presents the first lightweight robot, weighing 16 kg and having a payload capacity of 7 kg [104].

Table 2.1.1: Time-line of the milestones surrounding industrial robotic manipulators.

2007	Motoman, Japan launches the fastest arc welding robots at that time [105].
2016	FANUC, Japan, launches a heavy duty robot manipulator capable of lifting 2300 kg, making it into the Guinness World Records [106].
2019	NASA finished the installation of the Mars 2020 rover's arm which is 2.1 m long. It was designed for drilling and sample collection on Mars and has been described as "the most powerful arm ever installed on a Mars rover" [107]. Soft Robotics Inc. introduced a newer version of the mGrip system as a flexible gripper solution for robot manipulators [108]. Samsung's Bot Chef is unveiled [109].

Table 2.1.2: Time-line of the milestones surrounding industrial robotic manipulators (continued).

2.2 Applications

Robot manipulators are currently employed in an array of applications, but with further research and the development of new technologies, the realm of possible applications is set to become vast. Emerging technologies such as haptics, which involves force-feedback, provide a more immersive approach to the user so that they are able to ‘feel’ what the robot is touching. The use of this example is especially prevalent for tasks which require excellent dexterity in environments which are not safe for humans to work in. This could be in the absence of oxygen i.e. underwater or in space, or where there are other risks to life such as bomb disposal. The Harris T7 Multi-Mission Robotic System is intended for use by the armed forces for explosive ordnance disposal (EOD) missions, where the system can be used to detect, identify, disarm, recover and dispose of explosive devices. This robot is pictured in Figure 2.2.1 where it is being operated by a bomb disposal expert [110]. The system is modular, so that depending on the mission different equipment may be included in the system, but as can be seen in Figure 2.2.1 the main modules are the rover type platform and the robot manipulator mounted upon it. The haptic feedback technology is a vital addition to the control of this modular system given the intended application. Disarming an explosive device is an intricate and dangerous task, even with the operator at the maximum range from the robot of 1 km. A miscalculation of the robot tool’s position could prove disastrous, so with the system applying a force/vibration to the user when the robot comes into contact with a surface, the immersive technology of haptics provides more accurate motions to be obtained.



Figure 2.2.1: Image of the Harris T7 Multi-Mission Robotic System [110].

Space is another dangerous environment (as previously mentioned) in which a robot manipulator is used to carry out required tasks. The Canadarm2 [99] is the second Canadarm robot manipulator that was launched into space in 2001, and is pictured in Figure 2.2.2. It was an instrumental piece of equipment in assembling the space station, and is now still used to move supplies, equipment and astronauts outside of the station. The Canadarm2 is also used to ‘catch’ unmanned spacecraft that are sent to deliver scientific payloads and cargo. The Dextre is a “robotic handyman” and can be mounted onto the Canadarm2 to complete maintenance on the exterior of the space station and its components are outlined in Figure 2.2.3 [111]. Each of Dextre’s arms have seven degrees of freedom, and are equipped with the tools required for being able to undertake maintenance. These include retractable motorised wrenches, cameras, lights and retractable connections for power, data and video. The robot is capable of movements precise to a few millimetres and can be controlled from Earth, meaning its range is around 400 km. The combination of the Canadarm2 and the Dextre reduces the number of times astronauts have to work outside of the space station, reducing the risk to their safety.



Figure 2.2.2: Image of the Canadarm2 and Dextre carrying the RapidScat instrument assembly [99].

The main purpose of the da Vinci Surgical System (pictured in Figure 2.2.4) is to enable surgeons to operate on the patient via one or few small incisions [112]. Thus reducing the size of the scarring from the procedure and potentially reducing the risk of infection. This application does not need to address the issue of a dangerous working environment (at least not in the same manner as the Harris T7), but it still requires that the system have a high level of dexterity and accuracy. This surgical system

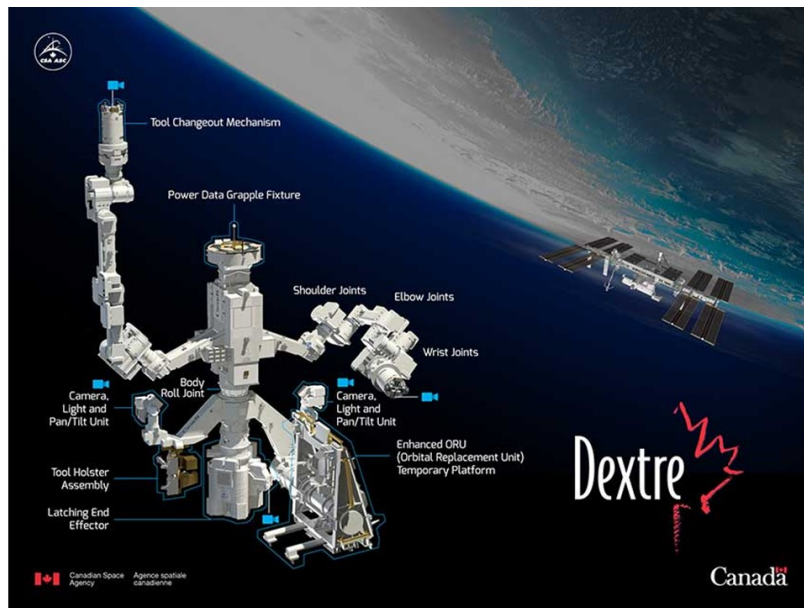


Figure 2.2.3: An image of the Dextre robot, outlining its components [111].

consists of three main devices; the ‘surgeon console’, the ‘patient cart’ and the ‘vision cart’. The surgeon uses the first of these devices, the surgeon console, to control the instruments mounted on the patient cart with the communication between the two devices enabled through the vision cart. The patient cart contains the manipulators and the small wristed instruments which “move like a human hand, but with a greater range of motion” [113]. It also houses high definition recording equipment capable of relaying three dimensional images to the surgeon console.



Figure 2.2.4: Image of the da Vinci Surgical System [112].

Loosely fitting into the classification of ‘robot manipulator’ is another medical device: the prosthetic limb. There are many variations of prosthesis, but few allow the individual to control the system using their thoughts. The Modular Prosthetic Limb (MPL) was created at the Applied Physics Laboratory (APL) at Johns Hopkins University in 2010, to accomplish this feat. The design replicates the human arm as closely as possible in terms of dexterity, weight, range of motion and force generation [114]. Its modular design allows for its use by individuals with varying levels of amputation, and utilises numerous sensors as highlighted in Figure 2.2.5 [115]. Johnny Matheny assisted in the research of this design after having his arm amputated for medical reasons in 2008, Figure 2.2.6 shows Matheny using the MPL [116]. To enable the use of the prosthesis Matheny underwent a procedure known as muscle reinnervation, this reassigns the nerves that control the limb. To prevent common issues experienced by prosthesis users such as pain, sores and blistering, a titanium implant was fixed within the bone marrow cavity of Matheny’s upper limb. The MPL utilises force sensors housed in bands (wrapped around Matheny’s upper arm in Figure 2.2.6) to modulate the stiffness of the MPL’s joint through commanding the motor torque [117]. These bands are also able to interpret the muscle activity (as a result of the muscle reinnervation procedure) through high density electrode arrays, to manipulate the prosthesis.

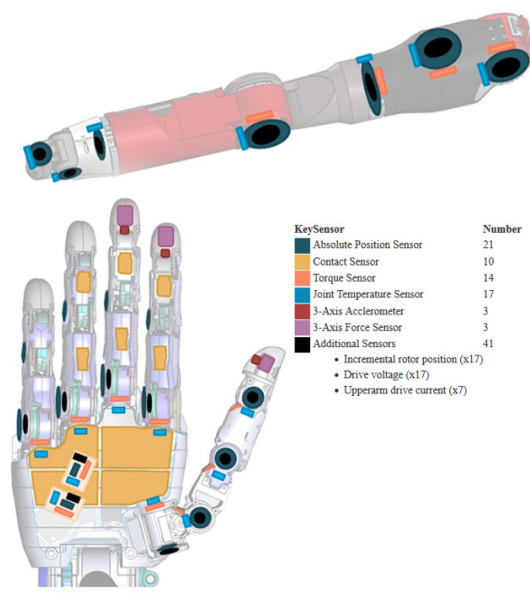


Figure 2.2.5: CAD model of the Modular Prosthetic Limb highlighting the sensors included in the design [115].

The MPL may be considered as a system designed to assist in everyday life, another such system is Samsung’s Chef Bot. Pictured in Figure 2.2.7 the Chef Bot is designed to assist in the kitchen utilising artificial intelligence (AI) [118]. It was designed to be highly versatile and intuitive through the use of voice commands, it can perform



Figure 2.2.6: Johnny Matheny testing the Modular Prosthetic Limb [116].

a variety of tasks with its six degrees of freedom achieved through four joints in the main arm and three fingers [109]. The AI used is also capable of instructing the user with certain tasks to perform that is not within the robot's workspace, it also contains numerous safety protocols to protect individuals in the vicinity, with specific actions that are employed when the system wields sharp utensils. The AI also supports the creation and implementation of new 'skills' either through downloading these skills from a library or by 'teaching' the robot through the physical manipulation of the arm. The overall cost of this design was something that Samsung considered as a priority, using custom gearboxes and electronics meant that the system becomes more affordable to a wider range of consumers. This comes with the compromise of the payload of the system, it is not capable of lifting/moving particularly heavy objects, but is able to manipulate those commonly found in household kitchens. This system may appear to be novel, reducing the need for repetitive and laborious tasks, but not necessarily a vital device. However, for some individuals with reduced mobility this device could greatly improve their independence and quality of life.

Industrial robots also aim to perform tasks that are repetitive and/or require a great level of dexterity. They are capable of fully autonomous movements and can perform an array of tasks at a fast pace. With advancing technology teams of cooperating robot manipulators may be employed, these teams are able to complete goals that would not be possible with an individual unit [119]. In industry robot manipulators may be utilised to perform such tasks as: assembly, welding, electronics testing, spray painting, measuring, cutting and moving parts.

The KUKA iiwa manipulator is pictured in Figure 2.2.8 mounted on a moveable

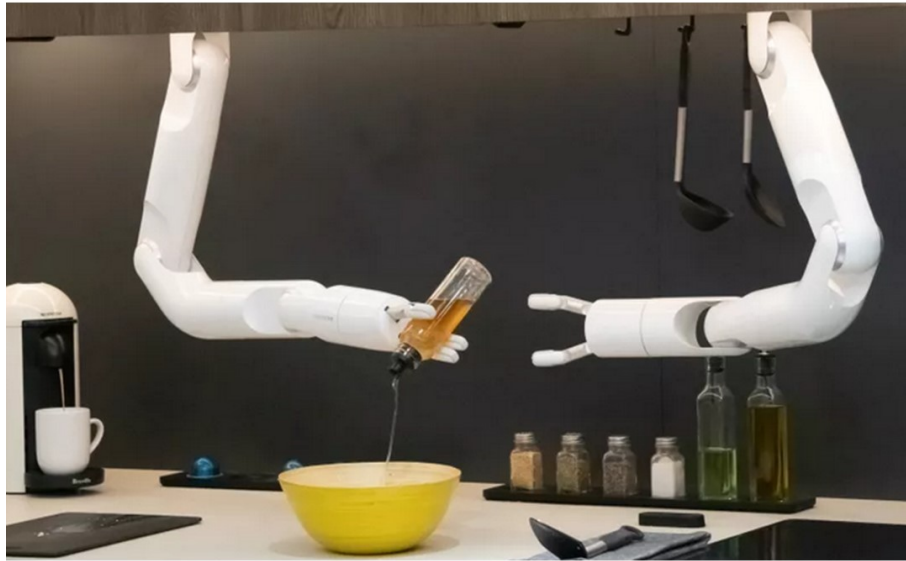


Figure 2.2.7: The Samsung Chef Bot making a salad on command [118].

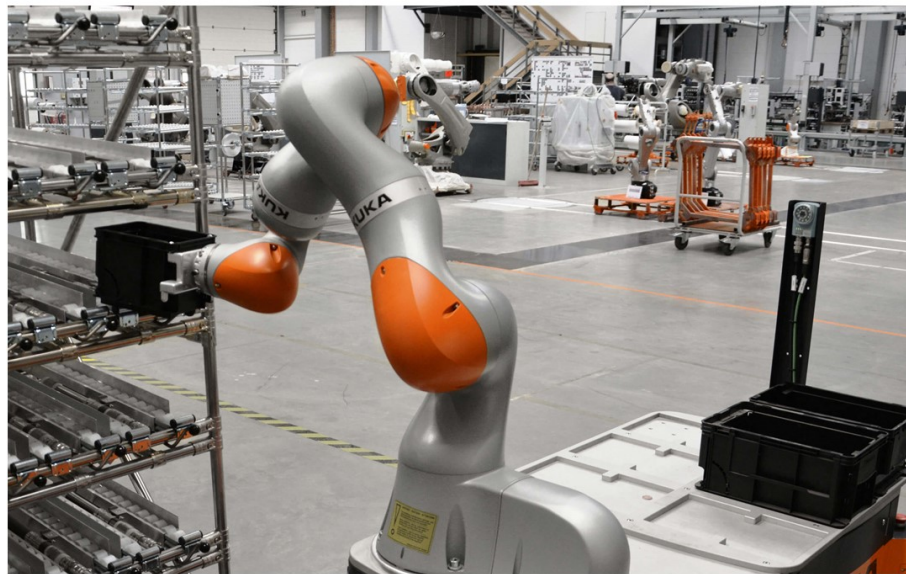


Figure 2.2.8: KUKA iiwa in industry moving components whilst mounted on a movable platform [120].

platform, this combination is known as the KUKA Mobile Robotics (KMR) iiwa [120]. Both entities in this combination are fully autonomous and have an array of safety features; the KMR iiwa can be taught its environment and sense any objects or individuals that are in its path [121]. This means that the system is an ideal addition to any warehouse environment, being able to perform repetitive tasks whilst working safely alongside warehouse employees. Another example of robot manipulators in industry is Universal Robots' R10 as shown in Figure 2.2.9 [122]. The R10 can be seen

working on an automotive assembly line alongside individuals. A case study of the use of the UR10 collaborative robots (cobots) provides an insight into the necessity for their introduction into the production line of the Nissan Motor Company [123]. The automotive plant had an aging workforce, which would have eventually led to the loss of vital skills. There were also issues with the efficiency of the production process, often leading to the employment of relief workers. At the plant two types of UR10 robots were installed granting employees more time to gain experience in other areas on the production line, and eliminating the overruns in the production process.



Figure 2.2.9: Universal Robots' UR10 collaborative robot working in an automotive assembly line alongside people [122].

These are just some of many applications for robot manipulators, and it may be concluded that they all provide vital assistance across many areas. They reduce the risk to safety in harsh environments, provide a unique approach to problems or improve the rate of completion of tasks. Through the use of collaborations with advanced technologies their control has become more intuitive and their automated movement safer, promoting their use in many fields. With further advancements in technology, and less expensive materials and manufacturing processes robot manipulators have the potential for integration in everyday life. Additionally, the tools employed alongside some of the robots mentioned here further increases the variety of applications in which they may be used. Indeed, these tools may be the same as those traditionally used in industrial practices (i.e. welding torches, drills and milling tools), but others may be more akin to a human hand for the movement and placement of objects. Such end effector tools are known as grippers, and come in a variety of configurations and sizes depending on the task required. However, most grippers consist of rigid components (or

small links) between their joints, which makes them difficult to set up for an automated process, particularly one in which the robot is to handle fragile or deformable items. Soft robotics (the manufacturer) provides a solution to this issue with their mGrip end effector tool, as pictured in multiple configurations in Figure 2.2.10 [124].

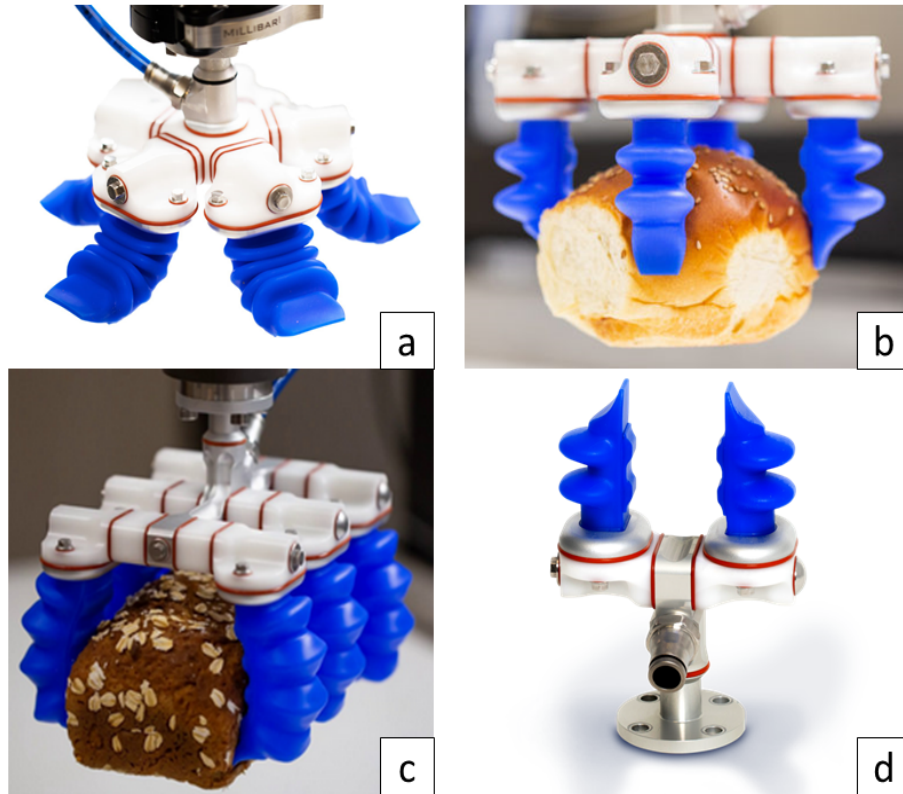


Figure 2.2.10: Images of Soft Robotics's mGrip modular end effector tool [124].

The mGrip system is modular, so that it may be used in different configurations such as those shown in Figure 2.2.10, depending on the requirements of the user. The system can be configured so the the pneumatic ‘accordion’ finger modules are arranged in a circular (Figures 2.2.10a and 2.2.10b) or a linear pattern (Figures 2.2.10c and 2.2.10d). The system uses an independent air supply, lending to it being able to be mounted upon a variety of robot manipulators, and hence its suitability for integration within industries that have some level of automation. The flexible nature of the mGrip system means that the user need only provide a rough estimation of the item to be manipulated, and the gripper will be able to hold it (within reason). This is especially advantageous in areas such as food production (the fingers are available in a food safe material option), where the items may not only be delicate but vary in size and shape for example baked goods, as can be seen in Figures 2.2.10b and 2.2.10c.

As the name of the manufacturer suggests, the mGrip system falls under the soft robotics category of autonomous systems, wherein part or all of the system is flexible. Systems that employ soft or flexible links, components and actuators have a great

amount of potential, and it has been theorised that “In the future, robotic components could be passed through small holes like a liquid and reformed on the other side into a shapes that allows them to start doing work” [125]. Unfortunately, such a system is currently far from reality, but there are many researchers implementing soft robotics with the currently available technologies and materials. One area of the application of soft robotics which has received a considerable amount of attention is in the support and rehabilitation of injured or otherwise disabled individuals. A collaboration of researchers realised this application and produced ‘the right trousers’, a wearable soft robotics systems designed to “work in harmony with the human body” [126]. As identified in Figure 2.2.11, these trousers implement an array of technology to not only support the wearer but aid in their rehabilitation. The power supply and electronics included in the design are small and lightweight, and allows the user to adjust how much assistance to their motion the system provides. Inertial measurement units (IMUs) are incorporated in the design to monitor the users motion, and provide an input into the control system to actuate the artificial muscles and the ‘active-stiffening brace’ which consist of electrically stimulated flexible smart materials. Additionally, this design includes functional electrical stimulation (FES) arrays, which subject the user’s muscles to safe level electrical current and voltage to stimulate their muscles. By stimulating the muscles in this manner it assists the wearer in their movements and their rehabilitation.

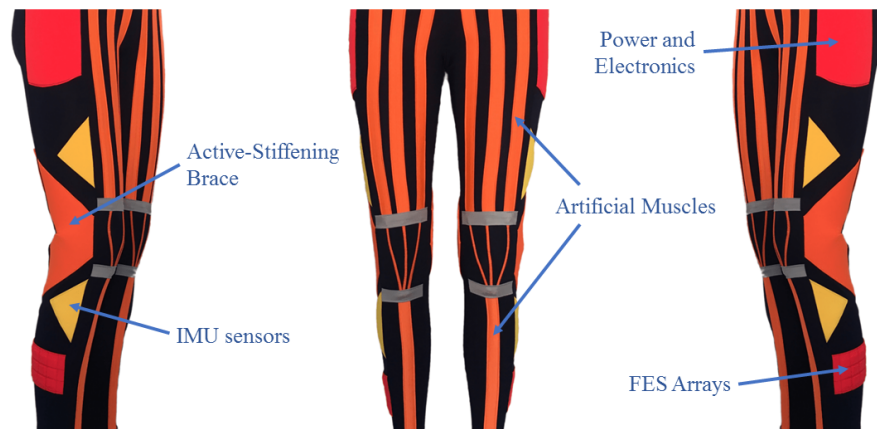


Figure 2.2.11: Images of ‘the right trousers’ by a collaboration of researchers.

Although soft (or purposefully flexible) robot systems are not explicitly relevant in relation to this research topic, the applications discussed here show further potential for the control system developed in this research. For example, the designed control system could be employed on a flexible gripper structure offering a more compliant solution, or it could be used in wearable technology (provided the system has some further safety provisions in place).

2.3 KUKA LBR iiwa 7 R800

This section aims to both justify the choice of and disseminate information regarding the selected robot manipulator to be used in this research, the KUKA LBR iiwa 7 R800. The manipulator is one of two versions in a series, where the ‘7’ in its name denotes its maximum payload capacity in kilograms, the other option is capable of manipulating a 14 kg payload. The acronyms LBR and iiwa stand for “Leichtbauroboter” (German for lightweight robot) and intelligent industrial work assistant, respectively [3]. The last term in its name denotes its reach i.e. the R800 model has a reach of 800 mm. This manipulator, as with others in the series has seven revolute joints yielding seven degrees of freedom, which makes it very versatile but also sits it in the redundant manipulator class. Weighing in at 22.3 kg it is relatively lightweight for an industrial robot and can be mounted on ceilings, floors and walls. This advantage along with the variety of media flange (MF) options which lend to the ability to use a multitude of tools makes this series of manipulators desirable to an abundance of end users.

KUKA suggests that this robot manipulator series is suitable for applications including: painting, glueing, assembly, palletising, packaging, handling, measuring, inspection and machining. Research has also been conducted utilising the KUKA LBR iiwa 7 R800 in applications other than industrial, which include medical [127, 128, 129], space [130], and even household chores [131]. Admittedly, even though this model of manipulator is considered lightweight in terms of an industrial robot at a mass of 22.3 kg it would still be considered too heavy for the suggested application. However, its popularity in research stems from its accuracy, manoeuvrability and intuitive motion planning software, all of which are deemed highly advantageous for the purpose of this research. Considering that the role of the manipulator is to be an excitation source for the flexible link, and to act as a method of observing the designed control system’s effect on the functionality of the manipulator, the conclusions drawn from its implication may be applied to other smaller, lighter manipulators.

A range of MFs is offered as their choice of use is dependent on the application, for example some options enable the connection of pneumatic or electric tools (or both) to the end effector of the manipulator. However, this research requires no such connectivity as the control system for the flexible link is to be designed to be independent from the existing system. In addition, all of the MF options have a hole pattern (threaded) that conforms to the same standard (DIN ISO 9409-1-50-7-M6). For these reasons the choice of MF mounted on the manipulator is irrelevant, as any clamp structure designed to be mounted on one option will also be suitable for the others. This robot series boasts excellent safety procedures employed during motion, resulting in the manipulator stopping should it sense a change in the torque of its joints i.e. when any part of the

manipulator makes contact with an object or person. However, these safety features would not be fully extended to the flexible link, the end joints may detect a difference in torque, but certainly would not stop the link from making contact with an object/person due to its weight and flexible nature. An additional hazard that can be identified is that the PZT actuators mounted on the link are subject to high voltages, posing a risk to those in the vicinity. To reduce this risk, the workspace of the robot (the region surrounding the manipulator that it can reach) should be considered so that a suitable area can be cordoned off. Figure 2.3.1 contains the workspace of the KUKA manipulator [132], where the dimensions labelled in the image are outlined in Table 2.3.1. It should be noted that in this case MF is equal to 0.035 m, and the length of the link/clamp structure needs to be incorporated into the workspace shown in Figure 2.3.1.

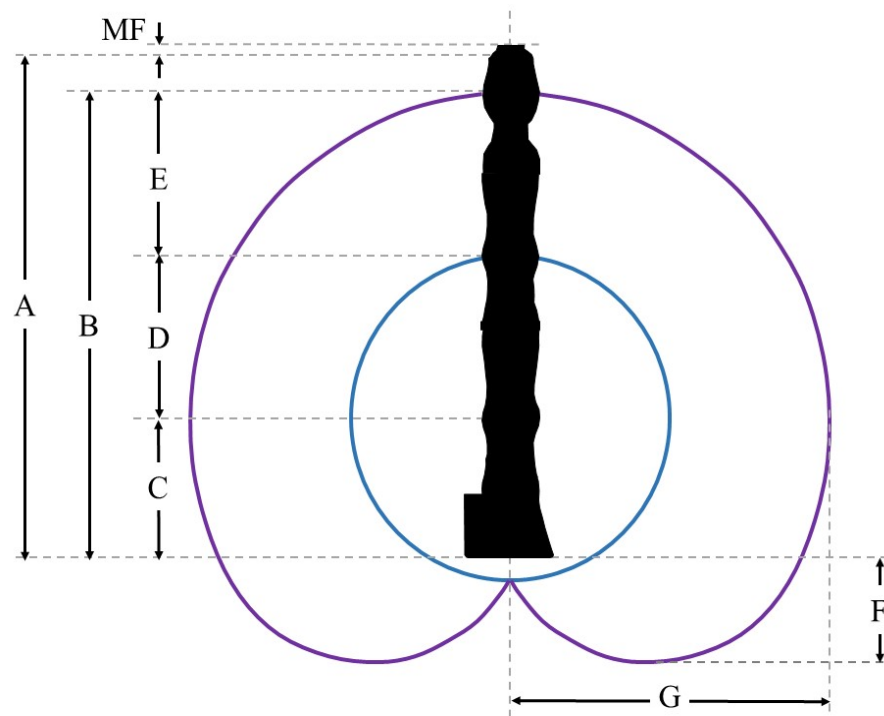


Figure 2.3.1: Image of the KUKA LBR iiwa 7 R800 workspace and joint lengths.

Label	A	B	C	D	E	F	G
Dimension (m)	1.266	1.14	0.34	0.4	0.4	0.26	0.8

Table 2.3.1: Labels of dimensions shown in Figure 2.3.1 outlining the KUKA LBR iiwa 7 R800 workspace.

2.4 Analytical Model

An analytical model of the KUKA LBR iiwa 7 R800 has been created with the purpose of obtaining accurate predictions of the end effector position from given joint angles (forward kinematics (FK)). The model has been created based upon a method originally proposed in 1955 by Denavit and Hartenberg, wherein the geometric properties of a joint and link series are described systematically [133]. This became a popular method known as the Denavit-Hartenberg (D-H) notation, which requires the knowledge of the coordinate frames associated with each joint. The convention which dictates each frame utilises the following rules:

- The x_i axis must be perpendicular to the z_i axis and the z_{i-1} axis.
- The z_i axis should be parallel with joint i , and the joint i should rotate about the z_i axis.
- The x_i should intersect the z_{i-1} axis. Note that this does not apply to the 0^{th} frame (F_0).
- The y_i axis is chosen such that the resultant frame forms a right-hand coordinate system (see Figure 2.4.1).

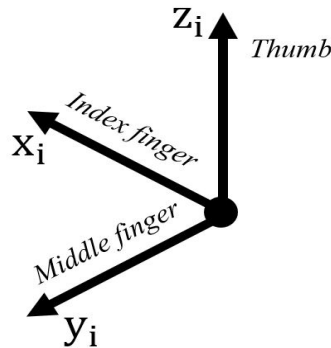
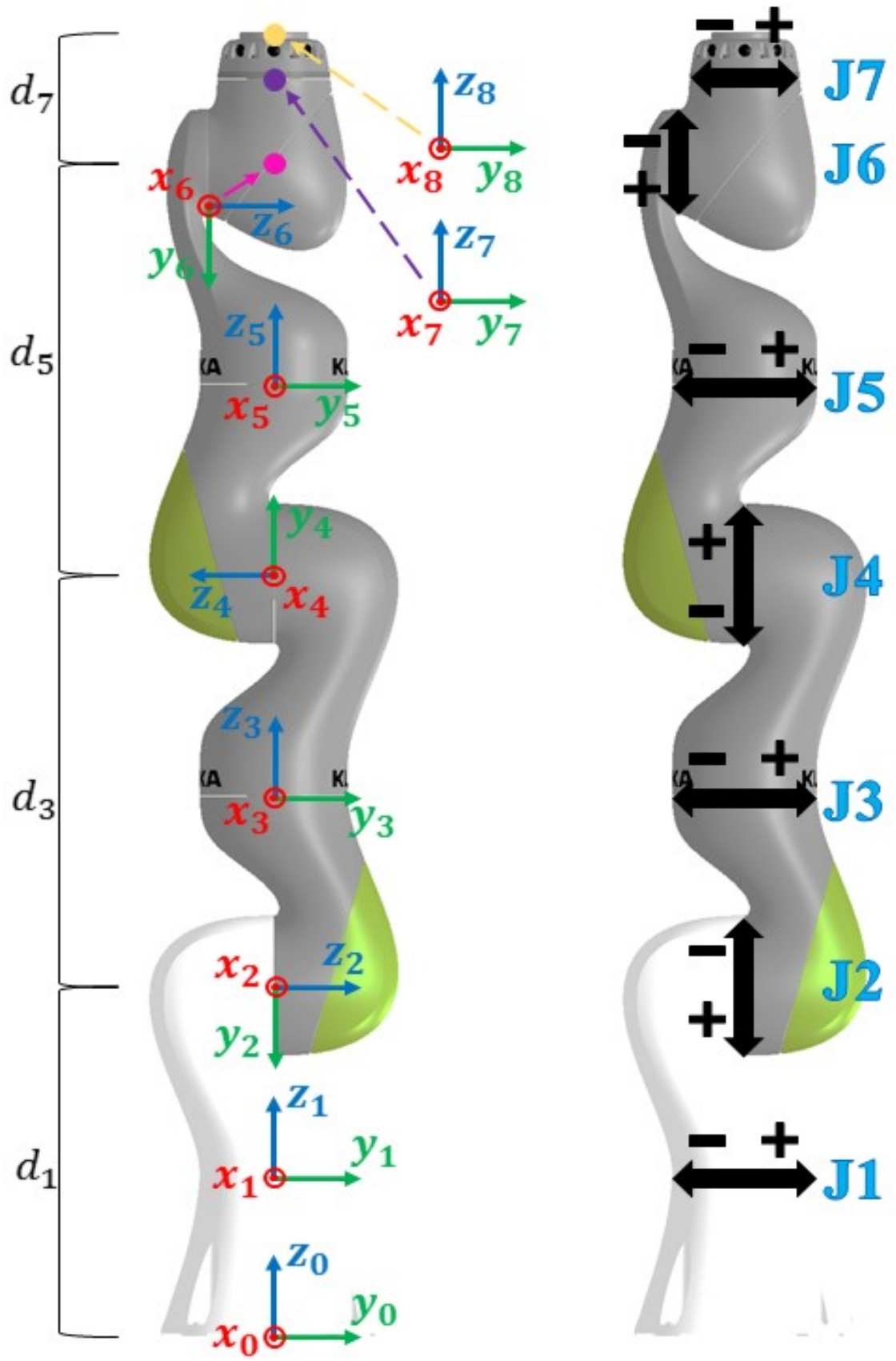


Figure 2.4.1: Illustration of the right-hand coordinate system

Obeying these rules, the joint frames were defined as in Figure 2.4.2a below, and Figure 2.4.2b shows the positive and negative rotations of each joint.



(a) Illustration of joint frames.

(b) Illustration of joint angles.

Figure 2.4.2: Illustration of the analytical model of the manipulator including coordinate frames and orientation of the joints.

The four variables in the D-H convention are as follows:

- Φ The angle between joint i and joint $i - 1$ about z_{i-1} .
- d The distance between the origin of frame $i - 1$ to x_i along z_i .
- a The distance between z_i and z_{i-1} along x_i .
- α The angle about the common normal from z_{i-1} to z_i .

Employing these definitions to the KUKA manipulator yields the D-H parameters outlined in Table 2.4.1, which also includes the range of motion (ROM) for each joint as well as the maximum joint velocity (MJV) for each joint [3]. Simplification yields the zero values for d_2 , d_4 and d_6 , which is achieved through envisioning those joints which rotate around the vertical axis of the world frame (z_0) as having the same origin as that preceding it [134]. This means the origin of frames 1, 3 and 5 are equivalently located at the origins of frames 2, 4 and 6, lending to no distance between frames 2,4 and 6 and those preceding them. This does not negatively affect the analytical model of the manipulator, but allows for the improvement of computation time.

Joint (i)	Φ_i (rad)	d_i (m)	a_i (m)	α_i (rad)	ROM (\pm deg)	MJV ($^\circ$ /s)
1	Φ_1	0.34	0	$-\pi/2$	170	98
2	Φ_2	0	0	$\pi/2$	120	98
3	Φ_3	0.4	0	$\pi/2$	170	100
4	Φ_4	0	0	$-\pi/2$	120	130
5	Φ_5	0.4	0	$-\pi/2$	170	140
6	Φ_6	0	0	$\pi/2$	120	180
7	Φ_7	0.126	0	0	175	180

Table 2.4.1: D-H parameters, range of motion (ROM) and maximum joint velocities (MJV) used in the analytical model.

These D-H parameters were then utilised to obtain the kinematics of the robot, and the range of motion for each joint was included to prevent the analytical model from producing unrealistic solutions. Describing the joint angles and then calculating the Cartesian coordinates of the end effector (FK) requires the use of the transformation matrix (T) which describes the rotation and translation of a frame with respect to the previous frame (Equation 2.1). Calculating each transformation matrix systematically and then multiplying yields the overall transformation matrix of the robot arm (Equation 2.2).

$$T_{i-1}^i = \begin{bmatrix} \cos(\Phi_i) & -\cos(\alpha_i) \sin(\Phi_i) & \sin(\alpha_i) \sin(\Phi_i) & a_i \cos(\Phi_i) \\ \sin(\Phi_i) & \cos(\alpha_i) \cos(\Phi_i) & -\sin(\alpha_i) \cos(\Phi_i) & a_i \sin(\Phi_i) \\ 0 & \sin(\alpha_i) & \cos(\alpha_i) & d_i \\ 0 & 0 & 0 & 1 \end{bmatrix} \quad (2.1)$$

$$T_0^n = T_0^1 T_1^2 T_2^3 \dots T_{n-1}^n \quad (2.2)$$

The rotation (Γ_{nm}) terms and translation in Cartesian coordinates (x, y, z) are located within the transformation matrix as shown in Equation 2.3. It should be noted that the subscripts n and m in the rotation terms denote the rows and columns of the matrix, respectively.

$$T_0^n = \begin{bmatrix} \Gamma_{11} & \Gamma_{12} & \Gamma_{13} & x \\ \Gamma_{21} & \Gamma_{22} & \Gamma_{23} & y \\ \Gamma_{31} & \Gamma_{32} & \Gamma_{33} & z \\ 0 & 0 & 0 & 1 \end{bmatrix} \quad (2.3)$$

From Equation 2.3 it can be seen that the Cartesian coordinates of the end effector can be readily obtained from the transformation matrix T_0^n , whereas in order to yield the rotations about the x , y and z axes require additional equations. There are two sets of equations that are to be used, and which set to be used is dictated by the value of Γ_{11} in Equation 2.3. If the magnitude of this value is one then the first set of equations is to be used (Equation 2.4), and if it is any other value then the second set is to be employed (Equation 2.5).

$$\begin{aligned} \Gamma_x &= 0 \\ \Gamma_y &= -\text{atan2}(\Gamma_{13}, \Gamma_{34}) \\ \Gamma_z &= 0 \end{aligned} \quad (2.4)$$

$$\begin{aligned} \Gamma_x &= \text{asin}(\Gamma_{21}) \\ \Gamma_y &= -\text{atan2}(\Gamma_{31}, \Gamma_{11}) \\ \Gamma_z &= \text{atan2}(\Gamma_{23}, \Gamma_{22}) \end{aligned} \quad (2.5)$$

Inverse kinematics (IK) is the calculation of the joint angles of a robot manipulator based on the end effector position. The IK of this particular robot arm with its seven degrees of freedom would require a complex analytical model which would render the calculations inefficient in terms of time. There is a multitude of research dedicated to

the predictions of the IK of redundant robot manipulator, and the calculation of the IK of the manipulator has been deemed both unnecessary to include in, and beyond the scope of this research. To further justify the choice to omit the calculation of the IK it should be noted that the motion of KUKA manipulator is capable of being programmed based on the end effector position. The joint angles that correspond to selected points along the motion path can be retained by the software. The points can either be selected based on steps in the path, or at specified intervals in time. The corresponding joint angles can then be used as an input into the FK model, and the analytically obtained end effector path may be compared with the experimental counterpart for validation.

To analyse the kinematic model of the robot manipulator a sensitivity study was conducted, where the joint angles of the robot manipulator were considered as inputs to the system (Ψ_1 to Ψ_7) and the coordinates of and rotations about the x , y and z axes of the end effector were considered as outputs ($E_{out,1}$ to $E_{out,6}$). The sensitivity matrix (S) was created using the matrix shown as Equation 2.6.

$$S = \begin{bmatrix} \frac{\partial E_{out,1}}{\partial \Psi_1} & \frac{\partial E_{out,1}}{\partial \Psi_2} & \frac{\partial E_{out,1}}{\partial \Psi_3} & \frac{\partial E_{out,1}}{\partial \Psi_4} & \frac{\partial E_{out,1}}{\partial \Psi_5} & \frac{\partial E_{out,1}}{\partial \Psi_6} & \frac{\partial E_{out,1}}{\partial \Psi_7} \\ \frac{\partial E_{out,2}}{\partial \Psi_1} & \frac{\partial E_{out,2}}{\partial \Psi_2} & \frac{\partial E_{out,2}}{\partial \Psi_3} & \frac{\partial E_{out,2}}{\partial \Psi_4} & \frac{\partial E_{out,2}}{\partial \Psi_5} & \frac{\partial E_{out,2}}{\partial \Psi_6} & \frac{\partial E_{out,2}}{\partial \Psi_7} \\ \frac{\partial E_{out,3}}{\partial \Psi_1} & \frac{\partial E_{out,3}}{\partial \Psi_2} & \frac{\partial E_{out,3}}{\partial \Psi_3} & \frac{\partial E_{out,3}}{\partial \Psi_4} & \frac{\partial E_{out,3}}{\partial \Psi_5} & \frac{\partial E_{out,3}}{\partial \Psi_6} & \frac{\partial E_{out,3}}{\partial \Psi_7} \\ \frac{\partial E_{out,4}}{\partial \Psi_1} & \frac{\partial E_{out,4}}{\partial \Psi_2} & \frac{\partial E_{out,4}}{\partial \Psi_3} & \frac{\partial E_{out,4}}{\partial \Psi_4} & \frac{\partial E_{out,4}}{\partial \Psi_5} & \frac{\partial E_{out,4}}{\partial \Psi_6} & \frac{\partial E_{out,4}}{\partial \Psi_7} \\ \frac{\partial E_{out,5}}{\partial \Psi_1} & \frac{\partial E_{out,5}}{\partial \Psi_2} & \frac{\partial E_{out,5}}{\partial \Psi_3} & \frac{\partial E_{out,5}}{\partial \Psi_4} & \frac{\partial E_{out,5}}{\partial \Psi_5} & \frac{\partial E_{out,5}}{\partial \Psi_6} & \frac{\partial E_{out,5}}{\partial \Psi_7} \\ \frac{\partial E_{out,6}}{\partial \Psi_1} & \frac{\partial E_{out,6}}{\partial \Psi_2} & \frac{\partial E_{out,6}}{\partial \Psi_3} & \frac{\partial E_{out,6}}{\partial \Psi_4} & \frac{\partial E_{out,6}}{\partial \Psi_5} & \frac{\partial E_{out,6}}{\partial \Psi_6} & \frac{\partial E_{out,6}}{\partial \Psi_7} \end{bmatrix} \quad (2.6)$$

Within this analytical analysis the partial derivatives may be approximated to the change of the output divided by the change of the input. For the initial pose all joint angles were set to 10° and each was moved individually to 10.001° ($\Delta\Psi = 0.001^\circ$). The initial joint angle of 10° was selected as opposed to 0° (the manipulator is in its straight pose) as a rotation of joints 1, 3, 5 and 7 would not change the end effector position, only its rotation. It should be noted that apart from the requirement to avoid the manipulator's straight pose, the selection of 10° was arbitrary. The change in angle was selected as this is the lowest step size of the joint angles of the robot manipulator. However, to determine if increasing this change in angle adjusts the magnitudes of the sensitivities a second study was conducted. This study used the same initial joint angle as the first, but the change in angle was increased to one hundred times that of the previous investigation ($\Delta\Psi = 0.1^\circ$). The matrix shown

as Equation 2.7 contains the values obtained through the use of Equation 2.6 for the first investigation ($\Delta\Psi = 0.001^\circ$). The values obtained from the second investigation ($\Delta\Psi = 0.1^\circ$) are presented as Equation 2.8.

$$S = \begin{bmatrix} -0.0076 & 0.9040 & 0.0202 & -0.4928 & -0.0109 & 0.1075 & 0 \\ 0.0915 & 0.1594 & -0.0669 & -0.1786 & 0.0190 & 0.0624 & 0 \\ 0 & -0.0914 & -0.0015 & 0.0202 & 0.0006 & -0.0209 & 0 \\ 0 & 0.5104 & 0.1519 & -0.3530 & -0.0131 & 0.1829 & 0.1600 \\ 0 & 0.8637 & -0.0875 & -0.9368 & -0.0274 & 0.9831 & -0.0583 \\ 1 & 0.0808 & 1.0089 & -0.0860 & 0.9975 & 0.0582 & 1.0110 \end{bmatrix} \quad (2.7)$$

$$S = \begin{bmatrix} -0.0077 & 0.9039 & 0.0202 & -0.4928 & -0.0109 & 0.1074 & 0 \\ 0.0915 & 0.1594 & -0.0669 & -0.1786 & 0.0190 & 0.0624 & 0 \\ 0 & -0.0922 & -0.0015 & 0.0197 & 0.0006 & -0.0210 & 0 \\ 0 & 0.5105 & 0.1518 & -0.3529 & -0.0131 & 0.1829 & 0.1600 \\ 0 & 0.8637 & -0.0876 & -0.9368 & -0.0273 & 0.9831 & -0.0585 \\ 1 & 0.0812 & 1.0088 & -0.0857 & 0.9975 & 0.0584 & 1.0110 \end{bmatrix} \quad (2.8)$$

From the sensitivity matrix of the first investigation (Equation 2.7) it can be seen that the position of the end effector ($E_{out,1 \text{ to } 3}$) is less sensitive to a change in the joint angles of the manipulator than the rotations about the x , y and z axes ($E_{out,4 \text{ to } 6}$). For some joint angle changes the change in one or more of the end effector positions with respect to the world frame is equal to zero, this is to be expected when considering the orientation of the joints (see Figure 2.4.2). The rotation of the seventh joint (J7 in Figure 2.4.2) would not affect the position of the end effector, only the rotation, regardless of the angles of the previous joints. Additionally, the change in the end effector's rotation about the z axis of the world frame will equate to the seventh joint's rotation. The values of the sensitivity matrix obtained for the second instance of the change of angle (Equation 2.8) are highly similar to those from the first instance. This shows linear behaviours for the range of increments chosen in this study and hence indicates the accuracy of sensitivities calculated by finite difference method.

2.5 Experimental validation

To validate the acquired analytical model, for use in the amalgamation of said model with the analytical model of the link and piezoelectric patches, results from the manipulation of the KUKA iiwa 7 were obtained. To observe the accuracy of the model with respect to all three axes a helix was chosen as the end effector path with its length parallel to the y axis of the world frame (akin to a global coordinate system) of the manipulator. The starting point of the helix was selected so that Cartesian coordinates were $(0.526, 0, 0.74)$ m and the corresponding joint angles ($\Psi_{1 \text{ to } 7}$) were $\left[0 \ 0 \ 0 \ -\frac{\pi}{2} \ 0 \ 0 \ 0\right]$ rad. This helix was programmed as a point-to-point trajectory of the end effector in the software of manipulator i.e. the motion was not smooth and paused at each point where the software recorded the corresponding joint angles. These joint angles were then used as an input into the FK analytical model of the manipulator to produce the equivalent end effector position for each set, which were then compared with the experimental results.

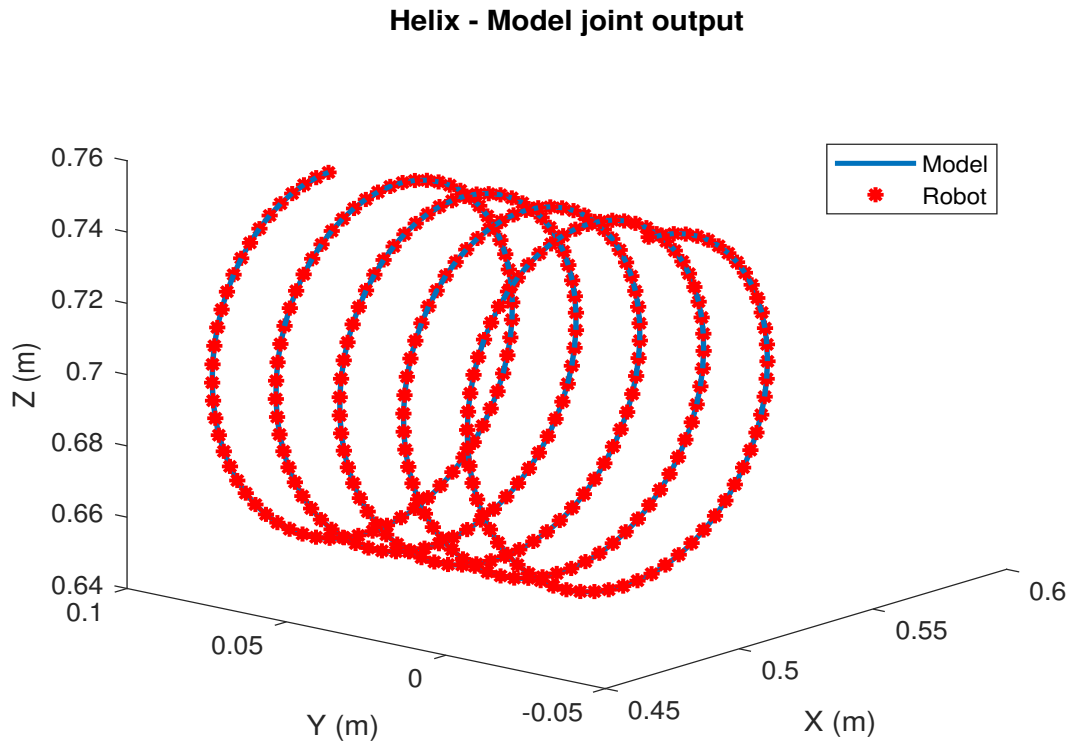


Figure 2.5.1: Cartesian coordinates of analytical model and the robot manipulator.

Figure 2.5.1 contains this comparison, and as can be interpreted from said figure the results from analytical model closely match those from the robot manipulator. With the percentage error for the x , y and z axes being 0.0107%, 0.0153% and 0.0067%, respectively, ultimately confirming that the model is a good approximation in terms of

displacement. Regarding the prediction of the velocity, a different approach was used for the validation. Each joint of the robot manipulator in turn was programmed to rotate from 0 to $\pi/2$ rad at maximum speed, and the joint angle was recorded using the KUKA Sunrise Workbench software at a rate of 100 Hz. For the same angular range (Λ_1 to Λ_n) the maximum joint velocities ($\vec{v}_{i,max}$) (see Table 2.4.1) were used to obtain the time taken between each angular step (t_i) (see Equation 2.9).

$$t_i = \frac{\Lambda_i - \Lambda_{i-1}}{\vec{v}_{i,max}} \quad (2.9)$$

A cumulative sum of t_{1-n} produces the equivalent time for each angle within the range. These analytical results for each joint were compared with their corresponding joint results retrieved from the robot manipulator.

From the results in Figure 2.5.2 it is clear to see that the prediction of the joint velocities is fairly accurate. However, a notable discrepancy can be observed between the two results which stems from the neglect of acceleration/deceleration within the analytical model. This difference is subtle enough to disregard, and still assume the analytical model to be an accurate prediction in terms of velocity.

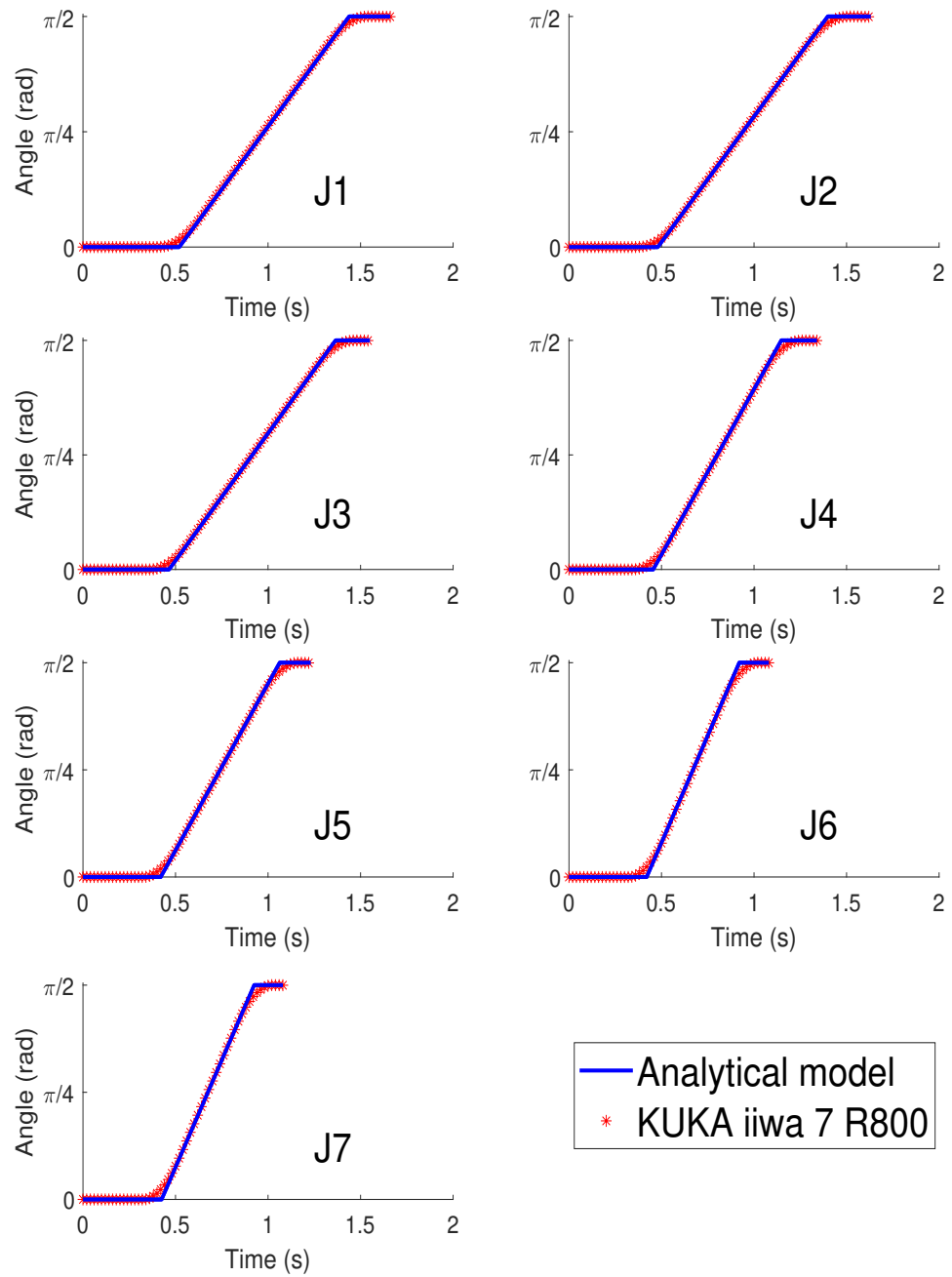


Figure 2.5.2: Joint velocities from analytical model and the robot manipulator for each joint (J1-J7).

2.6 Summary

This chapter provided a brief history and overview of robotics (with a focus on robotic manipulators), and identified statistically the most common applications. This was investigated further, focussing on specific examples of robot manipulators and related systems between which the versatility of robot manipulators was highlighted. This also provided an insight into a need for more compliant robot components, especially regarding flexible end effector tools, which led to a potential alternate application for the control of flexible structures in wearable robot systems. A specific manipulator was identified for use in this research based on its advantageous specifications, and a kinematic model of this manipulator was then developed and validated through the comparison with experimentally obtained results. The validation of this model means that it was able to be utilised to answer the concern of whether mounting the control system upon the manipulator would affect its functionality (addressed in a later chapter).

Chapter 3

Model and validation of open loop systems

3.1 Robot links

The links of a robot manipulator are its structure, where relative motion between two links is achieved through the movement of the joint between them. The shape, size, mass and material of the links are based on the required functionality of the manipulator. Links of robots with multiple degrees of freedom are especially required to have a certain level of rigidity to ensure the best possible accuracy of the end effector position. However, manipulator links are often comprised of materials which easily allow them to form a notable percentage of the total mass. In the majority of applications of robot manipulators the reduction of mass is held as high importance. The reasons for such a specification can be based on the functionality of the robot, the intended environment and/or its transportation amongst others. Utilisation of a smaller and lighter link design in lieu of more traditional designs, will achieve the goal of the reduction of overall mass.

Mild steel or annealed steel are options for use as the link's material, and are readily available, have a high strength and are relatively inexpensive. Aluminium and aluminium alloys offer around a third of the strength of steel, but have a lower density and are more easily machined in comparison making them a very viable choice in the construction of a robot manipulator [135]. A long slender rectangular beam of either aluminium or steel was therefore considered as the best solution in this research due to the advantages aforementioned. However the disadvantage of a lower stiffness arises from the replacement of conventional links with long slender ones, which can lead to the link experiencing unwanted vibrations along its length. Even if only one link is replaced the accuracy of the end effector position can be compromised due to said unwanted transverse oscillations, therefore a solution is required to attenuate them.

In this chapter analytical and simulation models of a link are created and validated experimentally for use in further experimentation described in proceeding chapters.

3.2 Inertial measurement units (IMUs)

An inertial measurement unit or IMU is an electronic device designed to measure a combination of acceleration, angular velocity and/or orientation. The measurements are achieved through the utilisation of an accelerometer, a gyroscope and a magnetometer, although the latter sensor is often not utilised due to its predisposition for ferromagnetic objects in the immediate surrounding affecting its functionality. However, even with all three types of sensors in one unit the electronic device is relatively small and of low mass, allowing for integration with a structure which results in little to no effect on the structure's properties/functionality. An IMU with an accelerometer measuring acceleration along all three axes, a gyroscope measuring the angular velocity about all three axes and a magnetometer measuring the magnetic field strength along all three axes would accrue nine degrees of freedom.

The three different sensors used within an IMU are micro-electromechanical systems (MEMS); systems of mechanical or electro-mechanical nature with dimensions in the order of micro-meters (μm). A MEMS accelerometer is typically created through the etching of a silicon substrate to form a structure with a static and a moveable part [136]. A simplified example is shown in Figure 3.2.1, where the image on the left hand side illustrates the static structure and the image in the left shows the structure when subject to an acceleration.

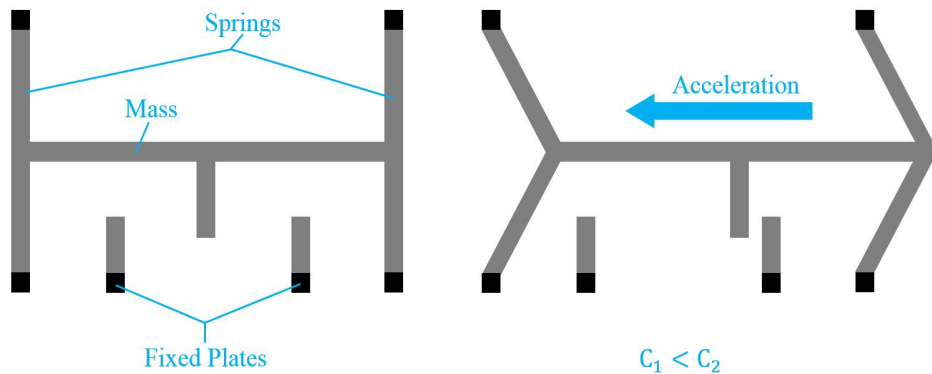


Figure 3.2.1: Simplified illustration of a MEMS accelerometer.

The springs outlined in Figure 3.2.1 are flexible pieces of the silicon substrate and allow the mass to move when subject to acceleration. As the finger (the piece of substrate that is part of the mass which extends between the two fixed plates) approaches a static finger (one of the pieces attached to the fixed plate) the capacitance of the

static finger is increased. The operational range and bandwidth of the accelerometer can be adjusted through altering the mass, spring stiffness and damping of the system.

The Coriolis effect is utilised within MEMS gyroscopes to measure the angular rate of a body. This effect is best described with an example; a rotating disc with its surface parallel to the ground. Figure 3.2.2 illustrates such a scenario, showing a plan view of a disc rotating parallel to the ground about its centre, O . A and B here denote positions of length L_1 and L_2 from the centre. Assuming $L_2 = 2L_1$ an object positioned at point B would experience a tangential velocity double in magnitude compared to an object positioned at A relative to the ground. Thus the Coriolis acceleration can be defined as rate of increase of tangential velocity as a result of radial velocity.

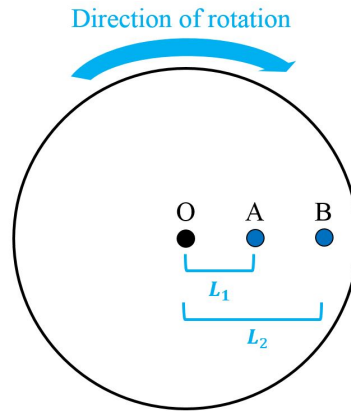


Figure 3.2.2: Illustration of the Coriolis effect.

As with a MEMS accelerometer, a MEMS gyroscope is manufactured through the etching of a silicon substrate. The structure of a MEMS gyroscope is more complicated than that of the accelerometer, containing a mass, an inner frame and an outer frame (see Figure 3.2.3). The mass is tethered to the inner frame so that its motion is limited to one axis, and likewise the inner frame is tethered to the outer frame so that it to can only move along one axis (perpendicular to the mass motion). The mass oscillates analogous to a body moving in line with positions A and B in Figure 3.2.2, effectively varying its radius. As the mass approaches the furthest point from the center of rotation (the first image within Figure 3.2.3) it is accelerated to the right and exerts a reaction force on the frame to the left. This in turn causes the moving fingers attached to the inner frame to approach the fixed (or sensing) fingers to their left thus altering the capacitance. The forces will occur in the opposite directions when the mass approaches the centre of rotation, the acceleration on the mass will be to the left and the force exerted on the frame will be to the right. As the amplitude of the motion of the mass is known, and the capacitance that is output based on the proximity of the fingers will yield the acceleration, the tangential velocity and thus the angular rate can be calculated.

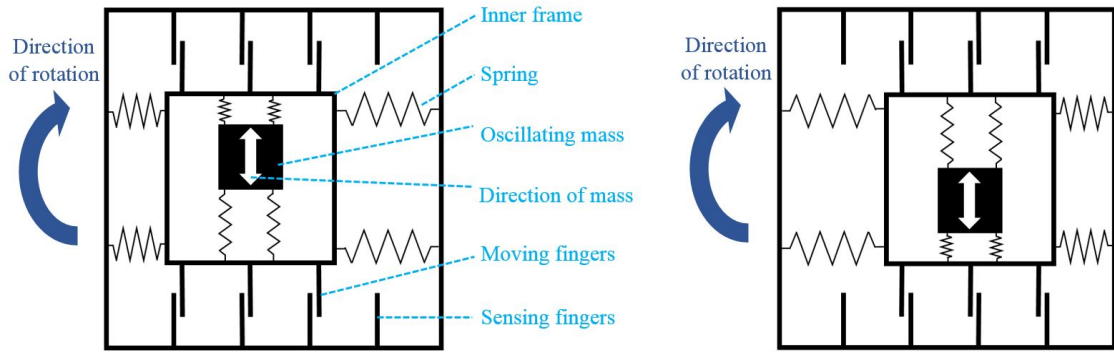


Figure 3.2.3: Simplified illustration of a MEMS gyroscope.

A MEMS magnetometer utilises the Hall effect to obtain the ‘heading’ of the body. Named after its discoverer Edwin Hall, this phenomenon observes the relationship between a current applied to, the magnetic field acting upon and the potential voltage across a thin plate of conductive material. The production of a short voltage pulse in the instant that a magnet is applied to a plate of conductive material and subsequently when the magnet is removed was well known by the late 19th century. However, the discovery made in 1879 was unique as the effect occurs in steady-state conditions; the voltage across the plate remains constant with the constant application of current and magnetic field [137]. Figure 3.2.4 illustrates the basic set-up required to observe the Hall effect. An electric current is applied across the conductive plate of material, in this case the current is supplied by a battery. When no magnetic field is present there is no voltage produced across the the plate, in the second instance shown in Figure 3.2.4 there is a magnetic field applied. A voltage is generated across the plate perpendicular to both the current and the magnetic field (combined to form an electromagnetic field). If the polarity of the magnetic field is reversed, then the voltage polarity will reflect this and will also reverse.

The voltage generated through the Hall effect is a result of the electromagnetic field’s influence on the charged particles within the plate. The field exerts a force on the particles which may be described through Equation 3.2 which is commonly known as the Lorentz equation. Where all of the variables apart from q_0 (the magnitude of the charge) are all vector quantities containing independent x , y and z components.

$$\vec{F} = q_0\vec{E} + q_0\vec{v} \times \vec{B} \quad (3.1)$$

The resultant force and electric field are denoted as \vec{F} and \vec{E} , respectively. \vec{v} and \vec{B} represent the velocity of the charge and the magnetic field, respectively. When the plate is subject only to an electric field (as in the first of the representations of Figure 3.2.4), a force proportional to the magnitude of the charge and the strength of the electric field

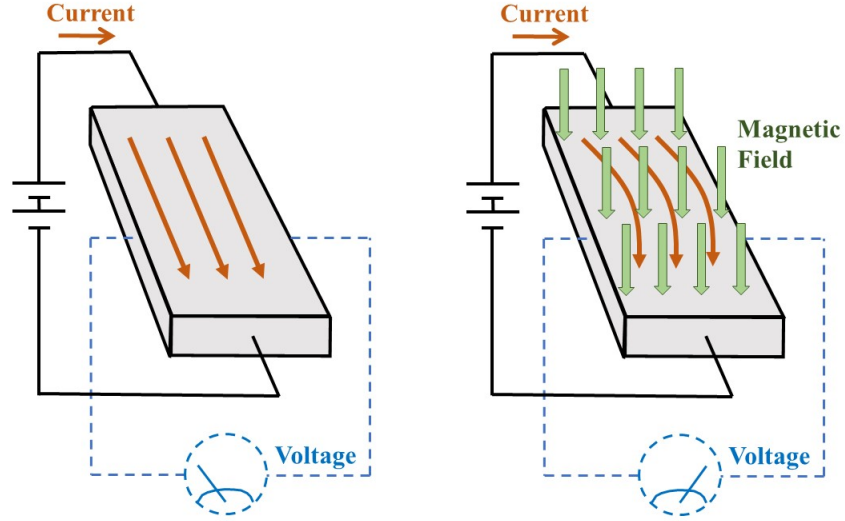


Figure 3.2.4: Illustration of the set-up to demonstrate the Hall effect.

is experienced by the charge. For the case where the plate is subject to a magnetic field the charged particles would not experience any force unless they are moving. With the application of current so that the particles are in motion the force they experience is a function of their individual charge, the direction of the particle and the orientation of the magnetic field through which it is moving. As shown by the arrows representing the charged particles for the second case in Figure 3.2.4, the force pushes the charges to one side of the plate, creating a potential difference across it. This force may be expressed in each direction as a function of the magnitude of the charge (q_0), its velocity (\vec{v}) and the magnetic field (B) as in Equations 3.2.

$$\begin{aligned}
 F_x &= q_0(\vec{v}_y B_z - \vec{v}_z B_y) \\
 F_y &= q_0(\vec{v}_z B_x - \vec{v}_x B_z) \\
 F_z &= q_0(\vec{v}_x B_y - \vec{v}_y B_x)
 \end{aligned} \tag{3.2}$$

A transducer is a device which converts observable variations in a physical quantity, such as sound or acceleration (as in an accelerometer), to an electrical signal. These devices can also work in reverse, converting electrical signals into physical quantities i.e. a speaker. Figure 3.2.5 illustrates a Hall transducer, which can be used to convert the direction of a magnetic field to a readable voltage. The voltage terminals are positioned perpendicular to the velocity of the charges with the direction of this velocity being constrained to the z axis (i.e. $\vec{v}_x = 0$ and $\vec{v}_y = 0$). Through this constraint Equations 3.2 may be simplified to one, as expressed in Equation 3.3.

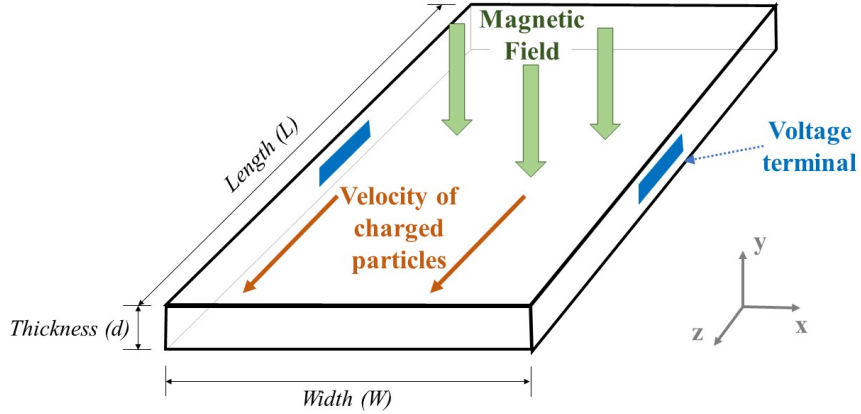


Figure 3.2.5: Illustration of a Hall transducer.

$$F_x = -q_0 \vec{v}_z B_y \quad (3.3)$$

Observing this reduced equation it can be concluded that this particular Hall-effect transducer will only be sensitive to the y component of the magnetic field. The movement of the charged particles to one side of the transducer by force induced upon them by the magnetic field is a process which is self-limiting. It provides a potential difference due to the imbalance of charges on the two sides, but these charges will attempt to redistribute themselves across the plate. Thus, an equilibrium develops between the magnetic force and the the electric force acting on the particles, yielding Equation 3.5.

$$q_0 E_H + q_0 \vec{v} \times B = 0 \quad (3.4)$$

where, E_H is the Hall electric field across the transducer, and solving for this variable yields:

$$E_{Hall} = -\vec{v} \times B \quad (3.5)$$

thus, it may be concluded that the electric field is a function of the strength of the electric field and the velocity of the charged particles. Referring to Figure 3.2.5 of a Hall-effect transducer with a given width W_{Hall} between the sensing terminals, the electric field (E_H) may be integrated over the width (under the assumption that it is uniform), to yield the Hall voltage (V_{Hall}).

$$V_{Hall} = -W_{Hall} \vec{v} B \quad (3.6)$$

from this equation outlining the Hall voltage it can be concluded that it is a function of:

- The velocity of the charged particles
- The applied magnetic field (along the ‘sensitive’ axis)
- The width of the transducer

Utilising all of these concepts, and a transducer for each axis required of the sensor leads to the design of a magnetometer. Trigonometry may be used to calculate the heading of the body from the magnitude of the Hall voltage produced by the transducers. MEMS transducers can be built with components having dimensions in the order of micro-meters (μm) as shown in Figure 3.2.6 [138]. Which means that they are easily incorporated alongside a MEMS accelerometer and gyroscope in one module to create an inertial measurement unit (IMU).

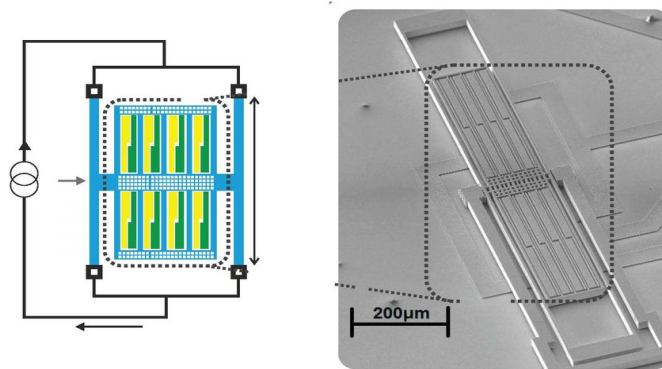


Figure 3.2.6: Image of a MEMS magnetometer [138].

3.3 Piezoelectric sensors and actuators

Smart materials can be described as materials which properties alter in accordance with external stimuli. Examples include shape memory alloys (SMAs) and magnetic shape memory alloys (MSMAs) which both alter their shape in accordance with applied forces, with SMAs reacting to temperature or stress changes and MSMAs to changes in a magnetic field. Exposure to light will cause photovoltaic materials and photomechanical materials to produce an electrical current and change their shape, respectively. Piezoelectric materials produce an electric current when stress is applied and can inversely alter their shape when an electric current is applied, bending, expanding and/or contracting. Such a material qualifies for use as both a sensor or and actuator and can be integrated with another material, being surface bonded or housed within.

Piezoelectric materials were first discovered in 1880 by Pierre and Jacque Curie, where piezoelectric properties were found to occur naturally in monocrystalline materials [139]. However such materials were found not to be as suitable for actuating purposes which led to the production of man-made polycrystalline ceramic materials. Lead zirconate titanate (PZT) elements, exhibit the significant electro-mechanical properties, and are relatively easy to produce. This material was developed by researchers at the Tokyo Institute of Technology in 1952 [140]. A piezoelectric ceramic (PZT element) is a collection of perovskite crystals, where each crystal is comprised of a small, tetravalent metal ion positioned within a lattice of larger divalent metal ions and oxygen. The following is the process used to create piezoelectric elements:

1. Fine powders of the component metal oxides are mixed in specific proportions.
2. A uniform powder is formed by heating the mixture.
3. An organic binder is mixed with the uniform powder and formed into the required shape.
4. The formed element(s) of the mixture are heated at a predetermined temperature for a specific amount of time. Forming a dense crystalline structure.
5. Once the element(s) are cooled electrodes are applied to the structure on the the appropriate surfaces.
6. A strong DC electric field is applied to the element, at a temperature just below the critical temperature to align the domains within the element. The domains most closely aligned with the electric field expand, forcing themselves into the space of those which are not.
7. The electric field is removed and the dipoles within the domains have been set into a configuration of close alignment.

At step five of the above process the dipoles in the PZT element are orientated randomly (denoted as arrows pointed in the direction of the positive charge), as shown in Figure 3.3.1 with the element labelled '5'. A dipole may be described as the separation of opposing charges, and the distance between these charges multiplied by the charge yields the dipole moment (μ). For the PZT element to function correctly these dipoles must be as in line as possible. The application of a strong DC electric aligns the dipoles which is step six of the process and is illustrated in Figure 3.3.1, element '6'. When this electric field is removed, the dipoles will not remain in perfect alignment, but their configuration will be close to this (Figure 3.3.1, element '7'). A material which is capable of altering its dipole alignment with the presence of a strong electric field is known as a ferroelectric material.

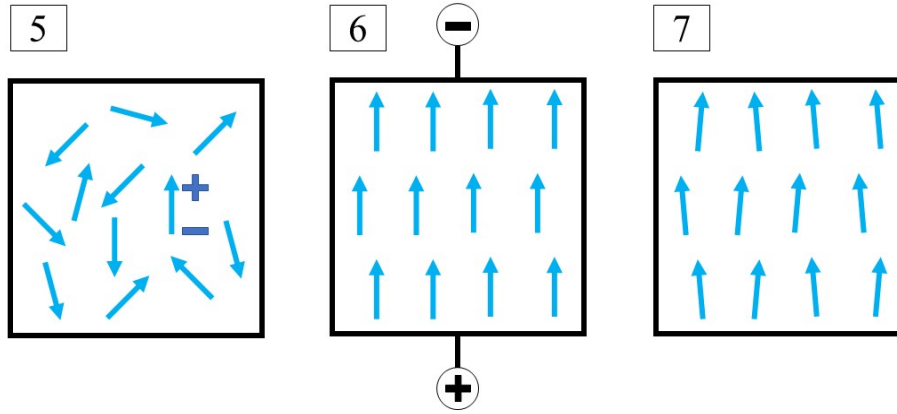


Figure 3.3.1: Illustration of dipoles in the PZT structure.

Compressing or applying tension to a PZT element causes a change to the dipole moment that is associated with the element, so that the element generates voltage. Up to a certain magnitude of stress this voltage is proportional to the compression/tension applied to the element, thus, the element may be used as a sensor. The polarity of the voltage is governed by the direction of the tension/compression with respect to the poling voltage of the element as outlined in Table 3.3.1.

Action	Direction	Polarity w.r.t. poling voltage
Compression	In line with polarization	Identical
Tension	Perpendicular to polarization	Identical
Compression	Perpendicular to polarization	Opposite
Tension	In line with polarization	Opposite

Table 3.3.1: Actions on the PZT element and the resultant polarity of the voltage output with respect to the poling voltage.

In this research two collocated PZT elements are surface mounted on the link near its clamped end for the second iteration of the designed control system (CSB). It is the bending of this structure that causes strain on the elements, effectively applying both tension and compression and generating voltage. The two sensors will be mounted so that their poling voltages are in opposing directions, thus for one direction of the transverse motion one sensor will produce a positive voltage, and the other a negative voltage. The reversal of the direction of the transverse motion will lead to a reversal of the polarity of the voltage output from each sensor. An example of this premise is

illustrated in Figure 3.3.2. Where the arrows denote the poling direction of the elements (from negative to positive).

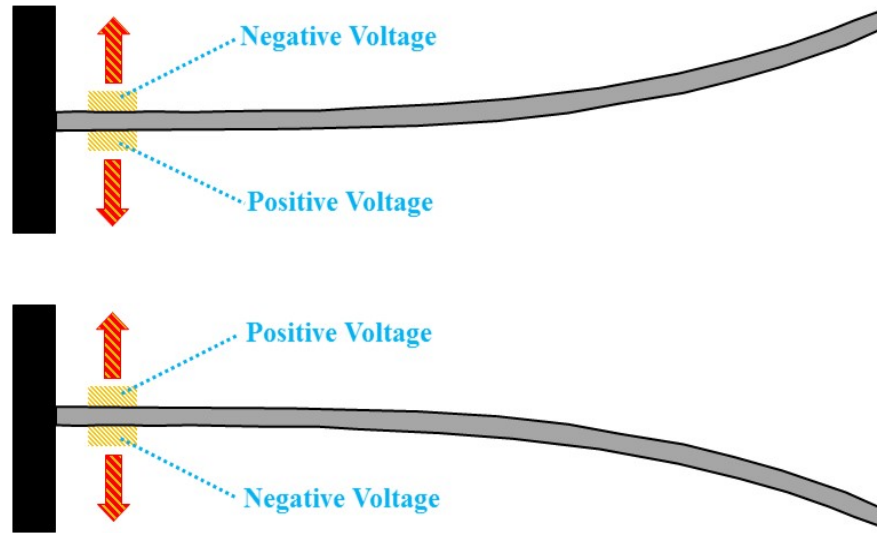


Figure 3.3.2: Illustration of the voltage output from the PZT sensors in relation to the direction of the transverse motion of the structure.

For use as an actuator, a voltage is to be applied across the element. If this voltage has an identical polarity to the poling voltage the element will expand in the direction of the dipoles and contract in the perpendicular direction. Reversing the polarity of the voltage applied will lead to the element contracting along the dipole direction and expanding along the perpendicular direction. This contraction/expansion due to the applied voltage will result in the element bending. Whilst mounted on the link structure a strain will be applied upon the link by the element, generating a bending moment on the structure. The amount of deformation the element experiences and hence the strain applied to the structure is proportional to the magnitude of voltage applied. A PZT element with a larger surface area is capable of producing higher magnitudes of strain than that with a smaller area.

This research utilises these concepts and uses two collocated PZT elements as surface mounted actuators. Noting that most PZT elements have maximum operational voltage that are be different for the polarities, for example those used in this research have an operating voltage range of -60 V to 360 V. Thus, in this instance the positive range of the operating voltages is applied as it allows for a greater level of strain to be achieved. Therefore only one of the two PZT actuators should be employed for a particular direction of the transverse motion of the link. Regardless of the sensors used, their readings should provide the control system with the direction of the link's motion so as to identify which to employ. This is illustrated in Figure 3.3.3 for the case where PZT elements are used as sensors. These sensors should also be able to identify through

some unit the magnitude of the motion leading to the calculation of the appropriate magnitude of the voltage. Too little voltage at a motion resulting in a large deformation of the beam would not produce enough force to effectively attenuate the vibration along the link. Too much voltage at smaller deformations would lead to the excitation of the link rather than reducing the deformations.

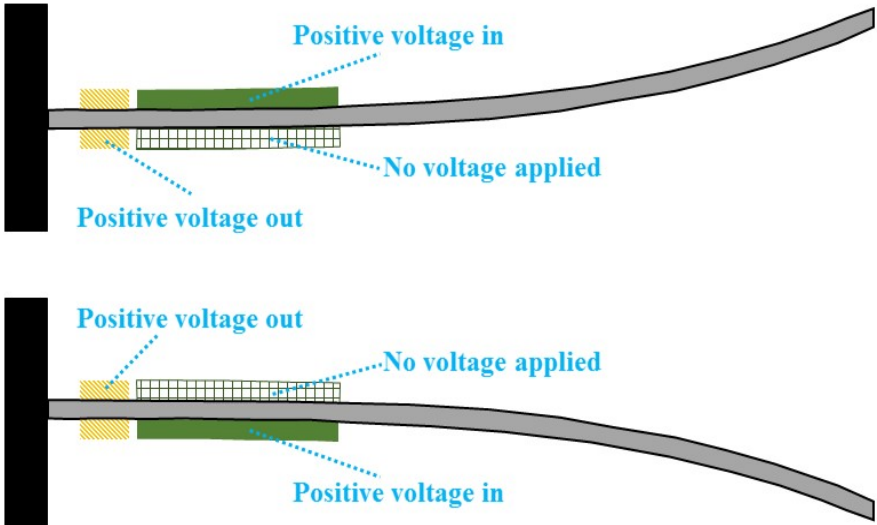


Figure 3.3.3: Illustration of the identification as to which PZT actuator should be employed for a particular direction of the transverse motion.

3.4 System A: Robot link, IMUs and piezoelectric actuators

This section presents the analytical model (open loop) developed to represent the link structure and components of CSA, followed by the presentation of a COMSOL model of the same structure. An experimental set-up is then introduced, which includes the clamp and associated structure designed to hold the link. This experimental set-up and the subsequent results are used to validate both the analytical and COMSOL models.

3.4.1 Analytical model

An analytical model of the link and surface bonded PZT patches was created based on Euler-Bernoulli Beam Theory (EBT), which describes the relationship between the load(s) applied to a beam and its deflection. From the review of existing research it was noted that Timoshenko beam theory (TBT) is often superior in the modelling of beam structures. However, this superiority is only valid prior to the convergence of the results of the two beam theories, and this convergence has been shown to occur when either the length/thickness or length/width ratio is greater than eighty. Additionally, a beam may be considered an Euler-Bernoulli beam (EBB) when one of these ratios is greater than ten as the shear deformation is likely to be very small and/or negligible. Acknowledging these points, the inclusion of shear deformation in the model (i.e. the employment of TBT) was deemed unnecessary providing that at least one of the aforementioned dimensional ratios of the links utilised in the experiments is greater than eighty. In this model of the link the boundary conditions were defined as clamped-free, where the clamped end of the link was envisioned as being attached to the end effector of the robot manipulator. Two collocated piezoelectric patches were included in the model on the upper and lower surfaces of the link, as well as the IMU used within the experimental validation (Figure 3.4.1). The axes shown in Figure 3.4.1 coincide with the world frame (global coordinate system) of the robot manipulator (frame zero in Figure 2.4.2a). y_1 and y_2 represent the start and end positions of the piezoelectric patches along the y axis of the link, respectively. y_{IMU} is the length along the y axis of the link at which the centre of the IMU is modelled. The relative transverse motion of the link is noted as $w(y, t)$, and the base excitation as $x(t)$, so that the absolute transverse motion of the link (w_{abs}) at some point y along its length may be obtained through Equation 3.7.

$$w_{abs}(y, t) = w(y, t) + x(t) \quad (3.7)$$

The following equations are used to create the analytical model of the link, the two piezoelectric patches and the IMU, it should be noted that the dimensions of the

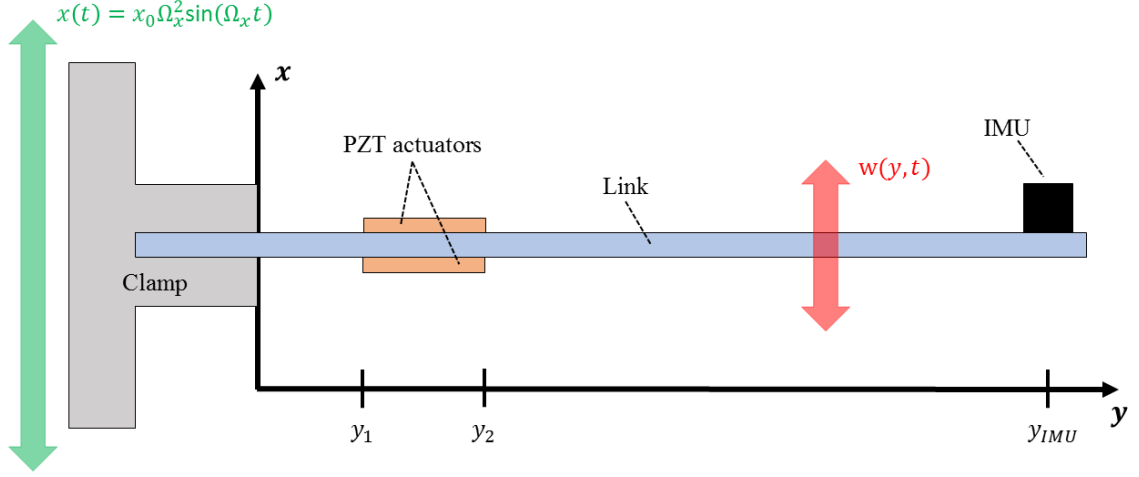


Figure 3.4.1: Visualisation of the analytical model for control system A.

piezoelectric patches will be set to zero when validating the link alone. Equation 3.8 describes the equation of motion of the structure. Where E represents the Young's Modulus of the structure, I the second moment of area, ρ the density, A the cross-sectional area, and M_{IMU} the mass of the IMU. The Dirac delta function is denoted as δ , the viscous damping coefficient as c_a , and the amplitude and frequency of the base excitation as x_0 and Ω_x , respectively. ϑ is the piezoelectric coupling term, $V_{in,pa}$ is the amplitude of the voltage applied to the PZT actuators, and Ω_V is the frequency at which it is applied. It should be noted that when control is applied, the frequency of the applied voltage will be equal to the frequency of the base excitation so that $\Omega_V = \Omega_x$. However, they have been denoted separately to differentiate the two frequencies.

$$\begin{aligned} & \frac{\partial^2}{\partial y^2} \left(EI(y) \frac{\partial^2 w(y, t)}{\partial y^2} \right) + \rho A(y) \frac{\partial^2 w(y, t)}{\partial t^2} + M_{IMU} \delta(y - y_a) \frac{d^2(y)}{dt^2} \\ & + c_a \frac{\partial w(y, t)}{\partial t} + \rho A(y) x_0 \Omega_x^2 \sin(\Omega_x t) = \vartheta V_{in,pa} \sin(\Omega_V t) \left(\frac{d\delta(y - y_1)}{dy} - \frac{d\delta(y - y_2)}{dy} \right) \end{aligned} \quad (3.8)$$

To incorporate the piezoelectric patches within the model, the stiffness and mass terms of the equation of motion utilise the Heaviside function (H) which accounts for the stiffness and damping changes along the length of the link where the PZT elements are mounted (as shown in Equations 3.9 and 3.10). The subscripts lk and pa in Equations 3.9 and 3.10 denote the parameters relating to the link and PZT actuators, respectively.

$$\rho A(y) = \rho_{lk} A_{lk} + \rho_{pa} A_{pa} [H(y - y_1) - H(y - y_2)] \quad (3.9)$$

$$EI(y) = E_{lk} I_{lk} + E_{pa} I_{pa} [H(y - y_1) - H(y - y_2)] \quad (3.10)$$

The relation between the Heaviside function and the Dirac delta function may be employed within this analytical model. To provide an insight into their relation, the definitions of the Heaviside function and the integral of the Dirac delta function are presented as Equations 3.11 and 3.12, respectively. In these definitions y_a is some arbitrary value (which may be thought of as some point along the length of the link). Both the Heaviside function and the integral of the Dirac delta function yield the same outcome, hence they may be equated as in Equation 3.13. On an additional note, regarding the Dirac delta function, the relation shown in Equation 3.14, may also be utilised in this analytical model. Where ‘*func*’ is some arbitrary function of y , and it should be noted that the upper and lower limits of the integral are selected to relate to the analytical model.

$$H(y - y_a) = \begin{cases} 0, & \text{if } y < y_a \\ 1, & \text{if } y > y_a \end{cases} \quad (3.11)$$

$$\int_{-\infty}^y \delta(y - y_a) dx = \begin{cases} 0, & \text{if } y < y_a \\ 1, & \text{if } y > y_a \end{cases} \quad (3.12)$$

hence,

$$H(y - y_a) = \int_{-\infty}^y \delta(y - y_a) dx \quad (3.13)$$

$$\int_0^{L_{lk}} func(y) \delta(y - y_a) dx = \begin{cases} func(y_a), & \text{if } 0 < y_a < L_{lk} \\ 0, & \text{otherwise} \end{cases} \quad (3.14)$$

Using Galerkin decomposition which multiplies the equation of motion by the mode shape (ϕ_n), and then integrates along the length of the link, a solution for the temporal equation can be yielded. Then assuming the separation of variables solution has the form:

$$w(y, t) = \sum_{n=1}^N P_n(t) \phi_n(y) \quad (3.15)$$

where, $P_n(t)$ is the n^{th} generalized coordinate, and $\phi_n(x)$ is the n^{th} mode shape of the link, the transverse motion of the link can be analysed. The mode shape for the clamped-free link may be defined as shown in Equation 3.16. It should be noted that the mode shapes of the beam are assumed to remain decoupled after the PZT elements are included. It is assumed that the resultant effects are minor.

$$\phi_n(y) = \gamma_n [\cosh(\beta_n y) - \cos(\beta_n y) - \sigma_n (\sinh(\beta_n y) - \sin(\beta_n y))] \quad (3.16)$$

where, γ_n is the arbitrary magnitude of the eigenfunction, β_n is the spatial frequency, and the dimensionless ratio (σ_n) may be written as:

$$\sigma_n = \frac{\sinh(\beta_n L_{lk}) - \sin(\beta_n L_{lk})}{\cosh(\beta_n L_{lk}) + \cos(\beta_n L_{lk})} \quad (3.17)$$

where the non-trivial solutions to

$$(\beta_n L_{lk}) \cosh(\beta_n L_{lk}) \cos(\beta_n L_{lk}) + 1 = 0 \quad (3.18)$$

yield the values of $\beta_n L_{lk}$. The division of said values by the length of the link (L_{lk}) yields the values for the spatial frequencies independent of length (β_n) for use in Equation 3.16. Applying the product rule (Equation 3.19) to the first term of Equation 3.8, yields the expanded version of this term as shown in Equation 3.20.

$$\frac{\partial^2}{\partial x^2} [f(x)g(x)] = f''(x)g(x) + 2f'(x)g'(x) + f(x)g''(x) \quad (3.19)$$

$$\frac{\partial^2}{\partial y^2} \left(EI(y) \frac{\partial^2 w(y, t)}{\partial y^2} \right) = \frac{\partial^2 EI(y)}{\partial y^2} \frac{\partial^2 w(y, t)}{\partial y^2} + 2 \frac{\partial EI(y)}{\partial y} \frac{\partial^3 w(y, t)}{\partial y^3} + EI(y) \frac{\partial^4 w(y, t)}{\partial y^4} \quad (3.20)$$

Due to the complexity of the stiffness term (see Equation 3.20), it was split into three separate terms before summing the said terms. The term on the left hand side of the expression (Equation 3.20) has been denoted as K_n , and the terms on the right hand side have been denoted as $K_{1,n}$, $K_{2,n}$ and $K_{3,n}$, respectively, to form Equation 3.21.

$$K_n = K_{1,n} + K_{2,n} + K_{3,n} \quad (3.21)$$

where, after employing the relationship shown in Equation 3.15, the terms of Equation 3.21 may be written as:

$$K_{1,n} = E_{pa} I_{pa} \int_0^{L_{lk}} [H(y - y_1) - H(y - y_2)] (\phi_n''(y))^2 + 2\phi_n'(y) \phi_n'''(y) + \phi_n(y) \phi_n^{iv}(y) dy \quad (3.22)$$

$$K_{2,n} = -2E_{pa} I_{pa} \int_0^{L_{lk}} [H(y - y_1) - H(y - y_2)] \phi_n'''(y) \phi_n(y) dy \quad (3.23)$$

$$K_{3,n} = \int_0^{L_{lk}} E_{lk} I_{lk} + E_{pa} I_{pa} [H(y - y_1) - H(y - y_2)] \phi_n^{iv}(y) \phi_n(y) dy \quad (3.24)$$

Recalling Equation 3.8, utilising the expressions from Equations 3.21 through 3.24 and employing Galerkin decomposition yields:

$$M_n \ddot{P}_n(t) + C_n \dot{P}_n(t) + K_n P_n(t) = \theta_{p,n} V_{in,pa} \sin(\Omega_V t) - x_b \sin(\Omega_x t) \quad (3.25)$$

where,

$$M_n = \int_0^{L_{lk}} \rho A(y) \phi_n^2(y) dy \quad (3.26)$$

$$C_n = c_a \int_0^{L_{lk}} \phi_n^2(y) dy \quad (3.27)$$

$$K_n = \int_0^{L_{lk}} \left[\frac{\partial^2 EI(y)}{\partial y^2} \phi_n''(y) + 2 \frac{\partial EI(y)}{\partial y} \phi_n'''(y) + EI(y) \phi_n^{iv}(y) \right] \phi_n(y) dy \quad (3.28)$$

$$\theta_{p,n} = \vartheta [\phi_n'(y_2) - \phi_n'(y_1)] \quad (3.29)$$

$$\vartheta = \frac{\bar{e}_{31} W_{pa}^\Psi}{2h_p} \left[\left(h_p + \frac{h}{2} \right)^2 - \frac{h^2}{4} \right] \quad (3.30)$$

$$x_{b,n} = x_0 \Omega_V^2 \int_0^{L_{lk}} \rho A(y) \phi_n(y) dy \quad (3.31)$$

Dividing Equation 3.25 by the mass (M_n) yields the temporal solution as a third order differential equation.

$$\ddot{P}_n(t) + 2\zeta \omega_n \dot{P}_n(t) + \omega_n^2 P_n(t) = \chi V_{in,pa} \sin(\Omega_V t) - X \sin(\Omega_x t) \quad (3.32)$$

where,

$$\zeta = \frac{C_n}{2M_n \omega_n}, \omega_n = \sqrt{\frac{K_n}{M_n}}, \chi_n = \frac{\theta_p}{M_n}, X_n = \frac{x_{b,n}}{M_n}. \quad (3.33)$$

Utilising Equation 3.15, multiplying the generalised coordinate by the mode shape yields the transverse motion of the link.

3.4.2 COMSOL model

COMSOL Multiphysics is a powerful simulation software and can be used to model a multitude of designs, processes and devices [141]. The core package can be used as a standalone simulation software, or add-on modules can be utilised in combination for different, more specialised areas of research/engineering. It is this ability which makes the software especially desirable, especially in the instance of this research where the structural mechanics of a long slender beam needs to be coupled with the electro-mechanical properties of piezoelectric elements. The structural mechanics module and the microelectromechanical systems module from COMSOL Multiphysics were simultaneously utilised to produce a three-dimensional finite element model of the link/PZT patch for the purpose of validation of the analytical model. Figure 3.4.2 shows the finite element model including the free tetrahedral mesh chosen for use due to its versatility to be applied to both larger and smaller surfaces and vertices of the structure.

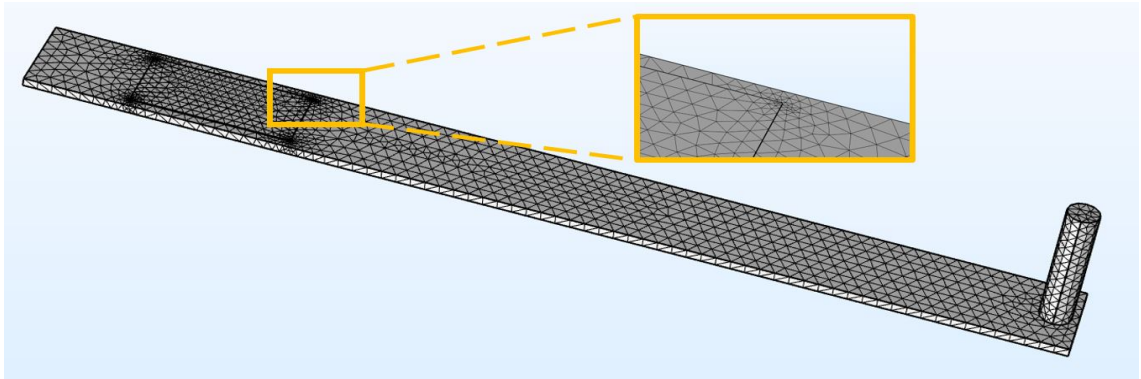


Figure 3.4.2: Image of the three dimensional finite element model including the mesh used.

It is immediately noticeable that the IMU in the model has a larger length to circumference ratio than the majority of standard IMUs. This elongation is to accommodate the addition of wires and petro wax to the overall mass of the IMU, without altering the stiffness of the structure as a whole. It should be noted that an alternative solution was tested, (adjusting the density of the IMU within the model) but this was found to provide a less accurate representation of the structure. It can also be seen that the free tetrahedral mesh alters the area of the elements based upon its proximity the edges and vertices of the structure. The predefined mesh size ‘finer’ was selected for use on the basis of the results from a mesh convergence study, with this option having a minimum element size of 0.00185 m. The results of said mesh convergence study are shown in Figure 3.4.3.

From this study it is clear to see that the chosen element size is acceptable; producing accurate results whilst limiting the necessary computation time. As with the analytical

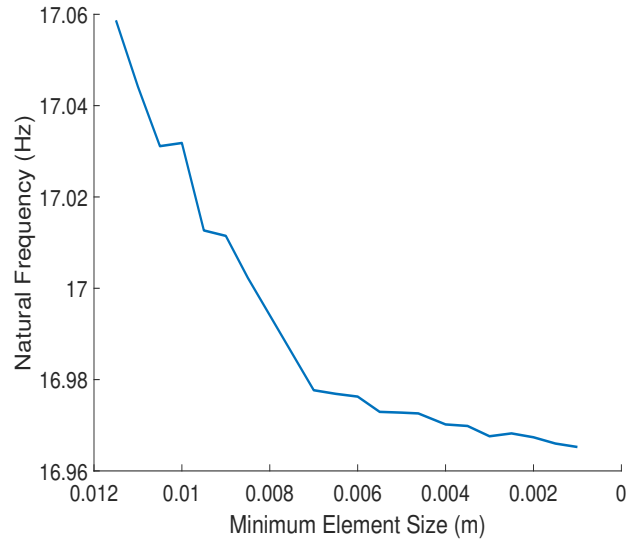


Figure 3.4.3: Mesh convergence study.

model the structure is effectively clamped on one end along two axes, with the third axis subject to a sinusoidal base excitation (see Figure 3.4.1), and the opposing end of the link is free. The electronic boundary conditions of the piezoelectric patches were defined on the upper and lower surfaces as ground and voltage out, respectively. To obtain the voltage generated through the motion of the link and subsequent bending of the PZT patches the potential differences between these two boundaries was obtained.

3.4.3 Experimental validation

Experimental results were obtained and compared with both the COMSOL Multiphysics and the analytical model for further validation of the latter. Figure 3.4.4 is a plan view illustrating the experimental set-up used to validate the analytical model.

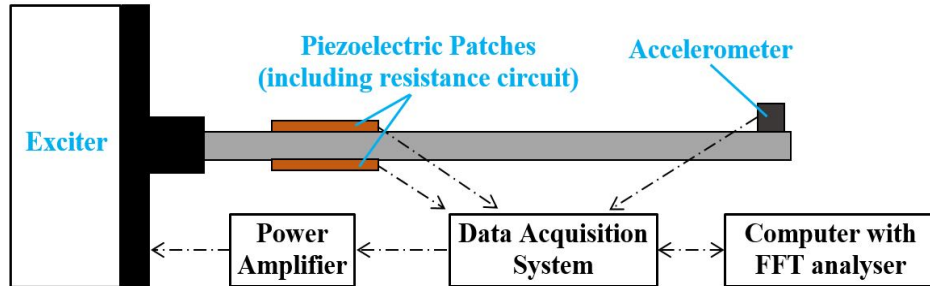


Figure 3.4.4: Illustration of the experimental set-up for the validation of the analytical model.

The exciter used was the APS 113 ELECTRO-SEIS R Long Stroke Shaker, which was powered by the APS 125 Power Amplifier. The control of the amplifier and the reading of data was performed by the data acquisition system (DAQ) (SignalCalc Abacus), which received and interpreted signals from two accelerometers (PCB Piezotronics 352C03), one placed at the base of the link and the other at the tip. It should be noted that for this open loop system validation the IMUs of the control system were not utilised, as it was deemed important to verify the analytical model independent of potential unknowns that would arise from the control system. Instead the aforementioned accelerometers were utilised as they are compatible with the DAQ, and the analytical and COMSOL models reflected this. It was necessary to produce a unique clamp and bracket system based upon the two excitation sources the beam is to be attached to; the exciter within this experiment and the KUKA iiwa 7 in future experiments. The clamp requirement was that it should be mountable on the flange of the robot manipulator which is shown in Figure 3.4.5 [142]. This meant that it was to be a unique shape, hence an equally unique bracket was required for use with the shaker.

From these dimensions a clamp was designed and created to fit upon the flange and utilise the threaded holes to attach the two parts together. Figure 3.4.6 contains an exploded view of the clamp design illustrating the nuts and bolts used to hold the beam in place. Figures 3.4.7 and 3.4.8 contain the dimensions of the two main parts of said assembly; A and B, respectively. Figure 3.4.9 illustrates the bracket design including its dimensions, where the nine square holes visible from the plan view are in line with those of the shaker table (APS 0078).

Dimensions: mm

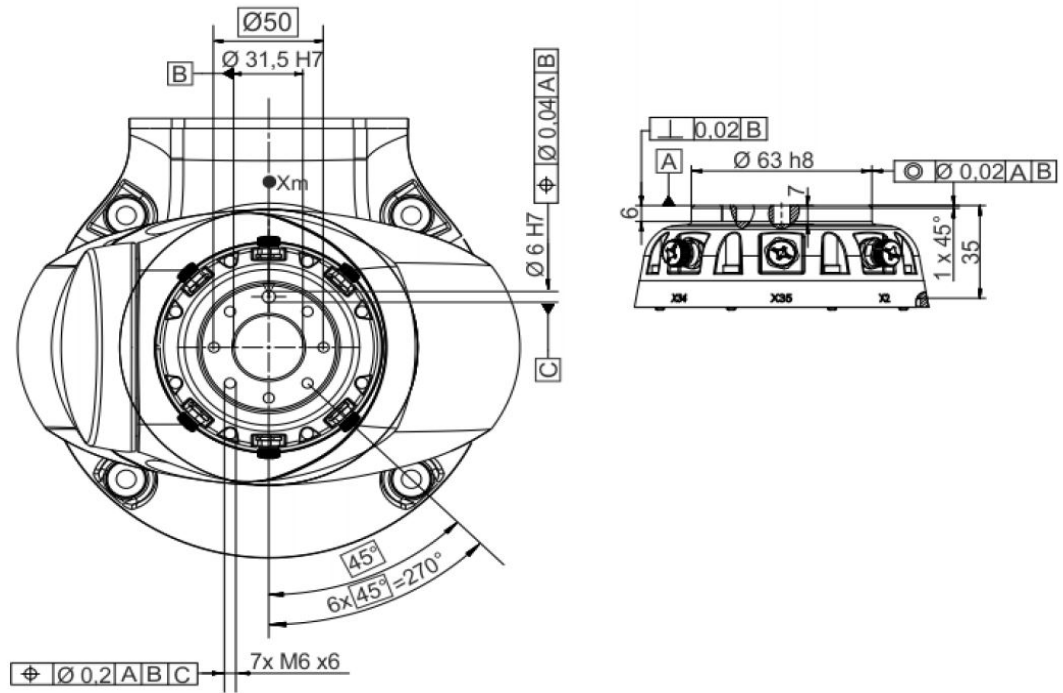


Figure 3.4.5: Dimensions of the KUKA manipulator's media flange [142].

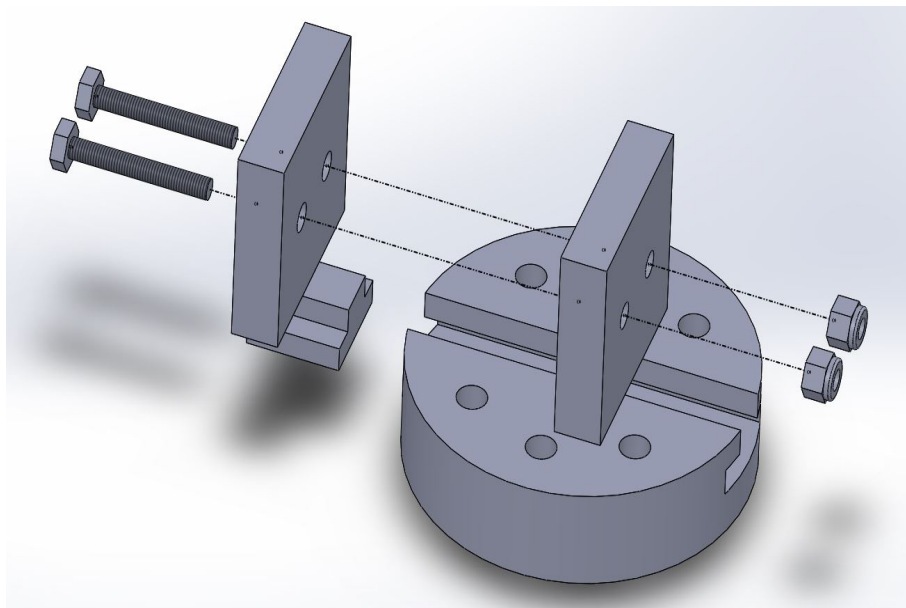


Figure 3.4.6: Exploded view of the clamp assembly design.

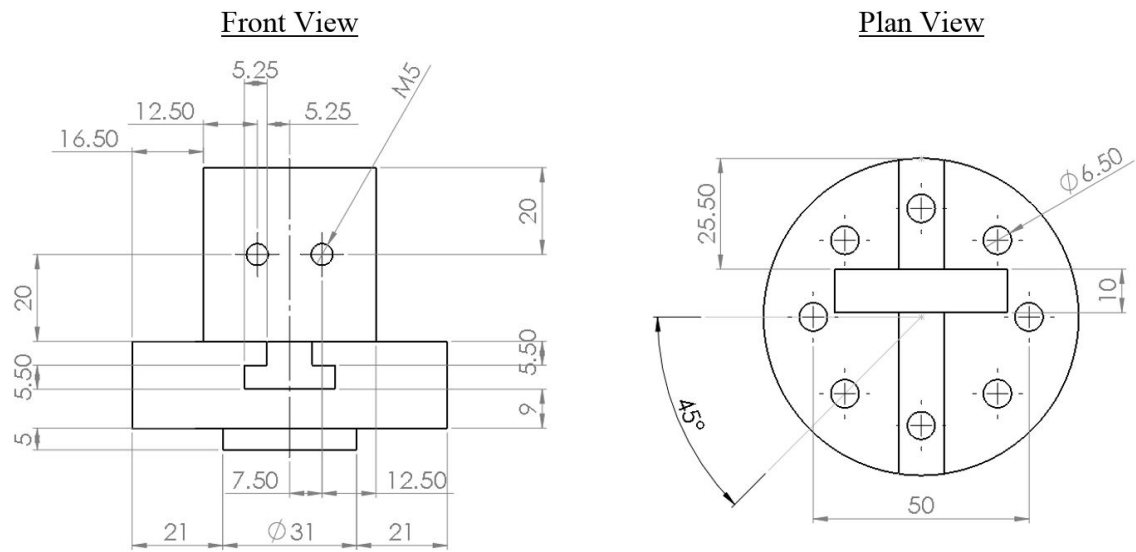


Figure 3.4.7: Dimensions of part A of the clamp assembly, from the front view and plan view.

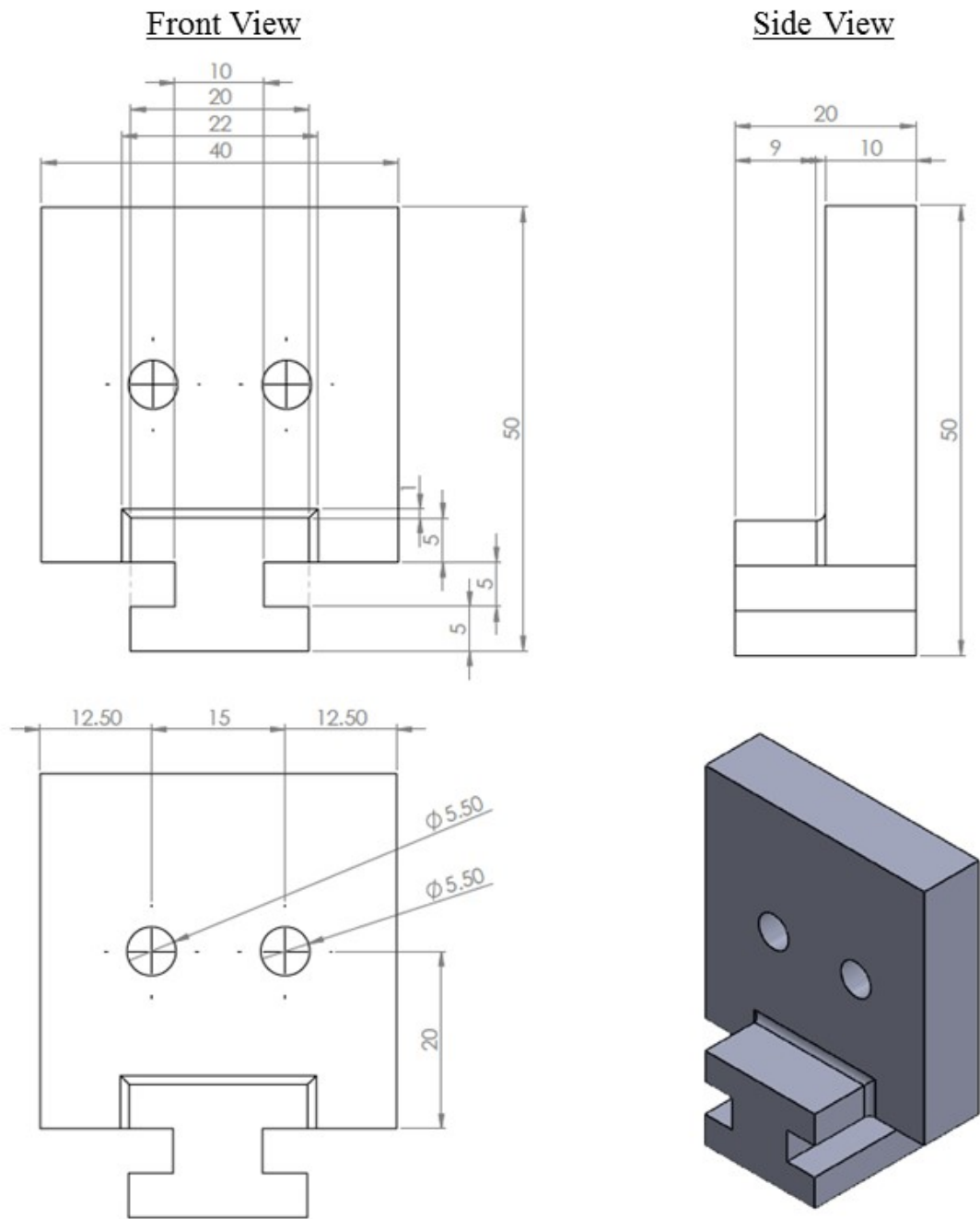


Figure 3.4.8: Dimensions of part B of the clamp assembly, from the front view and side view.

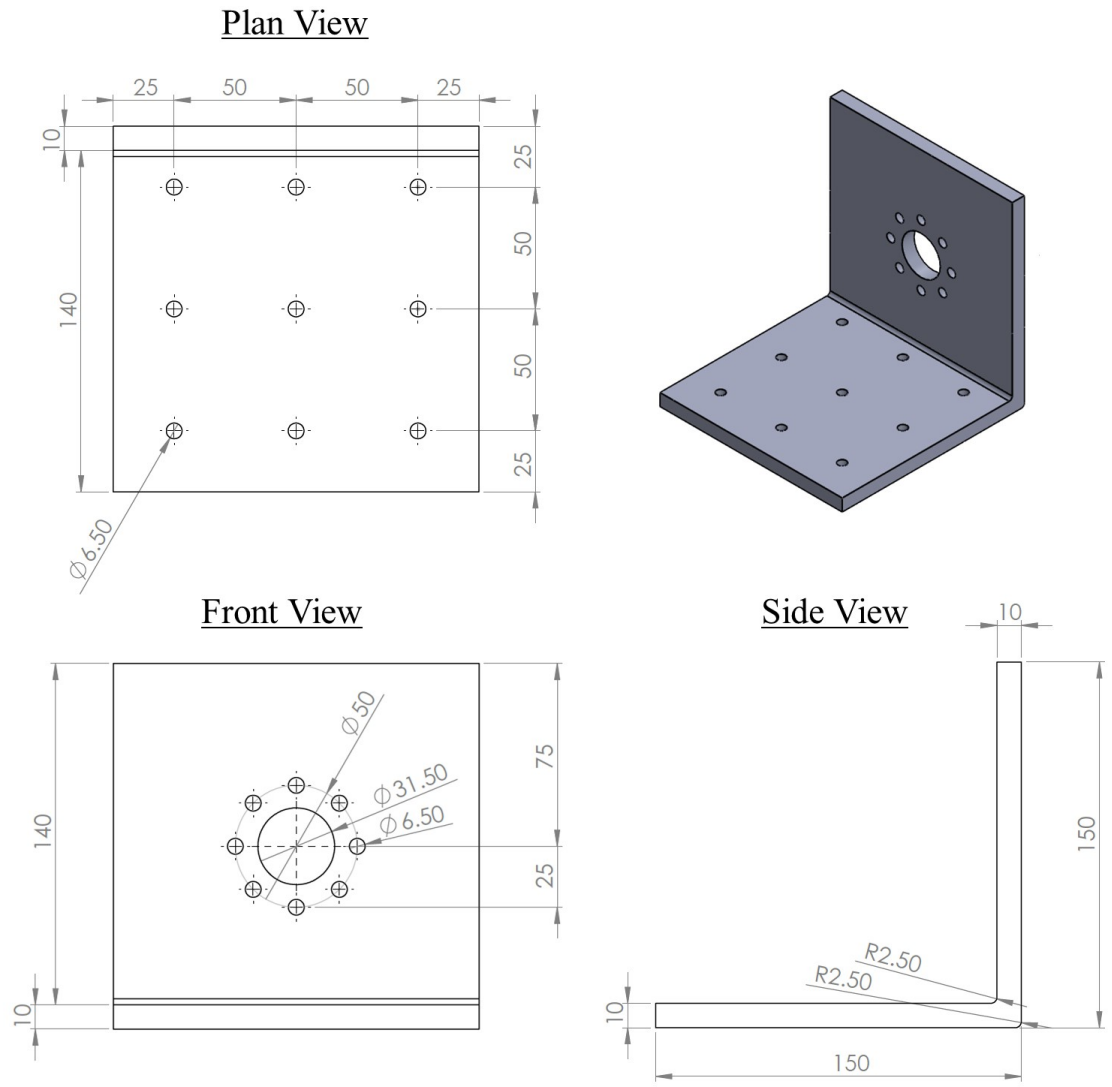


Figure 3.4.9: Dimensions of the bracket, from the front, side and plan view.

Parameters	Link (Aluminium)	Piezoelectric Patch (PZT-5A)
Length (m)	0.36	0.056
Width (m)	0.035	0.028
Thickness (m)	0.003	0.0003
Density (kg/m^3)	2700	5440
Young's Modulus (GPa)	70	30.336
Piezoelectric coefficient, \bar{e}_{31}	N/A	-11.6

Table 3.4.1: Geometric, mechanical and electric properties of link A and piezoelectric patches.

The geometric, mechanical and electrical properties of the link and PZT patches (actuators) are outlined in Table 3.4.1. From these dimensions the length to thickness ratio can be seen to be greater than eighty ($L/h = 120$), hence Euler-Bernoulli beam theory (EBT) may be employed to model the link structure. The PZT actuators were positioned at 0.036 m from the clamped end, the location was based on similar research [36] and corroborated through an observation of the predicted performance of the control system with varying PZT start positions. Previous research highlights that the largest strain is found nearer to the clamped end of a clamped-free beam. Thus, the PZT actuators should be positioned in this region, and an analytical study of varying start positions was conducted to provide further insight, and provide a narrower region for this particular structure.

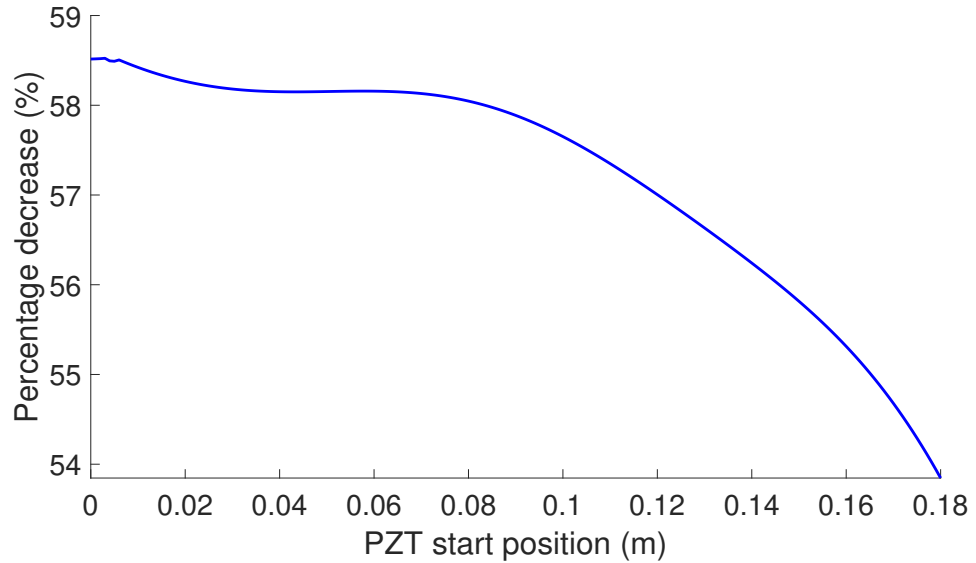


Figure 3.4.10: Trend of the percentage decrease of the amplitude of the link's response achieved by the actuator against the start position of the actuator along the length of the beam.

Figure 3.4.10 illustrates the trend of the performance of the control system against different start positions of the PZT actuators. The model of the link includes the accelerometer with its position kept constant, and the control system uses the product of a proportional gain with the magnitude of the tip displacement to obtain the magnitude of the voltage to be applied to the actuators. The proportional gain is kept constant at a value of one hundred, and the percentage decrease is calculated using the open loop response as a reference value. It can be seen from Figure 3.4.10 that the potential start positions nearer to the base of the link leads to a higher performance of the control system as opposed to those positions nearing the centre of the beam. The performance of the control system can be seen to remain fairly consistent for start positions less than 0.8 m. After this position the performance declines, thus narrowing the potential start position of the PZT patches from 0 m to 0.8 m, with a position closer to the clamped end being preferable. However, placing the PZT actuators immediately after the clamp would not allow for sufficient clearance between the clamp and the wires to be connected to the actuators. This clearance is important to prevent friction between the wires and the clamp assembly, and to avoid the wires being bent into acute angles making them more susceptible to degradation. Thus a start position of 0.036 m was selected.

The position of the accelerometer along the link's length was influenced by the design of the original control system (CSA). This system applied the control gain to the error between the base and tip velocities. The verification of the analytical model at this point does not include the control system but still requires a method of monitoring the response of the beam to a base displacement (as previously mentioned). The sensors used in the control system are not readily compatible with the data acquisition system (DAQs) chosen, as the verification is best performed with a system independent of the control system design, it follows that the sensor of the control system should be replaced with a sensor of similar mass that is compatible with the DAQs. Naturally, this sensor should be positioned where the control system sensor would for continuity.

The experimental set-up used to validate the open loop analytical model is shown in Figure 3.4.11. This figure has been edited for the purpose of simplification. The finite element analytical model was validated in stages; without and with the two PZT elements. The latter requires an external circuit due to the internal resistance of the DAQ which effects the readings from the PZT elements. The inclusion of a resistance of $300\text{ K}\Omega$ in parallel with the PZT elements produces accurate readings of the voltage produced. This is compared with the analytical model to validate its electromechanical aspect.

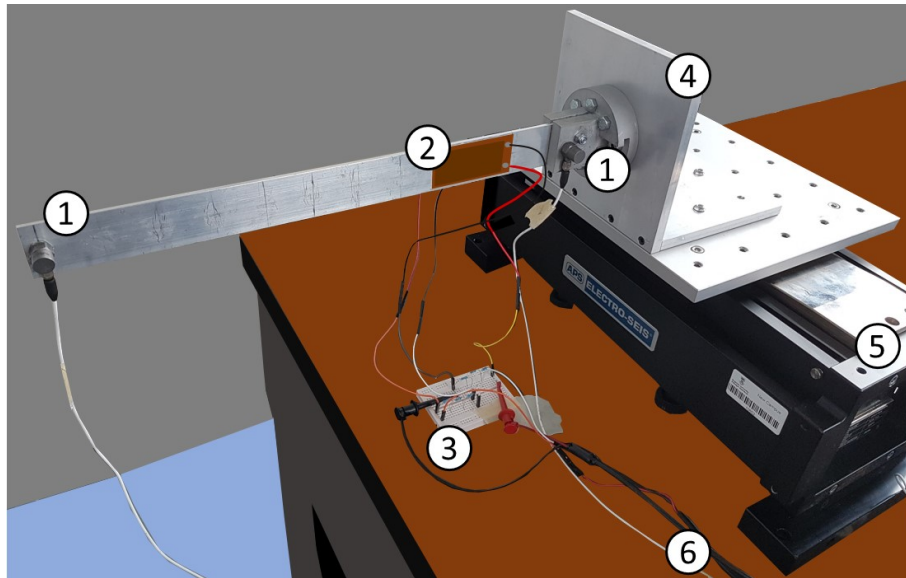


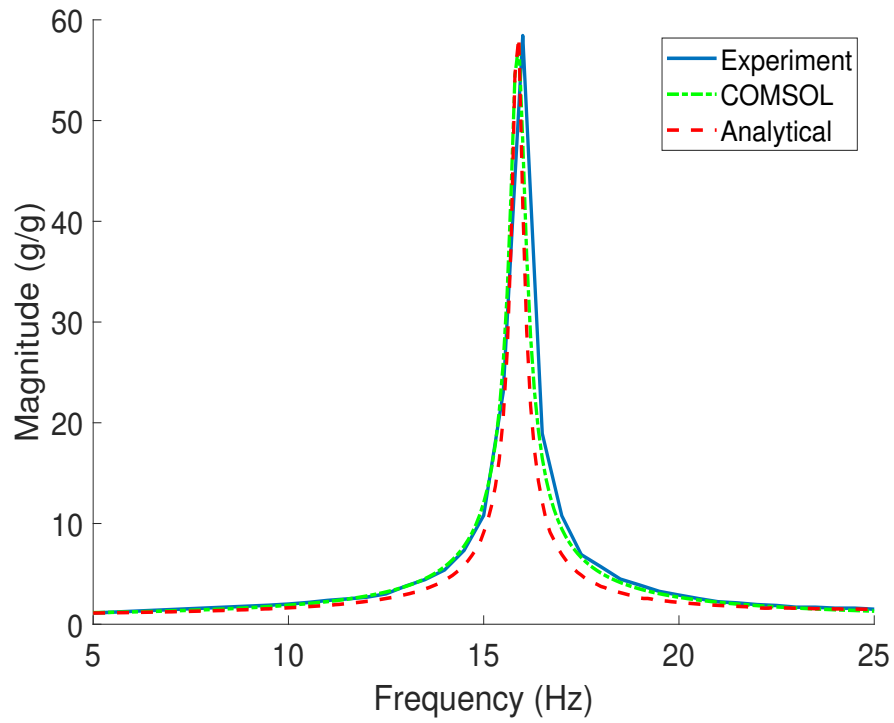
Figure 3.4.11: Experimental set-up for open loop validation.

The components in Figure 3.4.11 are numbered as follows:

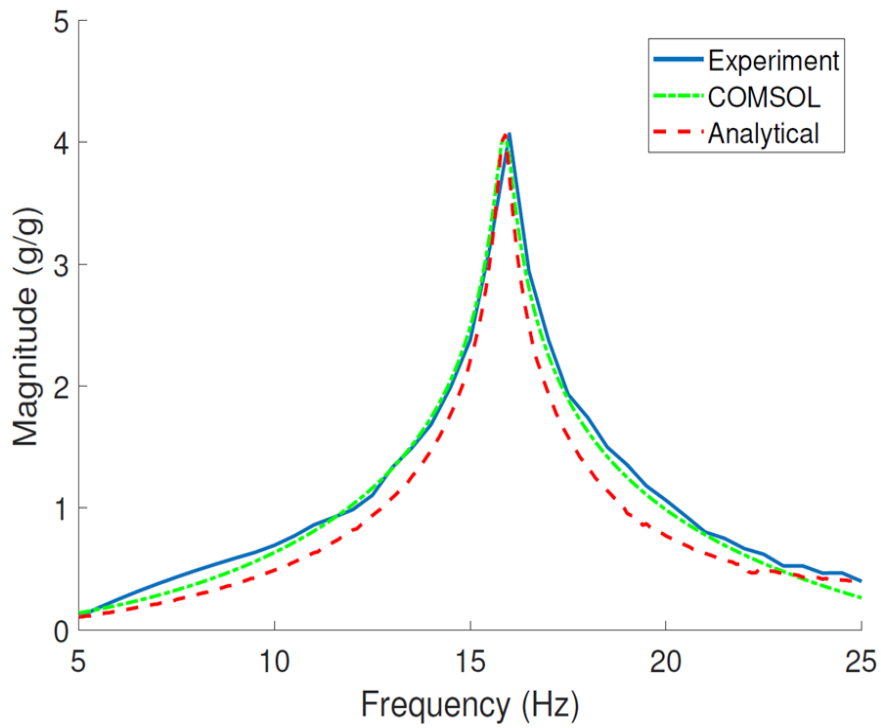
1. Accelerometer.
2. PZT element.
3. Resistor circuit.
4. Clamp assembly
5. Shaker.
6. Wires leading to the DAQ.

Figure 3.4.12 contains the FRF produced from the experimental, COMSOL and analytical results for the case in which no PZT elements are present on the beam. The magnitude of the response in Figure 3.4.12a is the tip acceleration of the link divided by the base acceleration, and the magnitude of the response in Figure 3.4.12b is the same magnitude in the logarithmic scale. Due to the additional mass of the petro wax used to mount the accelerometer to the tip of the beam at $y = 0.352$ m, and the mass of the wired connection, the mass of the accelerometer is increased from that stated on the data sheet. Hence, it should be noted that the mass of the accelerometer was increased to 0.012 kg from 0.0058 kg [143], in the COMSOL and analytical models. It can be seen from these figures that the COMSOL result is an accurate prediction of the link's response, and whilst there are some discrepancies to be observed from the analytical result, this too can be considered a good prediction of the experimental response.

Figures 3.4.13 and 3.4.14 contain the results from the experimental, COMSOL and analytical cases with the inclusion of the PZT elements. The magnitude of the response in Figures 3.4.13a and 3.4.13b are the result of the tip acceleration divided by the base acceleration, and the logarithmic scale of this response, respectively. For Figures 3.4.14a and 3.4.14b the magnitude of the response represents the voltage output from the PZT elements divided by the base acceleration, and the logarithmic scale of this magnitude, respectively. As with the case omitting the PZT elements the COMSOL response proves to be an accurate representation of the acceleration response (Figure 3.4.13), in this case the analytical model was also proven to be accurate. The same can be said for the voltage response (Figure 3.4.14), where the voltage response of PZT elements for the analytical model was obtained from the prediction of transverse displacement. This is possible as the transverse displacement of the link is proportional to the strain on the link, and this strain is also induced in the PZT elements. As previously mentioned the voltage output from a PZT element is proportional to the strain it experiences. Thus, it may be concluded that the transverse motion of the link is proportional to the voltage output from the PZT sensors. Therefore, multiplying the transverse motion by the mass normalised piezoelectric coupling coefficient (χ_n), as presented in Equation 3.33, yields the voltage from the PZT elements. The results prove that both the COMSOL and analytical models allow for a highly accurate prognosis of the experimental results and validate the electromechanical coupling aspect of the models. With the analytical model proving to be an accurate prediction with only slight discrepancies for all of the experimental results obtained, its use is favourable over the COMSOL model as it is less computationally expensive.

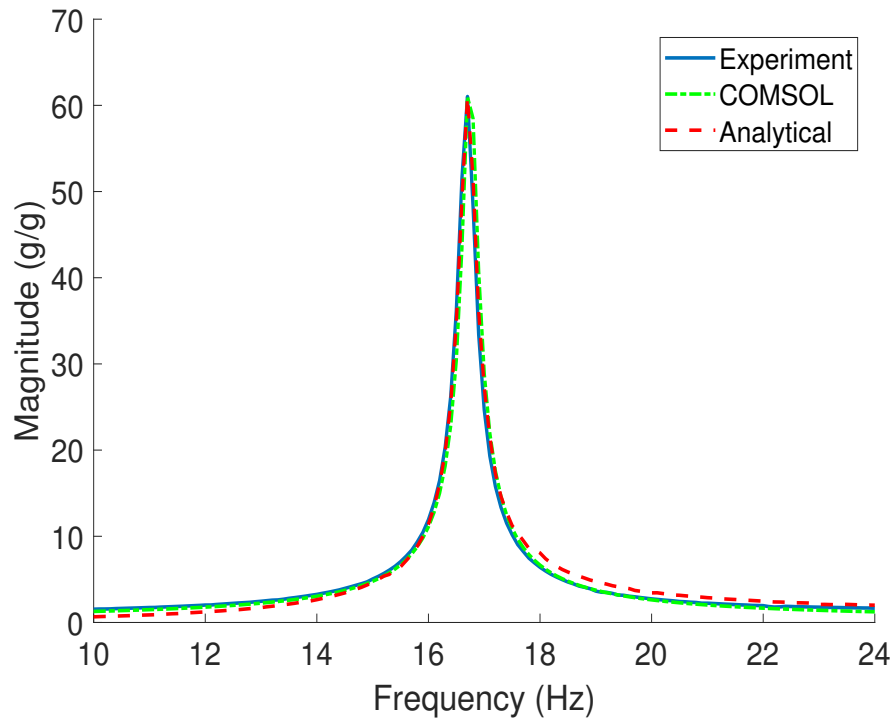


(a) Magnitude scale.

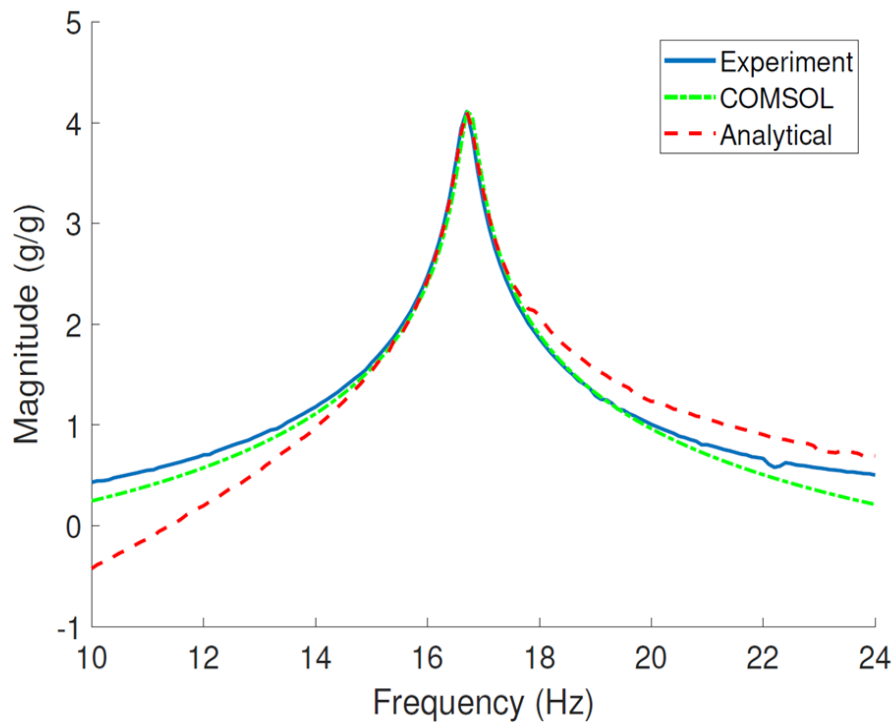


(b) Logarithmic scale.

Figure 3.4.12: FRF base excitation input, tip acceleration output, no piezoelectric patches.

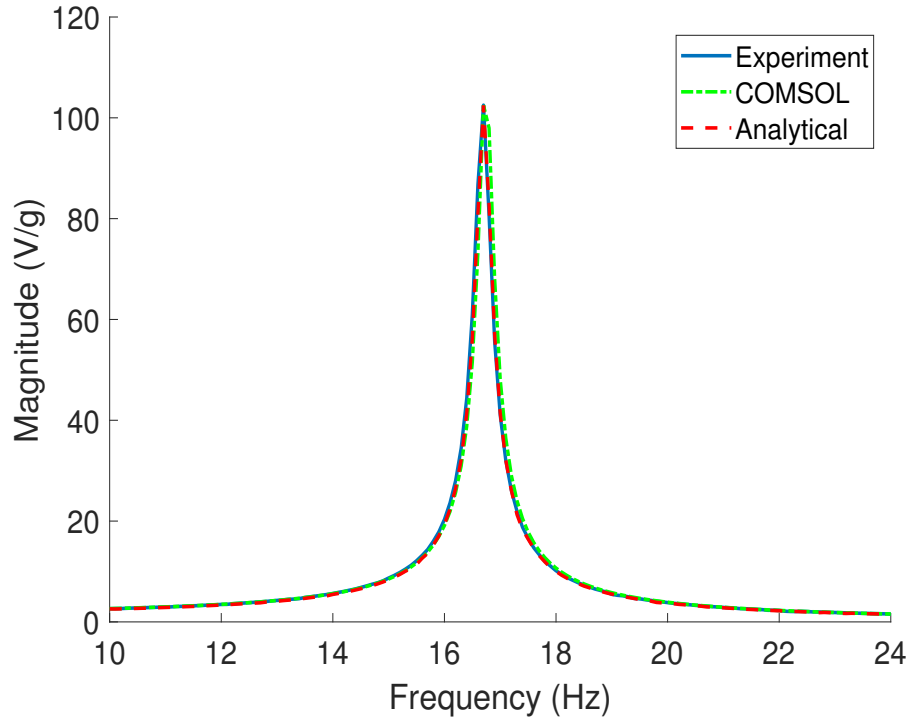


(a) Magnitude scale.

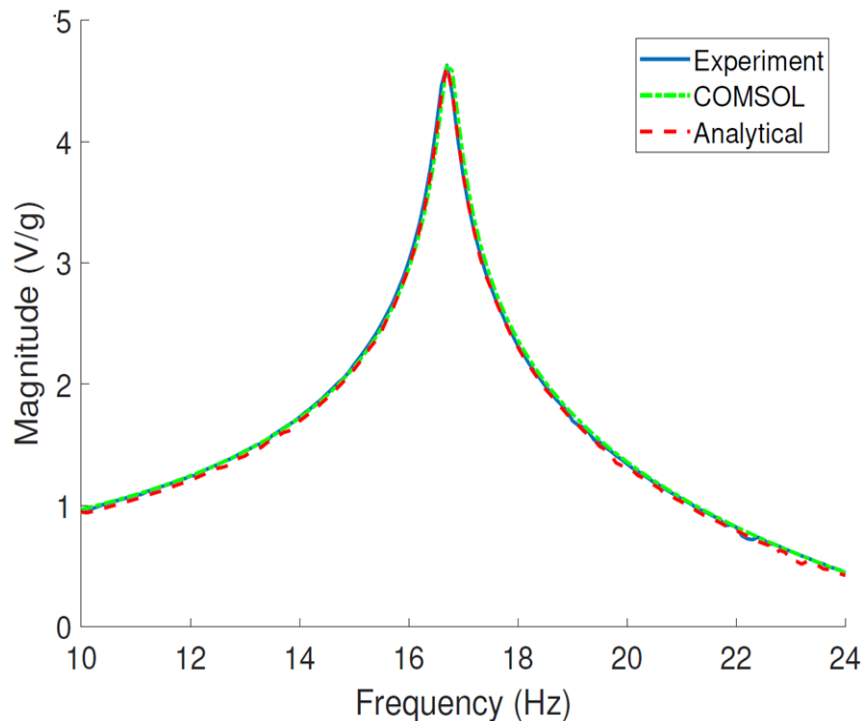


(b) Logarithmic scale.

Figure 3.4.13: FRF base excitation input, tip acceleration output, two piezoelectric patches.



(a) Magnitude scale.



(b) Logarithmic scale.

Figure 3.4.14: FRF base excitation input, voltage output, two piezoelectric patches.

3.5 System B: Robot link, piezoelectric sensors and piezoelectric actuators

The first topic of this section involves the motivation behind the exchange of the IMUs previously used to PZT elements that are utilised as sensors. Due to this exchange the analytical model presented in Section 3.4.1, is modified to incorporate the PZT sensors, this modified version is presented in this section. Some of the equations have been repeated for convenience and/or to highlight the differences when including additional PZT elements onto the structure. A similar experimental set-up to that of Section 3.4.3 is introduced, highlighting the importance of the exchange of the data acquisition system. The experimental results obtained are then presented and utilised in the validation of the analytical model.

3.5.1 Motivation behind altering the sensors

The initial beam dimensions (Beam A) were chosen with the only constraint that the beam would allow for PZT actuators of sufficient size to be mounted upon it (see Table 3.4.1). The modal parameters of the beam were not constrained, as the exciter was capable of high frequencies. However, when considering the KUKA iiwa 7 R800 as the excitation source these parameters needed to adhere to the manipulator's limitations. Namely, the natural frequency of the link should lie within the frequency range of which the manipulator was capable of providing. This allows for the control system to be observed in terms of its effects on both damping and natural frequency. Whilst the maximum velocity of each joint is known, and the software allows for this to be reached, it was found that, when using spline motion, the joint velocities would vary. This meant that the end effector velocity was consistent, but hard to predict using the kinematic model due to the changing joint velocities. Thus prompting the requirement of a study of the potential excitation frequencies, in lieu of utilising the robot model to obtain the required sinusoidal amplitudes for the frequency range. Figure 3.5.1 shows the results of the potential manipulator excitation frequency study. The previous experiments utilised a sinusoidal motion in a direction traverse to the length of the link. This was attempted using the manipulator at maximum velocity for varying amplitudes of displacement. The KUKA Sunrise Cabinet (control box) recorded the end effector position of this motion over time at each amplitude, and the frequency was obtained from this data (shown as the red dashed line in Figure 3.5.1). The amplitude of this sinusoidal motion is illustrated in Figure 3.5.2.

Figure 3.5.3 shows the end effector displacement against time for an amplitude of 0.1 m. It was found that this motion produced an ill form of a sinusoidal wave, with

a delay at the extremes of the displacement which can be attributed to the motors. This motion requires the motors within the joints to almost instantaneously change direction by 180° , which is not feasible. From Figure 3.5.1 it can be seen that this delay has a detrimental effect on the potential frequency range of excitation. Thus a solution was sought where the angular displacement of the joints was not instantaneous, producing a smoother, more repeatable motion. A circular motion (see Figure 3.5.2) was then tested, setting the joint velocities to maximum, and varying the radius to obtain different frequencies (solid blue line in Figure 3.5.1).

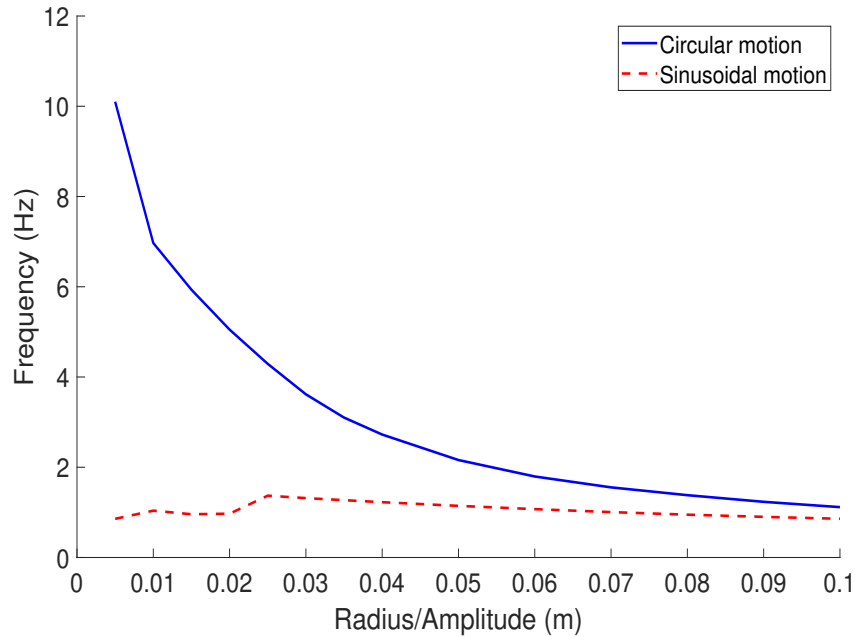


Figure 3.5.1: Comparison between sinusoidal and circular motion of the manipulator's end effector against the frequency obtained for the excitation of the link.

As can be seen from the comparison (Figure 3.5.1) a greater range of excitation frequencies is possible when utilising a circular motion, where the motors undergo a smoother transition. From Figure 3.5.3 the difference between the two motions is most evident, with no time delay present at the extremes of the circular motion. However, this favourable motion type does raise two issues: the frequency obtained at smaller radii (less than 0.01 m) has a different trend, and the link will be subject to excitation in the direction perpendicular to its vibration. The first issue can be overcome through the identification of the frequency range not including those relating to these smaller radii, thus producing a range of 1.5 Hz to 6.75 Hz. The second issue requires that an assumption be made, stating that the excitation in any other direction than that transverse to the length and thickness of the link will have little effect on the response. The frequency range obtained from the results yielded a constraint on the natural

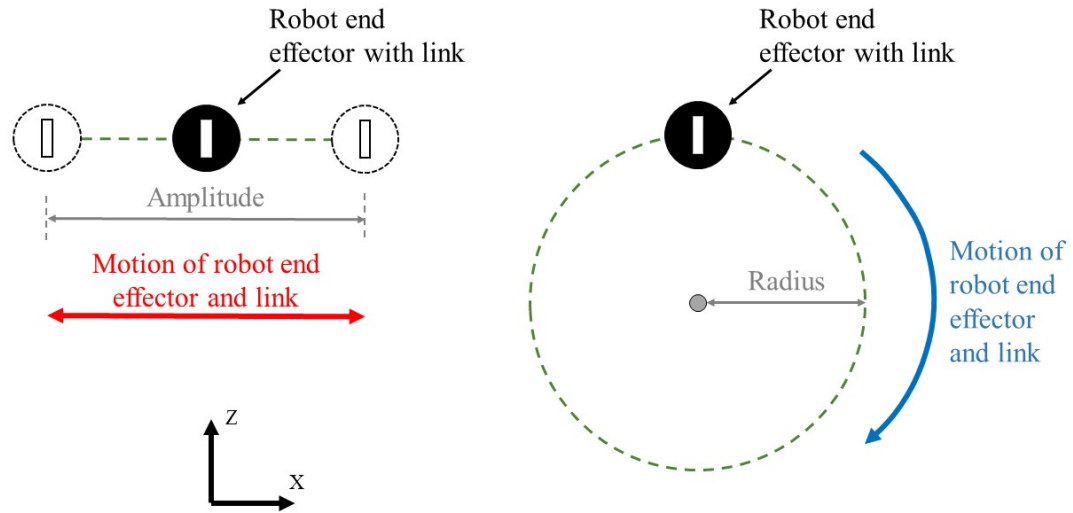


Figure 3.5.2: An illustration of the sinusoidal and circular motions of the robot manipulator's end effector.

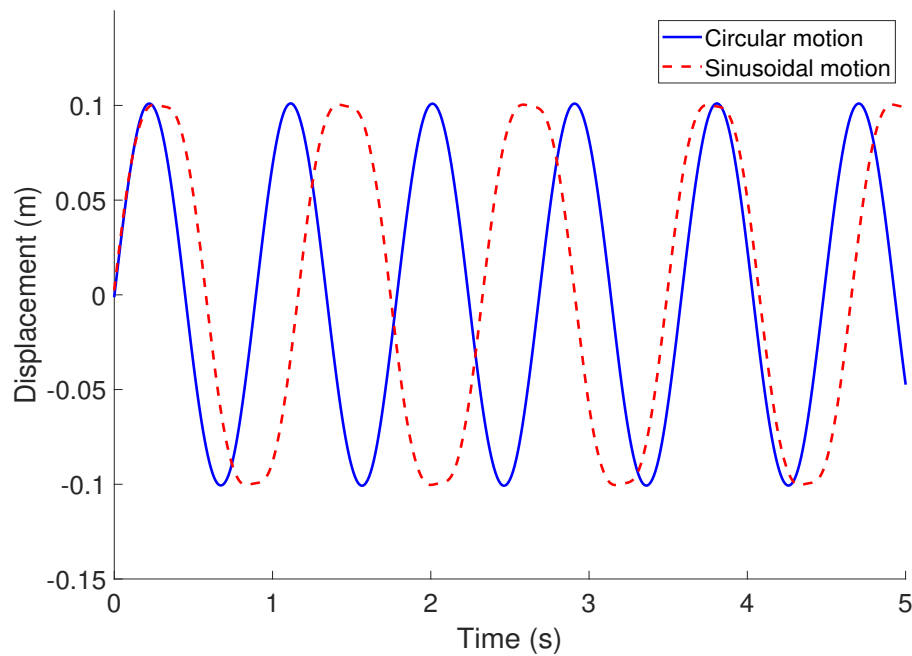


Figure 3.5.3: Comparison between sinusoidal and circular motion of the manipulator's end effector against time for the excitation of the link.

frequency of the link, thus a steel link of different dimensions was required to test the control theory and system when using the robot manipulator as an excitation source. These new dimensions and properties (link B) are outlined in Table 3.5.1 [144, 145], and the natural frequency of the link was found experimentally to be 5.59 Hz. This table

contains two lengths and widths relating to the PZT elements, the ‘overall length/width’ describes the dimensions of the PZT elements including the flexible plastic housing, and this is an important consideration in the analytical models to obtain an accurate insight as to the PZT elements’ influence of the stiffness and mass of the structure. The ‘active width/length’ denotes the dimensions of the PZT element that actually contains the PZT material, this is an important consideration when modelling the PZT actuators electro-mechanically. An illustration of the difference between these two dimensions can be seen in Figure 3.5.4 for the PZT actuators.

Parameters	Link (Steel)	Piezoelectric Sensor (PZT-5A)	Piezoelectric Actuator (PZT-5A)
Overall length (m)	0.272	0.016	0.066
Overall width (m)	0.0397	0.016	0.031
Thickness (m)	0.0004	0.0003	0.0003
Active length (m)	-	0.007	0.056
Active width (m)	-	0.014	0.028
Density (kg/m ³)	7844	5440	5440
Young’s Modulus (GPa)	204	60.48	60.48
Piezoelectric coefficient, \bar{e}_{31}	-	-11.6	-11.6
Electromechanical coupling term, k	-	0.34	0.34
Capacitance (nF)	-	7.89	113.06

Table 3.5.1: Geometric, mechanical and electric properties of link B and piezoelectric patches.

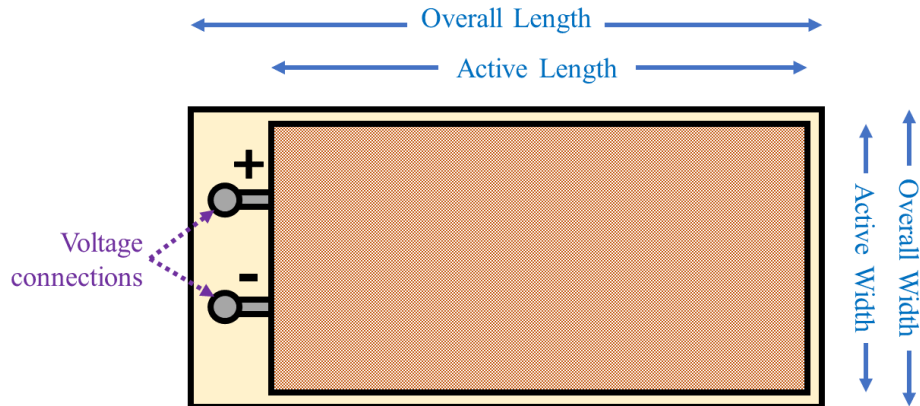


Figure 3.5.4: Illustration of the PZT actuator highlighting the difference between the active and overall dimensions.

As with the previous link, the length to thickness ratio of this link is greater than eighty ($L/h = 680$), so again EBT may be employed to model the link structure. With the addition of an IMU mounted at the free end of the link (at $y = 0.262m$), the natural frequency of the link was estimated (using the analytical model) to be 3.94 Hz, which lies comfortably within the excitation frequency range of the manipulator. However, upon attempting to experimentally validate this estimate it was found from the FRF that the dynamic response of the link structure was different from previous results. This response is represented by the black solid line in Figure 3.5.5, where the magnitude represents the tip displacement divided by the base displacement of the link. In the context of this research the response of the link with the IMU as shown in Figure 3.5.5 becomes an issue as the isolation of the first resonant frequency response is sought. With the inclusion of the IMU the resonant frequency is not readily distinguishable, leading to issues within the investigation of attenuating the response at the natural frequency of the link. This issue was not present when the IMU was mounted upon link A due to the link's thickness, and hence had a lower sensitivity to the additional mass and stiffness from the IMU. The alternative dynamic response was initially thought to be either result of the asymmetric tip mass on the link, the IMU's wires contributing to the stiffness and mass of the structure or a combination of both. If the former proposition was the case, then a simple solution was available; add additional mass to the opposing side of the link for balance. However, in any other case the solution would lie in removing the IMU from the control system.

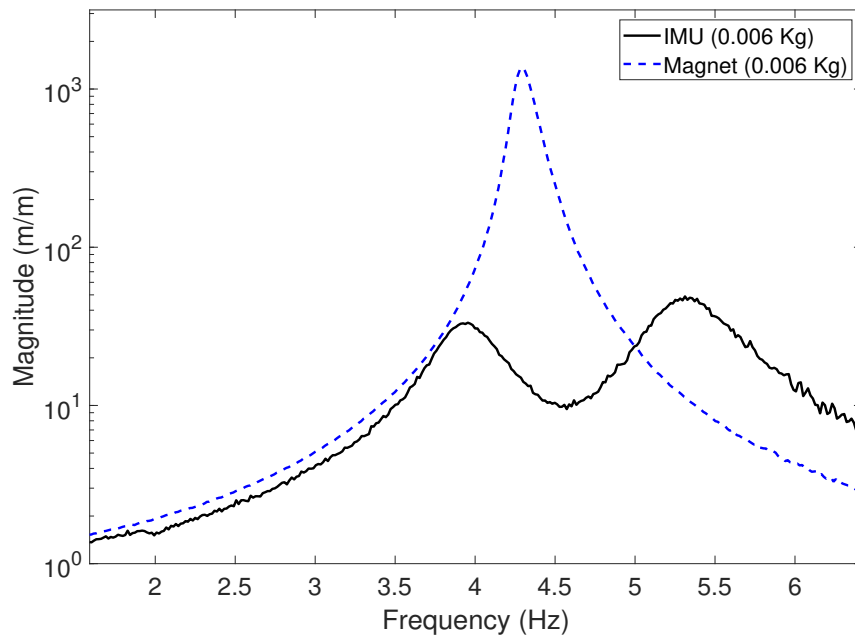


Figure 3.5.5: FRFs of the second link with the additional mass of an IMU and a magnet.

To ascertain the required solution a magnet was attached to the tip of the link and the FRF was then obtained. As can be seen from Figure 3.5.5 the case with one magnet of the same mass as the IMU (0.006 Kg) (dashed blue line) produced only one resonant response within the frequency range considered. This proved that the issue lay with the wires of the IMU and not the asymmetrical mass, and forcing a solution to be sought where the control system no longer employs an IMU. Figure 3.5.5 also shows that less noise in the readings is present without the IMU present, further justifying its removal.

The chosen alternative for sensing the motion of the link was two collocated PZT elements, because, as with the PZT actuators, their addition should have little effect on the functionality of the link. This is especially the case when the PZT sensors are of small dimensions, which drove the choice of element to that which had the dimensions outlined in Table 3.5.1. These PZT sensors will produce voltage that is directly proportional to the strain applied to them, allowing for an accurate prediction of the link's transverse motion. As the strain on the link is larger towards the clamped end the sensors were to be placed as near to the base of the link as possible. Although the addition of the PZT sensors to the link will have negligible influence on the functionality of the link, they would adjust its stiffness and mass and therefore its natural frequency. This provoked the necessity to conduct a study of the influence of a tip mass on the link in lieu of the mass of the original IMU as the dimensions of the beam were chosen based on some tip mass inclusion. Figure 3.5.6 illustrates the variation of the natural frequency of the link with different amounts of tip mass, obtained experimentally. From these results it is clear that in order for the natural frequency to lie within the manipulator's frequency range of excitation (1.5 Hz to 6.75 Hz). Hence, a tip mass of 0.012 kg should be mounted on the link so that $\omega_n = 3.59$ Hz which lies comfortably within the excitation range of the robot manipulator.

Another advantage of the inclusion of a tip mass of this weight is that it is representative of (or greater than) the mass of typical small cameras, especially those designed for use with the RPi. For example, the 'Raspberry Pi Camera Module' weighs 0.003 kg [146], and according to the results in Figure 3.5.6 this would render a natural frequency of the link structure of $\omega_n \approx 4.75$ Hz. This still lies within the excitation frequency range of the robot manipulator, and so the inclusion of this piece of equipment on the link structure would also render high amplitude responses. Whilst this is relevant with respect to the suggested application, in order to gain a good insight into the performance of the control system it is important to consider a range of frequencies both higher and lower than the natural frequency. A tip mass of 0.012 kg offers a larger range of surrounding frequencies compared to one which is 0.003 kg considering the excitation range of the robot manipulator, hence its selection.

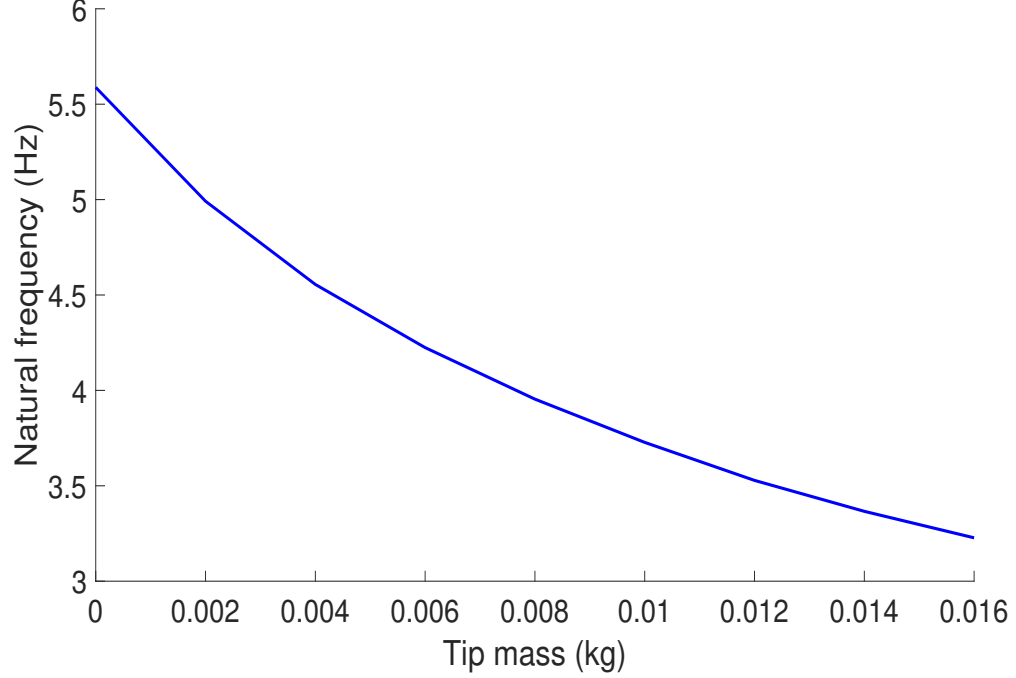


Figure 3.5.6: Tip mass influence on natural frequency of link B.

3.5.2 Analytical model

The exchange of sensors and subsequent requirement for the inclusion of a tip mass on the link lead to the necessity of alterations to the analytical model from that outlined in Section 3.5.1.

Figure 3.5.7 illustrates the new analytical model as a plan view of the link and mounted components (not to scale). The mass of the clamp and end effector of the robot visible in this image is not included as the link is assumed to be perfectly clamped, their illustration is just to aid in the visualisation of the set-up. $w_b(y, t)$ and $w_{rel}(y, t)$ represent the applied base excitation and the transverse motion of the link (as displacement), respectively. y_1 and y_3 are the positions of the start of the sensors and actuators, respectively, and their end positions are represented by y_2 and y_4 . The equation of motion of the structure may be written as Equation 3.34.

$$\begin{aligned}
& \frac{\partial^2}{\partial y^2} \left(EI(y) \frac{\partial^2 w_{rel}(y, t)}{\partial y^2} \right) + \rho A(y) \frac{\partial^2 w_{rel}(y, t)}{\partial t^2} + c_a \frac{\partial w_{rel}(y, t)}{\partial t} \\
& - \vartheta_{ps} V_{in,ps}(t) \left[\frac{d\delta(y - y_1)}{dy} - \frac{d\delta(y - y_2)}{dy} \right] - \vartheta_{pa} V_{in,pa}(t) \left[\frac{d\delta(y - y_3)}{dy} - \frac{d\delta(y - y_4)}{dy} \right] \\
& = - [\rho A(y) - M_{TM} \delta(y - L_{lk})] \frac{\partial^2 w_b(y, t)}{\partial t^2}
\end{aligned} \tag{3.34}$$

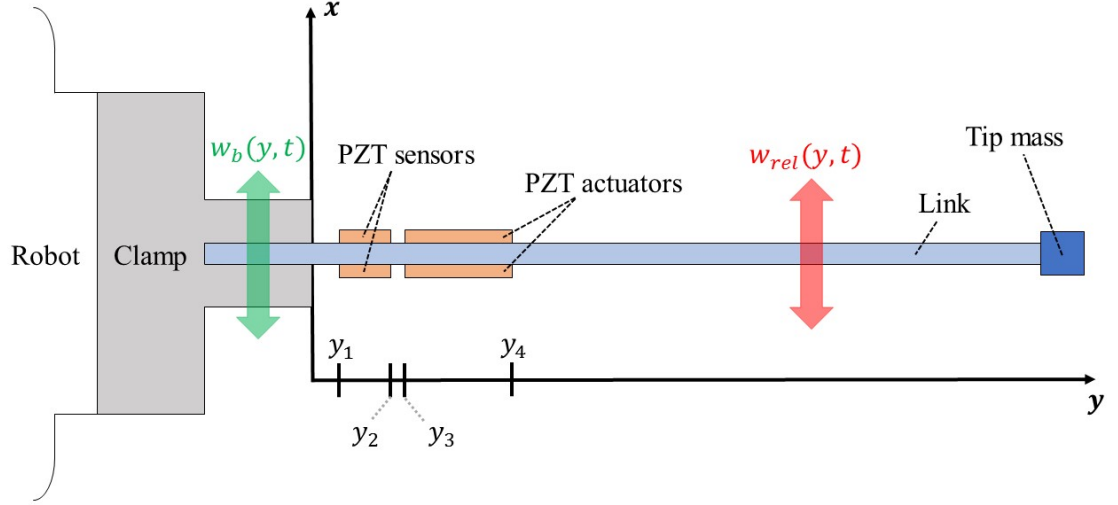


Figure 3.5.7: Illustration of the analytical model.

The inclusion of the two sets of collocated piezoelectric patches renders the inclusion of Equations 3.35, 3.36 and 3.37.

$$EI(y) = E_{lk}I_{lk} + E_{ps}I_{ps} [H(y - y_1) - H(y - y_2)] + E_{pa}I_{pa} [H(y - y_3) - H(y - y_4)] \quad (3.35)$$

$$\rho A(y) = \rho_{lk}A_{lk} + \rho_{ps}A_{ps} [H(y - y_1) - H(y - y_2)] + \rho_{pa}A_{pa} [H(y - y_3) - H(y - y_4)] \quad (3.36)$$

$$\vartheta_{ps} = \frac{\bar{e}_{31}W_{ps}^{\Psi}}{h_{ps}} \left[\left(h_{ps} + \frac{h_{lk}}{2} \right)^2 - \frac{h_{lk}^2}{4} \right] \quad (3.37)$$

$$\vartheta_{pa} = \frac{\bar{e}_{31}W_{pa}^{\Psi}}{h_{pa}} \left[\left(h_{pa} + \frac{h_{lk}}{2} \right)^2 - \frac{h_{lk}^2}{4} \right]$$

The subscripts in Equations 3.34 to 3.37, lk , ps , and pa represent the link, PZT sensor and PZT actuator, respectively. The superscript ψ represents the active dimensions. The nomenclature used in these equations is almost identical to that of the analytical model for link A (see Section 3.5.1), but has been repeated here as Table 3.5.2 for convenience. It should be noted that the voltage output from the actuators is negligible in comparison to the magnitude of the required input to generate strain, and therefore is not included in these calculations.

Variable	Definition
E	Young's modulus
I	Second moment of area
ρ	Density
A	Area
ϑ	Piezoelectric coupling term
V	Voltage (out from sensors, in from actuators)
δ	Dirac delta function
M_{TM}	Tip mass
L	Length
H	Heaviside function
W	Width
h	Thickness
\bar{e}_{31}	Effective transverse piezoelectric coefficient

Table 3.5.2: Nomenclature repeated for convenience.

The second moment of area for the link, the link with PZT sensors and the link with PZT actuators are outlined in Equations 3.38, 3.39 and 3.40.

$$I_{lk} = \frac{1}{12}W_{lk}h_{lk}^3 \quad (3.38)$$

$$I_{ps} = 2 \times \left[\frac{1}{12}W_{ps}h_{ps}^3 + W_{ps}h_{ps} \left(\frac{h_{ps}}{2} + \frac{h_{lk}}{2} \right)^2 \right] \quad (3.39)$$

$$I_{pa} = 2 \times \left[\frac{1}{12}W_{pa}h_{ps}^3 + W_{pa}h_{pa} \left(\frac{h_{pa}}{2} + \frac{h_b}{2} \right)^2 \right] \quad (3.40)$$

As with the analytical model for link A, the equation of motion in terms of the generalised coordinate ($P_n(t)$) is sought. With the first step requiring that the product rule (Equation 3.41) be applied to the stiffness term of Equation 3.34, before reducing the equation using the relation shown in Equation 3.42, yielding Equation 3.43.

$$\frac{\partial^2}{\partial y^2} [f(y)j(y)] = f''(y)j(y) + 2f'(y)j'(y) + f(y)j''(y) \quad (3.41)$$

$$w_{rel}(y, t) = \sum_{n=1}^N \phi_n(y)P_n(t) \quad (3.42)$$

$$\begin{aligned}
& \frac{\partial^2 EI(y)}{\partial y^2} \phi_n''(y) P_n(t) + 2 \frac{\partial EI(y)}{\partial y} \phi_n'''(y) P_n(t) + EI(y) \phi_n^{iv}(y) P_n(t) \\
& \quad + \rho A(y) \phi_n(y) \ddot{P}_n(t) + c \phi_n(y) \dot{P}_n(t) \\
& - \vartheta_{ps} V_{in,ps}(t) \left[\frac{d\delta(y-y_1)}{dx} - \frac{d\delta(y-y_2)}{dy} \right] - \vartheta_{pa} V_{in,pa}(t) \left[\frac{d\delta(y-y_3)}{dx} - \frac{d\delta(y-y_4)}{dy} \right] \\
& = - [\rho A(y) - M_{TM} \delta(y-L_{lk})] \frac{\partial^2 w_b(y,t)}{\partial t^2}
\end{aligned} \tag{3.43}$$

where, $\phi_n(y)$ represents the n^{th} mode shape of the link. The base excitation can be expressed as in Equation 3.44.

$$w_b(y,t) = g(t) + xh(t) \tag{3.44}$$

where, $g(t)$ is the transverse base displacement and $xh(t)$ is the superimposed rotational displacement. As $x \rightarrow 0$, $xh(t) \rightarrow 0$, with the base displacement at $x = 0$ the second term of Equation 3.44 reduces to zero. Performing Galerkin decomposition on Equation 3.43 omits the spatial dependence and yields Equation 3.45.

$$M_n \ddot{P}_n(t) + C_n \dot{P}_n(t) + K_n P_n(t) - \theta_{ps,n} V_{in,ps}(t) - \theta_{pa,n} V_{in,pa}(t) = f_n(t) \tag{3.45}$$

where,

$$M_n = \int_0^{L_{lk}} \rho A(y) + M_{TM} \delta(y-L_{lk}) \phi_n^2(y) dy \tag{3.46}$$

$$C_n = 2\zeta_n \omega_n M_n \tag{3.47}$$

$$K_n = \int_0^{L_{lk}} \left[\frac{\partial^2 EI(y)}{\partial y^2} \phi_n''(y) + 2 \frac{\partial EI(y)}{\partial y} \phi_n'''(y) + EI(y) \phi_n^{iv}(y) \right] \phi_n(y) dy \tag{3.48}$$

$$\theta_{ps,n} = \vartheta_{ps} \int_0^{L_{lk}} \left[\frac{d\delta(y-y_1)}{dy} - \frac{d\delta(y-y_2)}{dy} \right] \phi_n(y) dy \tag{3.49}$$

$$\theta_{pa,n} = \vartheta_{pa} \int_0^{L_{lk}} \left[\frac{d\delta(y-y_3)}{dy} - \frac{d\delta(y-y_4)}{dy} \right] \phi_n(y) dy \tag{3.50}$$

$$f_n(t) = \frac{d^2g(t)}{dt^2} \left[-\rho A(y) \int_0^{L_{lk}} \phi_n(y) dy - M_{TM} \phi_n(L_{lk}) \right] \quad (3.51)$$

Utilising the relation shown in Equation 3.52, Equations 3.49 and 3.50 can be rewritten to yield Equations 3.53 and 3.54.

$$\int_{-\infty}^{\infty} \frac{d^{(i)}\delta(y-y_0)}{dx^{(i)}} \gamma(y) dy = (-1)^{(i)} \frac{d^{(i)}\gamma(y)}{dy^{(i)}} \Big|_{y=y_0} \quad (3.52)$$

$$\theta_{ps,n} = \vartheta_{ps} \left[\frac{d\phi_n(y_2)}{dy} - \frac{d\phi_n(y_1)}{dy} \right] \quad (3.53)$$

$$\theta_{pa,n} = \vartheta_{pa} \left[\frac{d\phi_n(y_4)}{dy} - \frac{d\phi_n(y_3)}{dy} \right] \quad (3.54)$$

Equation 3.45 can be divided by the mass to yield Equation 3.55, which is the equation of motion of the link, PZT elements and tip mass in terms of the generalised coordinate.

$$\ddot{P}_n(t) + 2\zeta_n\omega_n\dot{P}_n(t) + \omega_n^2 P_n(t) - \chi_{ps,n} V_{in,ps}(t) - \chi_{pa,n} V_{in,pa}(t) = F_n(t) \quad (3.55)$$

where,

$$2\zeta_n\omega_n = \frac{C_n}{M_n}, \quad \omega_n^2 = \frac{K_n}{M_n}, \quad \chi_{ps,n} = \frac{\theta_{ps}}{M_n}, \quad \chi_{pa,n} = \frac{\theta_{pa}}{M_n}, \quad F_n(t) = \frac{f_n(t)}{M_n} \quad (3.56)$$

As previously mentioned the voltage output from the PZT actuators is not considered in this model, due to its relatively small magnitude in comparison to the input. However, calculating the voltage output from the sensors is a necessity, to do so the circuit of the PZT sensors connected in parallel needs to be envisioned (see Figure 3.5.8).

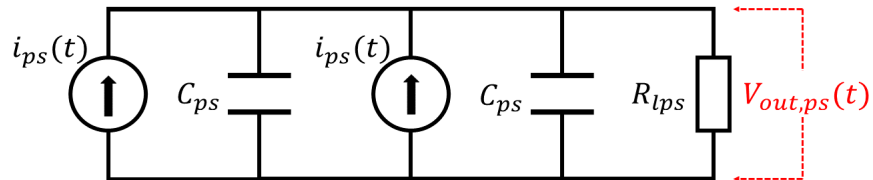


Figure 3.5.8: Circuit diagram of the PZT sensors.

A PZT element can be thought of as having an internal current source ($i_{ps}(t)$) parallel with internal capacitance (C_{ps}) and a resistive load (R_{lps}), across which the voltage potential difference ($V_{out,ps}(t)$) can be measured. Considering the experiments

in this research, although the sensors will not be physically connected in parallel, the controlling device will manipulate the potential difference across the patches such that they can be viewed as being of parallel connection. Using Ohm's laws as shown in Equations 3.57 and 3.58 as well as Kirchhoff's laws:

1. The algebraic sum of currents in a network of conductors meeting at a point is zero.
2. The directed sum of the potential differences around any closed loop is zero.

$$i_{ps}(t) = C_{ps} \frac{dV_{out,ps}(t)}{dt} \quad (3.57)$$

$$i_{ps}(t) = \frac{V_{out,ps}(t)}{R_{lps}} \quad (3.58)$$

the governing electrical equation for the PZT sensors can be produced (Equation 3.59).

$$C_{ps} \frac{dV_{ps}(t)}{dt} + \frac{V_{out,ps}(t)}{2R_{lps}} - i_{ps}(t) = 0 \quad (3.59)$$

where,

$$C_{ps} = \frac{\bar{\epsilon}_{33} W_{ps}^{\Psi} L_{ps}^{\Psi}}{h_{ps}} \quad (3.60)$$

$$i_{ps}(t) = - \sum_{n=1}^{\infty} \kappa_{nps} \frac{dP_n(t)}{dt} \quad (3.61)$$

where $\bar{\epsilon}_{33}$ is the dielectric permittivity coefficient, and the modal coupling term (κ_{nps}) is defined as:

$$\kappa_{nps} = \bar{\epsilon}_{31} \frac{(h_{ps} + h_{lk}) AW_{ps}}{2} \int_0^{L_{lk}} \frac{d^2 \phi_n(y)}{dy^2} dy \quad (3.62)$$

From Equations 3.55 and 3.59 the transverse motion of the link ($w(y, t)$) and the voltage output from the PZT sensors ($V_{out,ps}$) can be attained utilising Equation 3.42 and Equation 3.63.

$$w(y, t) = w_b(y, t) + w_{rel}(y, t) \quad (3.63)$$

Based on linear assumption the modal mechanical response ($T_n(t)$), the voltage output from the PZT sensor ($V_{out,ps}(t)$), the input to the PZT actuator and the forcing term ($F_n(t)$) are assumed to be harmonic at the frequency of excitation. Therefore to obtain the equation of motion (Equation 3.55) and the governing electrical equation

(Equation 3.59) in the frequency domain (Equations 3.65 and 3.66, respectively) the relations shown in Equations 3.64 can be utilised.

$$\begin{aligned}
P_n(t) &= P_0 e^{j\omega t} & \dot{P}_n(t) &= j\omega P_0 e^{j\omega t} & \ddot{P}_n(t) &= -\omega^2 P_0 e^{j\omega t} \\
V_{out,ps}(t) &= V_{out,ps} e^{j\omega t} & \dot{V}_{out,ps}(t) &= j\omega V_{out,ps} e^{j\omega t} & \ddot{V}_{out,ps}(t) &= -\omega^2 V_{out,ps} e^{j\omega t} \\
V_{in,ps}(t) &= V_{in,ps} e^{j\omega t} & \dot{V}_{in,ps}(t) &= j\omega V_{in,ps} e^{j\omega t} & \ddot{V}_{in,ps}(t) &= -\omega^2 V_{in,ps} e^{j\omega t} \\
V_{in,pa}(t) &= V_{in,pa} e^{j\omega t} & \dot{V}_{in,pa}(t) &= j\omega V_{in,pa} e^{j\omega t} & \ddot{V}_{in,pa}(t) &= -\omega^2 V_{in,pa} e^{j\omega t} \\
F_n(t) &= F_0 e^{j\omega t} & \dot{F}_n(t) &= j\omega F_0 e^{j\omega t} & \ddot{F}_n(t) &= -\omega^2 F_0 e^{j\omega t}
\end{aligned} \tag{3.64}$$

$$(-\omega^2 + 2\zeta_n \omega_n j\omega + \omega_n^2) P_0 - \chi_{ps} V_{in,ps} - \chi_{pa} V_{in,pa} = F_0 \tag{3.65}$$

$$\left(j\omega C_{ps} + \frac{1}{2R_{lps}} \right) V_{out,ps} + j\omega \sum_{n=1}^{\infty} \kappa_{nps} P_0 = 0 \tag{3.66}$$

3.5.3 Experimental validation

To validate the analytical model of link B a similar experimental set up to that used in the validation of link A. The link was clamped and mounted upon the APS 113 ELECTRO-SEIS R Long Stroke Shaker, which was powered by the APS 125 Power Amplifier. However, in this case, the combination of amplifier and exciter was controlled by a dSPACE MicroLabBox, which was also tasked with the reading and recording of both the laser displacement sensors (LDSs) (ZX2LD100) and the PZT sensors. The LDSs are introduced into these experiments as the relationship between the displacement of the link and the voltage output from the PZT sensors is to be obtained. Obtaining this relationship would assist in both the validation of the analytical model, and the justification for the reliance of the voltage output as a measure of the attenuation of the vibrations of the link when it is mounted upon the robot manipulator. Later experiments required the use of a speciality device which would be able to process an incoming signal and respond in real-time for the purpose of control, as the SignalCalc Abacus is incapable of this the dSPACE was employed. Thus, its use within this particular experiment, which requires no control, is based solely on continuity. Figure 3.5.9 illustrates the set up including the connections between the devices. The dimensions of link B and both types of PZT elements are given in Table 3.5.1, the tip mass consisted of two magnets with a total mass of 0.012 kg, and the starting positions of the PZT sensor (y_1) and PZT actuator (y_3) were 0.011 m and 0.0295 m, respectively. The LDSs were positioned so that they read the displacement of the base of the link (i.e. the clamp structure), and the tip of the link ($y = y_{LDS} = 0.262$ m).

The link was excited using a sinusoidal motion, increasing the frequency in steps over time, and measuring the displacement of the base and free end of the link as well as the output from the two PZT sensors. The sampling frequency was set to 1 kHz, which is sufficiently large enough to measure the excitation frequencies (the sampling frequency should be at least twice as large as the frequency being measured [147]), and is typical of that which can be achieved by the RPi. Although there was no comparison to be made between the dSPACE and RPi systems in this experiment, this decision of the sampling rate was apt for the sake of continuity. A fast Fourier transform was performed on all of the recorded data, and the tip displacement and voltage out from the PZT sensors were divided by the base displacement to obtain two FRFs with magnitudes of the units m/m and V/m. This method obtained clean results for both FRFs as can be seen in Figures 3.5.10 and 3.5.11 (blue solid lines).

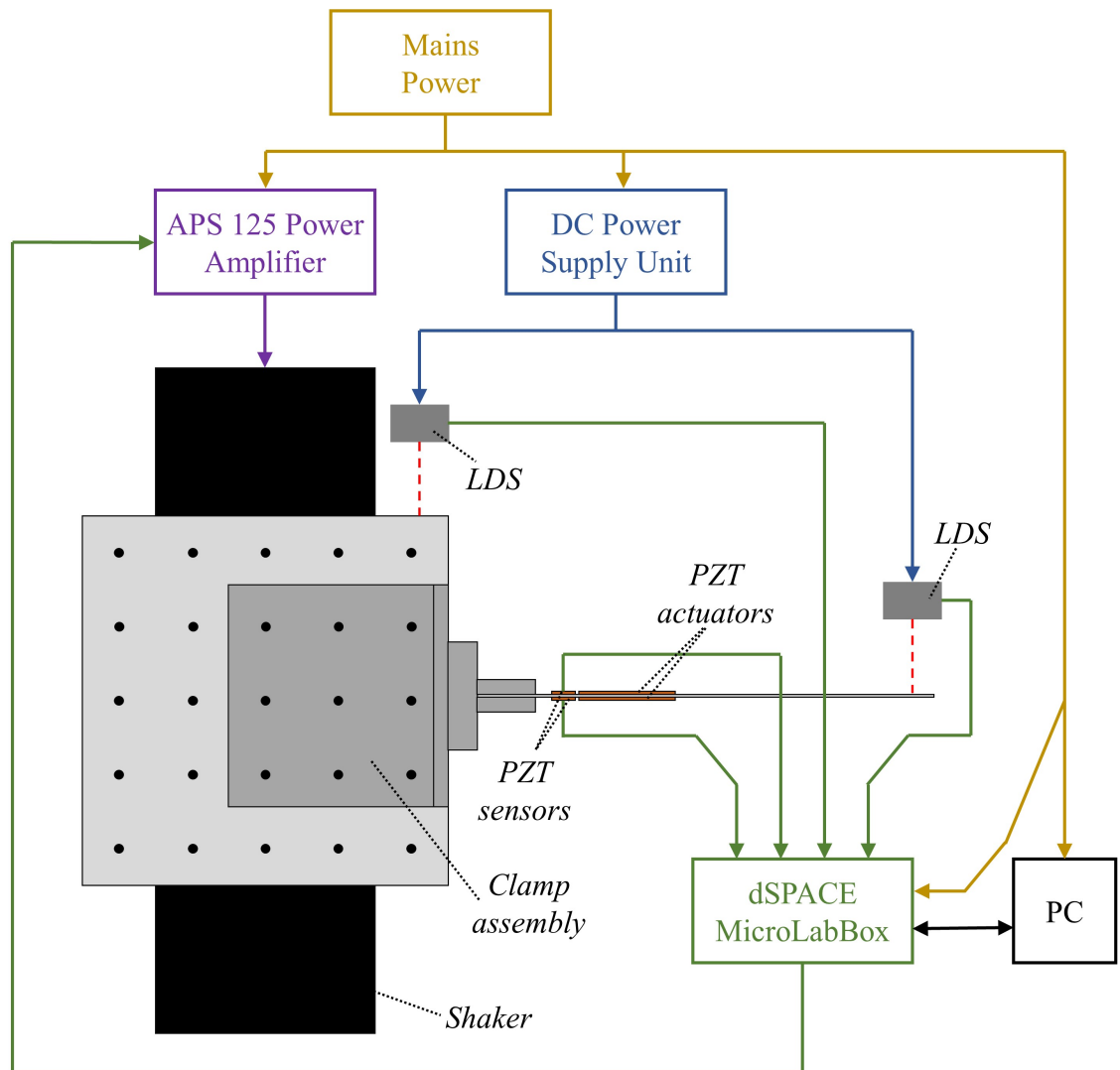
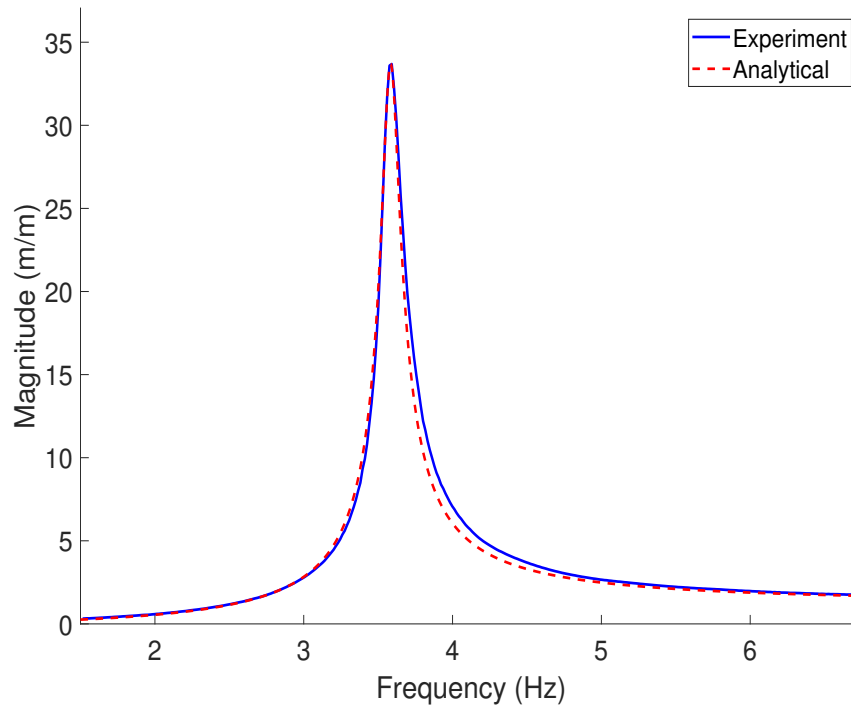
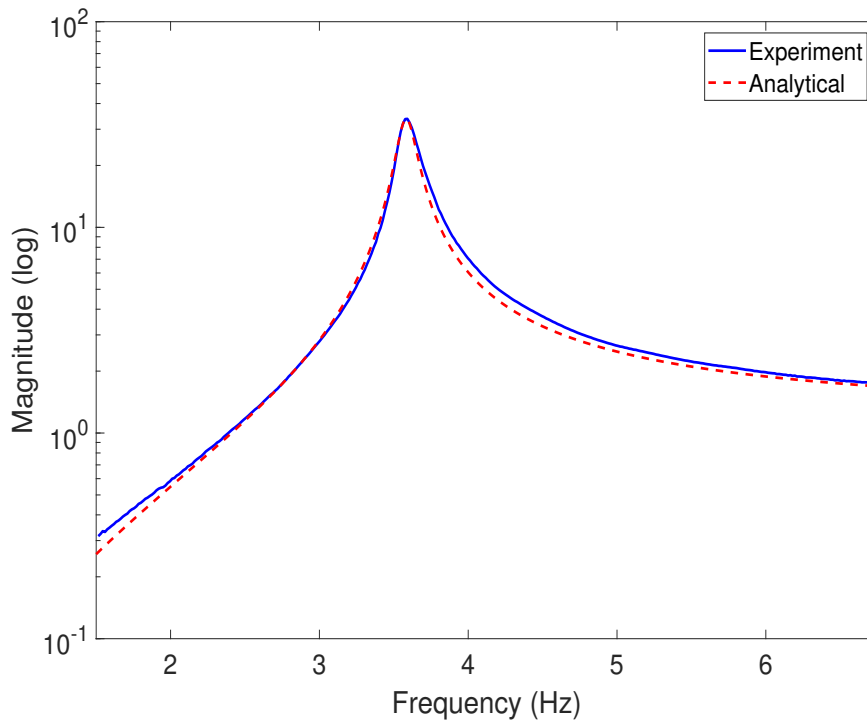


Figure 3.5.9: Illustration of the experimental set-up used to validate the analytical model of link B.

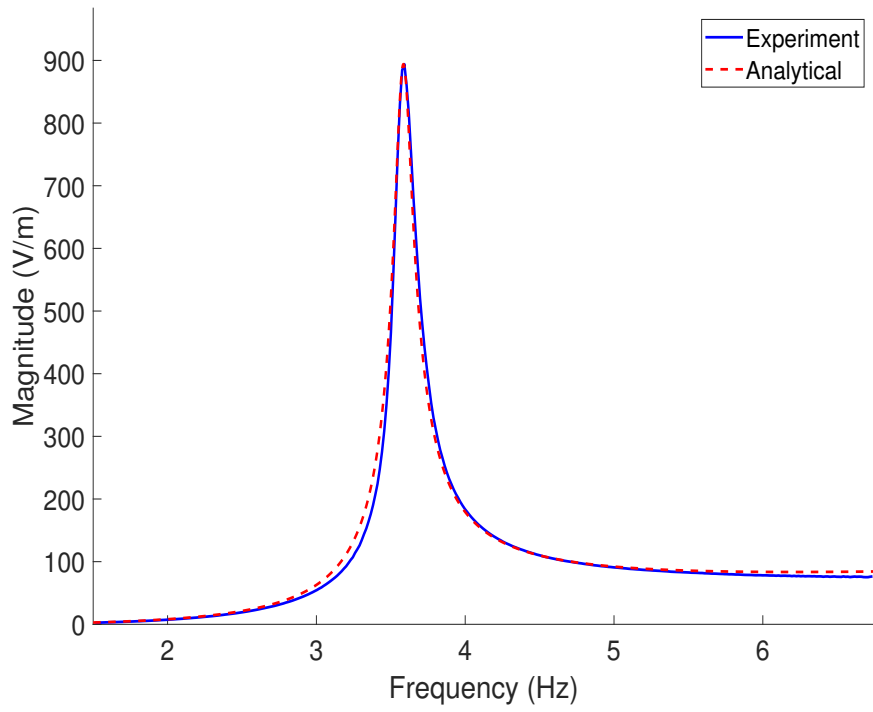


(a) Magnitude scale.

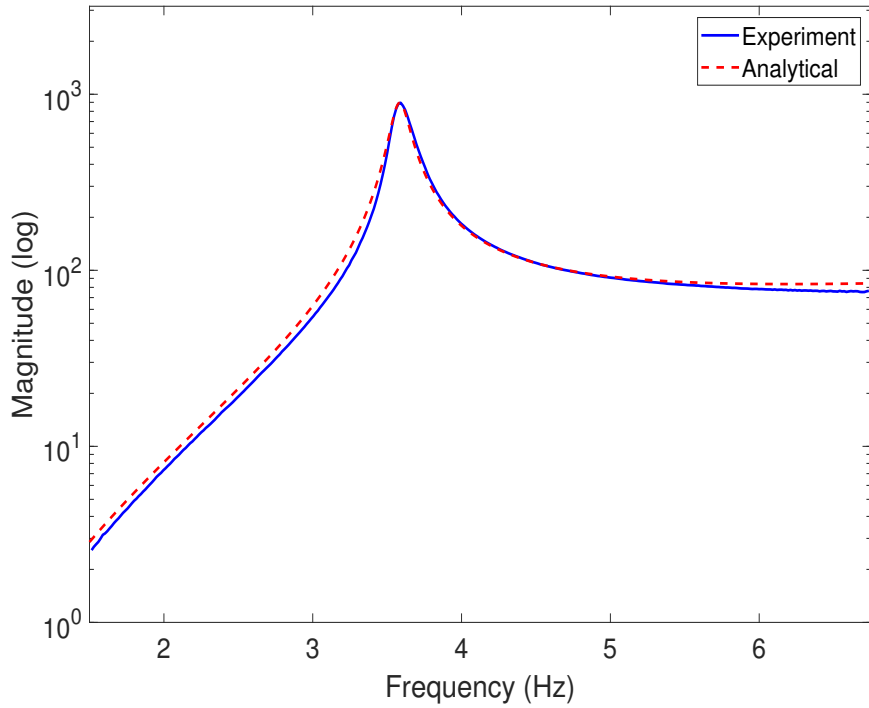


(b) Logarithmic scale.

Figure 3.5.10: FRFs of tip displacement divided by base displacement for the open loop system.



(a) Magnitude scale.



(b) Logarithmic scale.

Figure 3.5.11: FRFs of voltage output from PZT sensors divided by base displacement for the open loop system.

The results of the analytical model for the displacement FRF were obtained through the use of Equation 3.65, omitting the voltage dependent terms in this open loop case. The damping ratio (ζ) was obtained from the experimental results using the half power method (see Section 1.7.4), so that ($\zeta_1 = 0.018$). The analytical equation for the FRF produces a magnitude equal to the generalised coordinate divided by the excitation force (see Equation 3.67), and as the experimental results had a magnitude equating the tip displacement divided by the base displacement adjustments to this equation were required.

$$\frac{P_0}{F_0} = \frac{1}{(-\omega^2 + 2\zeta_n\omega_n j\omega + \omega_n^2)} \quad (3.67)$$

The generalised coordinate must be converted to the transverse motion of the link ($w_{rel}(y, t)$), and the forcing term (F_0) to the base displacement ($w_b(y, t)$). From equation 3.42, the relative displacement of the link at point y along its length may be calculated through the multiplication of the generalised coordinate (P_0) with the modal coordinate ($\phi_n(y)$), where y in this case is the position of the laser displacement sensor's beam on the link ($y = y_{LDS} = 0.262$ m). From Newton's second law (3.68) the magnitude of the base displacement (g_0) may be obtained, where m is the mass of the link structure including all PZT patches. This yields the FRF equation in terms of the tip and base displacements (Equation 3.69) where the arbitrary magnitude of the eigenfunction (γ_n) was found, through comparison with the experimental results, such that $\gamma_1 = 10.43$.

$$F = ma = m \frac{d^2 g(t)}{dt^2} = m(-\omega^2 g_0) \quad (3.68)$$

$$\frac{w_{rel}(y, t)}{w_b(y, t)} = \frac{-\omega^2 \phi_n(y_{LDS}) m \gamma_n}{(-\omega^2 + 2\zeta_n \omega_n j\omega + \omega_n^2)} \quad (3.69)$$

The analytical FRF of magnitude voltage divided by base displacement requires the rearrangement of Equation 3.66 which, with the assumption of one mode, may be written as:

$$V_{out,ps} = \frac{-j\omega K_{nps}}{j\omega C_{ps} + \frac{1}{2R_{lps}}} P_0 \quad (3.70)$$

Multiplying by the complex conjugate yields:

$$V_{out,ps} = \left[-\frac{\omega^2 \kappa_{nps} C_{ps}}{\omega^2 C_{ps}^2 + \left(\frac{1}{2R_{lps}}\right)^2} - \frac{\omega \kappa_{nps} \frac{1}{2R_{lps}}}{\omega^2 C_{ps}^2 + \left(\frac{1}{2R_{lps}}\right)^2} j \right] P_0 = [-RE - IMGj] T_0 \quad (3.71)$$

Substituting this relationship between the voltage output from the the PZT sensors and the generalised coordinate (T_0) into Equation 3.67, and utilising Newton's second law (Equation 3.68) as previously yields:

$$\frac{V_{out,ps}}{w_b(y, t)} = -\omega^2 m \frac{[-RE - IMGj] T_0}{F_0} = \frac{-\omega^2 m [-RE - IMGj]}{(-\omega^2 + 2\zeta_n \omega_n j \omega + \omega_n^2)} \quad (3.72)$$

For both types of open loop FRFs (displacement and voltage response), the analytical model can be observed to be an accurate representation of the response (Figures 3.5.10 and 3.5.11). Thus validating the analytical model including the electromechanical coupling aspect, which has the potential to be an invaluable tool for the next stage of the research.

3.6 Summary

This chapter presented the development of two analytical models of the link structure, one wherein the sensors employed were IMUs (although accelerometers of similar size and mass were utilised in lieu for the aforementioned reasons), and the other where they were PZT elements. The reasoning behind the exchange of sensors was discussed here so that the text follows the development of the models as opposed to the chronological order of the experiments. Both analytical models were experimentally validated and the results portray the models as a good representation of the structure when no control is employed.

Chapter 4

Control theory and system

This chapter concerns the control system designed and developed within this research, including the general design process, analytical models, the selection of components whilst the constraints (inexpensive and lightweight) are imposed, and the electrical and communication connections. Herein two sensors options are described; inertial measurement units (IMUs) and PZT elements, the former has been labelled ‘Control system A’ and the latter ‘Control system B’. The motivation behind the consideration of two sensor options, and consequently the preference of one over the other has been discussed. A purpose-built control system is introduced for use in the performance analysis of the designed control system. The results of this analysis, and the analyses of control systems A and B are included in the following chapter. Finally, in this chapter, the health and safety considerations are discussed; the hazards and risks present during the experiments are identified, and preventive measures are proposed.

4.1 An overview of the control system design

Control systems are commonly used in many areas, from home central heating systems to large industrial processes. Here a system is considered any structures, devices or other elements that are interconnected to perform a required task [148]. Introducing some form of control to a system ensures that the required response is obtained. For example, in a home central heating system the temperature in the building can be controlled by the user. The control system measures the temperature of the house, and compares this to the temperature required, if the measured temperature is too low then the central heating system is used to increase the temperature until the requirement is met. Conversely if the temperature is too high then the central heating is stopped until the required temperature is met. In a similar manner the motion of a structure may be controlled, if the amplitude of the response of a structure is too great then a

control system may be employed to reduce it.

Throughout this research the design of the Active Vibration Control (AVC) system has followed stages not dissimilar to those outlined in [7]. The steps used to complete the design are as follows:

1. The system should be analysed, identifying the specific parts within it to be controlled.
2. Identify the most appropriate method of modelling the system/or the parts affected by vibration.
3. Simplify the model if possible to reduce computation time.
4. Perform analysis on the simplified model, comparing its response to experimental results for approval, and adjusting the model accordingly.
5. Identify what is required of the sensor(s)/actuator(s) to be used in the system and obtain their optimal placement.
6. Select the most appropriate hardware and software to accompany the sensor(s) and actuator(s) and integrate them into the system.
7. Perform another analysis on the proposed system which includes the sensor(s) and actuator(s) to denote their influence on the original part of the system that is to be controlled.
8. Specify the performance criteria, the algorithm and the parameters of the control system.
9. Produce experiments to observe the performance of the system which will ensure that it matches the criteria previously specified.
10. Conduct the prescribed experiments and observe the results and the overall performance of the system. Repetition of the previous steps may be required, especially regarding the control system parameters.

In addition to utilising these steps throughout the investigative process further constraints were imposed on the control system design to ensure that it can be used for both the proposed and other applications. Aside from having an acceptable level of performance the control system should:

- be as inexpensive and as lightweight as possible.
- not significantly impair the functionality of the system on/in which it is included.

- be easily integrated into an existing system.
- be easily removed from the existing system.
- be easily maintainable.

It should be noted, that whilst the designed control system's performance was intended to be analysed in the control of nonlinear vibrations, the control scheme and system has not be specifically designed for such scenarios. Providing that the control system does not negatively affect the response of the system, it may still be considered suitable for use in applications that produce somewhat occasional nonlinear responses.

4.2 Analytical models

Here two control systems are presented as analytical models, the first employed in conjunction with control system A (CSA) which utilised inertial measurement units (IMUs). This is followed by control system B which implemented PZT elements as sensors. The input of the former control system is angular velocity, and the latter the voltage output from PZT sensors. Both systems employ PZT elements as actuators, and so the main difference between the two control systems lies in the sensor options or more importantly the influence of the sensors on the dynamics of the link. One of the IMUs should be placed towards the tip of the link to ensure the motion of the link is captured to the best extent, however, as previously discussed, this produces an undesired response. This was not present in the experiments which utilised a link with a larger thickness, hence the investigation into the use of PZT elements as sensors. These sensors required additional components for use with the SBC, which has the disadvantage of additional mass. However, as PZT elements effectively measure strain they are best placed towards the clamped end of the link, alongside the difference in the positioning compared to the IMU option the PZT sensors have a lower mass. This meant that the PZT elements have less of an impact on the dynamics of the structure. Here the analytical models for both control systems are presented so as to follow the development of the control system in this thesis as opposed to the chronological order of the experiments undertaken.

4.2.1 Control system A

The first control system designed in this research utilises a proportional control gain (K_p) which is applied to a ratio of the angular velocity. During this investigation the feasibility of the choice of components was a priority, and hence limiting the strain on the

processing capacity of the RPi would offer a fairer investigation. To do so the control scheme chosen for use was a proportional one, although it should be noted that an alternative control scheme is presented in a later chapter. In the experiments concerning CSA the voltage output to the actuators is obtained through the product of the control gain (K_p), and a ratio of the angular velocity reading and the angular velocity at the natural frequency. Although the IMUs allow for the reading of the acceleration, the angular velocity and the angular displacement, it was only the measurements from the gyroscope that were deemed suitable in this case. The polarity of the acceleration does not provide information on the direction of the transverse displacement of the link, and so would not allow for the selection of which actuator is to be employed at an instant in time. For example, a negative acceleration may occur in either direction, and so employing one PZT actuator for the negative accelerations may lead to the excitation of the link as opposed to attenuation. The magnetometer, as previously mentioned is sensitive to ferromagnetic objects, and as the experimental set-up contains various metals an accurate reading would not be provided. Hence the limitation of only using the gyroscope within the IMU, and the equation employed is shown in Equation 4.1:

$$V_{in,pa} = K_p \frac{\dot{\Theta}}{\dot{\Theta}_{\omega_n}} \times 360 \quad (4.1)$$

where V_{pa} is the voltage to be applied to the PZT actuators, $\dot{\Theta}$ is the angular velocity at the free end of the link, and the maximum steady-state angular velocity when the link is excited at its natural frequency is denoted by $\dot{\Theta}_{\omega_n}$. The angular velocity is measured about the z axis of the structure which is parallel to the width of the link. Multiplying by a value of 360 ensures that the maximum operating voltage of the PZT actuators (360 V) is reached when the largest amplitude of transverse motion is experienced by the link i.e. $V_{in,pa} = 360V$ when $K_p \dot{\Theta} = \dot{\Theta}_{\omega_n}$. The utilisation of this relationship to obtain $V_{in,pa}$ removes the necessity to obtain the optimal gain value when $\dot{\Theta}_{\omega_n}$ is known as a value of $K_p = 1$ will produce the maximum usable voltage when $\dot{\Theta} = \dot{\Theta}_{\omega_n}$. Whilst this method does not conform to the conventional application of a control gain, it does allow for the performance of the components to be easily analysed without the concern of the control system parameters. Should the control system prove to be effective when the control is applied based on Equation 4.1, then further studies were planned to obtain an insight into its effectiveness with $\dot{\Theta}_{\omega_n}$ being unknown. In this case the proportional gain (K_p) would be applied directly to $\dot{\Theta}$, and the value of K_p increased until the best level of performance is empirically obtained.

To employ this theory in the analytical model the temporal solution to the link's transverse motion (Equation 3.32) should be equated to the closed loop control signal (s) to yield Equation 4.2.

$$\ddot{P}_n(t) + 2\zeta\omega_n\dot{P}_n(t) + \omega_n^2 P_n(t) = \chi V_{in,pa} \sin(\Omega_v t) - X \sin(\Omega_x t) = sig = -K_p \dot{P}_n(t) \quad (4.2)$$

where,

$$V_{in,pa} = -\frac{K_p \dot{P}_n(t)}{\dot{P}_{n,max}} \times 360 \quad (4.3)$$

where, $\dot{P}_n(t)$ it the generalised coordinate at some time instant t , and $\dot{P}_{n,max}$ is a constant equal to the maximum steady state generalised coordinate when the link is excited at its natural frequency.

The applied voltage frequency (Ω_v) is equal to the base excitation frequency (Ω_x), and the forcing term that is a result of the voltage applied to the actuators is negative to counteract the force due to the base excitation. The transverse displacement of the closed loop system may then be found using the relation shown in Equation 3.15 repeated here as Equation 4.4.

$$w(y, t) = \sum_{n=1}^N P_n(t) \phi_n(y) \quad (4.4)$$

4.2.2 Control system B

The second control system observed in this research employs proportional control utilising the voltage output from two PZT sensors as an input. The control system applies a control gain (K_p) to the voltage input to produce a voltage magnitude to be applied to the PZT actuators. The closed loop system is illustrated in Figure 4.2.1, where the plant represents the application of the the voltage to the PZT actuators, and the reference signal (REF) was set to zero.

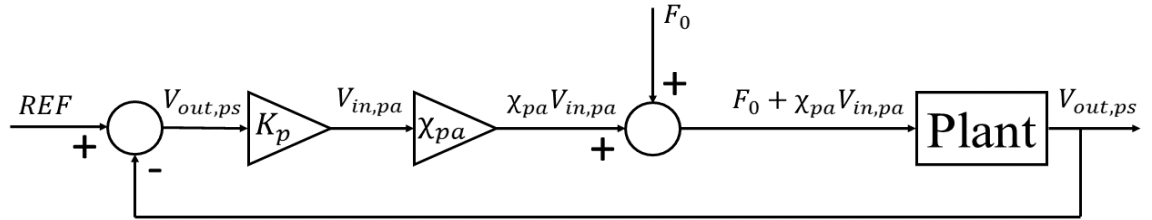


Figure 4.2.1: Illustration of the proportional control system.

To develop an analytical model of the control system it is necessary to observe and manipulate the governing equations of the link structure and the voltage output from the PZT sensors. Equation 3.65 details the response of the system in terms of

the generalised coordinate (P_0) and the amplitude of the base excitation force (F_0), repeated here as Equation 4.5.

$$(-\omega^2 + 2\zeta_n\omega_n j\omega + \omega_n^2) P_0 - \chi_{ps} V_{in,ps} - \chi_{pa} V_{in,pa} = F_0 \quad (4.5)$$

The voltage output from the PZT sensors in terms of the generalised coordinate (P_0) may be found using Equation 3.70, repeated here as Equation 4.6.

$$V_{out,ps} = \frac{-j\omega\kappa_{nps}}{j\omega C_{ps} + \frac{1}{2R_{lps}}} P_0 \quad (4.6)$$

Section 3.6.3 includes the manipulation of Equation 4.6, to isolate the real and imaginary terms, to yield:

$$V_{out,ps} = [-RE(\omega) - IMG(\omega)j] P_0 \quad (4.7)$$

where $RE(\omega)$ and $IMG(\omega)$ are frequency dependent stiffness and damping coefficients, respectively, that are defined as:

$$RE(\omega) = \frac{\omega^2\kappa_{nps}C_{ps}}{\omega^2C_{ps}^2 + \left(\frac{1}{2R_{lps}}\right)^2} \quad (4.8)$$

$$IMG(\omega) = \frac{\omega\kappa_{nps}\frac{1}{2R_{lps}}}{\omega^2C_{ps}^2 + \left(\frac{1}{2R_{lps}}\right)^2} j \quad (4.9)$$

The voltage to be applied to the PZT actuators is calculated using:

$$V_{in,pa} = K_p V_{out,ps} \quad (4.10)$$

which may be employed alongside the coefficients of the voltage output from the PZT sensors ($V_{out,ps}$) $RE(\omega)$ and $IMG(\omega)$, and substituted into Equation 4.5 to yield Equation 4.11. It should be noted that as no voltage is applied to the sensors they may be omitted from Equation 4.11, and the real and imaginary parts of the voltage output from the PZT sensors may be grouped with the real and imaginary parts of Equation 4.5.

$$\frac{P_0}{F_0} = \frac{1}{-\omega^2 + [2\zeta_n\omega_n\omega + \chi_{pa}K_p IMG(\omega)] j + \omega_n^2 + \chi_{pa}K_p RE(\omega)} \quad (4.11)$$

This equation may be manipulated through the observation of Newton's second law to yield the response in terms of the relative and base displacements to yield:

$$\frac{w_{rel}(y, t)}{w_b(y, t)} = \frac{-\omega^2 \phi_n(y_{LDS}) m \gamma_n}{-\omega^2 + [2\zeta_n \omega_n \omega + \chi_{pa} K_p IMG(\omega)] j + \omega_n^2 + \chi_{pa} K_p RE(\omega)} \quad (4.12)$$

where, $(w_{rel}(y, t))$ is the transverse motion of the link, where $y = y_{LDS}$ in this case, yielding the transverse motion at the position of the LDS along the length of the link. The base displacement of the link is denoted by $w_b(y, t)$.

Employing the relationship between the generalised coordinate (P_0) and the voltage output from the PZT sensors ($V_{out,ps}$) outlined in Equation 4.7, Equation 4.12 may be manipulated further to yield:

$$\frac{V_{out,ps}}{w_b(y, t)} = \frac{-\omega^2 \phi_n(y_{LDS}) m [-RE(\omega) - IMG(\omega)j]}{-\omega^2 + [2\zeta_n \omega_n \omega + \chi_{pa} K_p IMG(\omega)] j + \omega_n^2 + \chi_{pa} K_p RE(\omega)} \quad (4.13)$$

Both coefficients ($RE(\omega)$ and $IMG(\omega)$) are positive, which will lead to an increase of both stiffness and damping as the proportional gain K_p is increased. The larger the real part the higher the natural frequency of the response will be as the stiffness of the structure will have been increased. A reduction in the magnitude of the response can be attributed to the increase of the imaginary part as this increases damping.

4.3 Components

For an AVC system three main components are required, one with the capacity to measure the vibrations experienced by the link (sensors), another to counteract the vibrations through the application of force (actuators) and finally a component to read the data from the sensors and utilise the actuators accordingly (a computer). All components are to be chosen with the outlined parameters of the system preferably being lightweight and inexpensive, so as to render the overall system suitable for multiple applications. The justification for each choice of component and their specifications are outlined in this section.

4.3.1 Single board computer

A single board computer (SBC), contains components of a computer mounted upon a single circuit board including, but not limited to, a microprocessor, memory and storage. The advantages of utilising a SBC in lieu of alternate data acquisition and control systems revolves around their size, mass and price. Whereas the main disadvantage is their processing power, however, for the intended application the processing capacity of the majority of SBCs is suitable. Tables 4.3.1 and 4.3.2 compare the specifications of most suitable SBCs for the intended application.

Specification	Raspberry Pi 3	Raspberry Pi Zero W	BeagleBone Black
Equivalent Price	0.59	0.17	1
Weight (g)	42	9	39.68
Dimensions (mm)	85x56	66x35	86.4x53.3
CPU	64-bit quad-core ARM Cortex-A53	Single-core Broadcom	Octavo System ODS3358 ARM Cortex-A8
RAM	1GB (LPDDR2 SDRAM)	512MB (SDRAM)	512MB (DDR3)
Clock Speed	1.4GHz	1GHz	1GHz
GPIO Pins	40	40	92
USB Ports	4	0	1
Wifi	Yes	Yes	Yes
Bluetooth	Yes	Yes	Yes
HDMI	Yes	Yes	Yes (Type D)
I ² C Connection	Yes	Yes	Yes
SPI Connection	Yes	Yes	Yes
Memory Expansion	Yes	Yes	Yes
Input Power	5V 2A	5V 2A	5V 2A
Power Connection	Micro USB	Micro USB	AC/DC Adapter or USB

Table 4.3.1: SBC specification comparison.

Specification	Arduino Mega 2560	Rock 64 Media Board	Odroid C2
Equivalent Price	0.52	0.33-0.59	0.86
Weight (g)	37	49.9	40
Dimensions (mm)	101.6x53.3	85x56	85x56
CPU	ATmega2560	RK3328 Quad-core ARM Cortex A53 64-bit	Amlogic S905 SoC 4xARM Cortex-A53 64-bit ARM
RAM	256KB (Flash ROM)	1GB/2GB/4GB (DDR3L)	2GB (DDR3)
Clock Speed	16MHz	1.5GHz	1.5GHz
GPIO Pins	70	40	40
USB Ports	0	3	4
Wifi	No	No	No
Bluetooth	No	No	No
HDMI	No	Yes	Yes
I ² C Connection	Yes	Yes	Yes
SPI Connection	Yes	Yes	No
Memory Expansion	No	No	Yes
Input Power	7-12V 2A	5V 3A	5V 2A
Power Connection	AC/DC Adapter	AC/DC Adapter	AC/DC Adapter

Table 4.3.2: SBC specification comparison (continued).

The first six specifications outlined in Tables 4.3.1 and 4.3.2 are the more pertinent. In this context the clock speed is held as the most desirable aspect, with the larger the value meaning the faster computation and communication between components of the system connected to the SBC. From the comparison it can be seen that three SBCs have considerably lower clock speeds than the others (Raspberry Pi Zero W, Beaglebone Black and the Arduino Mega 2560), as a result they were not considered further. A Random Access Memory (RAM) of 1 GB was deemed appropriate for the application, as the SBC will only be required to perform one task at any one time. Although it is recognised that a larger value of RAM is generally more desirable; in this scenario other specifications are held in higher regard. In keeping with the general notion of the research that mass should be kept as low as possible, hence this is the next consideration. The Rock 64 Media board has a greater mass in comparison to both the Raspberry Pi 3 and the Odroid C2, and neither it or the Odroid C2 have the capacity for WiFi connections without the addition of an external module. This addition would increase both the mass and the dimensions of the SBC, making the Raspberry Pi 3 more favourable. The inclusion of WiFi connectivity in the SBC is especially desirable in this scenario so that it is possible to control from a safe distance when the control system is utilised with a robot manipulator.

The equivalent price was obtained through the comparison of the price of each SBC with that of the most expensive, including the price in this manner avoids the alteration of exchange rates and any economic inflation. This specification makes the Odroid C2 less favourable over both the Rock 64 Media Board (assuming the 4 GB RAM option) and the Raspberry Pi 3. However, again the Rock 64 Media Board would require an external module to use WiFi which would increase the overall cost, again revealing the Raspberry Pi 3 to be the most favourable. At this point the final comparison will exclude the Odroid C2 for the multiple aforementioned reasons. Turning the attention to the SBCs capacity for expandable memory, the Raspberry Pi 3's storage capacity can be expanded to 32 GB, whereas the memory of the Rock 64 Media Board cannot be expanded at all. Hence, overall the Raspberry Pi 3 B+ (RPi) has been chosen for use in the control system. A board diagram and the GPIO pinout diagram of the RPi can be seen in Figure 4.3.1.

From the pinout diagram in Figure 4.3.1 it can be seen that there are two numbering systems of the GPIO pins, and it is necessary to specify in any code which of these systems is used. The 'board' numbering system corresponds to the pin number as labelled on the board, in the pinout diagram these are the numbers immediately next to the pins. Whereas the the broadcom SOC channel (BCM) numbers are those which proceed the GPIO descriptions in the pinout diagram.

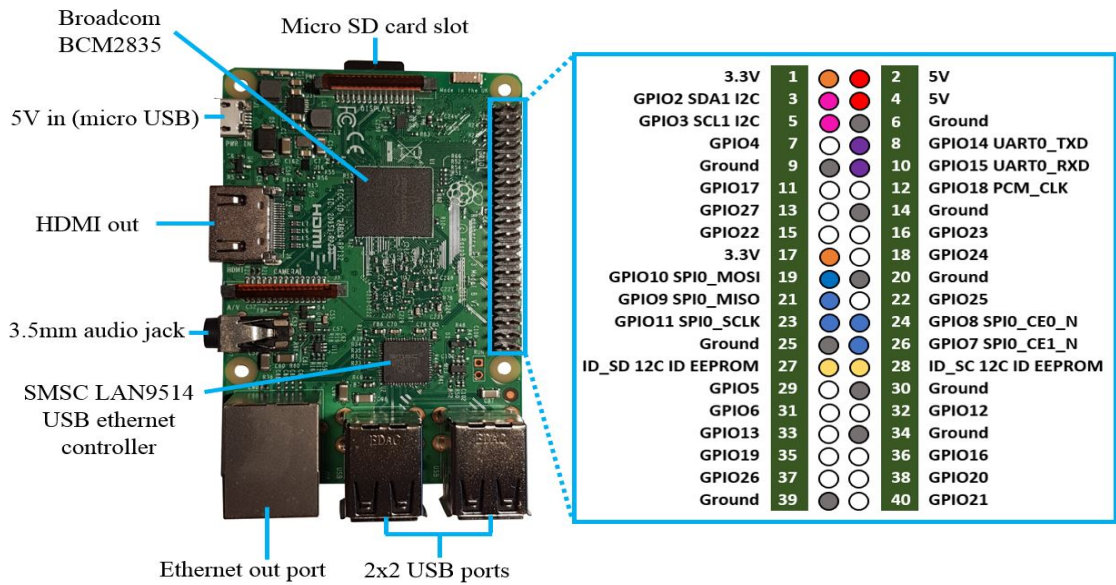


Figure 4.3.1: Board diagram of the Raspberry Pi 3 and the corresponding GPIO pinout diagram.

4.3.2 Actuators

The actuators for use in the system need to be lightweight and mountable on the link so as to have as little effect on the mass and functionality of the link. The most viable option is therefore PZT elements (see Section 3.2), due to their potential for easy incorporation to the link structure and their high force to mass ratio. The type of PZT element was based on the dimensions of the link, with the largest possible surface area being the most favourable as it is directly proportional to the force produced. This lends to the choice of piezoelectric patch being M-5628-P2 [149]. Table 4.3.3 below contains the specifications of the selected PZT patch [150].

It should be noted that under the manufacturer's recommendation the piezoelectric patches are mounted on the link using two part epoxy resin. The wires used to connect the actuators to the high voltage source were especially selected for the requirements of this connection. Whilst having a greater thickness than other wires used in the control system, these wires were capable of safely carrying voltages up to 500 V, hence the slightly greater overall mass due to this choice may be justified. These wires were soldered onto the PZT actuators, taking care to avoid any length of exposed wire that may come into contact with the link structure which would pose a risk. The voltage connections can be seen in an image of the PZT actuator shown in Figure 4.3.2.

Specification	Value
Active Length (mm)	56
Active Width (mm)	28
Overall Length (mm)	66
Overall Width (mm)	31
Overall Thickness (mm)	0.3
Capacitance (nF)	113.06
Free Strain (ppm)	-820
Blocking Force (N)	-205
Young's Modulus (GPa)	30.336
Effective Piezoelectric stress constant, e_{31}	-11.6
Operating voltage (V)	-60 to 360

Table 4.3.3: Specifications of the selected piezoelectric actuator.



Figure 4.3.2: Image of the PZT actuator employed in this research.

4.3.3 High voltage drivers

The necessity for the inclusion of high voltage drivers (HVDs) arises from the use of the Raspberry Pi 3. The output from the SBC's general purpose input/output (GPIO) pins has a maximum voltage of 3.3 V. This is a lot smaller than the operating voltage of the PZT elements, and thus to control the piezoelectric patches HVDs are required. The DRV2700EVM-HV500 is a module capable of amplifying a 5 V input up to 500 V, its typical usage is to power PZT elements making it ideal for use in this instance [151]. Figure 4.3.3 is a diagram of the DRV2700EVM-HV500 board which highlights all of the connections and signal routes [152].

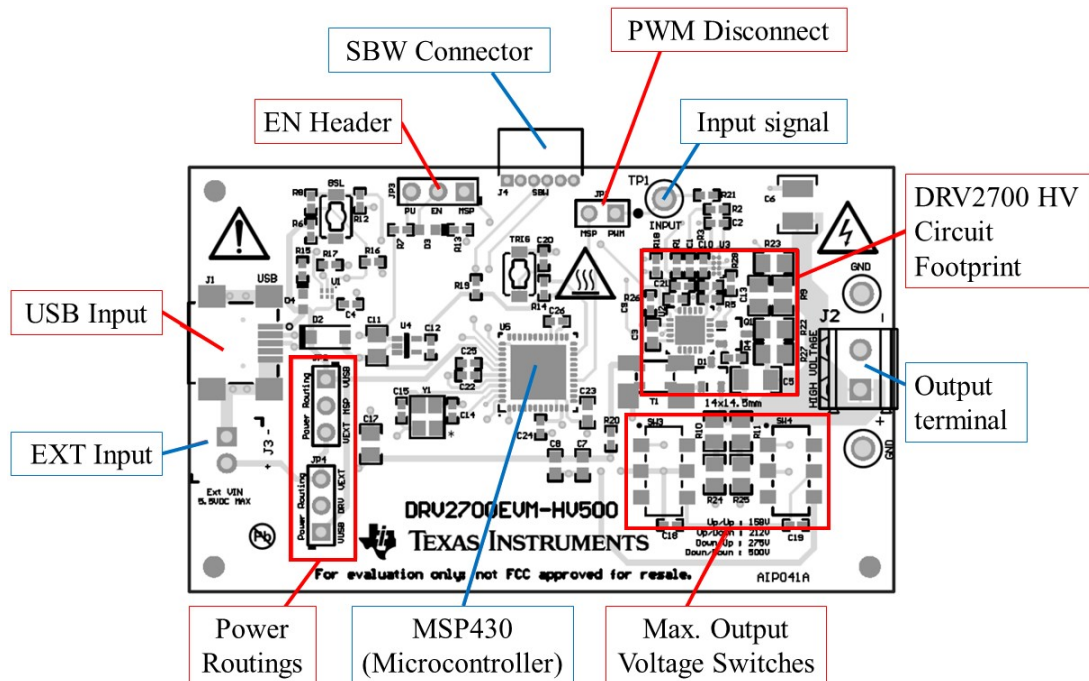


Figure 4.3.3: DRV2700EVM-HV500 board diagram.

The HVD can be powered using a micro USB B connection (USB Input) or by an alternate external input connected to the pins labelled ‘EXT Input’. Where the ‘Power Routings’ can be used to select which power source the HVD should use by moving the jumpers. The signal used to alter the output voltage can be fed to the board via the ‘USB Input’ (can be simultaneously powered with the same cable) or the ‘Input Signal’ pin. A computer can be used in conjunction with the EVM Control Software (GUI) when using the ‘USB Input’ option to control the output voltage. Removing the jumper from the JP1 pin on the board and connecting the ‘EN Header’ to the ‘PU’ option allows for the board to be controlled by an analog input instead. The maximum output voltage from the ‘Output Terminal’ is altered using the ‘Max. Output Voltage Switches’ (SW3 and SW4), where the maximum voltages and the corresponding switch positions are outlined in Table 4.3.4.

Maximum Voltage (V)	SW3	SW4
500	Down	Down
275	Down	Up
212	Up	Down
158	Up	Up

Table 4.3.4: HVD board switch positions for each maximum voltage selection.

As the maximum operating voltage of the PZT patches is 360 V the highest maximum output voltage should be selected, 500 V. However, applying a voltage greater than the maximum to the PZT patches will cause irreparable damage. Thus, it is important that the controller within the system maintains the output voltage of the HVDs to below 360 V.

4.3.4 Inertial measurement units

The choice of sensors is dictated by the following factors: the connection between them and the Raspberry Pi 3, their mass and their cost. The SBC has the capability of connecting a sensor directly via an inter-integrated circuit (I²C) or a serial peripheral interface (SPI) connection. As the Raspberry Pi 3 is not capable of directly reading an analog signal an analog to digital converter (ADC) is required. The disadvantages of using an ADC are that it adds to the mass of the system, and that the signals received by the Raspberry Pi 3 are more often than not affected by noise. This noise can be overcome, or at least reduced to an acceptable level, through the use of bandwidth filtration or through an ADC with improved specifications. The former of these options is computationally expensive and the latter will affect the overall mass and cost of the system negatively. For these reasons the use of an ADC with the Raspberry Pi 3 was initially considered unfavourable compared to alternate solutions.

Of the two remaining options for communication with the SBC the I²C protocol was favoured over the potential alternate; the SPI connection. This preference was heavily weighted on the number of wires each connection option required, with the I²C protocol requiring four wired connections, and the SPI connection requiring six. The mass of the wired connections is particularly important for the system as not only does their mass affect the overall weight of the system, but the functionality of the link as well. Whilst the addition of a sensor mounted at the free end of the link is unavoidable, the lower the overall mass of this sensor and subsequent connections the less impact on functionality will be observed. Although, it should be noted that the SPI connection would potentially allow for faster communication, the ‘fast-mode’ of

the I²C protocol allows for a clock speed of 400 kHz (this is limited by the capabilities of both the Raspberry Pi 3 and the sensors to 128 Hz), and was deemed appropriate for the intended use of the sensors. However, assuming that the sampling rate of the control system remains at 128 Hz, this limits the excitation frequency to 64 Hz [147]. Subsequently this imposes limits on the structure in that its natural frequency must be below 64 Hz for the mode being considered. Therefore, only sensors which have the potential to utilise the I²C protocol will be considered.

Whilst the presented control theory in Section 4.2.1 only utilises a gyroscope due to the employment of only proportional gain, this was with concern to the processing capacity of the SBC. Assuming a good level of performance of the control system the next stage would be to improve upon the control scheme used. A potential development to the original control scheme would be to include derivative and integral gains to create a proportional integral derivative (PID) controller. As this control theory would require both the integral and derivative of the error (as well as the error itself) with respect to time it would be more computationally effective to measure these required values. With the error being the velocity difference between the free end of the link and the base of the link, measuring both acceleration and displacement would acquire both the derivative and integral, respectively. Another consideration in the selection of sensors is that they need to be able to measure the required data regardless of the location or orientation of the link. When attached to the robot and envisioned as part of the existing structure the link could have numerous positions and rotations with respect to the world frame of the robot manipulator. Therefore any sensors which require the use of external frames for measurement, such as laser displacement sensors, will not be considered. These requirements effectively dictate that the sensors should be mountable on the link whilst being able to measure displacement, velocity and acceleration.

Inertial measurement units (IMUs) are often used in remote controlled vehicles for their ability to measure displacement, velocity and acceleration through some combination of a magnetometer, a gyroscope and an accelerometer. However, measuring displacement with a magnetometer poses another issue (as aforementioned): the metal-based (ferromagnetic) structure of the system negatively affects the data to a considerable extent. Thus, measuring the angular displacement with such a mountable device can be considered impractical. Leaving the only solution to obtain the displacement as the integration of the velocity, which is unfavourable. However, to attenuate an unwanted vibration any signal may be driven to zero, for example the acceleration or the angular velocity. In a scenario wherein there is less or no interference of the magnetometer readings this sensor may be utilised, hence the persistence of seeking the most suitable IMU. Table 4.3.5 contains a comparison of potential IMUs for use within the system.

Specification	MPU-9250	LSM9DS0	BNO055
Relative cost	0.25	0.97	1
Dimensions (mm)	25x15x6	33x20x2	20x27x4
Mass (g)	2.72	2.3	3
Accelerometer range (\pm g)	2, 4, 8, 16	2, 4, 6, 8, 16	2, 4, 8, 16
Accelerometer Sensitivities (LSB/g)	16384, 8192, 4096, 2048	16384, 8192, 5461, 4096, 2048	4095, 2047, 1023, 511
Accelerometer bits	16	16	14
Gyroscope range (\pm deg /s)	250, 500, 1000, 2000	245, 500, 2000	125, 250, 500, 1000, 2000
Gyroscope sensitivities (LSB/(deg /s))	131, 65.5, 32.8, 16.4	133, 65.5, 16.4	262, 131, 65.5, 32.8, 16.4
Gyroscope bits	16	16	16
No. of I ² C addresses	2	4	2
Supply voltage (V)	3-5	2.4-3.6	2.4-3.6

Table 4.3.5: Comparison between potential IMUs based upon their specifications

It should be noted that there are limited options of IMUs suitable for use based on both the chosen SBC and application. Three potential IMUs and their specifications have been outlined in Table 4.3.5. As can be seen their specifications are fairly similar, with the notable discrepancy being the cost. As with the comparison of potential SBCs (Tables 4.3.1 and 4.3.2), the relative costs have been calculated based on the most expensive option so as to avoid fluctuating exchange rates and economic inflation. The BNO055 module is the most expensive, has the largest mass and the accelerometer is 14-bit as opposed to the other IMUs' 16-bit accelerometers. For these reasons only the two remaining options (the MPU-9250 and the LSM9DS0) were considered further. The poignant differences between these remaining options include the cost, the dimensions and the weight. The other listed specifications are very similar and therefore offer little difference in terms of functionality (range, sensitivity and number of bits). Both supply voltages render the IMUs operable with the selected SBC, and the required number of I²C addresses for the application is two meaning in these terms either option is suitable. Returning to the first three listed specifications the MPU-9250 is smaller in terms of length and width, and is more cost effective in comparison to LSM9DS0, the slightly larger mass can be overlooked when considering these favourable specifications. Figure 4.3.4 is an image of the selected IMU module, the MPU-9250, and its pinouts.

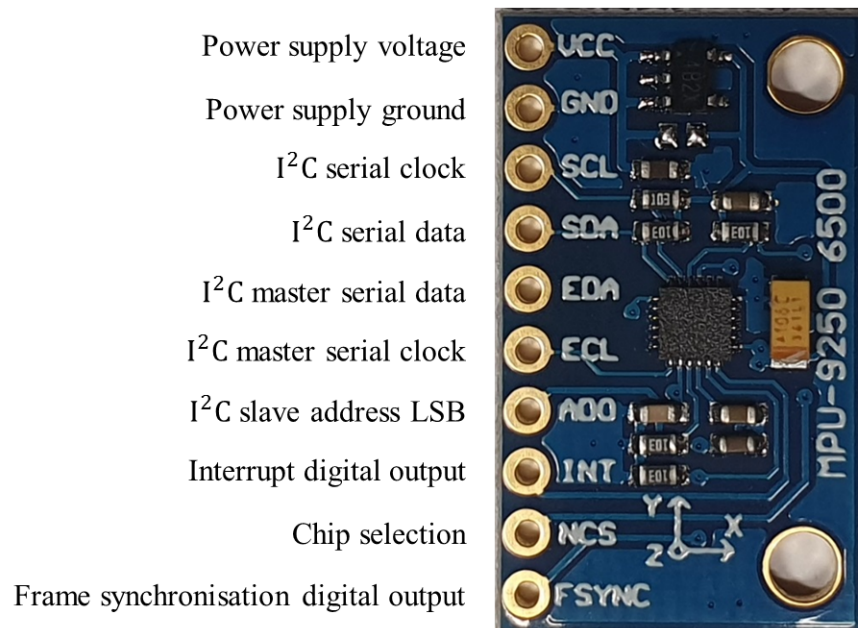


Figure 4.3.4: An image of the MPU9250 and its pinouts.

4.3.5 Analog to digital converter and piezoelectric sensors

The option to use piezoelectric sensors were originally deemed unfavourable due to the requirement of an analog to digital converter (ADC). However, for the reasons outlined in Section 3.5.1 it was necessary to incorporate this sensing combination in lieu of the IMUs. A successive approximation (SAR) ADC is one of the most commonly used types within a variety of applications.

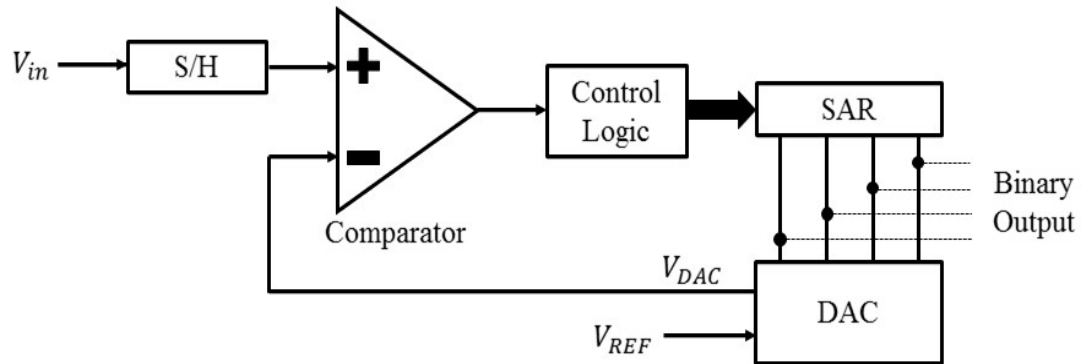


Figure 4.3.5: Illustration of SAR ADC operation.

Figure 4.3.5 outlines the operation of a typical SAR ADC (simplified to a four bit ADC), where, ‘S/H’ stands for sample/hold which physically would include a capacitor to ‘hold on’ to the voltage input, V_{in} . This is to prevent the voltage changing in magnitude before a final binary output is achieved. The comparator evaluates whether V_{in} is greater than the output from the digital to analog converter (DAC). The ‘control logic’ and SAR blocks alter the four bit binary code depending on the comparison between V_{in} and V_{DAC} . The reference voltage V_{REF} is a constant input and V_{in} should be in the range 0 V to V_{REF} inclusive. It should be noted that V_{REF} in the majority of ADC models has a limit, thus so does the input voltage. The system operates from the most significant bit (MSB) (in this case the furthestmost left) to the least significant bit (furthermost right). So that for each sample reading for a four bit ADC the initial binary code is 1000. Assuming that V_{REF} is equal to 5 V, then this will mean V_{DAC} is equal to 2.5 V. This is the starting point for the logic tree example illustrated in Figure 4.3.6. The blocks in the figure show the binary code currently being tested and the equivalent voltage (rounded to three decimal places) assuming V_{REF} is equal to 5 V.

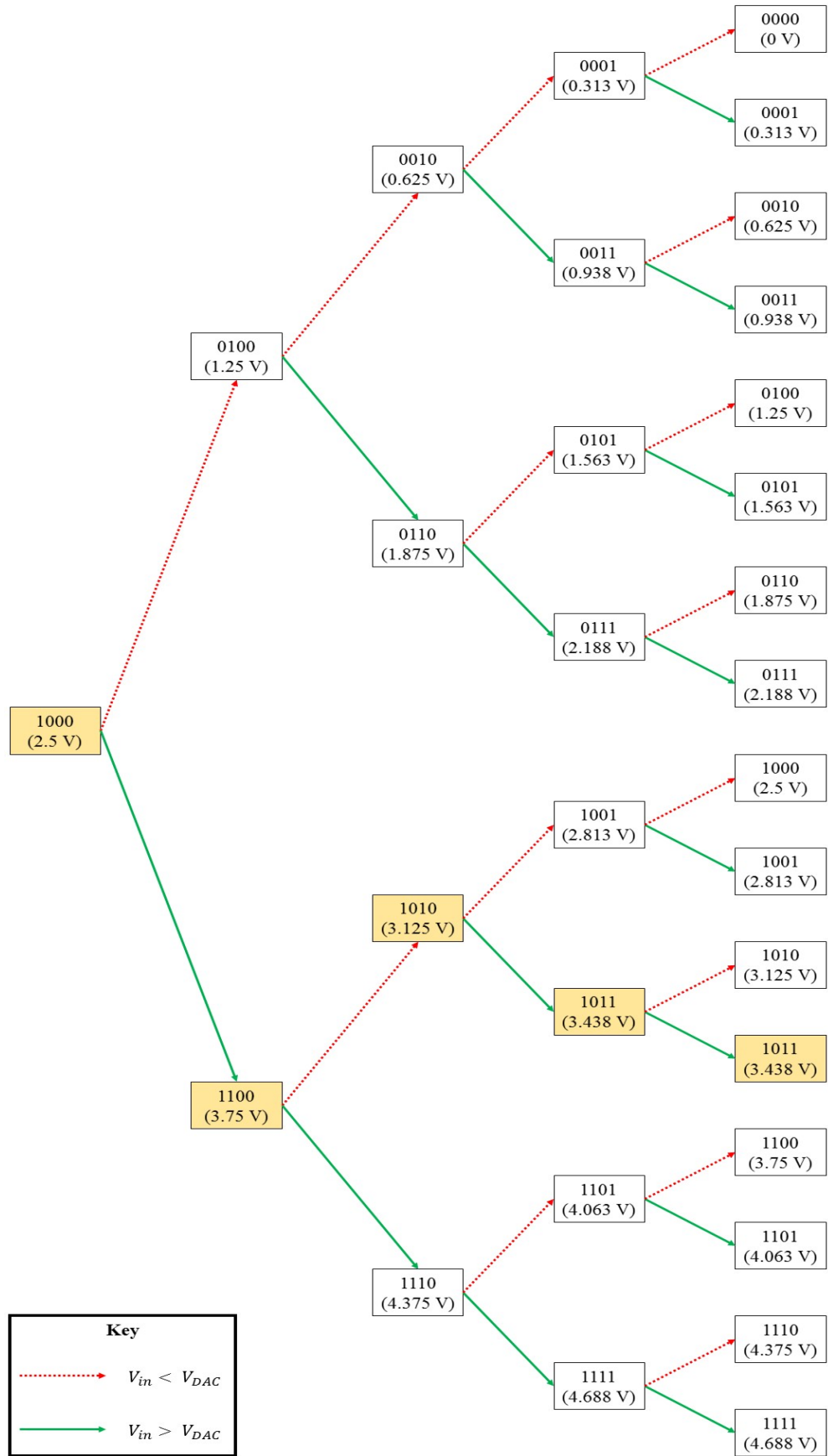


Figure 4.3.6: Illustration of SAR ADC logic.

If the initial value of V_{DAC} is less than V_{in} then the MSB is set high (equal to one), and the next bit is also set to one for the next test (i.e. the path follows the green solid line from the first block in Figure 4.3.6). If V_{DAC} is greater than V_{in} in the first comparison, then the MSB is set low and the next bit is set high, following the red dotted path. Assuming V_{in} is equal to 3.5 V then the logic path is that shown by the highlighted blocks with each iteration of testing setting a bit from the MSB to the LSB until a binary code of 1011 is reached. This yields a voltage of 3.438 V (percentage error is 1.8%), which is considered to be inaccurate, but is as close as a four bit ADC will allow. An ADC with larger number of bits will have a higher resolution, and therefore will offer a higher level of accuracy. There are ADCs available which sport a twenty bit resolution, but as the resolution increases, so does the cost.

Along with an ADC's resolution, its sampling rate is an important factor when deciding which is the most ideal model for an application. Different methods of communication between the ADC and the computer offer different sampling rates, and one method of communication can have different sampling rates depending on the ADC model. As previously mentioned it is essential to sample a signal at a rate at least twice as large as the frequency of the signal being sampled [147]. It should be noted that CSB was found to have an average sampling rate of 1.558 kHz, with the difference between the time between each sample varying insignificantly. This sample rate more than satisfies the requirement to be twice as large as the natural frequency of the link (3.59 Hz), and is a significant improvement on the sampling rate of CSB (128 Hz). A greater sampling rate will allow for structures of higher natural frequencies to be considered, and for structures of the first natural frequency of the same order as in this research is more likely to allow for investigations involving higher modes.

As with the other components it is important that the choice of ADC for the system has the highest level of functional specification at the lowest cost, dimensions and mass. The ADC must have at least two input channels (one for each of the piezoelectric sensors) with an input voltage range suitable for the output voltage of the PZT sensors and be able to communicate directly and readily with the RPi. The majority of low-cost ADCs have very similar specifications, and so the choice of this component was dictated by which was the most popular for similar applications and most readily available. The MCP3008 has been used in multiple research projects as previously discussed in the literature review. The specifications of the MCP3008 are outlined in Table 4.3.6, Figure 4.3.7 illustrates the pin functions of the device and Figure 4.3.8 shows its functional block diagram ([153]).

Specification	Value
Resolution (bits)	10
Sample rate (ksps)	200
Digital interface type	SPI
Output channels	8
Operating voltage (V)	2.7-5.5
Input voltage range (V)	0-5
Dimensions (mm)	19.05 x 6.35 x 3.3
Mass (g)	1.628

Table 4.3.6: MCP3008 specifications.

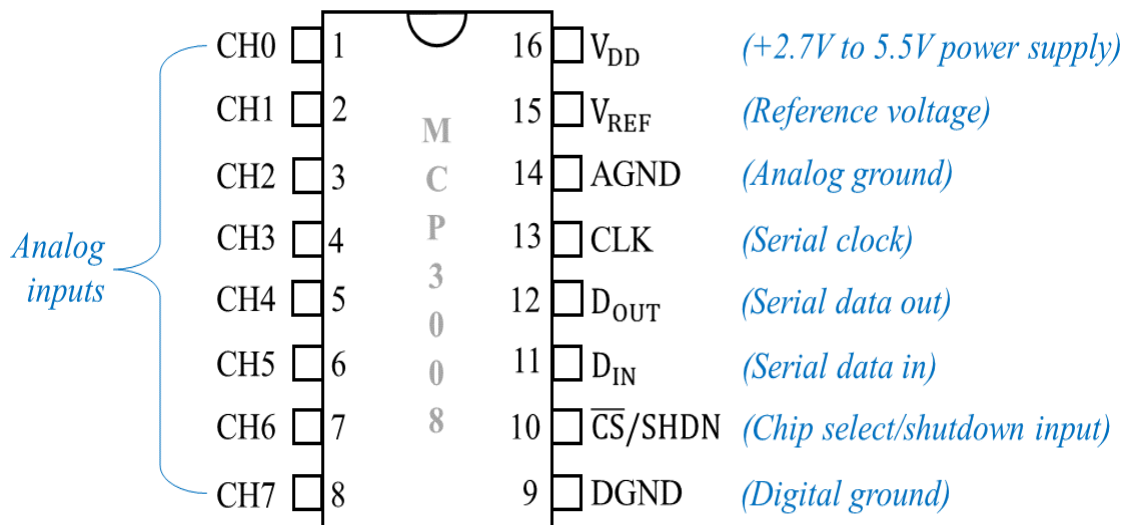


Figure 4.3.7: MCP3008 pin diagram.

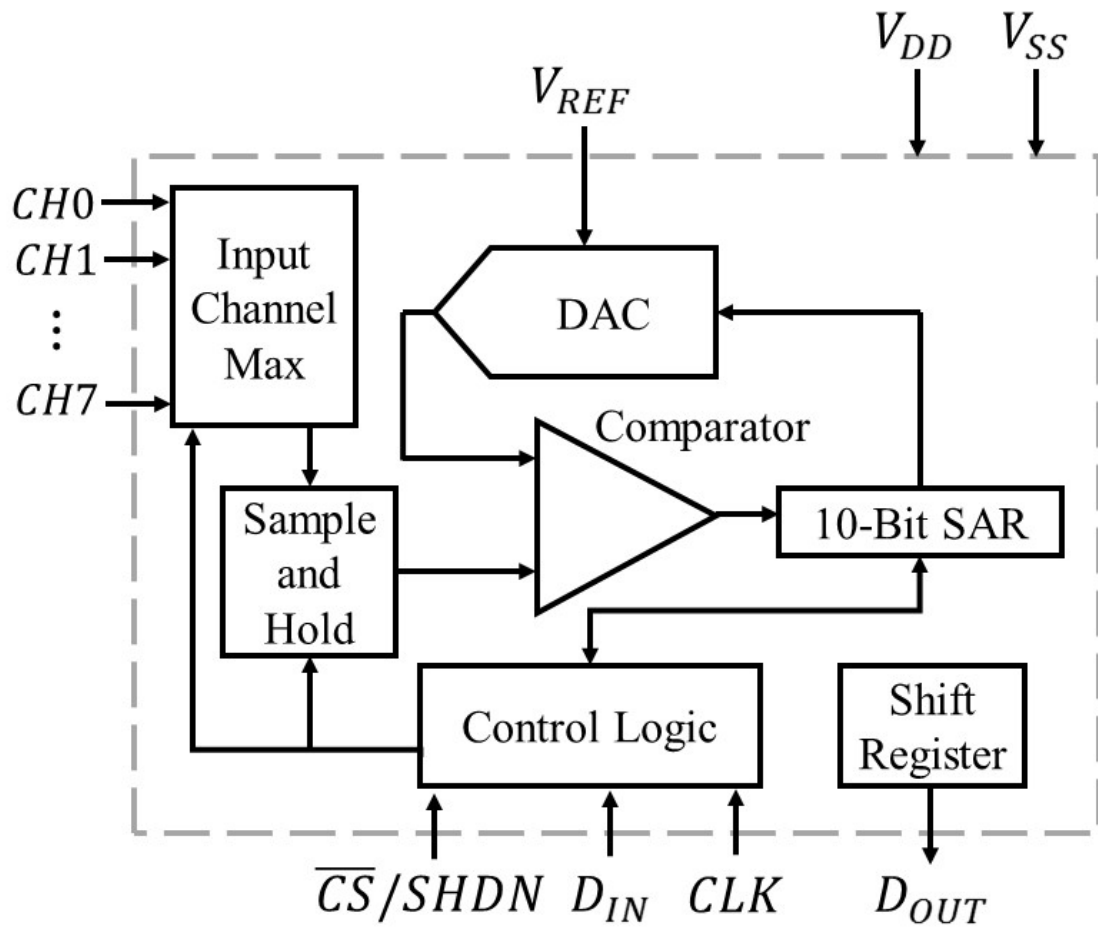


Figure 4.3.8: MCP3008 functional block diagram.

4.4 Integration of components

In this section the connections and interactions between components are shown and explained for both control system designs which utilise the Raspberry Pi 3B+ (RPI). Control system A utilises inertial measurement units (IMUs) to measure the velocity experienced at the base and free end of the link in order to calculate the magnitude of voltage to be applied to the piezoelectric actuators. Control system B employs piezoelectric sensors to obtain the voltage output due to the strain experienced on the link as an input to the control system. Both control systems use PZT patches as actuators requiring HVDs to amplify the voltage from the RPI to drive them. Firstly it is important to illustrate the wired connections between each component used within each control system. These illustrations of the wired connections will provide a better insight as to how the two systems are designed. Figure 4.4.1 illustrates the connections between the two IMU modules (MPU-9250), the two HVDs (DRV2700EVM-HV500) and the two piezoelectric patches (M5628-P2) to the Raspberry Pi outlining Control System A. Whereas Figure 4.4.2 contains the wired connections of Control System B where PZT sensors are used in lieu of the IMUs.

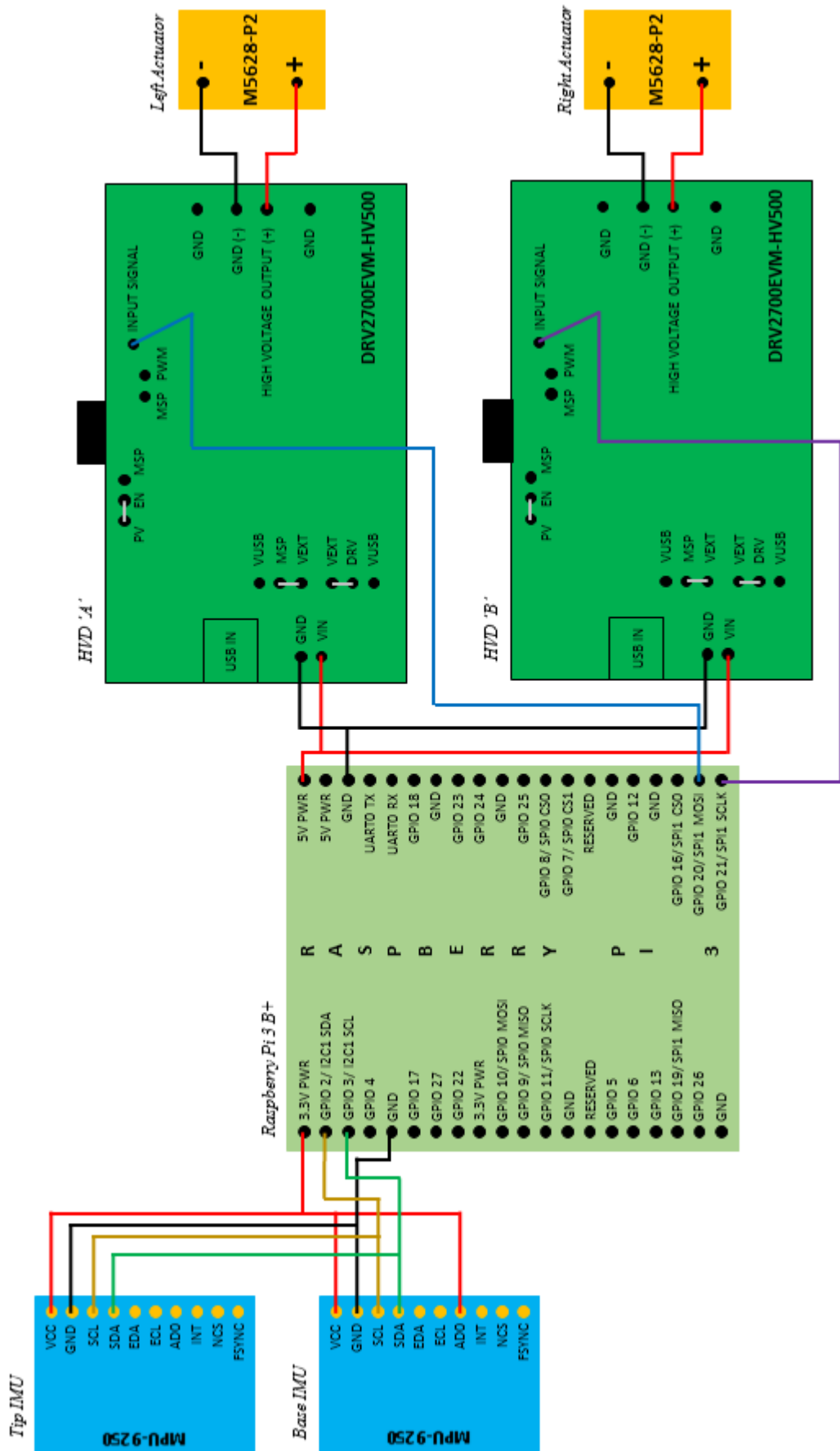


Figure 4.4.1: Visualisation of the physical connections within control system A.

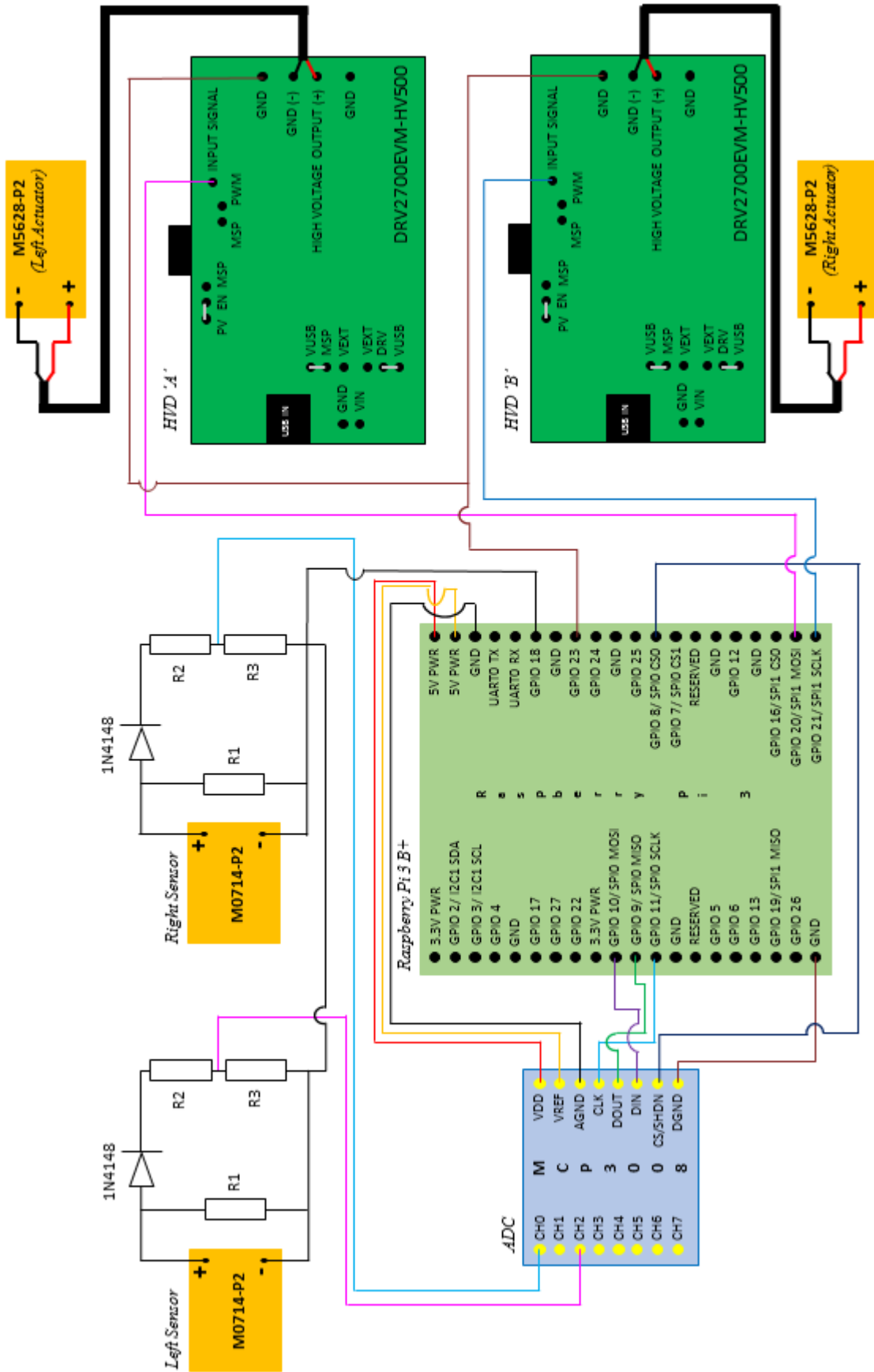


Figure 4.4.2: Visualisation of the physical connections within control system B.

4.4.1 Communication between Raspberry Pi 3 and IMUs

I²C protocol is the communication protocol between the RPi and the IMUs. This requires four (or five) wired connections as can be seen in Figure 4.4.1, where the VCC and GND connections provide power to the IMUs and the SCL and SDA are the clock and data connections, respectively. Communications sent along the data connection are split into two frames, with the first being the address and the second the data frame(s). In this case the two IMU modules have the option of two seven bit addresses, altered through the application of voltage to the AD0 pin. It should be noted that the gyroscope and accelerometer within an IMU will have the same address but the magnetometer does not. With the application of this voltage to said pin on one of the modules both IMUs can be connected to the same I²C bus of the RPi. For the purpose of reducing the influence of the sensor mass on the link during tests, the IMU without the additional wire was positioned on the tip of the link, and the other on the moving part of the structure providing the base excitation.

The selected IMU's address which starts with the most significant bit (MSB) combined with a read/write bit in the least significant bit (LSB) and thus totalling eight bits becomes the address frame. This is sent from the master (in this case the Raspberry Pi) identifying which slave (IMU module) should send/receive data, and the second frame will contain data required by either party [154]. This is sent after the start condition where the master leaves the SCL line high (binary 1) and brings the SDA line low (binary 0). After the address and data frames are sent, the end condition is emitted from the master where the SCL line is brought high before the SCL line follows. Figure Figure 4.4.3 below illustrates the communication between the master and the slave, noting the start/end conditions, the read/write bit, the acknowledgement bits and the two separate frames.

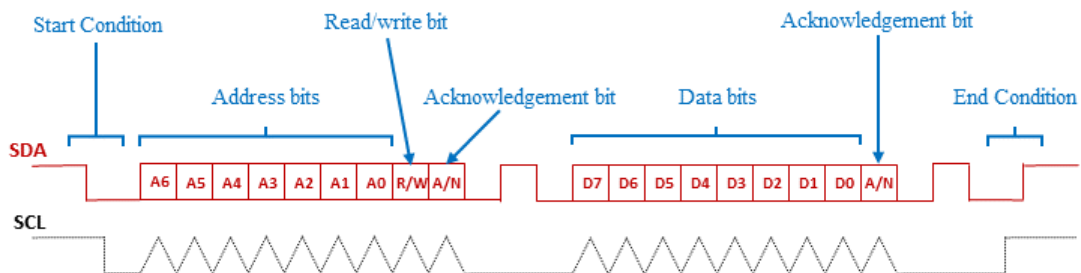


Figure 4.4.3: Visualisation of I²C protocol.

The MSB and LSB of the address frame are located in the bits labelled A6 and R/W, respectively. Whereas within the data frame the MSB and LSB are found in the bits D7 and D0, respectively. The acknowledgement bits are an opportunity for the slave device to return to the master whether or not it has received the data (either the

address or other data). The slave device has control over the SDA line after the eighth clock impulse, and if the slave does not pull the SDA line low before the ninth impulse then the master is able to conclude that either the slave did not receive the data or did not know how to interpret it. In the event of this it is the master device which decides how to proceed.

If certain settings are required of the slave, then the master will need to write to the slave informing the slave of which register to select and what to write to said register. Where registers can be thought of as ‘sub-addresses’ under the slave device’s main address. The following are the steps of the I²C protocol for writing to a slave.

1. Master sends the slave the start sequence.
2. The required I²C address combined with the read/write bit (set low) is sent along the SDA line. Informing the slave that it should communicate with the master and that it should expect to receive further commands.
3. The master sends the slave the address of the register to which it requires to write.
4. The data byte is sent from the master to the slave.
5. The stop sequence is sent from the master to the slave.

Table 4.4.1 below lists the registers of the sensors within the IMUs which are relevant to the settings which required alteration from their default, and the bits which needed to be written to these registers [155]. The symbol \ll denotes that the bits are to be shifted to the left, i.e. 00000001 \ll 3 becomes 00001000.

Register	Setting	Data (Hex)
Gyroscope delay time (0x1A)	Delay time (<i>ms</i>)	Data
	0.97	0x00
	2.9	0x01
	3.9	0x02
	5.9	0x03
	9.9	0x04
	17.85	0x05
	33.48	0x06
Gyroscope range (0x1B)	Scale selection (<i>deg/s</i>)	Data
	250	0x00
	500	0x01
	1000	0x02
	2000	0x03
Accelerometer range (0x1C)	Scale selection ($\pm g$)	Data ($\ll 3$)
	2	0x00
	4	0x01
	8	0x02
	16	0x03
Accelerometer delay time (0x1D)	Delay time (<i>ms</i>)	Data
	1.88	0x00
	1.88	0x01
	2.88	0x02
	4.88	0x03
	8.87	0x04
	16.83	0x05
	32.48	0x06
1.38	0x07	

Table 4.4.1: List of writing registers associated with the IMUs' sensors.

The address of the accelerometer and gyroscope without the AD0 pin set to high is 0x68, and with the pin set to high their address is 0x69. Due to the inability to alter and thus differentiate between the two magnetometers within the IMUs is another reason as to why they were not included in any experiments. Again, the other factor which rendered the use of these sensors mute revolves around the method of data collection; the magnetometers sense magnetic north. As the majority of the structures used within this research are metal a great level of interference is observed, rendering their measurements unusable.

Once the required settings are altered, the communication between the master and slave is able to switch to the reading of the data from the slave. To read the data from the slaves the following steps of the I²C protocol are used.

1. Master sends the start sequence along the SDA line.
2. The required I²C address combined with the read/write bit (set low) is sent along the SDA line.
3. The master sends the slave the address of the register from which it requires to read.
4. The start sequence is repeated along the SDA line from the master.
5. The address of the slave is then also repeated, except the read/write bit is set to high.
6. A block operation is sent (optional).
7. The slave sends the data byte along the SDA line for the master to read.
8. The stop sequence is sent.

The sixth step in the stages above is optional and is used to denote the length of the block operation, where the data bytes are sent from the slave to the master in blocks. This is a more efficient and convenient way of receiving the required data in terms of both time and number of commands. As an example: one command within the code will retrieve the six bytes of data from the slave (two data bytes for each axis). The registers from which these data bytes are obtained are listed in Table 4.4.2 below [155].

Register	Function
0x3B	High byte of accelerometer X axis data
0x3C	Low byte of accelerometer X axis data
0x3D	High byte of accelerometer Y axis data
0x3E	Low byte of accelerometer Y axis data
0x3F	High byte of accelerometer Z axis data
0x40	Low byte of accelerometer Z axis data
0x43	High byte of gyroscope X axis data
0x44	Low byte of gyroscope X axis data
0x45	High byte of gyroscope Y axis data
0x46	Low byte of gyroscope Y axis data
0x47	High byte of gyroscope Z axis data
0x48	Low byte of gyroscope Z axis data

Table 4.4.2: List of reading registers associated with the IMUs' sensors.

The two 8-bit sets of data for each axis are to be combined to one 16-bit byte of data which represents the reading from the slave. This is performed by shifting the high byte of data eight bits to the left, and using the 'bitwise or' operator to combine the two sets. An example of this method using arbitrarily chosen sets of data is included in Figure 4.4.4 below.

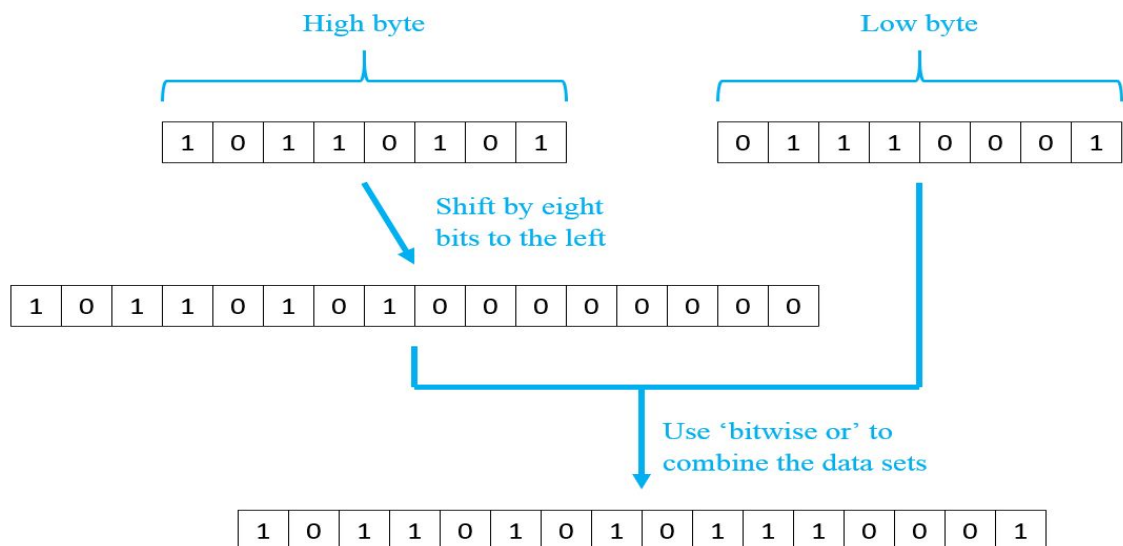


Figure 4.4.4: Visualisation of data manipulation.

To determine whether the new 16-bit set of data is positive or negative a 'check' is applied to the data to determine whether the MSB (in this case the furthestmost left

bit) is 0 or 1. A set of data where the MSB equates to 0 then the number is positive, and the number is negative if the MSB is 1. An ‘if’ statement when using bitwise operators will apply the proceeding command when the test within the ‘if’ statement does not equate to zero. Thus, the test required in this case is to utilise the ‘bitwise and’ (&) operator to determine whether the MSB is 1 or zero. If it is 1 then that bit is effectively removed and the result is designated as negative. A visualisation of this concept is shown in Figure 4.4.5.

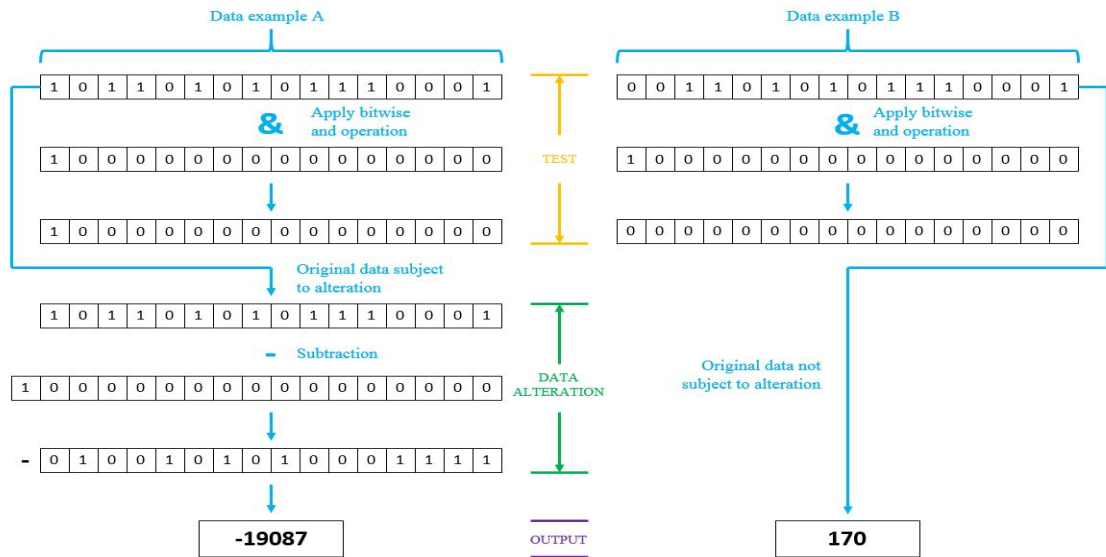


Figure 4.4.5: Visualisation of data check and manipulation.

With the data being identified as either positive or negative a sensitivity factor can be applied to obtain the result in the required units. The factors to be used can be found in Tables 4.4.3 and 4.4.4 below [155].

Scale selection <i>(deg/s)</i>	Sensitivity factor (LSB/(deg/s))
250	131
500	65.5
1000	32.8
2000	16.4

Table 4.4.3: List of sensitivity factors associated with the gyroscope.

Scale selection <i>(g)</i>	Sensitivity factor (LSB/(g))
2	16384
4	8192
8	4096
16	2048

Table 4.4.4: List of sensitivity factors associated with the accelerometer.

4.4.2 Communication between the RPi, ADC and PZT sensors

The sensing components of control system B consists of two PZT sensors (one mounted either side of the link) and an ADC (MCP3008) which communicates with the RPi. The PZT sensors produce a bipolar analog voltage, which during testing was found to reach a magnitude of up to 8 V at the link's natural frequency (in the situation analysed). The magnitude and bipolar nature of the PZT sensor output necessitates additional components to remove negative voltages and reduce the magnitude so that the signal can be fed to the MCP3008 which has an input range of 0 V to 5 V.

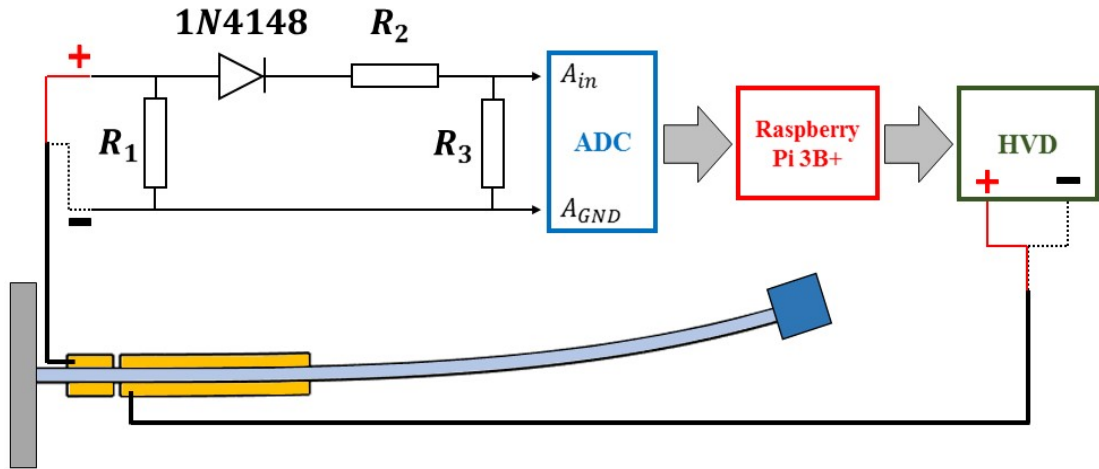


Figure 4.4.6: An illustration of the connections between the PZT sensors and PZT actuators, including the circuit diagram.

The components required to manipulate the voltage are shown as a circuit diagram in Figure 4.4.6. It should be noted that only one sensor circuit is shown as they are identical, and the illustration is not to scale. The issue of the bipolarity of the PZT sensors is addressed through the use of the 1N4148 diode and $10\text{ M}\Omega$ resistor. This creates the half wave rectifier circuit (HWRC), the diode and resistor are labelled in Figure 4.4.6 as '1N4148' and ' R_1 ', respectively. The magnitude of the voltage from the sensors is addressed via the utilisation of a potential divider circuit containing two resistors (denoted as R_2 and R_3).

A diode is an electrical component which allows current to flow in one direction only, from its anode to its cathode (left to right in Figure 4.4.6). Therefore in this particular circuit the diode will allow positive voltages to flow through the circuit, but not negative ones. The resistor in parallel (R_1) blocks any excess current produced by the diode and/or consumes any unused current in the circuit. The value of the resistor in this case must be larger than that of the PZT sensor, hence the choice of $10\text{ M}\Omega$. The effect of these components on the voltage from the PZT sensors is illustrated in the plots in Figure 4.4.7 with respect to both the left-hand side (LHS) and right-

hand side (RHS) voltages (viewing from the free end to the clamped end of the link). The magnitude and frequency of the voltage inputs are chosen arbitrarily and are for illustration purposes only, where the waveform of the voltages is a typical result of a sinusoidal harmonic excitation applied to the base of the link. The PZT sensors are connected to individual HWRCs and PDCs, then both signals from these circuits are fed to the same ADC via separate input channels. Prior to any circuitry the voltages from the two collocated sensors can be seen to have the same amplitude but with a phase difference of π rad.

The HWRC (1N4148 diode and $10\text{ M}\Omega$ resistor) will prevent any negative voltages from reaching reaching circuitry beyond this point. However, as noticeable in the second row of graphs in Figure 4.4.7 there is a forward voltage drop across the diode ($\sim 0.7\text{ V}$ for this type of diode), which is corrected at a later stage in the system. The PDC then reduces the voltage to be in-keeping with the input voltage range of the ADC, where this reduction is proportional to the ratio of the values of the two resistors.

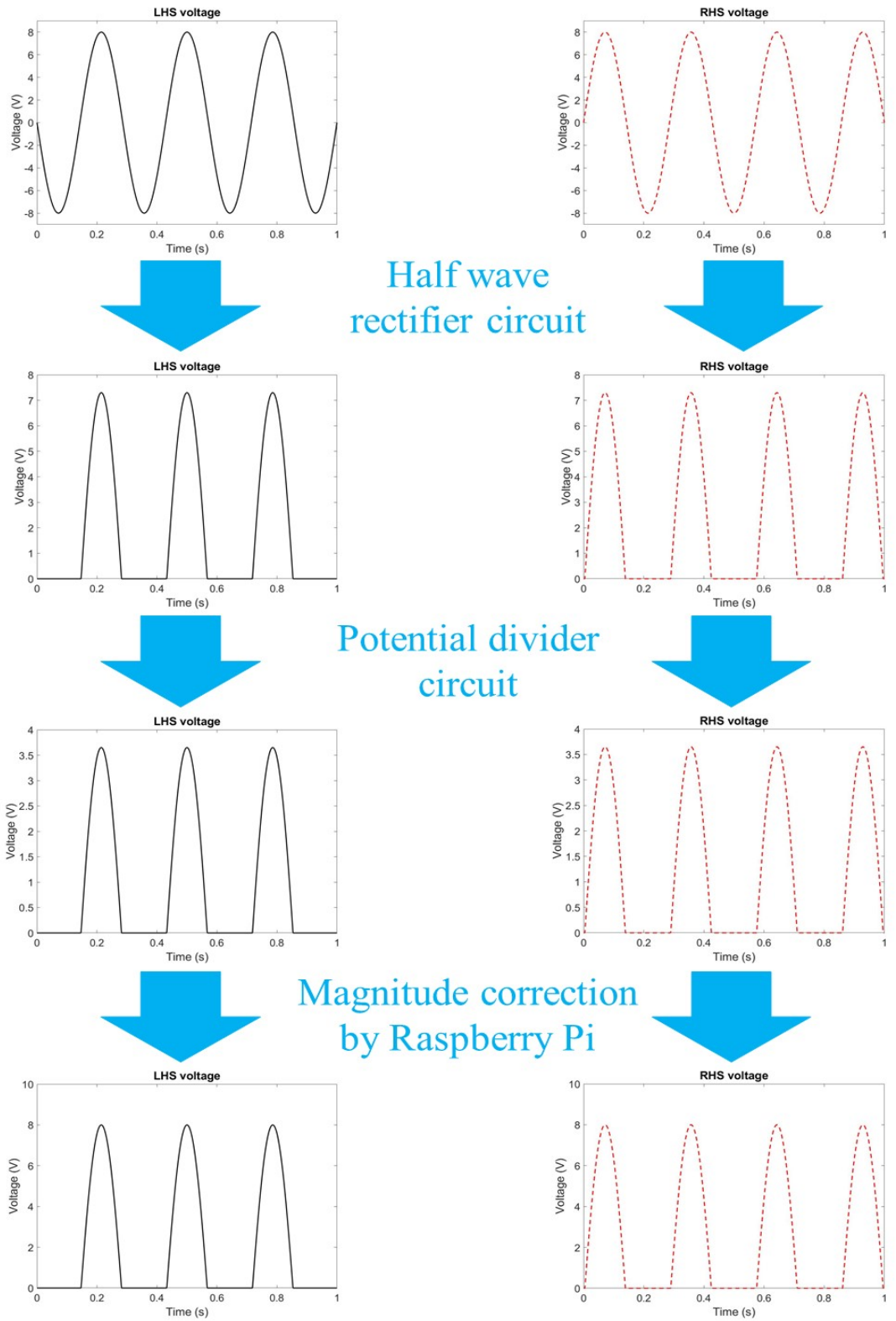


Figure 4.4.7: Manipulation of voltage by the circuits and the Raspberry Pi.

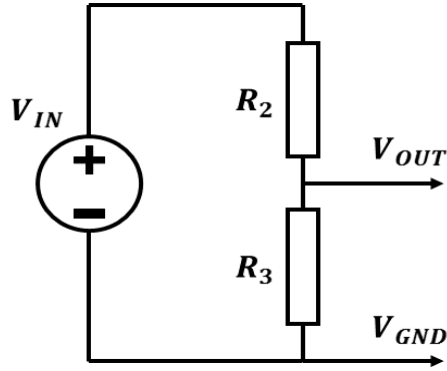


Figure 4.4.8: Circuit diagram of a potential divider circuit.

Figure 4.4.8 shows a circuit diagram of a typical potential divider circuit with a DC voltage source. V_{IN} , V_{OUT} and V_{GND} are the input and output voltages, and ground, respectively. The two resistors are denoted by R_2 and R_3 , connected in series with R_2 connected to V_{IN} and R_3 to V_{GND} . The voltage output (V_{OUT}) is the reduced voltage and is obtained from betwixt the two resistors.

$$V_{OUT} = \frac{V_{IN}R_3}{R_2 + R_3} \quad (4.14)$$

Equation 4.14 outlines the relationship between the resistors' magnitudes and the voltage output of the circuit. In the case where R_2 is equal to R_3 the voltage output should equal half of the voltage input. Figure 4.4.7 illustrates that with two resistors of $10\text{ M}\Omega$ the voltage is halved by the PDC. The decision to use this ratio of reduction was based upon the voltage output from the PZT sensors and the ADC input voltage range. At a base excitation of the link producing a transverse displacement of the link at a magnitude large enough to clearly provide an insight to the response without risking degradation of the system or its components, the voltage output was found to be 8 V . Dividing this magnitude by two yields 4 V which lies within the 0 V to 5 V input range, whilst allowing for any spurious voltage outputs from the PZT sensors which may be greater than this value.

The final stage of the manipulation is to reverse the effects of the two circuits on the magnitude of the voltage, which is preformed by the RPi. As can be seen in Figure 4.4.7 the final row of the graphs is equal in magnitude to the first of the graphs. It should be noted that the RPi does not combine the voltages into one bipolar waveform. Instead the signals continue to be treated separately, the gain is applied and two separate signals are produced from the RPi which are received by the high voltage drivers. This method is a direct result of the limitations of the RPi GPIO pins and is explained in more detail in the following section.

The communication between the ADC and the RPi is preformed via the Serial Peri-

peripheral Interface (SPI) protocol. This option was previously deemed the unfavourable choice against the inter-integrated circuit (I²C) due to the larger number of wired connections required. However in this case the number of wires between the ADC and the RPi would not affect the mass of the link, and so SPI communication was utilised based on its superior communication rate, and thus sampling rate. Figure 4.4.9 illustrates the SPI protocol in general terms between a master (i.e. the RPi) and a slave device (i.e. the MCP3008 ADC) [156]. This communication type is synchronous, where a line controls when the data is written and read and from which device. This line is known as the clock (CLK) and in the majority of cases is governed by the master device. Depending on the devices the data can either be read when the clock signal changes from low to high or high to low, the example shown in Figure 4.4.9 reads data based on the former option. In this general case the master is first to send the data to the slave via the master-out, slave-in (MOSI) line. Depending whether the MISO line is high or low at the time the clock line changes specifies the value of the bit, here a byte is defined as 0100101. The clock line is then held high (or low) for a specific time which is dependent on the slave device's pre-set specification. This enables the communication exchange to occur in the opposite direction, from slave to master using the separate line master-in, slave-out (MISO). The bits are read in the same way as with those on the MOSI line, and in this example the slave sends the master a byte of value 0110010. The slave select (SS) line activates the slave, this line is normally held high, and is set low when communication is required, this line is also used to reset the cycle.

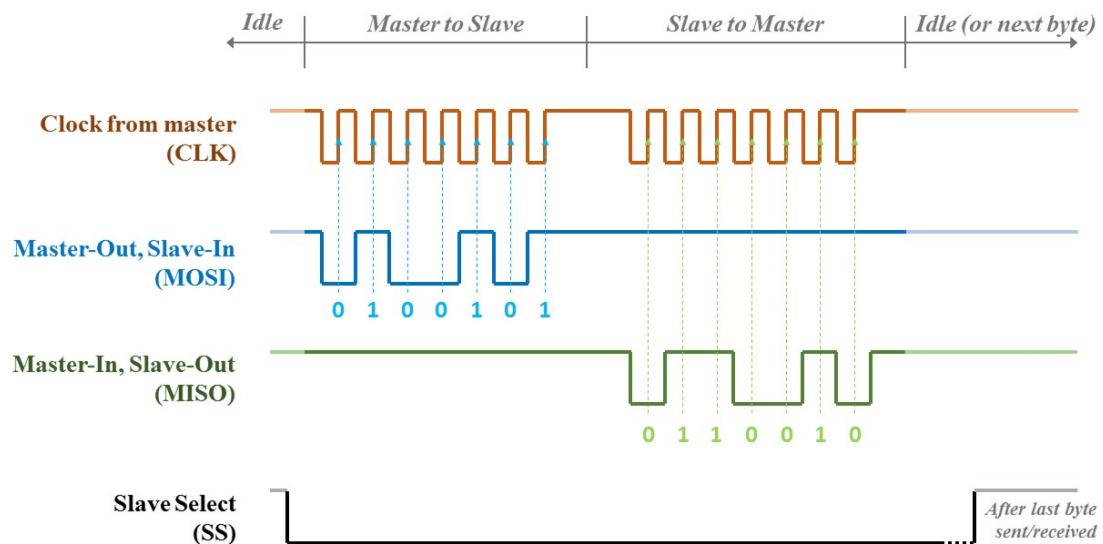


Figure 4.4.9: Visualisation of general SPI protocol.

From the MCP3008 data sheet the relevant clock timing parameters have been

retrieved and are shown as in Table 4.4.5 [153]. These values are when the ADC is powered at 5 V, in which case the clock frequency (f_{CLK}) is 3.6 MHz. In this table the chip select (akin to slave select) is denoted as \overline{CS} , and D_{OUT} represents the serial data out.

Parameter	Symbol	Time (ns)
Clock high time	t_{HI}	125
Clock low time	t_{LO}	125
\overline{CS} Fall to first rising CLK edge	t_{SUCS}	100
\overline{CS} fall to falling CLK	t_{CSD}	0
Data input set-up time	t_{SU}	50
Data input hold time	t_{HD}	50
CLK fall to output data valid	t_{DO}	125
CLK fall to output enable	t_{EN}	125
\overline{CS} rise to output disable	t_{DIS}	100
\overline{CS} disable time	t_{CSH}	270
D_{OUT} rise time	t_R	100
D_{OUT} fall time	t_F	100

Table 4.4.5: MCP3008 clock timing parameters.

This data allows for a better understanding of the SPI communication, and is included in a visualisation of the MCP3008-RPi connection (Figure 4.4.10). There are four connection lines shown, labelled as the pins of the ADC, the correlating pins on the RPi are shown in Figure 4.4.2 and are repeated as follows:

MCP3008 ↔ **Raspberry Pi 3B+**
 CLK ↔ SPI0 SCLK (GPIO 11)
 D_{OUT} ↔ SPI0 MISO (GPIO 9)
 D_{IN} ↔ SPI0 MOSI (GPIO 10)
 \overline{CS} ↔ SPI0 CS0 (GPIO 8)

From Figure 4.4.10 it can be identified that the reading of the data line occurs when the clock rises from low to high. With the \overline{CS} and CLK lines initially held high it is their changes which initiate communication and the reading of data, respectively. Where there is a time delay of 100 ns (t_{SUCS}) between initiating the communication and the CLK line's first rise. The first bit of data is then read from the D_{IN} line after

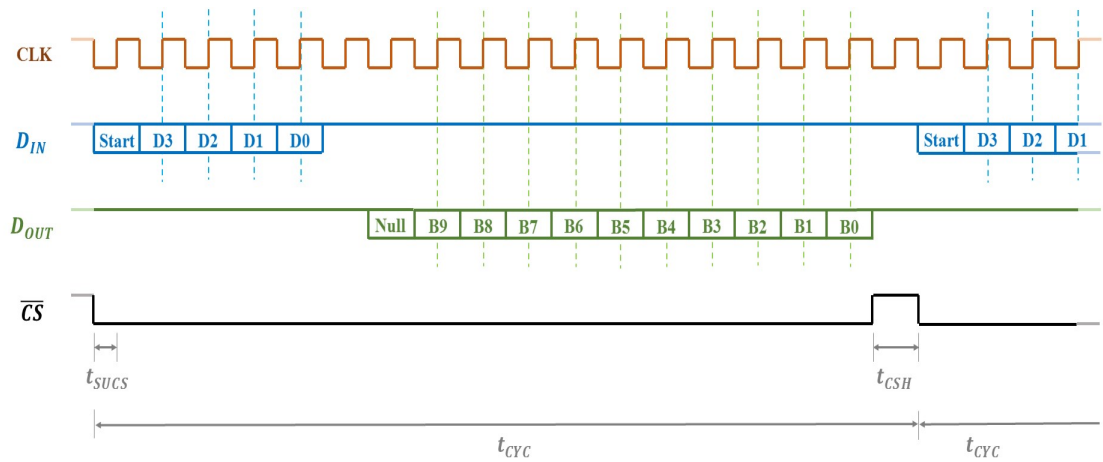


Figure 4.4.10: Visualisation of the MCP3008 SPI protocol.

the CLK is held high for 125 ns (t_{HI}) and then low for 125 ns (t_{LO}). Three bits of data are then sent and read at each rise of the CLK line thereafter, these four bits of data (D3, D2, D1 and D0) select the input configuration and the channel selection of the MCP3008 and are outlined in Table 4.4.6 [153].

From this information it can be seen that the ADC is capable of reading single-ended signals from its eight channels, or four pseudo-differential inputs from a combination of channels. The latter allows the signal read by the IN+ channel to be offset from ground by a DC voltage input to its corresponding IN-. This option was considered in lieu of the half wave rectifier circuit, but would have lead to a reduction in the resolution of the reading by approximately half, and would have required an external voltage supply to the IN- channel(s) to avoid noise in the signal. Thus, for the control system to be effective and lightweight the single-ended configuration was chosen.

Returning to Figure 4.4.10, it can be discerned that the ADC and the RPi switch the direction of communication on the third CLK rise after the D0 bit. This data is sent in order from the most significant bit (MSB) to the least significant bit (LSB), and is the 10-bit number representing the voltage value read by the ADC. The value of the LSB is found through the division of the value of the reference voltage (V_{REF}) by the maximum of a 10-bit value (1024). Once the LSB has been read the \overline{CS} line is pulled high, this should be the case for 270 ns (t_{CSH}) for a new communication cycle (t_{CYC}) to begin.

D3	D2	D1	D0	Input Configuration	Channel Selection
1	0	0	0	Single-Ended	CH0
1	0	0	1	Single-Ended	CH1
1	0	1	0	Single-Ended	CH2
1	0	1	1	Single-Ended	CH3
1	1	0	0	Single-Ended	CH4
1	1	0	1	Single-Ended	CH5
1	1	1	0	Single-Ended	CH6
1	1	1	1	Single-Ended	CH7
0	0	0	0	Differential	CH0 = IN+, CH1 = IN-
0	0	0	1	Differential	CH0 = IN-, CH1 = IN+
0	0	1	0	Differential	CH2 = IN+, CH3 = IN-
0	0	1	1	Differential	CH2 = IN-, CH3 = IN+
0	1	0	0	Differential	CH4 = IN+, CH5 = IN-
0	1	0	1	Differential	CH4 = IN-, CH5 = IN+
0	1	1	0	Differential	CH6 = IN+, CH7 = IN-
0	1	1	1	Differential	CH6 = IN-, CH7 = IN+

Table 4.4.6: MCP3008 configuration bits.

4.4.3 Communication between the RPi, HVDs and PZT actuators

Once the Raspberry Pi 3 has received the signals from the IMUs (control system A) or piezoelectric sensors (control system B), and has produced the voltage that is to be applied to the piezoelectric patches, a signal should be sent to the HVDs to achieve this voltage. This is due to the aforementioned issue of the SBC only able to produce a maximum output voltage of 3.3 V. Another issue is that the output pins are digital and can only ever output 0 V or 3.3 V, however this can be overcome by using pulse width modulation (PWM). This method works on the basis that the output signal is square and switches between low and high (in this case 0 V and 3.3 V), the pulse width of this low/high signal can be altered to achieve analog values between the low and high voltages. This method is illustrated in Figure 4.4.11.

The light blue lines represent approximately 1.7 ms as the PWM frequency of the Raspberry Pi 3 is 585 Hz. As can be seen from Figure 4.4.11, any value of voltage between 0 V and 3.3 V can be achieved through setting the duty cycle to a particular percentage. Another issue arises when utilising the HVDs; an input to the board of 0 V will produce the maximum voltage output as selected via the switches SW3 and

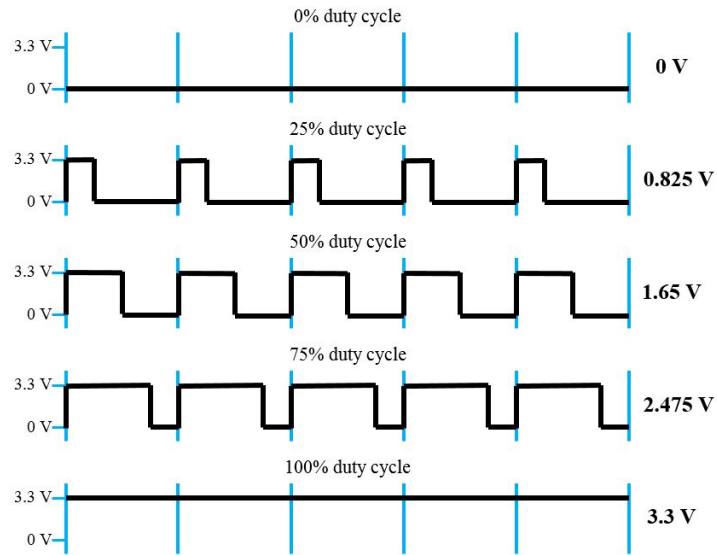


Figure 4.4.11: Illustration of PWM method.

SW4 (see Table 4.3.4), whereas higher input voltage signals will produce lower output voltages. However this inverse relationship is not entirely linear, and so a study was conducted to obtain the relationship when the maximum voltage output is set to 500 V and the input voltages were in the HVD's range, 0 V to 5 V (via an external power source).

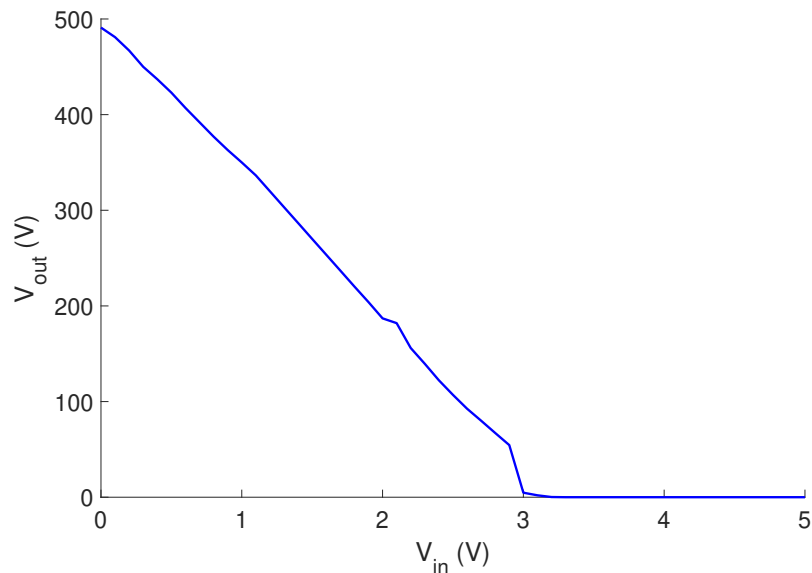


Figure 4.4.12: Relationship between the input and output voltage of the HVDs.

From Figure 4.4.12 it can be seen that applying voltages of greater than 3 V will produce an output of 0 V. Therefore the range of output voltages can be achieved through the range of voltages from the RPi (0 V to 3.3 V). Although a large portion of

the relationship appears to be linear, some sections are not, therefore an interpolation of the results shown in Figure 4.4.12 was implemented to obtain the required input voltage for the necessary output. The diagram in Figure 4.4.13 illustrates the communication between the RPi, one HVD and a PZT actuator. This is a simplification where in actuality there would be two sets of HVDs and PZT patches would be controlled by the SBC, and the controller would dictate which set was used based on the direction of link response. The response of the link in this diagram refers to the angular velocity about the z axis of the global coordinate system (parallel to the width of the link) for Control System A. For Control System B the response is based on the voltage output from the PZT sensors after the circuitry (HWRC and PDC) and the manipulation of these voltages by the RPi.

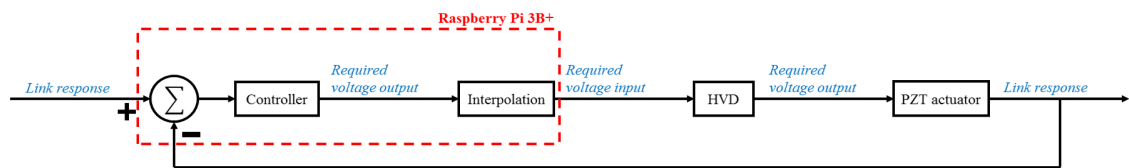


Figure 4.4.13: Flow diagram illustrating the connection between the SBC, a HVD and a PZT actuator.

4.5 dSPACE controller for validation of component selection

Through the selection of a single board computer (SBC) to interpret the signals from the sensors, apply a control gain, and then produce a signal to control the PZT actuators, some compromises were necessary. The driving factors of the processor were its cost, mass and dimensions, and whilst the Raspberry Pi 3B+ (RPi) may be small, inexpensive and lightweight it does have a lower processing capacity compared to purpose-built control systems. This SBC was selected after a detailed comparison with others available on the market (see Tables 4.3.1 and 4.3.2) for its favourable specifications. Although some specifications of these other SBCs were superior to those of the chosen SBC, the RPi was shown to have a good balance over all of the specifications considered. However, even those SBCs with more desirable processing capabilities still do not compare to those of a purpose-built control system such as the dSPACE MicroLabBox (pictured in Figure 4.5.1). It is described as a “Compact all-in-one development system for laboratory purposes” [2], and has been utilised in multiple research applications. To provide an insight into the differences between the Raspberry Pi 3B+ and the dSPACE MicroLabBox another comparative study was conducted as shown in Table 4.5.1.



Figure 4.5.1: Image of dSPACE MicroLabBox.

From this comparison it can be seen that the majority of the RPi’s specifications are more favourable, with the main exception being the clock speed. The dSPACE MicroLabBox has a clock speed of 2 GHz whereas the RPi has a clock speed of 1.4 GHz. Whilst this may not seem like a significant difference, the RPi system is burdened

Specification	Raspberry Pi 3B+	dSPACE MicroLabBox
Equivalent Price	0.0033	1
Dimensions (mm)	85.6x56.5x17	310x250x115
CPU	64-bit quad-core ARM Cortex-A53	NXP (Freescale) QorIQ P5020, dual-core
RAM	1GB (LPDDR2 SDRAM)	1GB (DRAM)
Clock Speed	1.4GHz	2GHz
GPIO Pins	40	48
USB Ports	4	1
Wifi	Yes	No
Bluetooth	Yes	No
HDMI	Yes	No
I ² C Connection	Yes	No
SPI Connection	Yes	Yes
Memory Expansion	Yes	Yes
Input Power	5V 2A	240V 60Hz
Power Connection	Micro USB	Mains power

Table 4.5.1: Comparison between the RPi and the dSPACE MicroLabBox.

with the additional communication between itself and the analog to digital converter (ADC) as the SBC is not capable of interpreting analog signals alone. This inevitably reduces the sampling rate of the RPi system. The dSPACE MicroLabBox has a built-in analog to digital converter, and the entire system is purpose-built for reading and producing analog signals for experimental purposes. Conversely the RPi was designed for an array of applications, not necessarily for use in control experiments, and so the use of additional components is justifiable. Using the RPi in the control system requires the use of an ADC, which in turn requires a half-wave rectifier circuit (HWRC) and a potential divider circuit (PDC) to convert the bipolar voltages of $> \pm 5$ V to a signal which is within the limit of the ADC. Although this signal is then reverted back to that which was output from the PZT sensors, there is the potential for a loss of resolution. This is not an issue with the dSPACE MicroLabBox with its built in ADC that is capable of reading signals between -10 V to 10 V.

Another feature not included in the comparison outlined in Table 4.5.1 is the manner in which the user may program the system. The dSPACE MicroLabBox can be programmed using the MATLAB application SIMULINK, where the signal may be manipulated from an input through a series of SIMULINK blocks to an output known as a SIMULINK model. Such designs are created on a computer which has the ControlDesk software and SIMULINK compiler, and is connected to the dSPACE MicroLabBox through an Ethernet connection. This method of creating a control program may be considered advantageous for its ease of use and intuitive creation of the signal manipulation models. Another advantage is that the SIMULINK software has several blocks which are designed for control systems including a real-time Butterworth filter which aids in the noise reduction of the input signals. Such filters are hard to include within the Python script of the RPi as they would require the definition of specialist functions and would lead to a reduction in the sampling rate. However, for the purpose of this research this method of designing the control program becomes a disadvantage. The addition of a computer which must be connected to the dSPACE MicroLabBox through a wired connection only adds to the total size, mass and expense of the system. The RPi does require either a computer that is used to remotely access it via WiFi, or a screen and peripheral devices to control it. However once the Python script used to dictate how the input signals are read and manipulated to produce output signals is complete (i.e. the gain value is set), the RPi may be programmed to run without external devices. For example the script may be set to run when the RPi is powered, and warning lights may be used to tell the user when it is safe to power the HVDs, at which point an external switch may be used. Although none of these ideas have been included in the RPi during the experiments (due to consistently having to alter certain parameters) they would lend to the RPi system having a greater number of potential applications in future.

The dSPACE MicroLabBox is capable of producing analog outputs of ± 10 V via pulse width modulation (PWM), which as with maximum output voltages of the RPi, is not a large enough amplitude to be directly applied to the PZT actuators. Thus the dSPACE MicroLabBox also requires high voltage drivers (HVDs) to amplify the voltage applied to the actuators. The same relation as shown in Figure 4.4.12 was used to calculate the voltage to be applied to the HVDs to obtain the required voltage output. Thus, when comparing the two control systems the majority of components remain the same, it is only the HWRC, the PDC, the ADC and the RPi that should be exchanged for the dSPACE MicroLabBox. The main difference between the two systems in terms of control lies in the programming; a Butterworth filter is utilised within the dSPACE program in lieu of the resistors in the RPi circuit which assist in noise reduction. The dSPACE system will be used to control the shaker which excites the link for both

cases for consistency, and to relieve the RPi of the processing required to do so. The voltage readings of the PZT sensors by both systems are to be compared to ensure that there is very little discrepancy present prior to conducting any experiments. In the interest of a fair comparison only the positive voltages from the PZT sensors will be used in the case where the dSPACE system is used for control, as the RPi system is only capable of reading such voltages. As outlined, the connections between the components and the dSPACE MicroLabBox requires no additional circuit, so they can be directly connected to its analog inputs/outputs. Figure 4.5.2 highlights the channels of the dSPACE MicroLabBox to which the components and personal computer (PC) are connected.

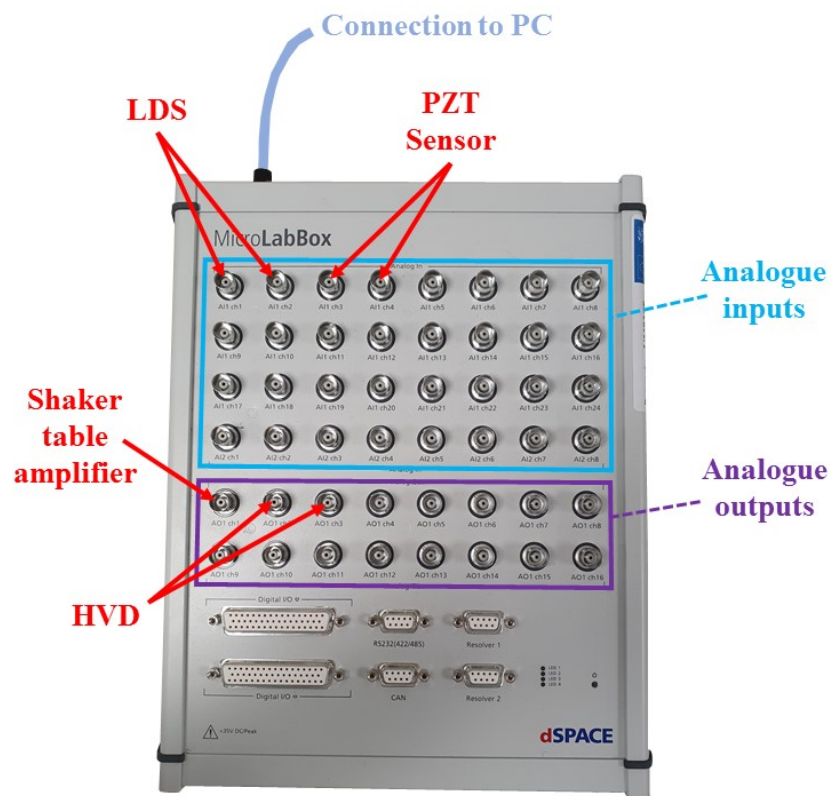


Figure 4.5.2: Image of the connection ports on the top side of the dSPACE MicroLab-Box, highlighting those related to the connections of the control system.

4.6 Health and safety considerations

When working with experimental equipment it is of the utmost importance that the health and safety of the user and individuals within the vicinity is considered at all times. Multiple hazards are present in the experimental set-ups (both during use and assembly), which pose a risk to individuals, and require preventative measures to reduce this risk. All aspects of the experimental set-ups have been scrutinised, identifying any hazards which are included in Table 4.6 and are continued in Table 4.6. These tables contain the associated risks, threats, and preventative measures to the identified hazards.

Hazard	Risk	Threat	Preventative measures
High voltage output from HVDs to PZT actuators.	Electric shock.	Death.	Electrically isolate all connections and ground HVDs. Switch off HVDs when not in use. Create prompts in code which ensure it is safe to turn HVDs on. Cordon off experimental set-up to prevent accidental contact. Use warning signs to inform individuals of the risk.
Robot manipulator	Electric shock. Collision with an individual.	Death. Bruises, limb fractures and/or concussion.	Cordon off the manipulator workspace. Ensure all safety features are working properly. Only use the SmartPad to operate the manipulator as this contains safety switches and emergency stop switches.
Shaker table	Contact with an individual at high velocity. Trapping of body, clothing items or hair.	Severe injuries to fingers, hands, face and head.	Cordon off any moving parts. Ensure warning signs are in place. Turn off the shaker table when not in use or adjusting the attached components. Avoid loose clothing in the laboratory and tie hair back where possible/necessary.
Wiring	Tripping and/or falling over wires.	Bruises, limb fractures and/or concussion.	Avoid wires being positioned across floor space. Secure any loose wiring to surfaces, using tape of hazard colouring where possible/necessary.
Temporary fittings	Accidental exposure of high voltage connections. Parts breaking free and colliding with an individual.	Cuts, bruises, limb fractures and/or concussion.	Avoid temporary fittings where possible. If temporary fittings are necessary reduce any risks by testing and fortifying these connections.

Table 4.6.1: Risk assessment of experiments.

Hazard	Risk	Threat	Preventative measures
Magnets	Breaking or chipping. Crushing. Effect on pacemaker users.	Optical damage, cuts, bruises and temporary alteration of the function of a pacemaker.	Wear eye protection. Avoid collision of magnets. Ensure pacemaker users remain a safe distance from the magnets.
Epoxy resin	Skin/eye contact.	Skin/eye irritation.	Wear eye protection and gloves when using the substance. Remove any excess from any and all surfaces.
Laser Displacement Sensors	Laser directed at eye(s).	Eye damage.	Ensure sensors are switched off when not in use. Position sensors in a manner which minimises the risk.
Soldering components	Contact with the heating element or hot components. Solder flux 'spitting'.	Burns and eye damage.	Avoid contact with the heating element, use tools to assist with this where possible. Wear eye protection.
Electronic Components	Sharp pieces and edges of components. Breaking of components. Short circuiting components can cause them to overheat.	Optical damage, cuts, bruises and burns.	Handle components with care and address and sharp edges through housing. Wear eye protection for brittle components or for any modifications. Ensure that components are always grounded and that operating voltages are never exceeded, using resistors when necessary. Ensure workspace is clear of any debris.

Table 4.6.2: Risk assessment of experiments (continued).

One of the main hazards identified for the experiments was the high voltage output of the circuit to the piezoelectric patches which posed the risk of electric shock if an individual was to make contact. The following preventative measures were identified and implemented during these experiments:

- Electrically isolate all connections.
- Electrically ground the high voltage drivers (HVDs).
- Ensure the HVDs are switched off when not in use.
- Create prompts in the control code which tell the user when it is safe to power the HVDs.
- Use warning signs to inform individuals of the risk posed.
- Cordon off the experimental set-up to prevent accidental contact.

The majority of these measures (along with others associated with other hazards) are easily transferred to, and implemented within the experiments concerning the robot manipulator. However, cordoning off the area was a simpler task in previous experiments due to the location of the set-up within the laboratory. The workspace and components were unreachable to individuals not participating in the experiments due to the room layout and a few barriers. Preventing individuals from coming into contact with the high voltage components accidentally required further preventative measures in addition to multiple barriers when working with the robot manipulator. The location of the robot manipulator was in a laboratory which saw significantly more thoroughfare, and the robot manipulator had a larger workspace than the shaker. This meant that there was a higher level of risk posed by this hazard due to the volume of people, and a new risk in which the manipulator could inadvertently move the hazardous components to a reachable location. Hence a solution was sought to fully encapsulate the circuit of the control system, and prevent any high voltage components from being powered whilst they are accessible.

Figure 4.6.1 illustrates the designed box to house the circuits of the control system. Consisting of 6 mm plywood and 5 mm acrylic the sides of the box were designed so that they interlock, providing stronger joints when coupled with wood glue. The dimensions of the box were calculated based on the size of the components in addition to spacing required between them and access to power sources, removable memory drives, and signals from and to the PZT elements. The round holes which can be seen in both Figure 4.6.1 and the exploded view, Figure 4.6.2 do not exceed 13 mm in diameter. The rectangular holes do not exceed this value in either their width or their height.

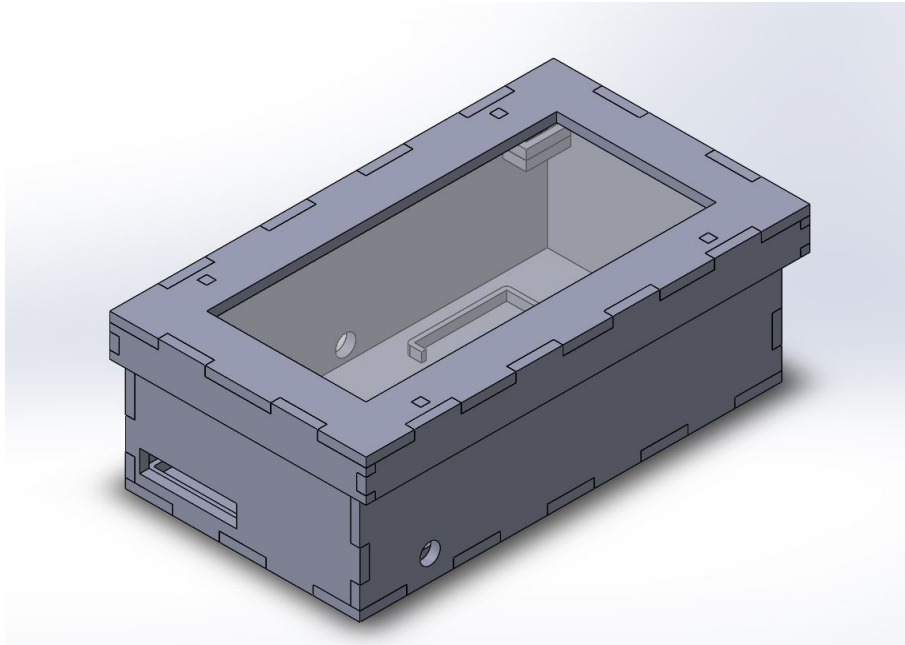


Figure 4.6.1: Circuit enclosure design.

Keeping the dimensions of these cut-outs within this specification ensures that the majority of individuals would not be able to access the inside of the enclosure without removing the lid, especially when the wires etc. are in place. When the lid is removed two circuits each containing two switches in series are broken, preventing power from reaching the HVDs.

The exploded view of the design is shown in Figure 4.6.2 where the features are numbered as follows:

1. Lid assembly.
2. Acrylic viewing panel.
3. Pieces that interact with the switches.
4. Access for the RPi's power supply.
5. Access for the HVDs' power supply.
6. Component holders.
7. Switch mounts
8. Access for PZT elements' voltage in/out.
9. Access to enable use of external memory drive.
10. Miscellaneous access for testing the circuit.

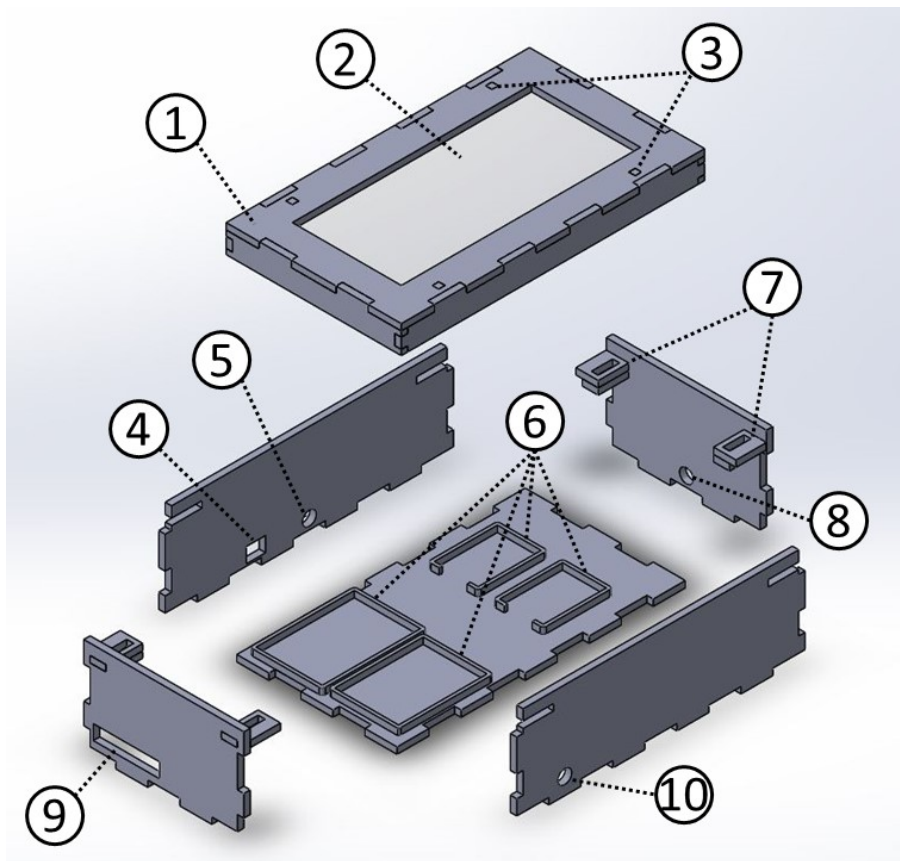


Figure 4.6.2: Exploded view of circuit enclosure design.

The circuit used to prevent the 5 V power supply reaching the HVDs is illustrated in Figure 4.6.3, where $S1$ and $S2$ represent the switches connected in series. The paired switches are located on either end (lengthwise) of the enclosure, for a total of four switches controlling the power to the two HVDs. The positioning and number of switches were chosen so that the lid has to make contact with all four corners of the box in order for the HVDs to have power, therefore greatly reducing the risk posed.

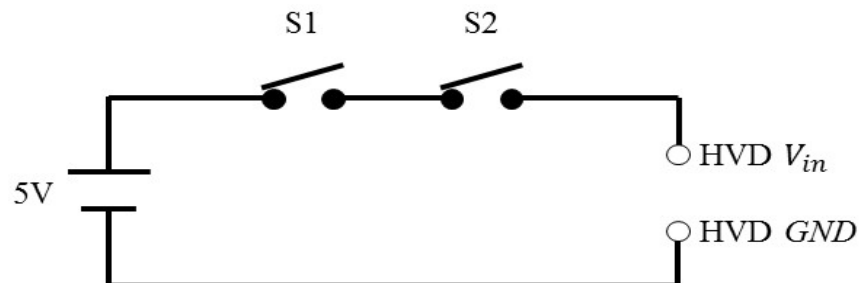


Figure 4.6.3: Circuit diagram of the circuit used to prevent accidental contact with high voltage source.

The layout of components within the enclosure are best shown in Figure 4.6.4, and are numbered as follows:

1. Half wave rectifier and potential divider circuits, and analog to digital converter.
2. Raspberry Pi 3B+
3. Switches.
4. High voltage drivers.

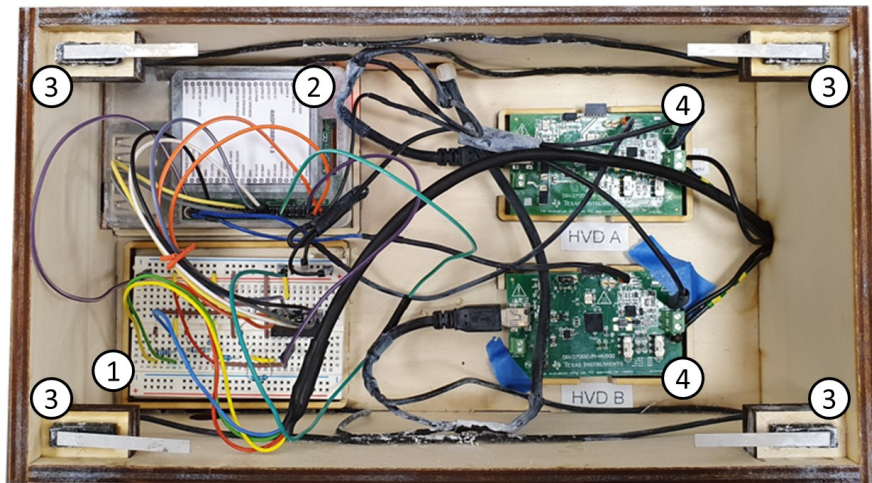


Figure 4.6.4: Image of the circuit enclosure.

4.7 Summary

This chapter presented the analytical models of the two control systems considered in this research, with consideration to the two respective sensing options. The components of these two options were then introduced with more detail than previously, highlighting their operation and connections. Where appropriate the selection of these components over alternatives was justified. The connection and communication between the components was discussed for both control systems. A purpose built controller was introduced and its specifications compared with those of the selected SBC. Finally, the health and safety considerations with respect to the components and experimental set-ups were discussed, including the presentation of a protective enclosure for the components. All of this information was used to create the experimental set-ups for the investigation of the designed control systems' performance and the validity of the analytical models.

Chapter 5

Experimental results of the control systems and validation of the analytical models

This chapter analyses the results of multiple experiments conducted to observe the performance of both iterations of the control system design. Where Control System A (CSA) utilises inertial measurement units (IMUs) and Control System B (CSB) employs PZT sensors (both systems employ PZT actuators). To avoid any issues posed through the excitation of the link using the robot manipulator, a shaker was used to excite the beam in initial experiments for both systems. This concept was also employed when comparing Control System B's level of performance with that of a purpose-built control system (the dSPACE MicroLabBox). This comparison was employed for the justification of the compromises made when the Raspberry Pi 3B+ (RPi) was selected as the processor of the control system, and to provide an insight on how these compromises affected the overall performance of the control system. Testing three different base excitation scenarios to ascertain the level of attenuation attained by the RPi system with reference to the dSPACE system, in an attempt to provide an insight into its performance for different applications of the robot manipulator. The final analysis of the control system sees the link mounted upon the robot manipulator, to corroborate the previous findings with respect to the performance of the RPi system. To ensure continuity, the same base excitation scenarios were executed when the additional link was part of the robot system.

For all experiments which analyse the performance of the control system in the frequency domain (barring the comparison between the dSPACE and the RPi system) the analytical model was validated. The results of these comparisons are presented, and any amendments to the analytical models (for CSA and CSB) are discussed. These

adjustments to the models were reflective of the base excitation type applied to the link, the circuit used in the RPi system and any other unexpected issues with the experimental set-up that should be included within the model. In the case where the robot manipulator is used to excite the link, the analytical model also assists in the investigation of the hypothesis that the kinematic model of the robot need not be incorporated alongside the analytical model of the link. This hypothesis stems from the fact that the manipulator has a considerably larger mass than that of the link, therefore the inertial effects of the link on the robot may be omitted.

5.1 Control System A

This section observes the results obtained using control system A (the sensor is the IMU: MPU9250), where the error is the difference between the angular velocity at the tip of the link and its base. In these experiments the base excitation signal was controlled by the data acquisition system (DAQs) SignalCalc Abacus, which was also used to read and interpret the voltage output from two laser displacement sensors (LDS) (OMRON ZX2-LD100). These sensors are not included in the control system, but are used to observe the control system's performance avoiding any potential errors in the readings from the IMUs. The APS 113 ELECTRO-SEIS R Long Stroke Shaker in conjunction with the APS 125 Power Amplifier were employed to apply base excitation to the link. The Raspberry Pi 3B+ (RPi) is employed to interpret the signals from the IMUs (via an I²C connection), and to apply a proportional gain (K_p) before converting the signals to one to be used by the high voltage drivers (HVDs). In turn the HVDs apply a voltage to the PZT actuators which apply a strain on the link to attenuate the vibration. Figure 5.1.1 illustrates the connection between the components, where some of the components have been simplified and the illustration is not to scale. Figure 5.1.2 is an edited image of the experimental set-up, altered in an effort to better highlight the connections between the components.

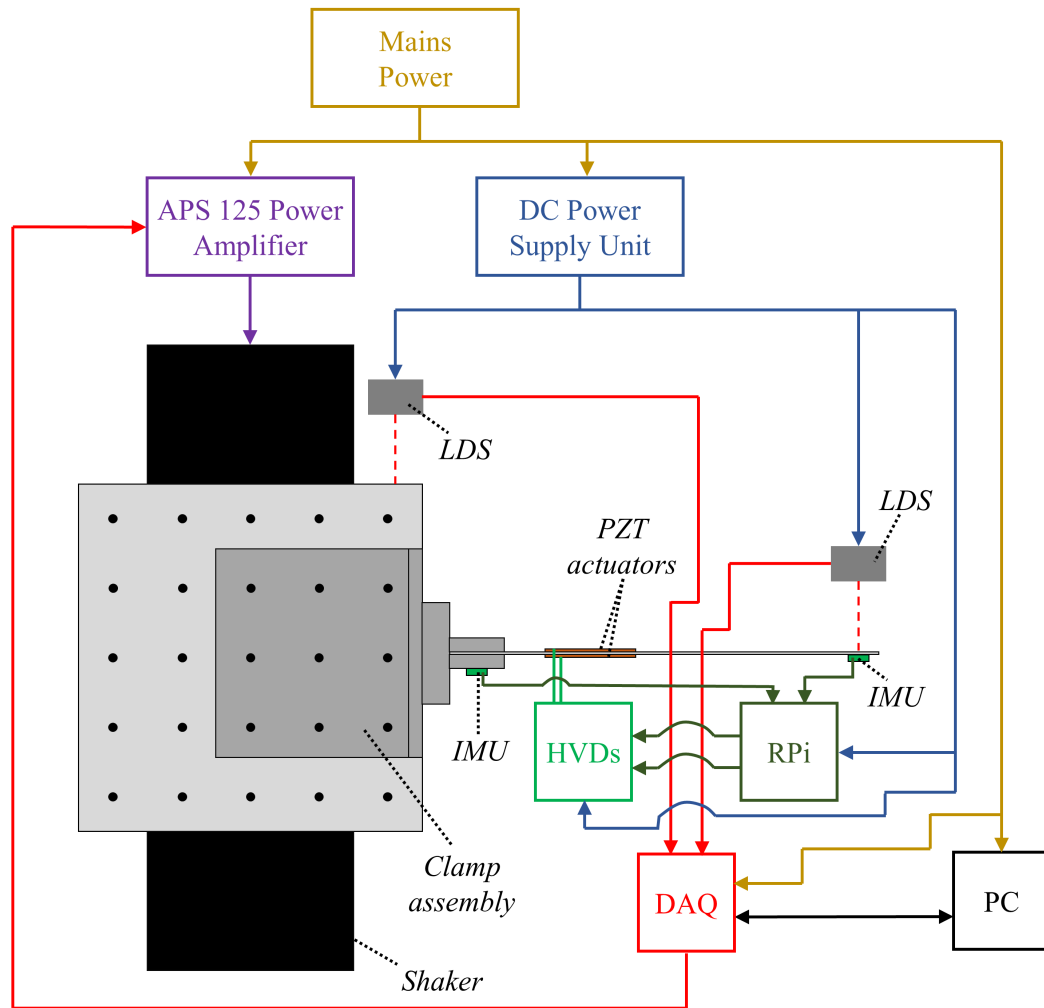


Figure 5.1.1: Illustration of the experimental set-up used to validate the closed loop analytical model of control system A.

The components in Figure 5.1.2 are numbered as follows:

1. IMU.
2. Connection of I²C lines.
3. Raspberry Pi 3B+.
4. High voltage drivers.
5. PZT actuators.
6. Laser displacement sensor.
7. Clamp assembly.
8. Shaker table.
9. Wires leading to power source/DAQ.

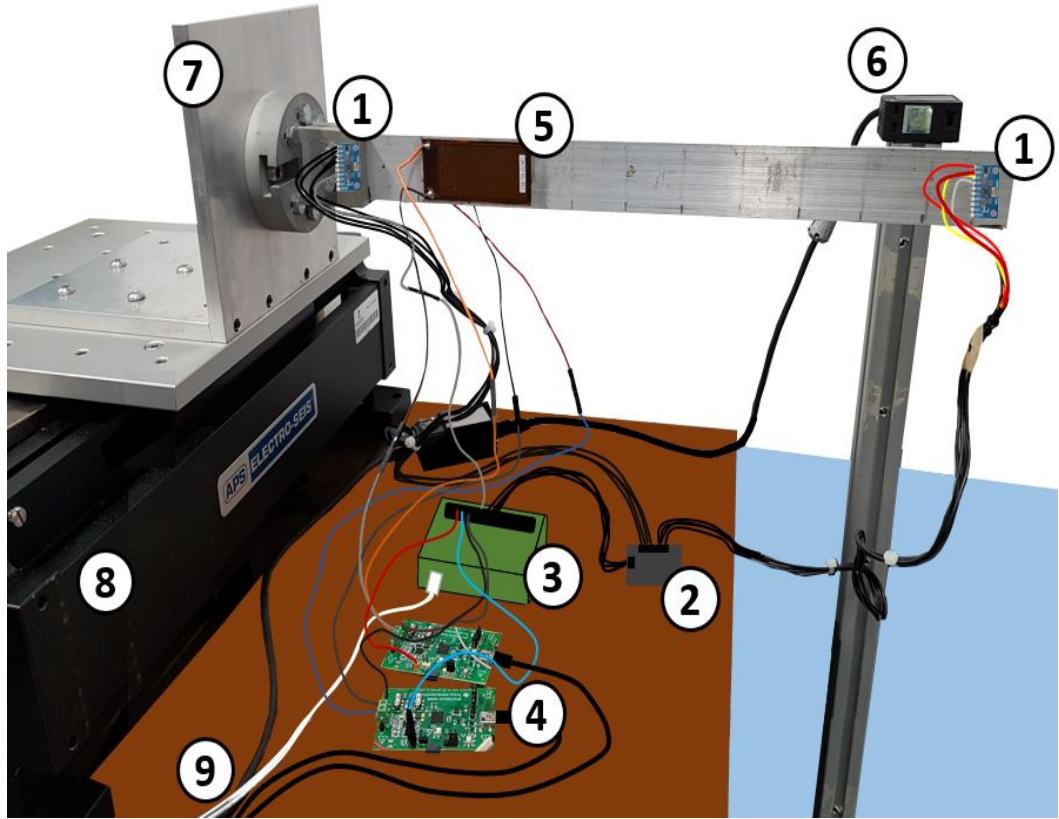


Figure 5.1.2: Image of the experimental set-up used to validate the closed loop analytical model of control system A.

As previously mentioned in Section 4.2.1, the voltage to be applied to the PZT actuators ($V_{in,pa}$) is a product of the gain value (K_p), the ratio between the angular velocity ($\dot{\Theta}$) and the angular velocity at the resonant frequency of the link ($\dot{\Theta}_{\omega_n}$) (both angular velocities are about the global z axis), and the maximum operating voltage of the PZT actuators (see Equation 5.1). Utilising the ratio of the calculation avoids the requirement for a parametric study to determine an optimal gain value when the angular velocity amplitude at the natural frequency of the link is known. Therefore, whilst this method is unconventional and limits the potential applications of this system, it does lead to an easier analysis of the performance of the control system components as a separate entity from the control design.

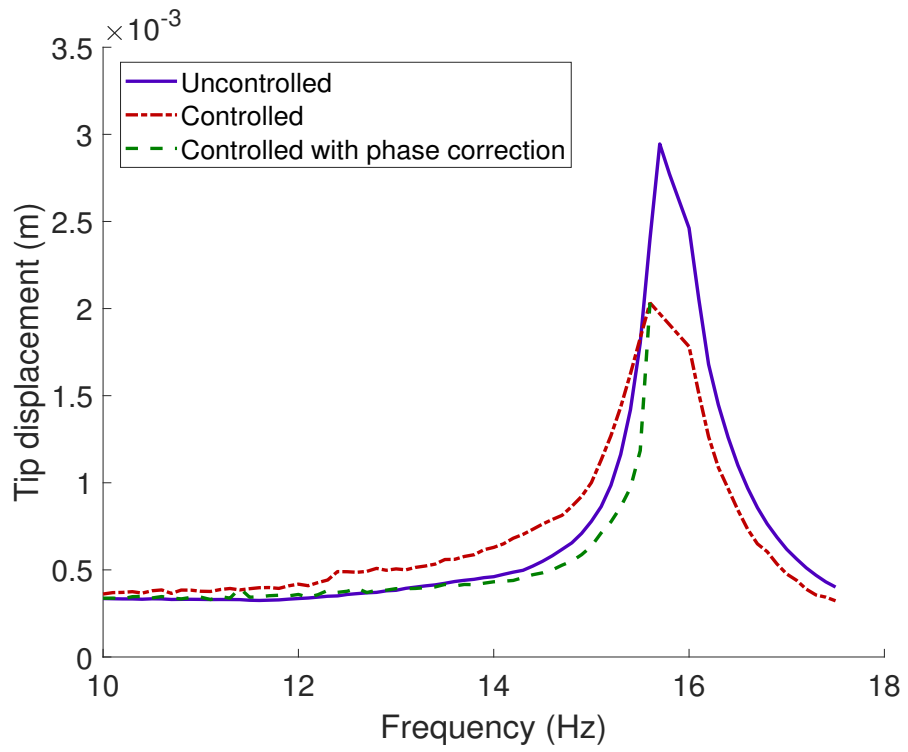
$$V_{in,pa} = K_p \frac{\dot{\Theta}}{\dot{\Theta}_{\omega_n}} \times 360 \quad (5.1)$$

The link was excited in a stepped sine manner over a frequency range of 0 Hz to 17.5 Hz in intervals of 0.1 Hz. This interval size was selected to allow for a good observation of the response of the link over different frequencies whilst being time effective. At each frequency the link was excited for 30 s to allow for sufficient data which avoids

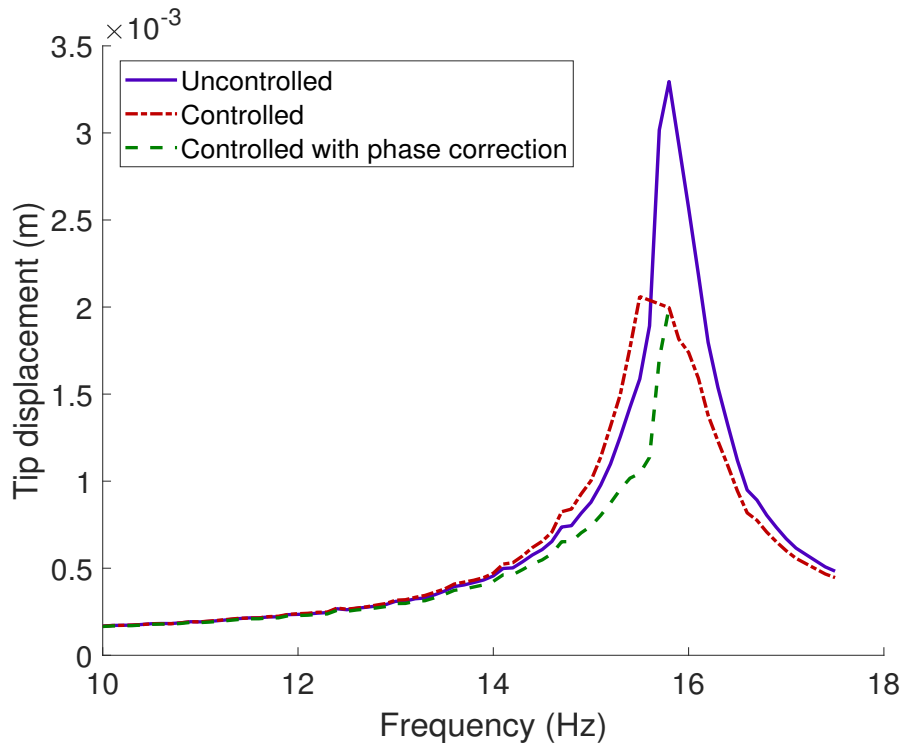
any transient response and/or contributions from other modes. Excitation of the link utilising a swept sign method was considered, which uses an automated increase of frequency between an upper and lower limit which has smaller increments in frequency. The data obtained from such a method would be put into the frequency domain through the use of the fast Fourier transform (FFT). However using this method would not provide enough data at each frequency to observe the phase and magnitude of both the response and the voltage applied to the PZT actuators. For this reason the results have been presented as the raw experimental data rather than a modally fitted curve, as this best highlights the findings. On an additional note, this experiment and subsequent validation of the analytical model only considers the first mode of the link, this decision was based on the limitations of the robot manipulator in its capacity to apply base excitation.

The experimental and analytical results are shown in Figures 5.1.3a and 5.1.3b, respectively, and it should be noted that analytical model has been adjusted to better reflect the experimental data (to be discussed shortly). The open loop or (uncontrolled responses) are shown by the solid purple lines, the dot-dash red lines show the closed loop (or controlled) responses. In these results it can be seen that the control system initially excites the link at frequencies lower than its natural frequency, which is far from ideal. This led to a further investigation yielding the more successful results as shown in Figures 5.1.3a and 5.1.3b as green dashed lines after the implementation of phase correction. Within the additional investigation the sampling rate of the RPi/IMUs (128 Hz) was the maximum possible rate when using the I²C which was considerably slower than previously identified due to the number of lines of code required in the control system. It was hypothesised that this led to a delay in the application of control which resulted in the response of the link at lower frequencies being increased rather than decreased. However, at frequencies at or greater than the natural frequency, when the underlying phase of the link changes, the system is capable of attenuating the response of the link to a suitable degree as can be seen from the results. To address the unwanted increase in response at the lower frequencies a delay time was introduced to shift the phase of the voltage application, based on the hypothesis. As can be seen in Figures 5.1.3a and 5.1.3b this adjustment led to the successful rectification of the issue (green dashed lines).

It is important to note that a delay in the time between the sample taken from a sensor in a control system to the application of control by means of an actuator can lead to instability [157]. Hence, introducing such a delay is considered poor practice, and researchers commonly seek to reduce the delay instead. However, acknowledging this and realising it is not a suitable solution, a delay is introduced in this research to further investigate and provide a better understanding of the control system.



(a) Experimental results.

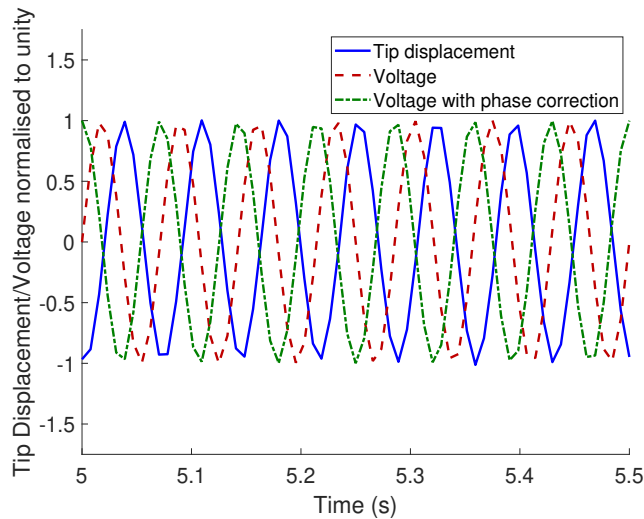


(b) Analytical results.

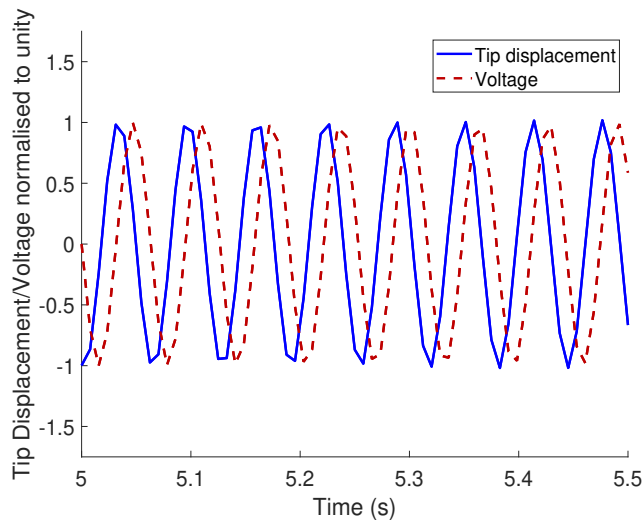
Figure 5.1.3: Results of control system A; open loop, closed loop and closed loop with phase correction.

The investigation and implementation of the phase correction of the voltage input to the PZT actuators can be observed further in Figures 5.1.4 and 5.1.5 for the experimental and analytical data, respectively. The amplitude of the response (the tip displacement of the link) and the voltage input to the PZT patches have both been normalised to unity for a better comparison. It should be noted that a positive voltage shown in the figures will result in a strain on the link causing a transverse motion in the opposite direction to the tip deflection of the link, so that the voltage and tip displacement should be 180° out of phase. An excitation frequency lower than the natural frequency has been observed (14 Hz), and in the experimental case the 5.1.4a it can be seen that the unadjusted voltage input signal (red dashed line) is close in phase with the tip displacement (far from the ideal 180° difference). The higher frequency case (Figure 5.1.4b) also does not see the application of the voltage being completely out of phase with the tip displacement. However, the noticeable difference between the two frequency cases is that the voltage peaks are prior to the displacement in the 14 Hz case, but are then after the displacement in the 15.8 Hz case. This suggests that delaying the application of the voltage in the 14 Hz case would lead to a reduction in the amplitude of the response of the link, but according to the results showing in Figure 5.1.3 such a delay would not be necessary at higher frequencies.

The analytical model, as aforementioned, has been adjusted to yield similar results to those obtained experimentally for the purpose of further investigation and understanding. This adjustment was necessary as the analytical model would contain no delay in the application of the voltage, instead this was induced. The magnitude of this induced time delay was based on the recorded time difference between the line of code in the control program reading the input from the IMUs, and the line sending the required signal to the HVDs. The recorded time delay differed slightly when repeating the experiment, but on average (based on ten results) was found to be approximately 0.031 seconds. The results obtained from the analytical model Figure 5.1.5 containing the introduced delay corroborate with the findings from the experimental results. The higher frequency case does show a very similar phase difference in the application of voltage and the displacement, as well as mirroring the experimental results in that the voltage peaks occur after the displacement peaks. The results in Figure 5.1.5a (the 14 Hz case) are not as similar, the applied voltage is in phase with the tip displacement. This can be explained through the estimation of the time delay between the previously specified lines of code. The controlled FRF of the analytical model presented in Figure 5.1.3 confirms that little to no phase difference yields unfavourable results. Whilst the voltage application results in the time domain obtained the analytical model and the experimental investigation were not an exact match, the model may still be used to understand the experimental results. The model shows the voltage as being applied



(a) 14 Hz base excitation.

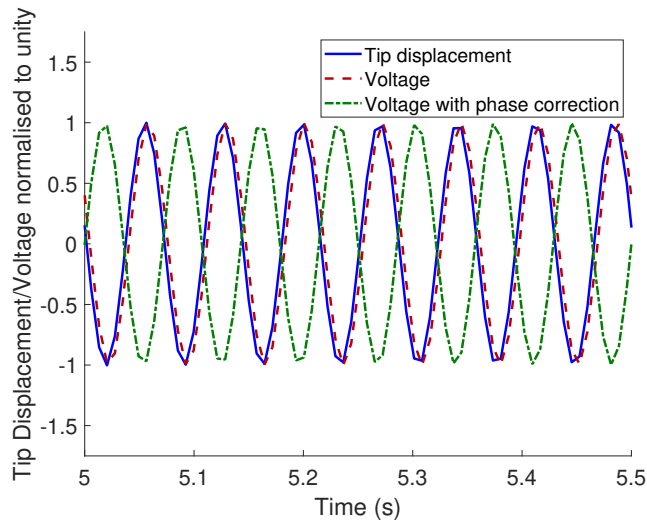


(b) 15.8 Hz base excitation.

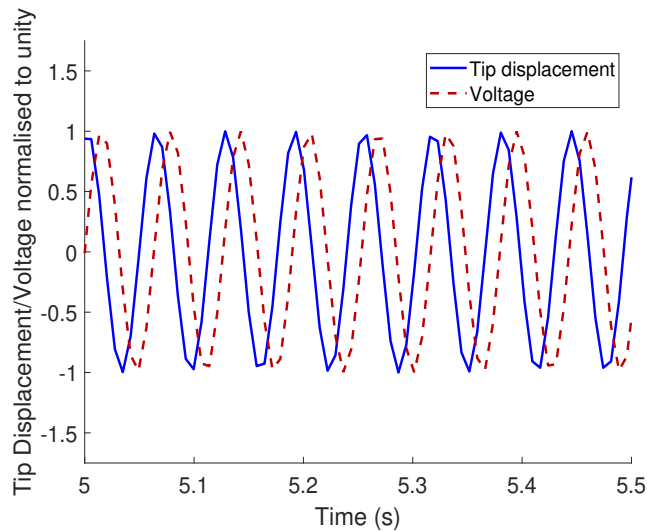
Figure 5.1.4: Experimental results in the time domain showing the influence of the phase correction on the voltage application.

later than the experimental results, and so if a delay was induced in the model of a sufficient magnitude that the response of the link is reduced then it was hypothesised that the same delay magnitude would be sufficient for the experimental case.

The analytical model was employed to further investigate the effect of a time delay of varying magnitudes on the two previously investigated frequency cases (14 Hz and 15.8 Hz). The results of this investigation are presented in Figure 5.1.6, where the amplitude of the tip displacement is shown for a range of delay times from 0 s to 0.06 s for the uncontrolled and controlled scenarios. Figure 5.1.6a contains the results for the 14 Hz case where it is clear to see that with no additional delay time the response is increased, and as the delay time is increased to the empirically determined optimal



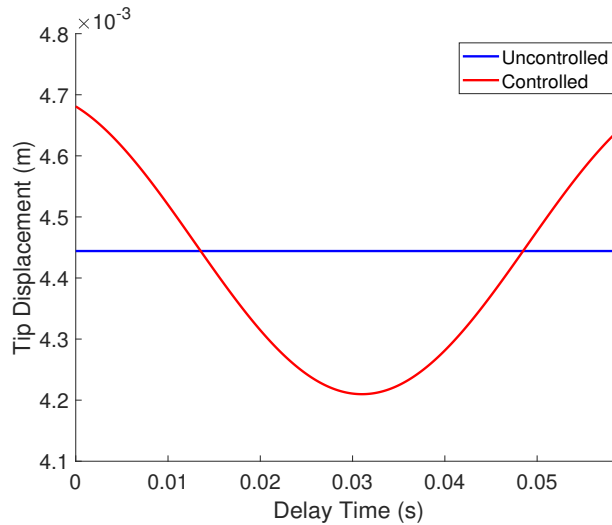
(a) 14 Hz base excitation.



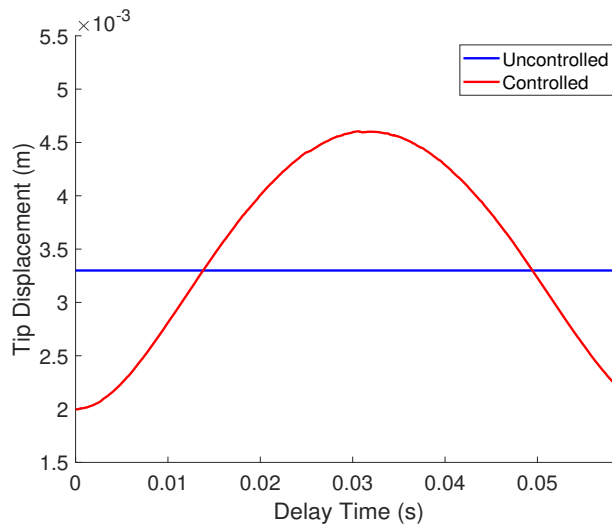
(b) 15.8 Hz base excitation.

Figure 5.1.5: Analytical results in the time domain showing the influence of the phase correction on the voltage application.

delay time of 0.031 seconds the response decreases. If the delay time is increased further than this point then the magnitude of the response increases to the response magnitude where there is no delay time present. Comparing this case with the optimisation of the delay time for the case where the excitation frequency is identical to the link's natural frequency (15.8 Hz) a different value of optimal delay time is yielded. In this case increasing the additional delay time only increases the response, the opposite to the 14 Hz case. The largest response is obtained when the delay time is equal to 0.031 seconds, and increasing the delay time reduces the response until it reaches the same value as when the additional delay time is not present. This further validates the theory that no delay time is required at higher frequencies. However, this suggests that an optimal



(a) Delay time optimisation (14 Hz).



(b) Delay time optimisation (15.8 Hz).

Figure 5.1.6: Analytical time delay results comparing uncontrolled and controlled tip displacement with varying time delay on the controlled results.

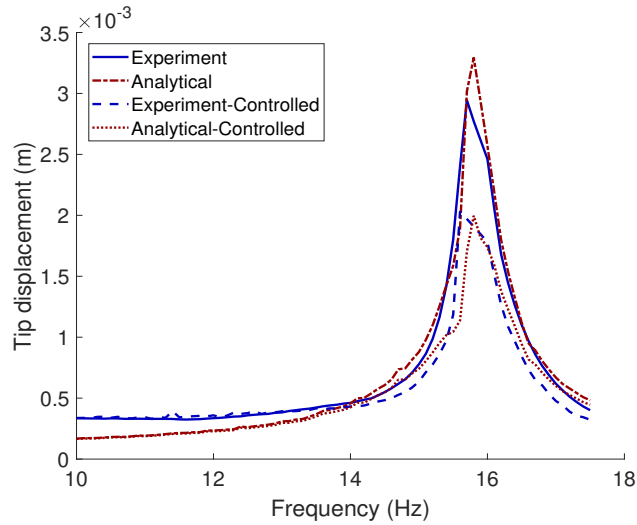
delay time at each frequency interval for those less than 15.8 Hz is present based on the difference between the two cases presented.

The experiment pertaining to the investigation of the response in the frequency range was repeated whilst including a time delay of 0.031 seconds for frequencies 10 Hz to < 15.8 Hz, and the analytical model was once again employed. This greatly improved the attenuation of the response (see the green dashed lines in Figure 5.1.3), however when observing the experimental results it is noticeable that the response is slightly increased in comparison with the uncontrolled case (blue solid line) for frequencies between 10 Hz to 13 Hz. So, in order to obtain the desired response across the entire frequency range addressed in this experiment it would be necessary to find an optimal

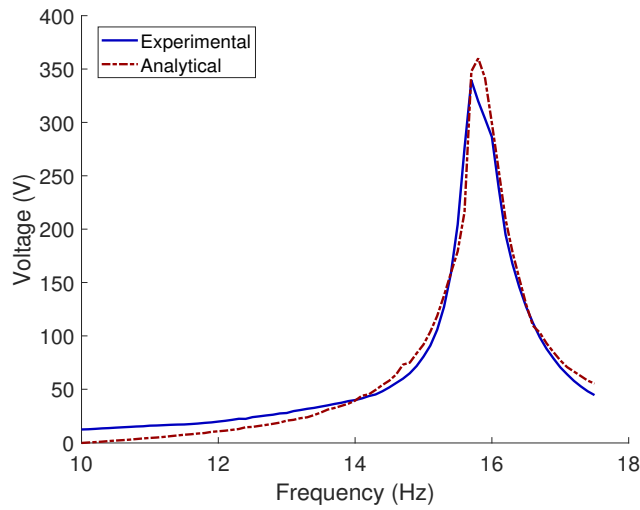
value of additional delay time for each frequency. This excitation between 10 Hz to 13 Hz is not present in the analytical results 5.1.3b as the time delay originally induced in the model to obtain a representation of the unfavourable results is cancelled out.

To further validate the analytical results the response (tip displacement) for both the uncontrolled and controlled cases have been included in Figure 5.1.7a alongside the experimental results. Figure 5.1.7b contains the voltage applied to the PZT actuators for both the experiment and analytical model. From both figures it can be observed that the analytical model is a close prediction of the experimental response in terms of the damping. However there is a noticeable discrepancy when analysing the amplitude and natural frequency of the responses (Figure 5.1.7a); the analytical model yields a higher amplitude of response for the uncontrolled case and a higher natural frequency for both the uncontrolled and controlled cases. These discrepancies can be explained through the size of the frequency intervals used. The analytical model has a smaller frequency interval than the experimental case, and a larger frequency interval will mean that the response in between the frequencies sampled is omitted. In the case of the uncontrolled response this is very noticeable, the experimental result shows that the natural frequency is around 15.8 Hz, as this produces the largest amplitude of the response in comparison to those immediately surrounding this. Whereas, the analytical model considers more frequency values within the same range and as a result is able to produce a more accurate prediction of the natural frequency and a more idealistic representation of the response. With the exception of the aforementioned discrepancies the closed loop analytical model (controlled) provides an acceptable prediction of the experimental response, and the same can be said for the analytical model's prediction of voltage (Figure 5.1.7b).

As the results used to observe the response of the link for a range of frequencies were obtained in the time domain (steady state response), it is possible to compare the result from the experiment with the equivalent prediction by the analytical model. The experimental result of this comparison is shown in Figure 5.1.8a, and the analytical counterpart in Figure 5.1.8b. In both cases the base excitation is set to 15.8 Hz, the natural frequency found through the experimental results (see Figure 5.1.3), and control is applied at approximately 15 seconds. A few differences between the results can be observed; the magnitudes of the both the uncontrolled and controlled tip displacement are larger in the analytical case, and no transient response is observed in the analytical case at the point that control is engaged. The former can be explained through choices and amendments that were made to the model in terms of the base excitation amplitude, damping and frequency intervals used. These parameters were all adjusted so that the analytical model portrayed an accurate representation of the experimental response in the frequency domain, leading to the slight discrepancies in the magnitudes



(a) Tip displacement with and without control.

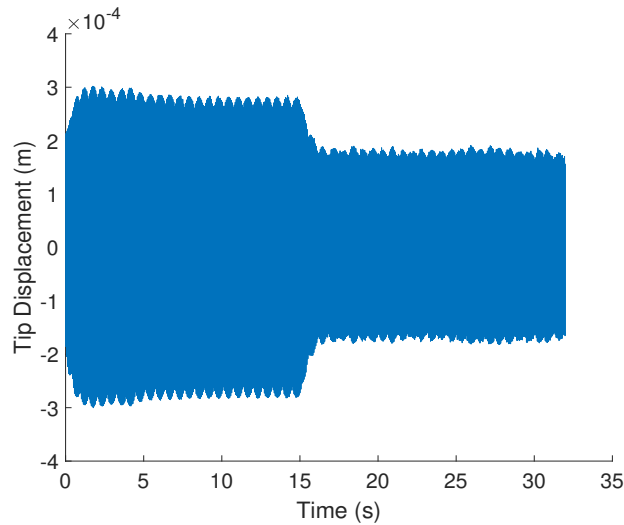


(b) Voltage applied to piezoelectric patches.

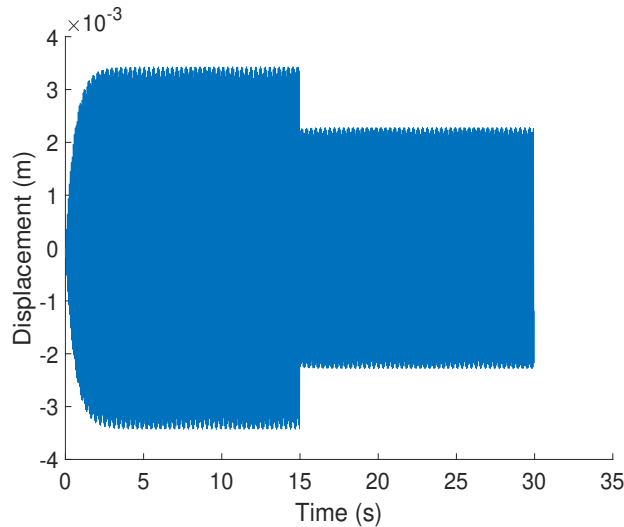
Figure 5.1.7: Comparison between analytical and experimental results.

of the response. The lack of transient response in the analytical model is due to the control being effectively implemented in an ideal manner, which is unrealistic hence the presence of the transient response between the uncontrolled and controlled states in the experimental case.

Before moving forward it was deemed pertinent to discuss the results presented for this control system option. Upon the review of the results obtained for the implementation of control system A, three main conclusions have been developed regarding; the system's components, the experimental method and the analytical model. Firstly the choice of components is not ideal, whilst the system was able to attenuate the response across a range of frequencies, amendments to the control system were required to obtain results closest to those desired. In particular the requirement for the additional



(a) Experimental data.



(b) Analytical data.

Figure 5.1.8: Results in the time domain with and without control (base excitation frequency: 15.8 Hz).

delay time at certain frequencies imposes a limitation on the system: in order for the maximum attenuation to be achieved the frequency must be constant and known in order to include the relevant optimal additional delay time. Thus, for a base excitation that is anything but harmonic and within a frequency range for which the additional delay time required is unknown, the control system is unlikely to achieve maximum attenuation. An solution to this could potentially lie in the inclusion of a method to deduce the current excitation frequency and interpolate the required additional delay time from values obtained through a series of optimisation studies. However, this solution would mean the inclusion of auxiliary functions within the control code leading to a further decrease of the already sub-par sample rate, further decreasing the efficiency of

the control system. Therefore, it becomes pertinent to seek an alternate solution which offers a higher sampling rate, which would be best addressed through using an alternate communication method between the sensors and the RPi. The IMUs do support Serial Peripheral Interface (SPI) as an alternate to the Inter-Integrated Circuit (I²C) used in this experiment, which offers a higher potential sample rate, but requires more wired connections. This would add additional mass and stiffness to the link, negatively influencing its functionality. Therefore, in corroboration with the motivation outlined in Section 3.5.1 it was concluded that the best course of action was to replace the sensors.

Secondly, the experimental method used in this experiment was selected based on the necessity to observe the response of the link and the voltage application in the time domain for the purpose of fault finding. Whilst allowing for the requirement of additional delay time to be found, utilising this method meant that the frequency interval was governed by time constraints, leading to a less accurate frequency-response study. To become more time efficient the experimental method should be swapped to an automated swept sine wave excitation using FFT to obtain the response in the frequency domain. Alternatively, a random excitation test may be employed to generate the required FRFs, however this would not highlight any nonlinearities present in the structure. Whilst these alternate methods of testing proved highly impractical for control system A, these alternative experimental methods would be more efficient for future experiments. Finally, the analytical model provides a good prediction of the response with the exception of a few discrepancies. However, as with the experimental method, the analytical results were produced in the time domain, for continuity. Even though the analytical model was more time efficient, it was far from optimal in terms of time efficiency. Converting the model into the frequency domain has the potential to overcome this issue and providing a faster method of predicting the response.

5.2 Control System B

This section describes and discusses the experiments used to observe the performance of control system B, where two collocated PZT patches are employed as sensors. The reasons for the exchange of sensors have been outlined previously (see Section 3.5.1). The experimental results are used to validate the closed loop analytical model developed in Sections 3.5.2 and 4.2.2.

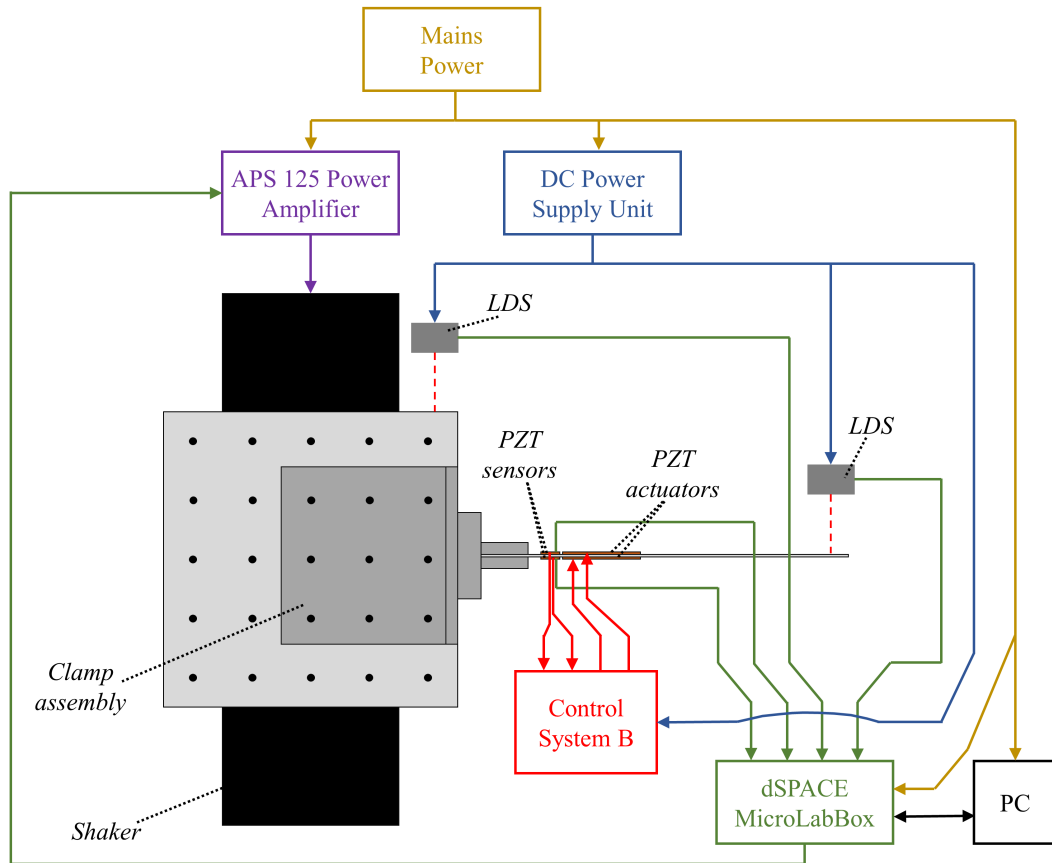


Figure 5.2.1: Illustration of the experimental set-up used to validate the closed loop analytical model of control system B.

The connections between the components of the experimental set-up are illustrated in Figure 5.2.1, which is not to scale, and some parts of the system have been simplified to blocks. For a more detailed outline of the block labelled ‘Control System B’ the reader is referred to Figure 4.4.6. It should be noted that the ‘DC Power Supply Unit’ actually represents different sources of power for the different components, but in this illustration these have been amalgamated for simplification. The control system consists of the PZT sensors which produce a voltage read by the components in the ‘Control System B’ block which then produces a voltage to be applied to each of the PZT actuators. The laser displacement sensors (LDSs) are read by the dSPACE MicroLabBox in an effort to observe the response whilst negating any potential errors made in the reading of the

voltage from the PZT sensors by the RPi. The dSPACE MicroLabBox is also used to produce a voltage signal (amplified by the APS 125 Power Amplifier) to control the shaker table.

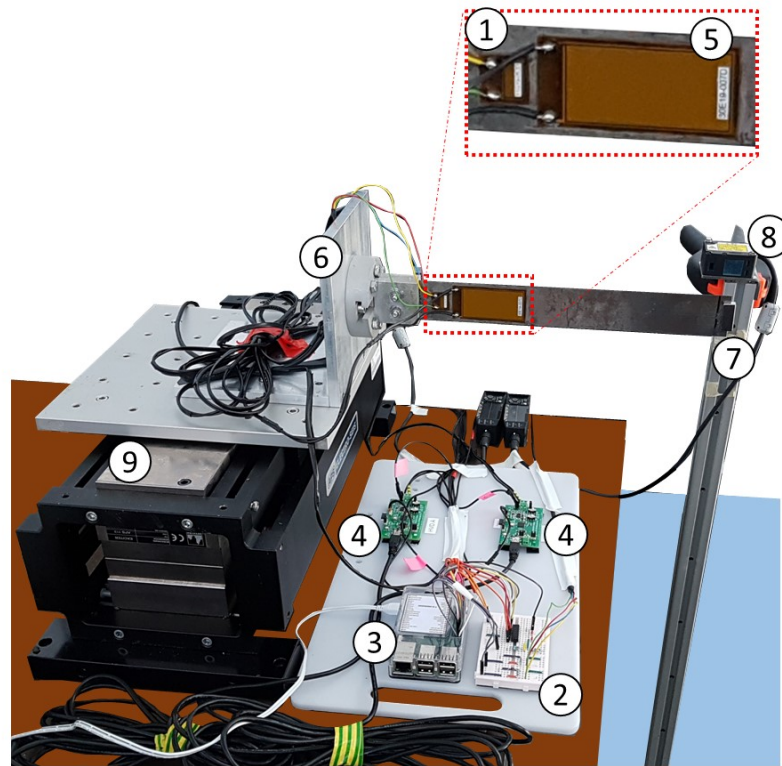


Figure 5.2.2: Image of the experimental set-up used to validate the closed loop analytical model of control system B.

The components used in the experimental set up shown in Figure 5.2.2 are numbered as follows:

1. PZT Sensor
2. Half wave rectifier and potential divider circuit
3. Raspberry Pi 3B+
4. High voltage driver
5. PZT Actuator
6. Clamp assembly
7. Tip mass (magnets)
8. Laser displacement sensor
9. Shaker table

The image shown in Figure 5.2.2 has been edited to better highlight the components used in the experiment. The wires at the bottom of the image lead to a power source for the components. Omitted from this image is the dSPACE MicroLabBox which is connected to the two laser displacement sensors (LDSs), one of which is situated behind the shaker table/clamp assembly. Prior to analysing the performance of the RPi control system across the given frequency range, a parametric study was conducted to empirically obtain the optimal gain value. In this study the link was excited at its natural frequency, and the gain value (K_p) was increased, at each value of gain the amplitude of the transverse displacement at the free end of the link was recorded. The gain was applied proportionally to the voltage output from the PZT sensors. The percentage decrease was calculated based on the displacement at the case where no control was applied. The results shown in Figure 5.2.3 show a clear convergence at the proportional gain value $K_p = 1040$ which achieved a percentage decrease of 89.9%. Hence, this gain value was taken to be the optimal for the conditions in this experiment.

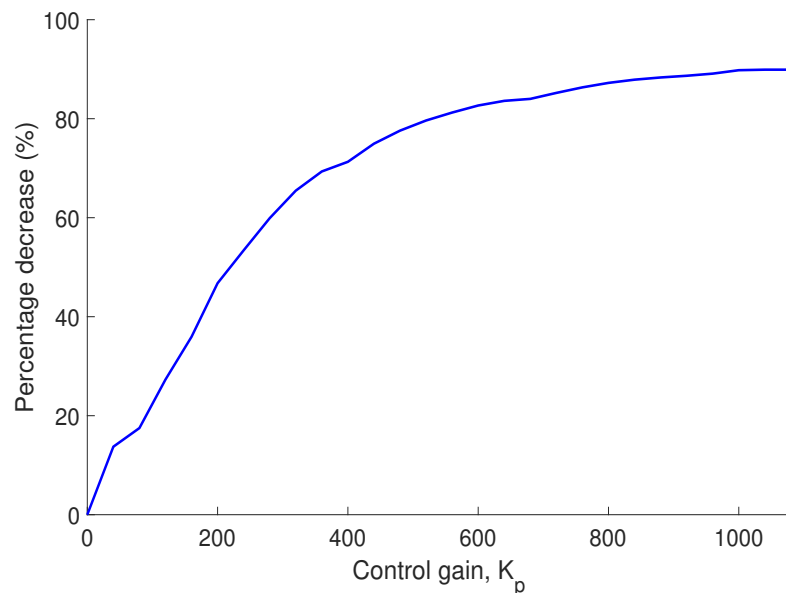


Figure 5.2.3: Percentage decrease attained by the RPi for a range of gain values ($K_p = 0$ to 1040).

The link was excited using a swept sine wave input of constant acceleration and increasing frequency, and the tip displacement, base displacement and voltage output from the PZT sensors were recorded. The frequency range used was chosen so that it comfortably contained the link's first natural frequency (3.59 Hz); a range of 1.5 Hz to 6.5 Hz (see Section 3.5.1). A fast Fourier transform (FFT) was applied to the data to obtain the results in the frequency domain, and the tip displacement and voltage output were both divided by the base displacement to obtain two frequency response

functions (FRFs) of the magnitudes m/m and V/m , respectively. This experimental method was repeated for four cases of varying gain value ($K_p = 0, 260, 520$ and 1040), with these values governed by the obtained optimal value.

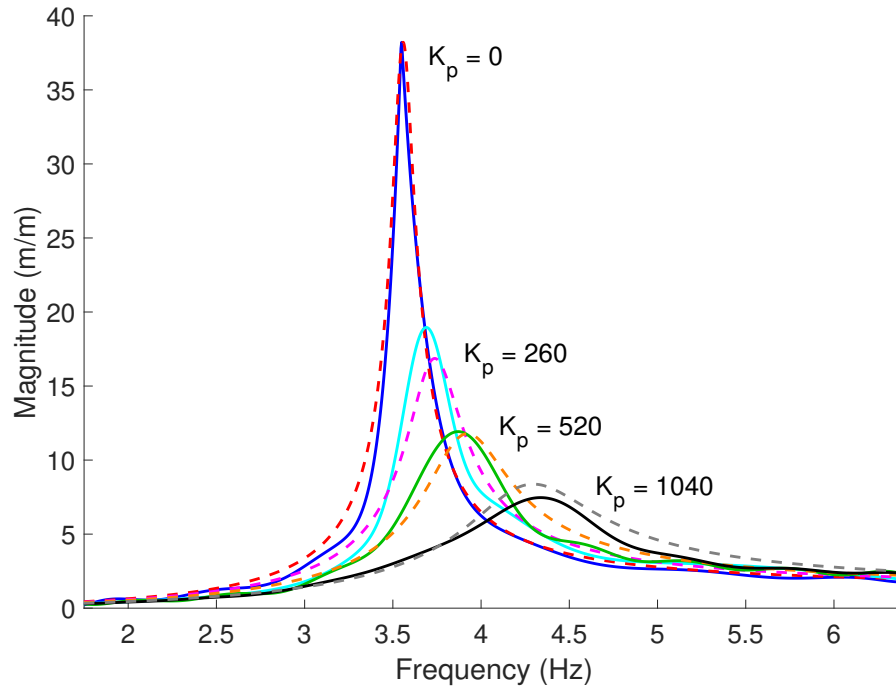


Figure 5.2.4: FRF of tip displacement divided by base displacement for multiple gains for the experimental (solid lines) and analytical (dashed lines) results.

Figure 5.2.4 contains the experimental (solid lines) and analytical results (dashed lines) for the four values of proportional gain, it should be noted that the experimental results presented are the outcome of curve fitting. The method of curve fitting used was selected on the basis of the best representation of the experimental results whilst removing any anomalies. MATLAB's 'modalfit' function was utilised to obtain 'cleaner' FRFs [158]. These results have the magnitude produced through dividing the tip displacement by the base displacement. Observing the experimental values it can be seen that the control system increasingly attenuates the magnitude of the response with increasing values of gain for those frequencies immediately surrounding the natural frequency. From the comparison between these different cases it can be seen that the control system achieves this attenuation through the increase of stiffness and damping, leading to an increase in the natural frequency and a decrease in the magnitude of the response. This type of response from the control system is not traditionally seen when only a proportional gain is used, as in this case where a proportional gain is applied to the voltage output from the PZT sensors, it is more indicative of proportional-derivative control. The reason for this anomaly can be found through analysing the governing

closed loop equations of the PZT sensors and the link structure, which are used to predict the voltage output from the strain induced upon them by the link's vibrations. These equations were developed in Section 4.2.2, where it was suggested that two coefficients are present which influence the stiffness and damping of the system, $RE(\omega)$ and $IMG(\omega)$ (see Equations 4.12 and 4.13). These coefficients are positive, and their magnitude is dependent upon the resistance (R_{lps}) and capacitance (C_{ps}) of the control circuit. The fact that these coefficients are positive lends to both the damping and stiffness of the system increasing when the proportional gain (K_p) is increased, thus explaining the response obtained from the results.

Comparing the analytical results with those obtained experimentally, it can be seen that a good prediction is obtained, validating the equations, principles and theories used in the analytical model. Noticeably, the open loop response (the case of $K_p = 0$) has a better prediction in comparison with the other cases, however, these cases are still considered a good prediction. This is due to the coefficients $RE(\omega)$ and $IMG(\omega)$ having no influence on the system in the open loop case, however as K_p increases so does their influence. With these coefficients being based upon the values of resistance and capacitance in the circuit it was important to obtain an accurate prediction of these values through optimisation. The FRF produced by the closed loop analytical model was compared with that produced by the experiment in terms of damping and natural frequency, utilising the objective function in Equation 5.2.

$$O = u_1 \left(\frac{\omega_n^{ana}}{\omega_n^{exp}} - 1 \right)^2 + u_2 \left(\frac{\zeta_n^{ana}}{\zeta_n^{exp}} - 1 \right)^2 \quad (5.2)$$

where the superscripts *ana* and *exp* denote the analytical and experimental results, respectively. u_1 and u_2 , are weights within the function and were respectively set to 0.9 and 0.1, resulting in a higher level of importance being placed on the natural frequency of the response whilst still considering the damping. These weights effectively alter the importance of the natural frequency and damping in terms of how closely the resultant analytical FRF should match these experimental values. Through this optimisation the values of resistance and capacitance were found to be: $C_{ps} = 0.01$ F and $R_{lps} = 2.88$ Ω . Whilst the values of the resistors in Figure 4.4.6 ($R_1 = R_2 = R_3 = 10$ M Ω), would suggest that $R_{lps} = 15$ M Ω , the RPi manipulates the voltage reading so that the voltage to which the proportional gain is applied is equivalent to the voltage immediately from the PZT sensors. This omits the inclusion of the resistors in the analytical model. The resistance value found through the optimisation is equivalent to the resistance of the wires and other components in the system. The voltage manipulation conducted by the RPi may have some effect on the value of capacitance required in the analytical model, however the optimal capacitance obtained is a lot greater than that of the PZT

sensors (7.89 nF). So this value is more likely a result of the capacitance contributions from the other components (i.e the RPi, the MCP3008, the diode and the HVDs).

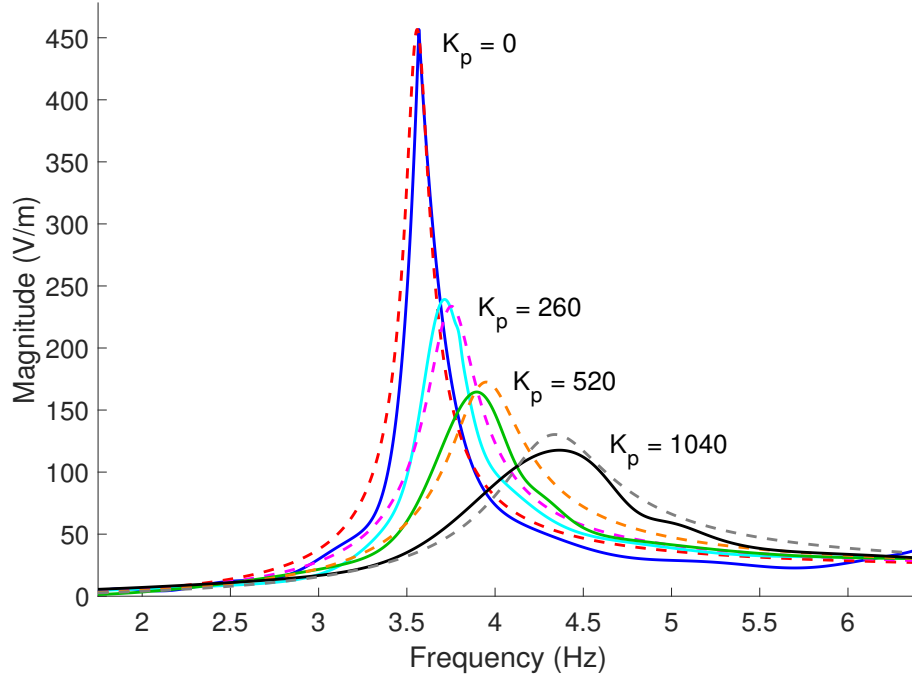


Figure 5.2.5: FRF of voltage output from PZT sensors divided by base displacement for multiple gains for the experimental (solid lines) and analytical (dashed lines) results.

The results of the FRFs where the magnitude is the voltage output from the PZT sensors divided by the base displacement are shown in Figure 5.2.5. Again, first focusing on the experimental results, it can be seen that a similar trend is present as with the previous FRFs (Figure 5.2.4): the natural frequency and damping of the results both increase with increasing values of K_p . As with the previous FRFs related to this experiment this shows that the control system is effective in attenuating the vibrations along the link, and that comparing the voltage output between cases of different values of K_p is a good method of observing the system's performance. However, the alteration in stiffness and damping results in the proportionality between the voltage FRFs and the displacement FRFs varying in magnitude. In the open loop case, the voltage output is proportional to the free end of the link in the relation:

$$W_{rel}(L_{lk}, t) = \alpha_V V_{out,ps} \quad (5.3)$$

where $\alpha_V = 0.0837$. However, increasing the value of K_p leads to a decrease in this factor of proportionality.

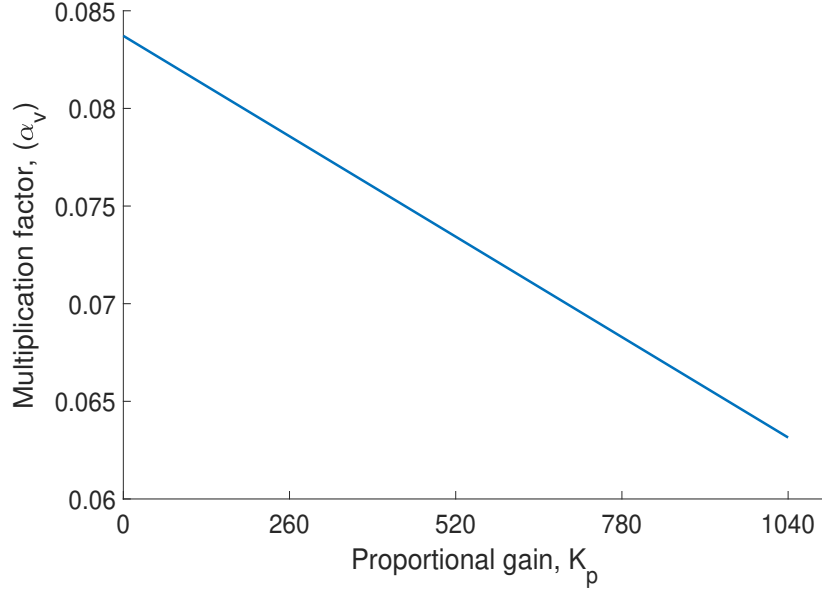


Figure 5.2.6: Proportionality between tip displacement and voltage output from piezo-electric sensors for varying gains.

The relation between α_V and the proportional gain K_p is shown in Figure 5.2.6. It is clear to see that the multiplication factor, α_V linearly decreases as the proportional gain, K_p increases. This enables the alteration of the coefficients' influence on the stiffness and damping of the structure, so that the values of $RE(\omega)$ and $IMG(\omega)$ and may be multiplied by some weighting values; u_{RE} and u_{IMG} respectively. Thus Equation 4.13 may be altered to include these weights to yield:

$$\frac{V_{out,ps}}{w_b(y,t)} = \frac{-\omega^2 \phi_n(y_{LDS}) m [-u_{RE} RE(\omega) - u_{IMG} IMG(\omega) j]}{-\omega^2 + [2\zeta_n \omega_n \omega + \chi_{pa} K_p IMG(\omega)] j + \omega_n^2 + \chi_{pa} K_p RE(\omega)} \quad (5.4)$$

The weights that account for the multiplication factor (α_V) were found (through optimisation) to be: $u_{RE} = 1.1$ and $u_{IMG} = 0.8$. With the inclusion of these weights, and maintaining the values of resistance and capacitance as found through the previous optimisation the analytical model is capable of predicting the voltage output FRF to an acceptable degree.

5.3 A comparison of performance: dSPACE vs. Raspberry Pi 3 (Control System B)

The choice of components, in particular the single board computer (SBC), was driven by their perceived practicality and expense. Whilst Raspberry Pi 3B+ (RPi) does adhere to these specifications, its utilisation within the control system design leads to a compromise regarding the processing capabilities. Even when considering other SBCs on the market (see Tables 4.3.1 and 4.3.2) there would still be a significant deficit in processing capacity when compared with a purpose-built control system such as the dSPACE MicroLabBox. However, when comparing the dimensions of the RPi (0.0856 m \times 0.0565 m \times 0.017 m) with those of the dSPACE MicroLabBox (0.31 m \times 0.25 m \times 0.115 m), and noting that the dSPACE system is 300 times more expensive, the reasons for the preference towards the RPi become evident.

To establish the performance of the RPi system and compare it to that of the dSPACE system two experimental studies were conducted. The dSPACE MicroLabBox replaced the RPi, the analog to digital converter (ADC) and the circuits used to amend the signal between the PZT sensors and the ADC (the HWRC and the PDC). All other aspects of the configuration remained identical, and so the reader is referred to 5.2.1 where the remaining components in the ‘Control System B’ block are the HVDs, and the PZT sensors are connected directly to the dSPACE MicroLabBox. The first of the experiments compares the settling time reduction achieved by the two systems. Here the link was excited at its natural frequency (3.59 Hz) using a sinusoidal base excitation until a steady state response was present, before instantaneously stopping the excitation and applying the control. For both systems the dSPACE MicroLabBox was used to produce a signal to control the shaker table. For the experiments also utilising this control system the simultaneous stopping of the excitation and starting of the control application was easily incorporated into the SIMULINK/ControlDesk application. However, when the control was performed by the RPi some form of communication was required to employ the control at the instant the excitation stops. This was achieved by including an output signal within the SIMULINK/ControlDesk application which is low (0 V) when the excitation is applied (control off) and high (3.3 V) when the excitation is stopped (control on). This binary signal is sent to one of the RPi’s digital input pins, and the Python script used was slightly amended to incorporate this signal. The signals that are sent to both the shaker and the RPi by the dSPACE system have been illustrated in Figure 5.3.1. It should be noted that the signal shown in this plot representing the signal sent to the shaker has been simplified through the normalisation of the magnitude to unity and the reduction of the frequency to 0.25 Hz. This provides a better visualisation of the signals.

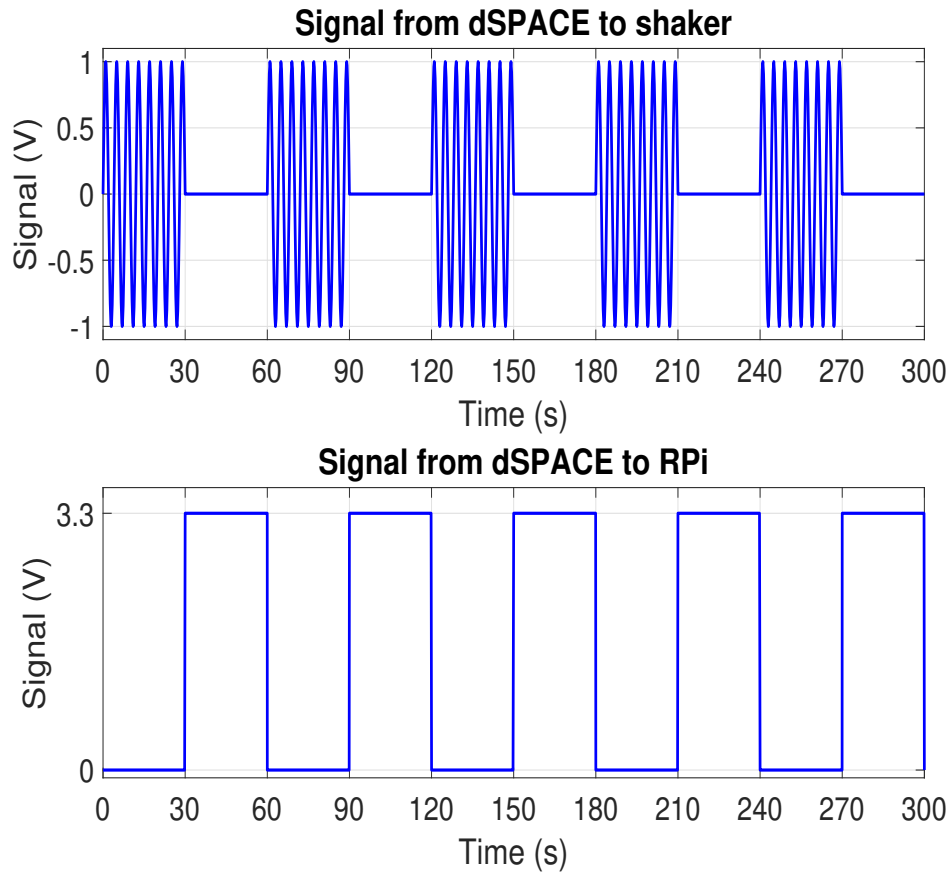


Figure 5.3.1: Example of the signals from the dSPACE governing the shaker and RPi outputs.

The proportionally applied gain (K_p) was increased after each cycle (excitation on and control off followed by excitation off control on) to observe the effect of the increasing gain value on the settling time. Again, this alteration during the experiment was easily incorporated within the SIMULINK/ControlDesk application, and hence the experiment where the dSPACE MicroLabBox applied the control was as easily conducted. Whereas, for the RPi case another communication signal was required between the two systems to adjust the control gain value at the correct time. This secondary signal was analog and was to be converted by the MCP3008 for the RPi to interpret as a 'bit' value. An issue arose in that the bit value varied from the predicted value by approximately ± 5 bits (± 0.0245 V) at the most, due to unavoidable noise in the signal. This meant that the required K_p value was governed by a range into which the read bit value fell, and these ranges should have suitable gaps between to allow for anomalous readings. This issue coupled with the constraint of the input voltage range of the MCP3008 lead to a constraint of the number of gain values able to be included within the Python script. Thus, the overall experiment to observe the settling

time attained by the RPi was split into sections, with each section containing twenty gain values corresponding to multiples of 0.25 V ranging from 0 V to 5 V. A maximum value of gain was arbitrarily chosen as 3160, which led to the gain values increasing in multiples of 40. This led to a total of eighty gain values to be tested, however the voltage range of the ADC meant that only twenty different voltage values were available to be assigned to a value of gain. Hence the control code was run four times producing as many sets of results. A simplified version of the bit reading by the RPi and the allowable range can be found in Figure 5.3.2, along with the corresponding gain value (K_p) as interpreted by the RPi.

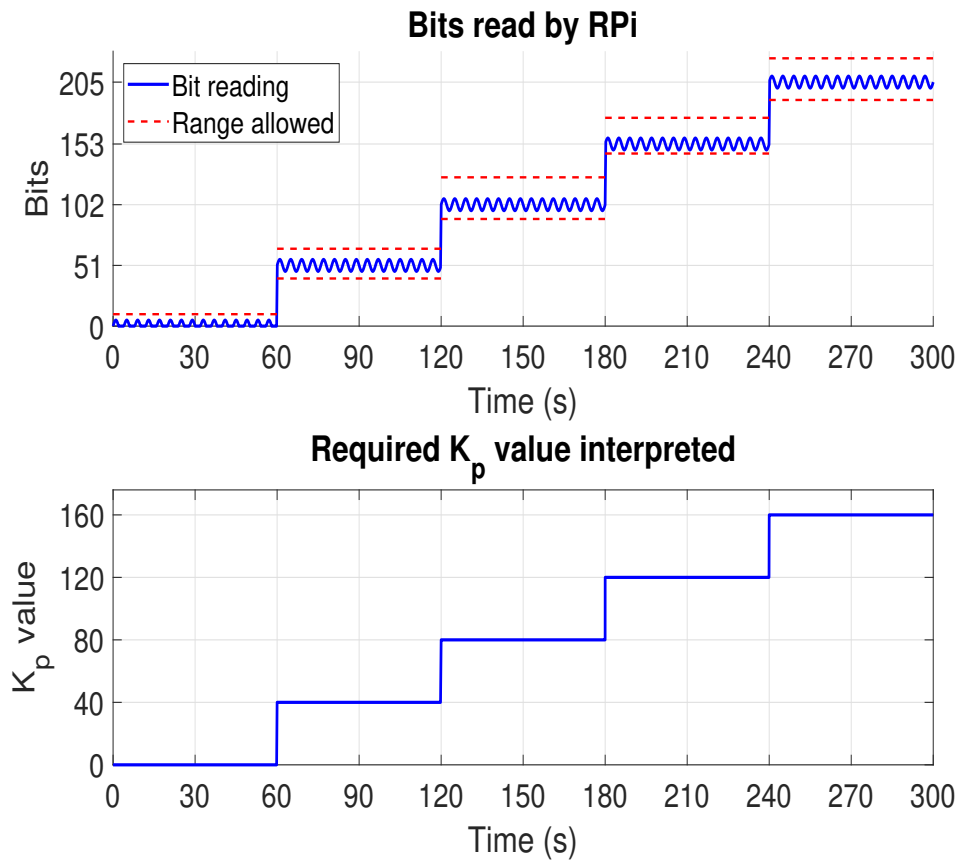


Figure 5.3.2: Example of the signals from the dSPACE governing the change of gain value at each cycle.

For this first comparison of performance the settling time was taken to be the time between the excitation stopping and the tip displacement becoming less than 0.00035 m. Figure 5.3.3 shows the experimental results of the dSPACE and RPi control systems for increasing values of proportional gain (K_p). From the results it can be seen that when no control is applied ($K_p = 0$) that the settling time is approximately 22.7 seconds. Both control systems are capable of reducing this settling time to approximately 2.3

seconds, with both results converging at this time. As the results both converged at a time of 2.3 seconds the higher values of gain used in the experiment were not included. It can be seen from Figure 5.3.3 that the RPi system has the same level of performance as the dSPACE system with regards to the reduction of the settling time of the link. However, there is a difference in the rate at which the two systems show a convergence of settling time, the RPi achieves a settling time of 2.7 seconds at $K_p = 120$, whereas the dSPACE system achieves the same at $K_p = 360$.

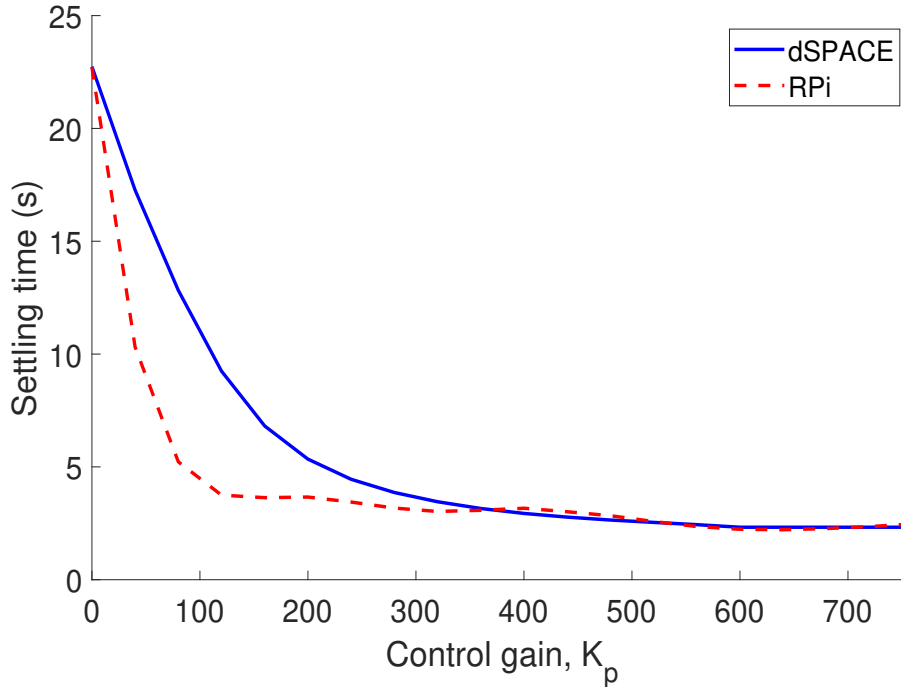


Figure 5.3.3: Comparison of the settling time achieved with increasing proportional gain between the dSPACE and Raspberry Pi 3 systems.

Studying Figure 5.3.4 yields some insight into the reason behind the difference in convergence rates. Whilst both systems show a reduction in the amplitude of the transient response, the RPi system notably increases the frequency, more so than the dSPACE system. Thus, for a better observation of how the two systems influence the damping and natural frequency of the response an additional experiment was conducted. In this experiment the link was subject to a base excitation of a swept frequency sinusoidal wave form for three different cases of control gain using both control systems. The time domain results of the tip and base displacements were subjected to a fast Fourier transform (FFT), before dividing the former by the latter to produce the frequency response functions (FRFs) shown in Figure 5.3.5. The case of no control ($K_p = 0$) for both systems were practically identical, hence only one representation of this has been included in the results. Whereas for the other values of control gain ($K_p = 240$ and

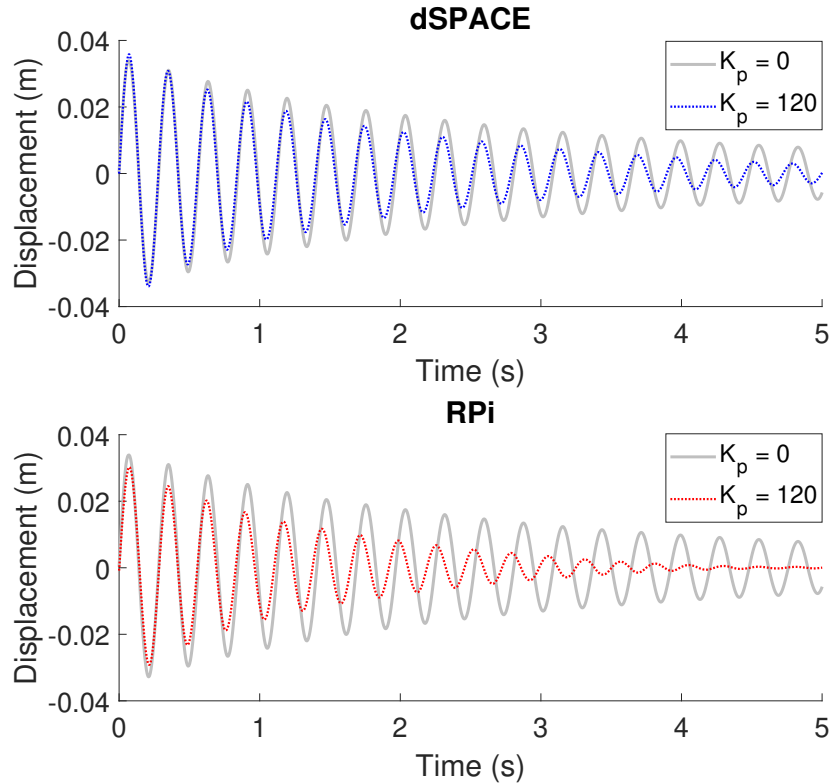


Figure 5.3.4: Experimental results of the dSPACE and RPi control systems for two gain values.

$K_p = 640$) there are significant differences to be seen between the two control systems.

The RPi system, for both cases of control (referring to Figure 5.3.5), shows a clear increase in natural frequency of the response, which is quintessentially proportional control. However, the dSPACE system produces a response which has negligible increase in the natural frequency but greater damping in comparison to the RPi results of the same gain values. Thus, the dSPACE results are more indicative of derivative control. Neither the RPi or the dSPACE system conform to either type on control, but rather a combination of both. Referring to Equation 5.4 developed in Section 5.2, it was found that two coefficients ($RE(\omega)$ and $IMG(\omega)$) are present which influence the the natural frequency and damping respectively. These coefficients are a product of the control system's resistance and capacitance, thus when comparing the dSPACE and RPi control systems it may be concluded that these values differ between them. This lends to the difference in convergence rate of the settling time observed in Figure 5.3.3. However, as both systems achieve the same reduction in settling time, both systems were considered to have the same level of performance.

A second experiment was conducted to further ascertain the performance of the RPi system, again using the dSPACE system as a reference. This experiment saw the

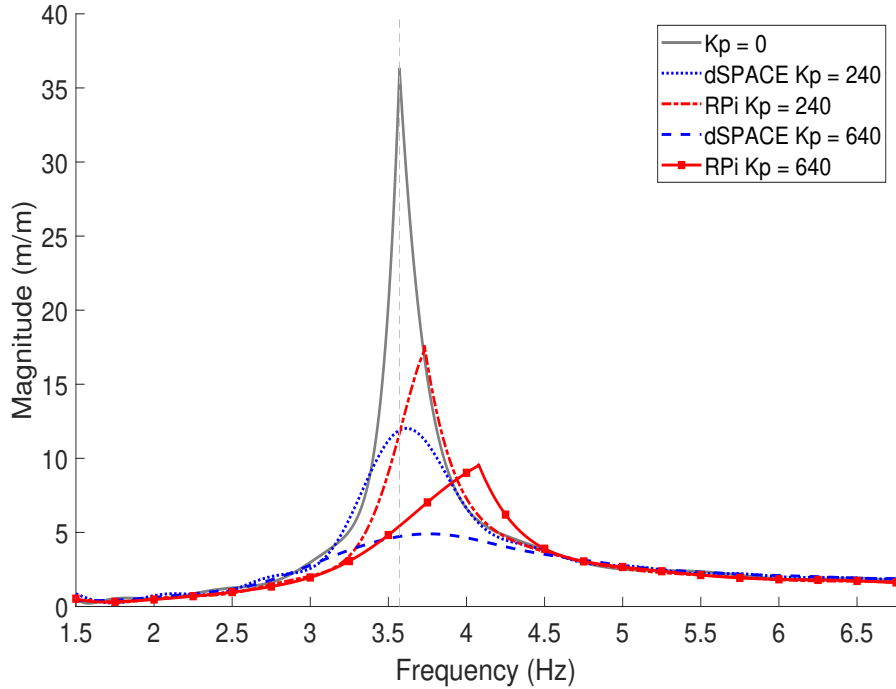


Figure 5.3.5: Comparison between the FRFs of the RPi and dSPACE control systems for different cases of gains.

link excited at its first natural frequency (3.59 Hz), and control was applied across a range of proportional gain values (K_p), unlike the previous experiment the excitation and control were applied simultaneously. So, as the dSPACE MicroLabBox was used to define the base excitation for both control systems, only an analog signal was required to set the gain value for the RPi system as previously (see Figure 5.3.2). The percentage decrease was obtained for each gain value based on the case where no control was applied ($K_p = 0$) for both systems, and the results of this experiment were used to find an optimal value of the control gain.

Figure 5.3.6 contains the results of this experimental comparison of the two control systems. Aside from some minor discrepancies the results of this experiment corroborate with those of the settling time experiment in that the performance of the two systems may be considered identical. Both systems converge to the same percentage decrease of approximately 89.9% at a gain value of $K_p = 1040$, where the differences between the two results at lower gain values can be attributed to minor unavoidable discrepancies between the voltage readings of the two systems. It should be noted that higher values of gain were employed in the experiment than those shown in Figure 5.3.6, however the results between the two systems differed. When $K_p > 1040$ the percentage decrease attained by the RPi system increased slightly, whereas that of the dSPACE decreased to a similar degree before both results converged again at $K_p = 3040$ at a percentage

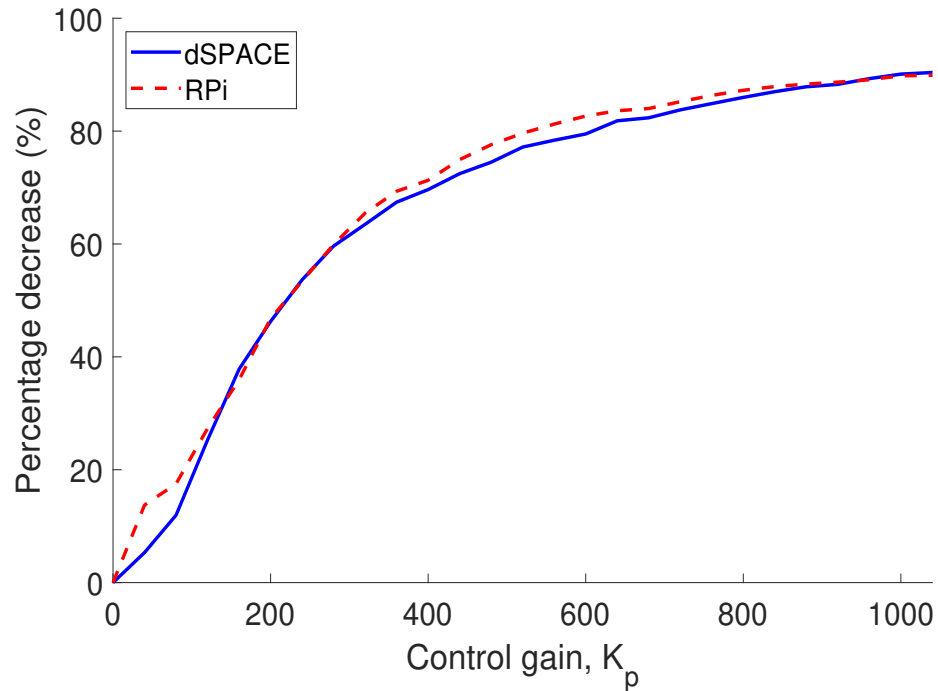


Figure 5.3.6: Comparison of the percentage decrease of tip displacement achieved with increasing proportional gain between the dSPACE and Raspberry Pi 3 systems.

decrease of 85.4%. This may, again, be attributed to discrepancies in the voltage readings. However, to ensure that this was the most likely reason the experiment was repeated twice more, yet the same trend in the results was observed. Therefore it was concluded that the optimal gain value be $K_p = 1040$ due to the difference in the results between the two control systems when applying higher values of gain, and the fact that the converged percentage decrease value after this was lower.

5.4 Link mounted on robot manipulator (Control System B)

With the link mounted on the robot manipulator and the circuit housed in an enclosure to reduce the risk of injury, three different experiments were conducted, with each having different base excitation types. Prior to conducting the intended experiments, and with the link mounted on the robot manipulator, the circular motion at the radii defined in Section 3.5.1 was exerted on the link. Upon observing the response of the beam it was clear that at 100% joint velocity and the pre-determined radii for the frequency range resulted in large deformations of the link. Under other circumstances these large deformations could be included in the experiment to observe the capabilities of the control system under these conditions. However, as the experimental set-up contains components which are not connected in a permanent manner (for the purpose of maintenance and alterations during experiments), these large deformations were deemed unacceptable. The connections between components were likely to become loose or even fail altogether posing a risk to not only the system, but to individuals in the vicinity as well.

To avoid these large deformations it was concluded that the centripetal acceleration at the end effector of the robot needed to be reduced. In addition this centripetal acceleration should remain constant throughout the frequency range so that the force applied to the link also remains consistent. This led to conducting a study of the frequency obtained at a range of lower velocities and radii than that previously tested (with the link removed for safety). It was found in the previous study (see Figure 3.5.1) that lower radii at maximum velocity were inconsistent with the general trend, thus it will be important to observe these smaller radii at lower velocities to ascertain whether there is a better relation. The range of velocities used in this study were from 2% to 13% and at each velocity the radii tested ranged from 0.0005 m to 0.015 m. The end effector position was recorded using the KUKA sunrise software at a sampling rate of 1 KHz, and the frequency produced for each case was obtained through the displacement along the x axis. The centripetal acceleration (a_c) was calculated using Equation 5.5.

$$a_c = r \times \omega^2 \quad (5.5)$$

where r is the radius of the circular motion and ω is the frequency of the motion (in radians/s).

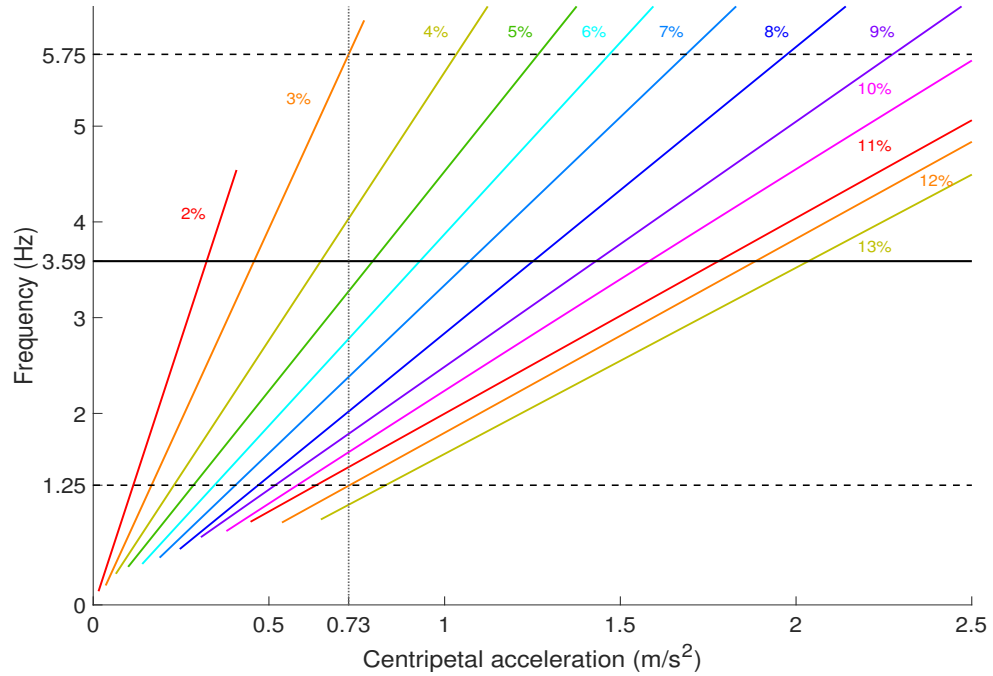


Figure 5.4.1: The relationship between centripetal acceleration of the end effector against the frequency for a range of maximum joint velocities.

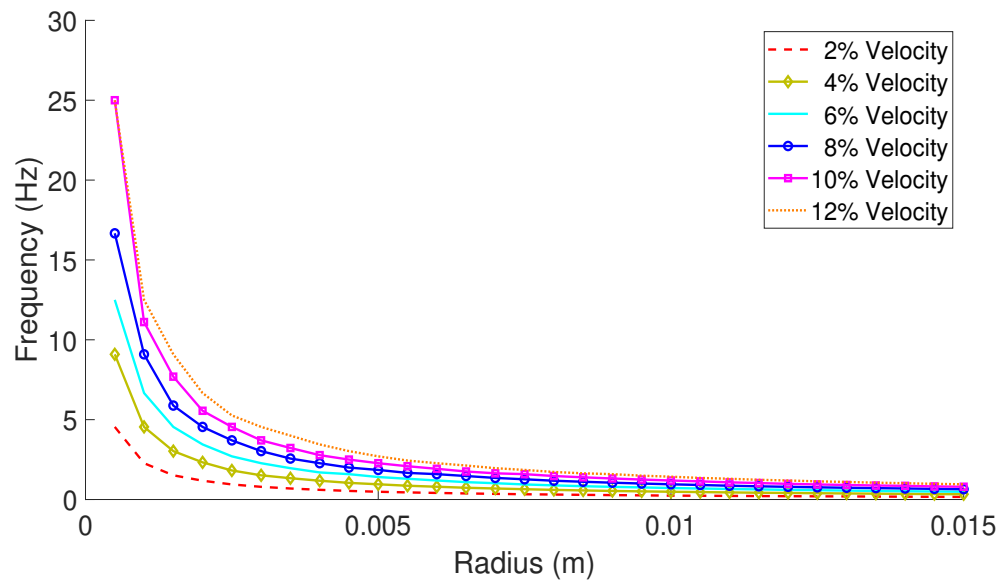


Figure 5.4.2: The relationship between the radius of the motion of the end effector against the frequency for a selected range of maximum joint velocities.

The results of the centripetal acceleration study are shown in Figure 5.4.1. From these results, it can be seen that there are no issues with the relationship between the frequency and smaller radii when the velocities used are low. The centripetal acceleration is proportional to the radius, hence obtaining a linear relationship between this acceleration and the frequency absolves any aforementioned issues. Yet, Equation 5.5 suggests that the frequency and centripetal acceleration would not have a linear relationship. However, this is with the assumption that the relationship between the radius of the motion of the end effector and the resultant frequency is linear. From Figure 5.4.2 which shows this relationship for selected maximum joint velocities, it can be seen that this is not the case. This explains the linear relationship observed in Figure 5.4.1. It can be seen from this figure that lower velocities and radii produce low magnitudes of centripetal acceleration, in the range suitable for the experiments. The frequency range required for the experiments (1.25 Hz to 5.25 Hz) is included alongside the results as dashed black lines, with this range governing the magnitude of the centripetal acceleration to be used. Hence, the lowest value of a_c whilst still including all frequencies in the required range was determined to be 0.73 m/s^2 . Through interpolation and Equation 5.5 the required radii and velocities were obtained for each frequency in the range. The values corresponding to the natural frequency of the link (3.59 Hz) were used to observe the deformation of the link at what should be the highest level excitation. Observing the link's response to the excitation revealed that the selected centripetal acceleration results in an acceptable level of deformation; large enough to justify the use of the control system and small enough so as to not pose a risk.

Initial testing and calibration of the control system revealed a presence of noise in the readings of the voltage output from the sensors. A noise which was not experienced by the system in the previous environment, and may be attributed to other devices interfering with the analog to digital converter (ADC) readings. It was found that through adjusting the resistance values within the circuit (see repeated image of Figure 4.4.6 shown in Figure 5.4.3) the noise was reduced. R_2 and R_3 were previously both $10 \text{ M}\Omega$, but exchanging both of these resistances to $1 \text{ M}\Omega$ led to a reduction in the noise. However, even with this amendment there was still a low level of noise present which would have caused inaccuracies in the experiments. So this noise was removed through the subtraction of the bit readings within the control script. As only a low level required removal (20 bits or 0.098 V), this noise reduction technique had little effect on the overall reading of the voltage output from the sensors and hence the control system.

To observe the performance of the control system when the robot manipulator performed a short impulse like motion, the first joint of the robot was tasked with moving

10° at its maximum velocity of 98°/s. For all of the experiments where the link is mounted on the manipulator it was deemed impractical to use laser displacement sensors (LDSs), due to the motion of the end effector being along two axes. Thus, the performance of the control system was analysed based on the voltage output from the sensors, which is proportional to the strain on the link and therefore its transverse motion. The experimental set-up of this first and the proceeding experiments is outlined in Figure 5.4.4, where the robot pose shown in the image is the initial pose for all experiments.

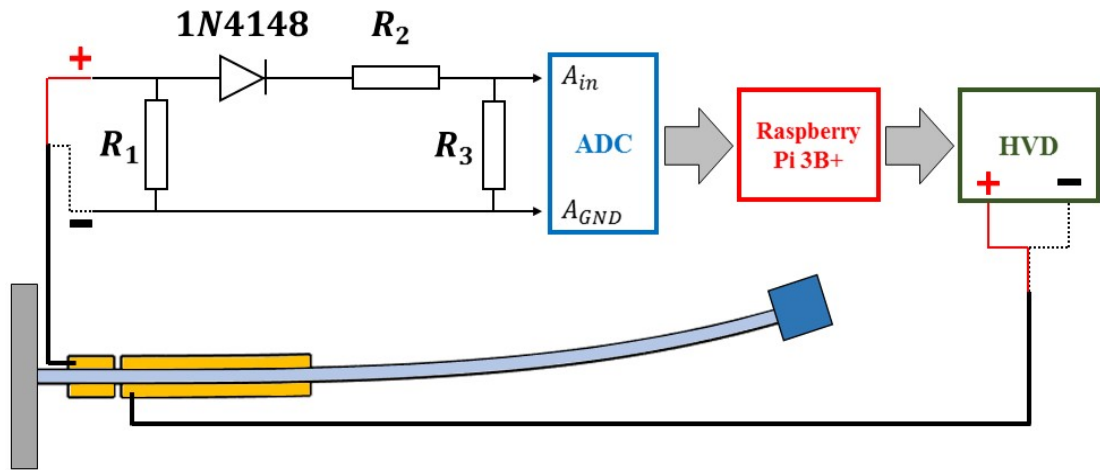


Figure 5.4.3: An illustration of the connections between the PZT sensors and PZT actuators, including the circuit diagram (repeated).

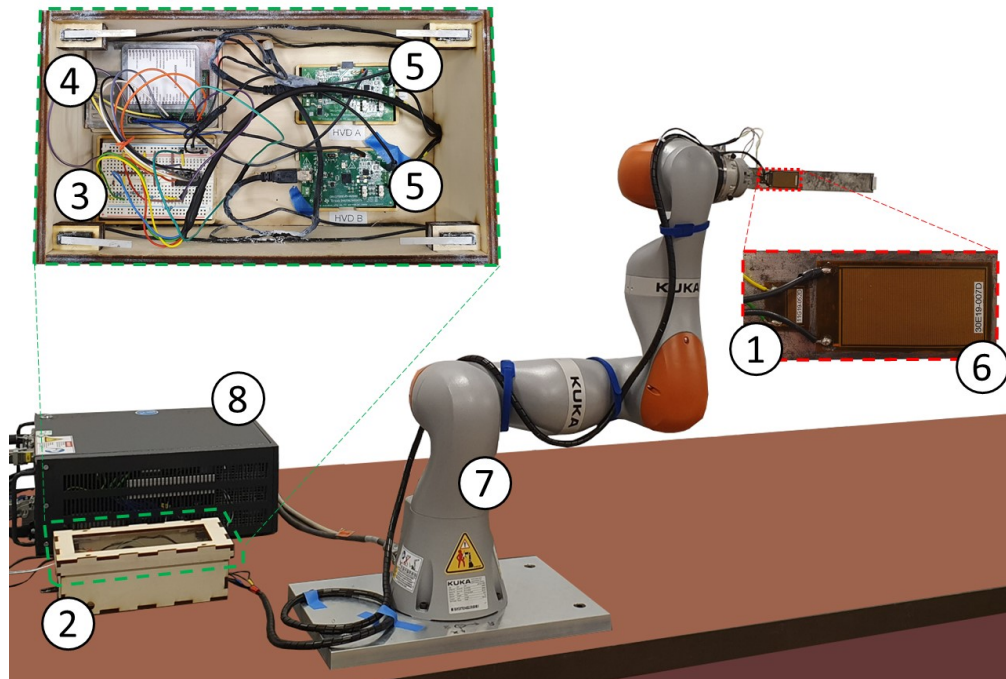


Figure 5.4.4: Experimental set-up of the link mounted upon the robot manipulator.

The image has been simplified with certain aspects of the set-up highlighted, and the pieces of equipment in Figure 5.4.4 are numbered as follows:

1. PZT sensor.
2. Circuit enclosure.
3. Half wave rectifier and potential divider circuits, and the analog to digital converter.
4. Raspberry Pi 3B+.
5. High voltage drivers.
6. KUKA iiwa 7 R800.
7. KUKA Sunrise cabinet.

The results of the first experiment to ascertain the effectiveness of the control system for reducing the settling time of the link when it was subjected to a short sharp impulse are shown in Figure 5.4.5. The settling time was taken to be the time between the impulse from the robot and the voltage output reducing to zero volts. The range of gain values shown in these results are from $K_p = 0$ to $K_p = 400$ in increments of 10. Higher gain values were included in the experiment, but as can be seen from the results the settling time converged at a gain value of $K_p = 340$. With no control applied to the system the settling time of the system was approximately 9.04 s, the convergence occurs at a time of around 2.76 s. A lower settling time is not achieved by the control system due to the limitations of the PZT actuators. These components have a maximum operating voltage of 360 V, which was limited to 350 V to reduce the risk of damage. When the proportional gain value is equal to or greater than 340 this voltage limit is reached, hence no greater force from the actuators is achievable. Taking into account this limitation, the reduction in settling time can be viewed as a very acceptable outcome for the designed control system.

There is a noticeable difference between the results shown in Figure 5.4.5 and the results of the experiment which utilises the shaker as an excitation source. In the latter the settling time was shown to converge at $K_p = 120$, whereas in these results this convergence occurs at $K_p = 340$ (see Figure 5.3.3). This discrepancy is a result of the voltage output from the sensors, which is directly proportional to the strain near the clamped end of the link. The impulse generated by the robot produces a smaller amount of strain on the link compared to that attained through the shaker excitation. Hence, as the voltage applied to the actuators is proportional to the voltage output from the sensors, a larger gain value is required to produce the same amount of voltage, thus the same amount of force to be exerted on the link by the actuators.

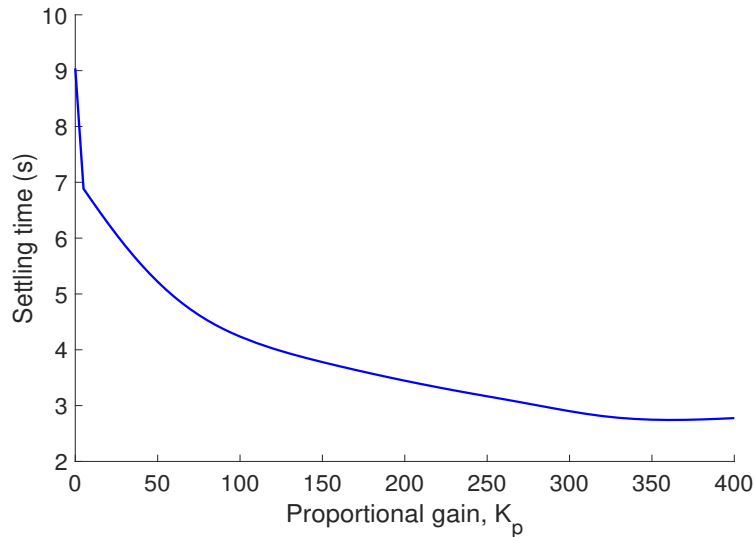


Figure 5.4.5: Settling time against proportional gain (K_p) for joint one of the KUKA manipulator moving 10° at 100% velocity.

In the second of the experiments the robot was moved in a circular motion at the radius and a joint velocity of 0.0015 m and 5%, respectively. Achieving an excitation frequency of approximately 3.59 Hz (the link's first natural frequency), and a centripetal acceleration of 0.73 m/s^2 . This circular excitation was held at constant at the natural frequency for 60 seconds so as to observe the steady state response, and was repeated for a range of proportional gain values (K_p). Through the use of this second excitation type it was possible to determine the percentage decrease of the voltage output from the sensors for each gain value based on the case where no control was applied.

The results of this second experiment are shown in Figure 5.4.6. As with the previous experiment, the gain values tested include higher magnitudes than those shown in the results, but the percentage decrease is shown to once again converge at and above a particular gain value. This convergence may, as previously, be attributed to the limitations of the PZT actuators. These results show that the control system is capable of a reduction in the voltage output from the sensors of 74.93% at $K_p = 200$ (approximately). Which not only evidences the performance of the control system but also yields the optimal gain value to be used in the proceeding experiment. As with the previous experiment this optimal gain value is different to that found through the experiments using the shaker ($K_p = 1040$). In an opposing manner to the impulse test the optimal gain acquired for the robot excitation is smaller than that of the case when the link is mounted upon the shaker. This stands to reason that the robot manipulator exerts a larger amount of force on the link than the shaker, hence a larger voltage is produced from the PZT sensors. In turn the convergence of the percentage decrease occurs at a lower gain value for the robot manipulator case due to the relation between

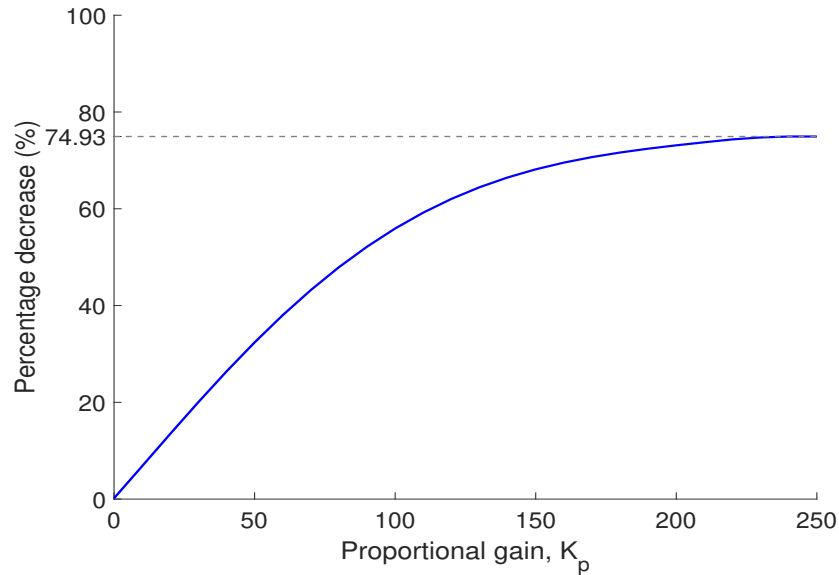


Figure 5.4.6: Percentage decrease of voltage from sensors when excited at the natural frequency, when mounted on the KUKA manipulator.

the voltage applied to the actuators and the voltage output from the sensors.

In the third experiment the link was again excited in a circular manner, only this time over varying frequencies for three gain values ($K_p = 0, 100$ and 200). The range of these values was based upon the previously obtained optimal value. Idealistically the robot would have been programmed to excite the link through the full range of frequencies (2.3 Hz to 5.25 Hz) in one ‘run’. However, there was a software limitation regarding the file size able to be sent to the SmartPad (a touch screen hand held device) to control the manipulator. This meant that to include all frequencies within one script each frequency would only be excited for a short amount of time, not allowing for the steady state response to be observed and leading to inaccurate results. Therefore the frequency range was split into sections to maintain time efficiency as best possible whilst still attaining accurate results. The required radius of the circle and velocity setting corresponding to the required frequency whilst maintaining a centripetal acceleration of 0.73 m/s^2 were obtained through the interpolation of previous results (see Figure 5.4.1). This yielded the results shown in Figure 5.4.7 for the frequency range in question.

Prior to utilising this relation for the purpose of observing the control system’s performance, the frequency prediction from the interpolated data was verified through experimental results. At each frequency the end effector was moved in a circular motion for ten turns, and the KUKA Sunrise Software was tasked with recording the end effector position at a sampling rate of 1 kHz. The frequency of the motion was obtained through the observation of the x axis data as a result of the calculated radius/velocity combination, and compared the required frequency. The results of this comparison are

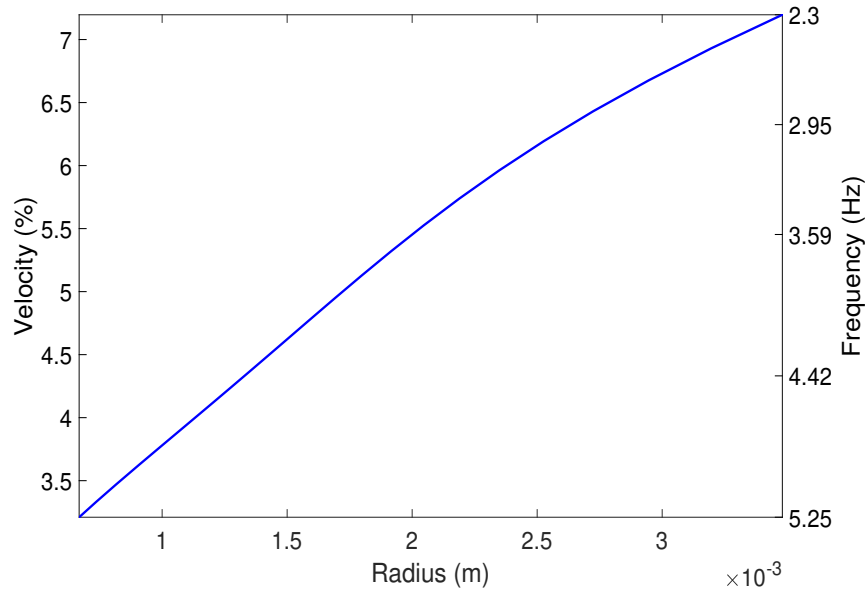


Figure 5.4.7: Relationship between radius of the end effector motion and velocity of the robot manipulator, and the excitation frequency produced.

shown in Figure 5.4.8, where the test number relates to each radius/velocity combination. From these results it can be seen that the interpolated radius/velocity combination produces a frequency that is a very close match to the required frequency, therefore the values can be used for the proceeding experiment. Figure 5.4.8 also gives an insight into the discretisation of the frequency range, which allows for more accurate results without effecting time efficiency. The frequency interval (Δf) is smaller at the region immediately surrounding the natural frequency, and larger in other regions, i.e.:

$$2.3 \text{ Hz to } 3.4 \text{ Hz: } \Delta f = 0.1 \text{ Hz}$$

$$3.5 \text{ Hz to } 3.6 \text{ Hz: } \Delta f = 0.01 \text{ Hz}$$

$$3.7 \text{ Hz to } 4.3 \text{ Hz: } \Delta f = 0.1 \text{ Hz}$$

$$4.5 \text{ Hz to } 5.25 \text{ Hz: } \Delta f = 0.25 \text{ Hz}$$

The frequency response functions (FRFs) obtained for the three values of proportional gain ($K_p = 0, 100$ and 200) are shown in Figure 5.4.9. Where the magnitude of the response was obtained through the amplitude of the voltage output at each frequency divided by the amplitude of the base displacement of the link (i.e the manipulator's end effector displacement). The voltage was recorded using the RPi and the base displacement was recorded using the KUKA sunrise software. The experimental results are denoted by the solid lines, and the results from the analytical model by the dashed lines. The FRFs obtained from the experiment show that the RPi control

system is highly capable of attenuating the vibration experienced along the link, for those frequencies in the region of the link's natural frequency. As with previous experiments it can be seen that the controlled response is akin to what would be expected of proportional-derivative control (see Section 5.2 for further details).

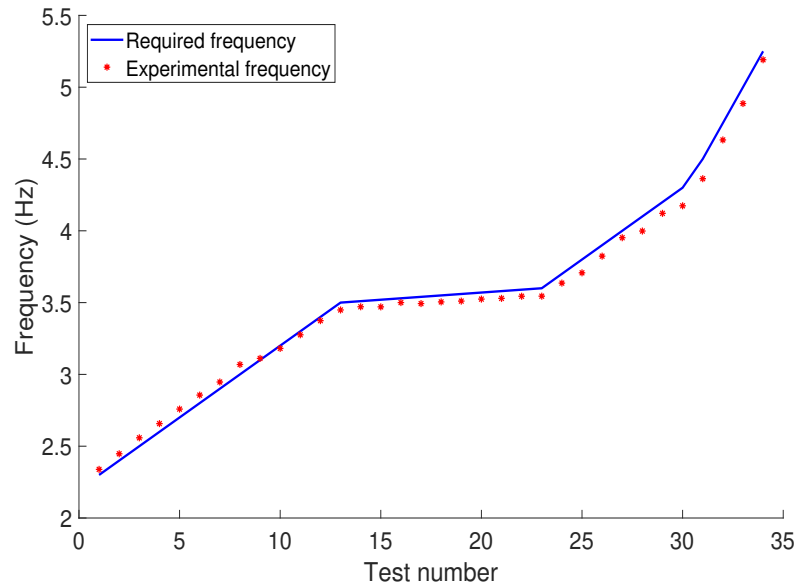


Figure 5.4.8: A comparison between the predicted frequencies obtained from interpolating data, and the experimental frequencies attained.

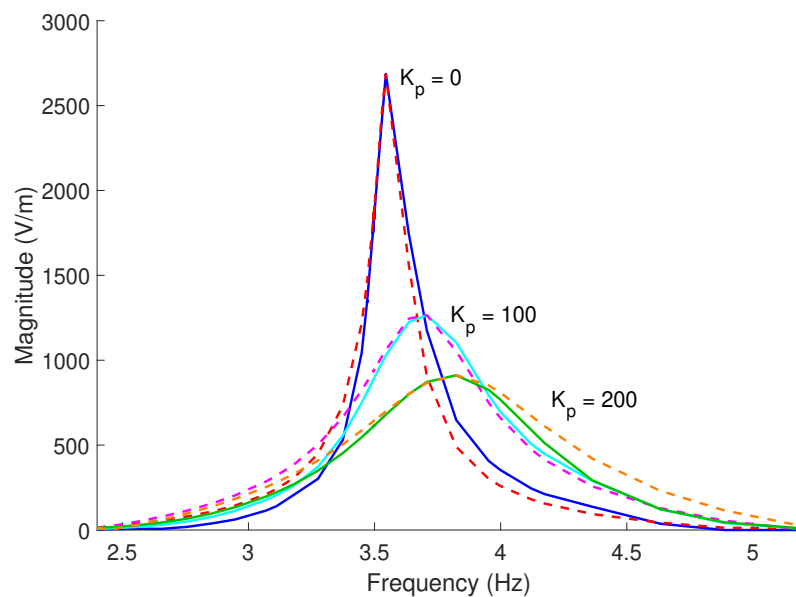


Figure 5.4.9: The response of the system against the frequency of excitation for three cases of K_p , for the experimental results (solid lines) and the analytical results (dashed lines).

To obtain the analytical results (dashed lines) in Figure 5.4.9 a few minor adjustments were made to the model previously developed. As the noise in the readings was not fully quashed through the exchange of the resistor in the circuit (so that $R_2 = R_3 = 1 \text{ M}\Omega$), the remaining noise was removed from the readings. Thus, the same level of voltage needed to be removed from the analytical model to obtain accurate results. Given the multiple changes to the circuitry, including its housing and rewiring, and the noise reduction technique it is understandable that the required values for the capacitance and the resistance in the circuit required alteration. Through the same method of optimisation as used previously, these values were found to be $R_{lps} = 4.8 \text{ }\Omega$ and $C_{ps} = 0.0033 \text{ F}$. These magnitudes are still within a reasonable range as dictated by influence of the values by the multiple components within the circuit. With these adjustments it can be seen that the analytical model are a close match to, and hence a reasonable prediction of the experimental results.

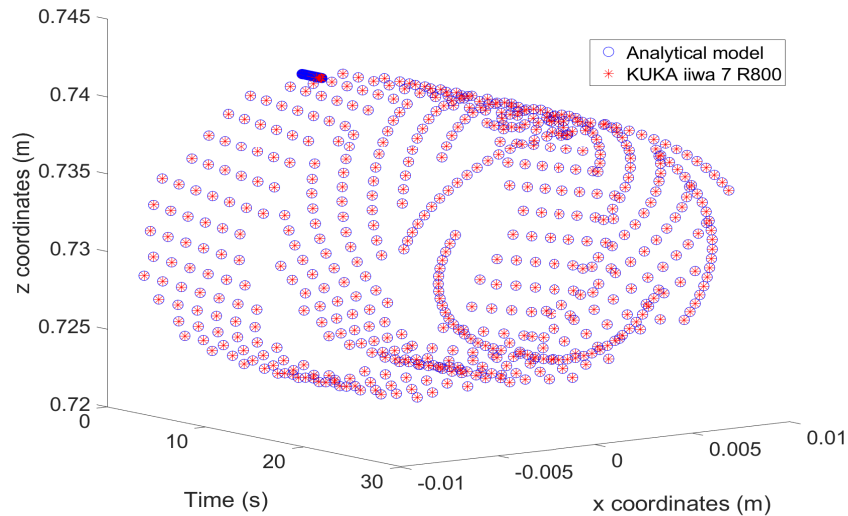


Figure 5.4.10: A comparison of the calculated end effector position from the analytical model and the end effector position retrieved from the experimental studies.

Another data comparison is necessary in order to provide insight into whether the control system affects the functionality of the manipulator. Previously the analytical model of the manipulator was proven to be an accurate representation of the manipulator with no clamp/link structure mounted upon it. Utilising this model again with no changes made, the joint angles obtained during an experiment in which the control system was employed were used as an input to the model. A comparison was then made between the analytical results (of the robot manipulator only) and the experimental results with the link mounted and the control system active, as shown in Figure 5.4.10. The average percentage errors for each axis (x, y, z) between the two sets of results were

calculated to be 0.0042%, $6.88 \times 10^{-8}\%$ and $9.68 \times 10^{-7}\%$, respectively. With the errors obtained through this comparison being negligible, it may be concluded that the link had no influence on the motion of the robot manipulator. As a result of this finding, the models of the link and manipulator need not be coupled to provide an accurate representation of the system, the end effector motion alone may be used as an input into the analytical model of the link.

5.5 Summary

This chapter presented the results of multiple experiments, all of which were conducted with the aim of ascertaining the performance of the designed control system. The experimental results were compared with the results of the respective analytical models, with this comparison suggesting that the models were a good approximation of the structure and designed control system. These experiments included two possible sensor options (IMUs and PZT elements), highlighting the advantages and disadvantages of both before concluding that PZT elements as sensors was the more suitable option. The designed control system was then compared with a purpose-built control system, the results of this comparison led to the conjecture that the performance of the designed control system was of the same caliber as its counterpart. Finally, the designed control system was observed in a scenario reflective of the suggested application, wherein the flexible link structure was mounted on a robot manipulator. The results of these experiments not only confirmed the effectiveness of the control system in the reduction of the transverse displacement of the flexible link, but also led to the conclusion that the models of the robot manipulator and flexible link need not be coupled.

Chapter 6

Control of a nonlinear response

This chapter considers the capability of the designed control system to attenuate a nonlinear response of the link structure. A brief overview and history of nonlinear dynamics is included to introduce the topic and further highlight its prevalence in research, the induction of a geometric nonlinearity is then presented including the development of the experimental set-up. The results obtained through the employment of the control system on the nonlinear response of the system are then presented. A description of the analytical model used as an initial parameter estimate of the system is included as well as an explanation of the optimisation technique utilised to obtain the unknown or inaccurate parameters of the model. Finally the results obtained from the updated nonlinear model are validated through the comparison with the experimental results.

6.1 A brief overview and history

A nonlinear system may be described as one which has a change of output which is not proportional to the change of its input. Nonlinear research as a result is the study of any system which is not inherently linear, and solutions are often sought to find linear approximations of these systems [159]. A nonlinear system may be represented by a set of nonlinear equations, which may in turn be one or a combination of: algebraic, functional, differential (ordinary or partial) or integral [160]. A common method to initially observe systems and determine their characteristics is to obtain their governing equation(s), and manipulate them to provide an insight into their stability at different levels of energy [161]. This qualitative approach to observing nonlinear systems is a practice first envisioned by Poincare in 1889.

Nonlinear systems and their associated phenomena and especially chaos theory appear throughout the universe. A famous mathematician, Stanislaw Ulam once remarked that calling the study of chaos “nonlinear science” was akin to referring to zoology as “the study of non elephant animals” [162]. This quote alone gives the sheer magnitude of the contribution of nonlinear systems in comparison to those which may be deemed (or simplified to be assumed as) linear. Whilst the acknowledgement of nonlinear systems is not new within the scientific community, there are still many aspects of this topic which are still highly prevalent in current research. These investigations focus on an array of nonlinear phenomena including chaos, singularities, multi-stability and limit cycles. A brief history of nonlinear dynamics is included (as Table 6.1.1) to provide an insight to the development of the research in this field and the recent heading of this research [163]. This overview highlights the complexity of the analysis of nonlinear systems, as it was not until the invention of the high-speed computer in the 1950s that major advances in analytical solutions to nonlinear problems were possible.

1671	Newton invents differential equations, discovered his laws of motion and universal gravitation. Combining these with Kepler's laws of planetary motion yielded a solution to the two-body problem.
1700s	An era in which calculus and classical mechanics were prevailing topics.
1800s	Further analytical studies of planetary motion were a common topic in dynamics research in an effort to solve the three body problem.
1890	Poincare revolutionised the approach to nonlinear science, with a focus on the three body problem. Qualitative rather than quantitative questions about nonlinear systems were emphasized in his work, resulting in the development of the geometric approach. In his work the first glimpse of chaotic systems was presented.
1920-1950	Research was focussed on nonlinear oscillators and their potential applications, leading to the development of radio, radar and lasers. The subject of nonlinear oscillators also prompted the generation of new mathematical techniques in an effort to understand the complex aspect of dynamics.
1950s	The high-speed computer was invented, allowing for experiments involving equations to be conducted that previously would have been impossible, and allowed further insight into nonlinear systems.
1963	Lorenz discovered the chaotic motion on a strange attractor, made possible through the invention of the high speed computer. His work implied that such a system was inherently unpredictable (chaotic), and that it was highly sensitive to initial conditions.
1970s	A connection was made between chaos and phase transitions. This was the work of physicist Feigenbaum which showed that different systems can transition into chaos in the same manner.
1980s	From point the interest in chaos, nonlinear oscillators and the applications surrounding these topics has been widespread, with numerous works focussing on the subject.
1990s	Notable contributions to the theory of input-to-state stability for nonlinear systems [164], and geometric control theory were made [165].

Table 6.1.1: A brief history of dynamics that includes some of the major milestones and notable works leading to current research on nonlinear dynamics.

The complexity of nonlinear systems is best realised through comparison with the generation of analytical solutions to linear systems. Of course, in certain cases some assumptions may be made which remove or minimise the nonlinear aspects of the system for simplification of analysis and pedagogical reasons. A common assumption/system used to introduce dynamics relates to a simple pendulum, which often utilises the small angle approximation for the sine function ($\sin \theta \approx \theta$). Thus, the nonlinear aspect of the equation of motion of the system may be omitted, transforming it into a linear equation. Such systems may be split into parts, and these parts solved individually before recombining to provide an analytical solution. However, the same idea cannot be applied to most nonlinear systems due to the overwhelming complexity that arises from different interactions surrounding the system. Hence a quantitative approach to analysing nonlinear systems is often preceded by a qualitative one. A methodology first introduced by Poincare in 1889. Relating to Poincare’s work on the three body problem he posed questions such as “Is the solar system stable forever, or will some planets eventually fly off to infinity?” [163], in opposition to inquiring as to the exact position of the planets.

The nonlinear response of a system may result from a variety of reasons including; the material properties, geometric properties, external forces and constraints. For any material the constitutive relationships are typically nonlinear, however when considering the stress-strain relationship of the material a linear relationship exists. The magnitude of stress at which the relationship becomes nonlinear is dependent on the material properties [77]. Regardless of the material of a structure, the typical approach to a simple structural analysis is to assume that the geometry is subject to relatively small displacements and/or rotations. However, when the forces act on the structure result in large displacements or rotations geometric nonlinearity has to be considered. A common method of representing a nonlinear system is through the use of an equation of motion which includes a quadratic (or higher order) displacement term, which is usually referred to as the Duffing oscillator [77]. This is shown as Equation 6.1, where x is the displacement, ζ is the damping ratio, ω_n is the natural frequency, and α_{NL} is a factor which controls the amount of nonlinearity in the restoring force. In addition F is the harmonic forcing term, where Ω is the frequency of the force and t is time. The Duffing oscillator may be used to represent a system which exhibits nonlinear force-displacement behaviour (i.e. hardening or softening) as shown in Figure 6.1.1 for arbitrary values of k and k_1 .

$$\ddot{x} + 2\zeta\omega_n\dot{x} + \omega_n^2x + \alpha_{NL}x^3 = F \sin(\Omega t) \quad (6.1)$$

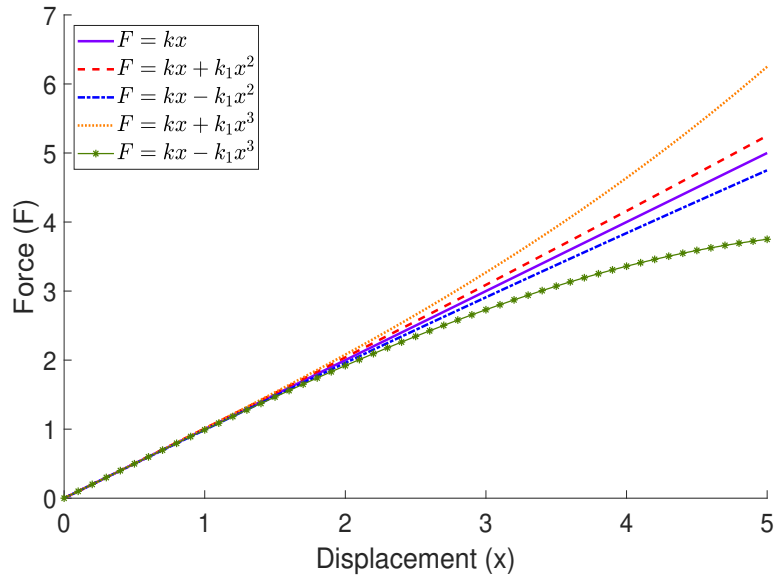


Figure 6.1.1: Relationship between the static deflection of a system due to increasing levels of force for five different definitions of the stiffness term.

As previously discussed and evidenced the investigation into the control of nonlinear vibrations is a highly prevalent topic. A multitude of research is dedicated to finding a solution to unwanted nonlinear vibrations. As discussed in Section 1.1 the application of linear control to a nonlinear system has the potential to effectively attenuate the response. Hence, no significant changes have been made to the designed control system prior to its employment in this new scenario. The following sections aim to investigate the induction of a nonlinear response (hardening) of the link structure, so that the designed control system may be employed to observe its performance. A further consideration is included within the investigations, the effect of the control system on the second mode to ensure that no spillover effects are present. This chapter presents the results of these investigations with the aim to make a contribution to the field with the novelty of the control system stemming from the previously defined constraints of being lightweight and inexpensive.

6.2 Inducing a geometric nonlinearity

Experimentation relating to nonlinear vibrations has, as often is the case, proved challenging. Multiple attempts at obtaining a nonlinear response based on the material properties of link structure proved futile. Thus, the attention was turned to the induction of a nonlinear response based on a geometric nonlinearity through the inclusion of springs located at the free end of the link. To obtain results indicative of a geometric hardening nonlinearity there are multiple aspects of the system which are required to have a specific stiffness and location. Observing an initial set-up as shown in Figure 6.2.1 and the improved set-up (Figure 6.2.3), the required adjustments become apparent. Initially the springs were supported using a wooden structure and held at the correct displacement by nails. The original set-up applied the force to the link via a metal stinger, which had threaded bolts on either end. One end was connected to the shaker and the other to the force sensor. A bolt was attached to the other side of the force sensor, which in turn was adhered a plastic rod, that was attached to the link between the PZT elements with Ethyl 2-cyanoacrylate (super glue). The plastic rod was necessary to reduce the chance of the glue reaching the PZT elements, as its diameter was smaller than that of the bolt connected to the force sensor. Issues were found with both of these parts of the set-up, and were first identified through the random excitation of the link used to ascertain the influence of increasing force on the first natural frequency. Figure 6.2.2 shows the results of these random excitation tests for multiple cases where adjustments were made to the set-up, where Table 6.2.1 describes these changes.

The components and parts shown in Figure 6.2.1 are numbered as follows, although it should be noted that the plastic rod between the bolt and the link has been removed i.e. Case 2 in Table 6.2.1:

1. Shaker (Dataphysics V4)
2. Force sensor (ICP 208 B02)
3. Bolt adhered to beam and connected to force sensor
4. PZT elements
5. Springs
6. Spring bracket
7. Laser displacement sensors (LDSs)

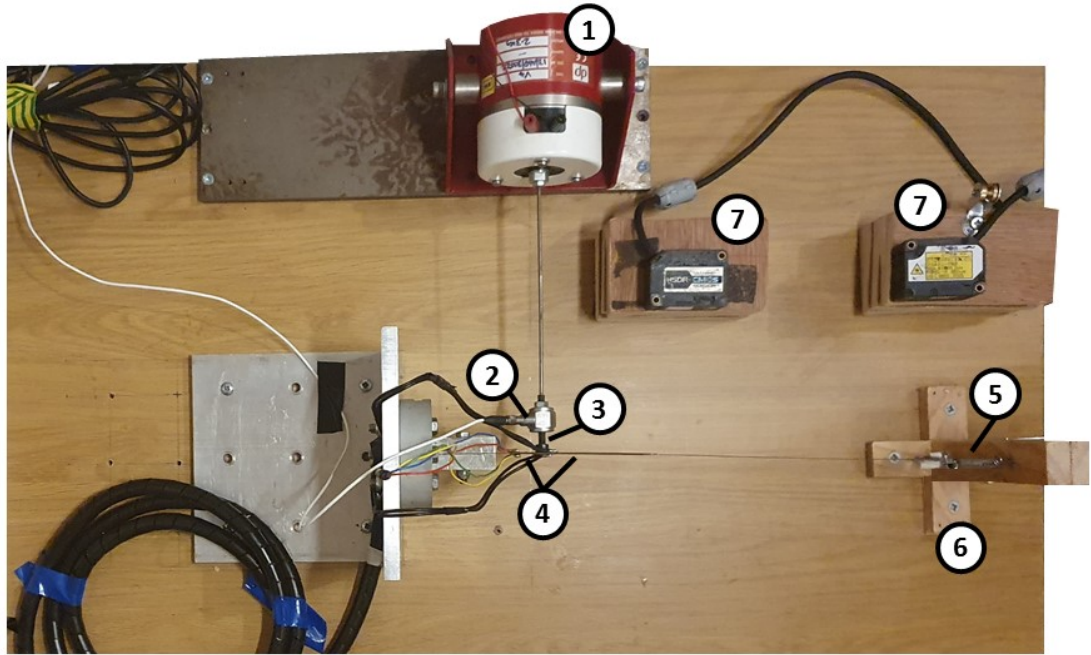


Figure 6.2.1: Image of an initial set-up used in the nonlinear experiments (see ‘Case 2’ in Table 6.2.1).

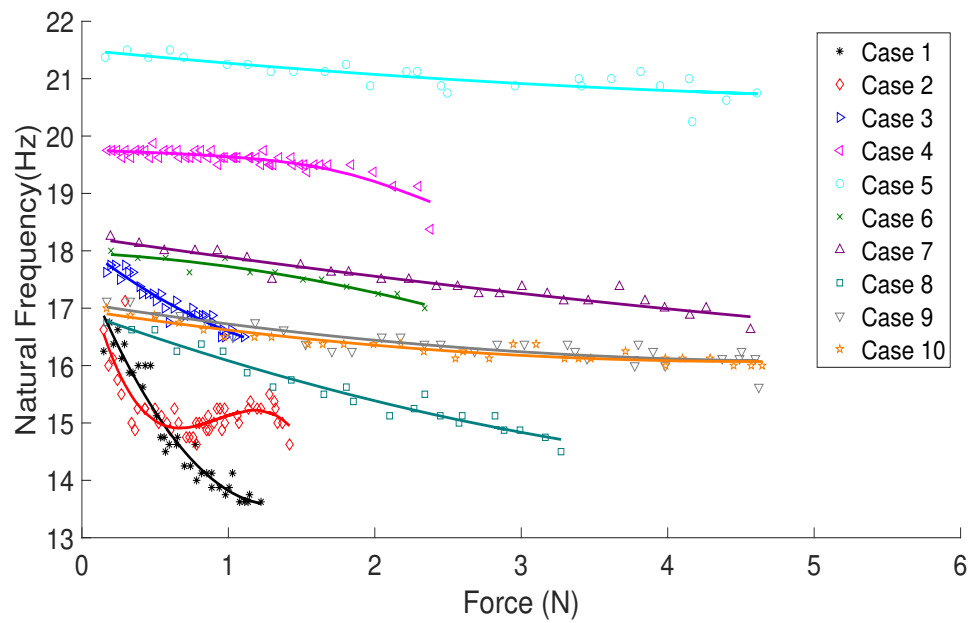


Figure 6.2.2: The change in the natural frequency of the system in relation to an increase in the magnitude of force for multiple cases wherein the structure is altered.

- Case 1 Original set-up, where no adjustments were made. From Figure 6.2.2 it can be seen that the system shows softening.
- Case 2 Wooden bracket is reinforced with metal ‘L’ brackets, the plastic rod that was part of the stinger is removed, and the bolt is carefully adhered to the link between the two PZT elements. In addition all bolts/nuts within the system were tightened as much as possible.
- Case 3 The wooden blocks on which the laser displacement sensors were held, were super glued to the main board, and extra bolts/screws/nails were added to the system where possible.
- Case 4 Insulating tape was added to the nails supporting the springs to prevent the springs movement along them whilst still allowing rotation.
- Case 5 The springs were exchanged for shorter counterparts of the same diameter and wire thickness, the size of the loops of these springs were decreased to further prevent displacement along the length of the nails.
- Case 6 The wooden spring bracket was exchanged for a metal counterpart of higher stiffness. Bolts were used to hold the springs in place vertically and nuts were added to these bolts to prevent the springs’ displacement along their length. Again, the loops of the springs were decreased to a diameter not dissimilar to that of the bolts.
- Case 7 The additional self-locking nuts were added to the stinger structure, as well as additional super glue in places to prevent it from rotating, but not bending. It is important to note that in this case, the joint between the stinger and the link failed at a force greater than approximately 4.57 N.
- Case 8 A new stinger structure was created, to improve the connection between the end of the stinger and the link. This new structure clamped the link within the stinger and its main body was stiffer than the original stringer, and to account for the bending of the link in relation to the stinger a hinge was included.
- Case 9 The hinge in the stinger was found to be too loose, therefore was tightened to reduce the softening of the system, but not to an extent where the hinge became ineffective. Thin copper wire was coiled around the bolts in lieu of the nuts which had limited the rotation of the springs.
- Case 10 Previous case repeated to verify results.

Table 6.2.1: Alterations made to the experimental set-up, leading to the suppression of its softening aspects.

The results of the majority these cases as shown in Figure 6.2.2, imply that a softening nonlinearity is present in the system. However, cases nine and ten appear to produce results in which the gradient of the slope is initially low before tending towards zero at higher amplitudes of force. The data acquisition software will produce a linearised FRF when employing the random excitation method. This explains why the natural frequencies are not seen to increase with force, hence a swept sine test is employed to gain further insight regarding the response (presented shortly). The components and parts of the experimental set-up in case eight are shown in Figure 6.2.3, and are numbered as follows:

1. Shaker (Dataphysics V4)
2. Force sensor (ICP 208 B02)
3. Clamp and hinge structure connecting beam to force sensor
4. PZT elements
5. Springs
6. Spring bracket
7. Laser displacement sensors (LDSs)

It should be noted that the copper wire coils introduced in case nine are not shown in Figure 6.2.3, but have been included in Figure 6.2.4 which focusses on the spring configuration. As briefly mentioned in Table 6.2.1, the nuts originally used were preventing the free rotation of the springs around the bolts thus affecting the dynamics of the link. Noting that the issue was not the tightness of the nuts on the loops of the springs, but rather the outer diameter of the bolts being large enough to make contact with the main body of the springs, the copper coil solution was employed. With the spring pre-extension present the thickness of the copper coils was of a sufficient magnitude to prevent the motion of the springs along the length of the bolts, but not so large as to prevent the rotation of the springs about the bolts. The insulating tape used to prevent the loops of the springs from moving along the length of the nail attached to the free end of the link is also visible in Figure 6.2.4 (see Table 6.2.1, case 4).

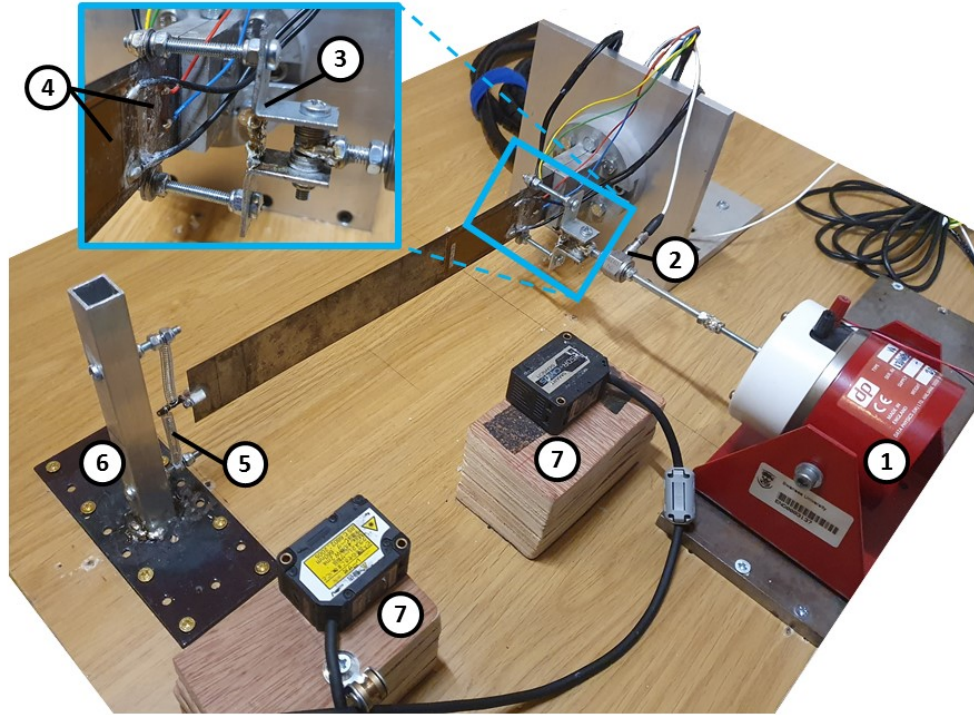


Figure 6.2.3: Image of the improved set-up used in the nonlinear experiments.

The connections between the components and devices in the experimental set-up are illustrated in Figure 6.2.5, where it should be noted different DC power supplies were utilised, but have been simplified to one block. The reader is referred to Figure 6.2.6 for more information regarding the block labelled ‘Control System B’. The parameters of the beam and piezos are the same as those outlined in Table 3.5.1, repeated here as Table 6.2.2 for convenience. The PZT sensors were positioned at a distance from the clamped end of the link of $y_1 = 0.011$ m, and the actuators at a distance of $y_3 = 0.0295$ m. The force was applied at a distance from the clamped end of the beam of $y_F = 0.0223$ m, which lies between the PZT sensors and actuators. The stinger, connecting the shaker to the beam, is intrusive, affecting the stiffness and mass of the link. This effect would be true regardless of the location of the stinger along the length of the link, however its location as seen in Figure 6.2.3 was selected based on the aim to prevent the limitation of the PZT actuator. The ‘mid displacement’ and ‘tip displacement’ refer to the lengths along the link at which the transverse displacement was measured, $y_{mid} = 0.136$ m and $y_{tip} = 0.257$ m, respectively. The ends of the springs were located midway along the width of the beam, with their respective opposing ends held at a distance of sufficient magnitude to provide a pre-extension. The relaxed length of the springs was 0.03728 m, and with the pre-extension this was increased to 0.03769 m. This pre-extension was included based on the work by [166], where the author’s experimental set-up was

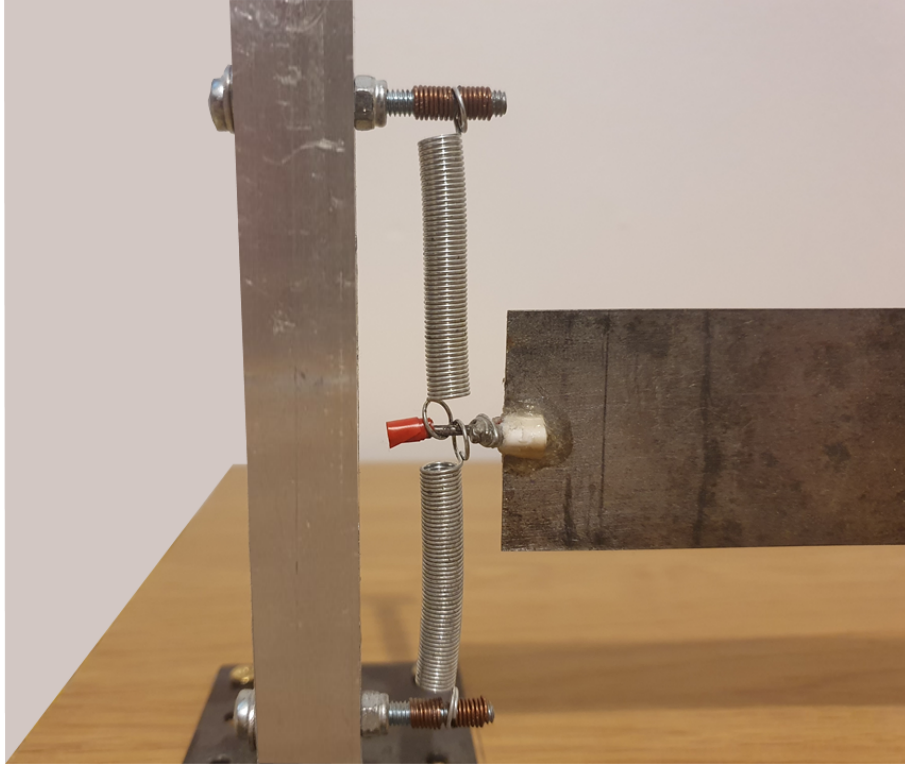


Figure 6.2.4: Image of the spring configuration utilised in the nonlinear experiments.

similar to that presented in this research (see Figures 6.2.4 and 6.2.6). The authors state that the force-displacement curve ($F(x)$) for the arrangement of the springs used in both their and this research can be approximated as Equation 6.2.

$$F(x) \approx k_1x + k_2x^3 \quad (6.2)$$

where, the linear and nonlinear stiffness terms (k_1 and k_2 respectively) can be represented as the original (or relaxed) spring length ($l_{spring,0}$) and their length with pre-extension applied ($l_{spring,ext}$) as in Equations 6.3 and 6.4.

$$k_1 = 2k(1 - l_{spring,0}/l_{spring,ext}) \quad (6.3)$$

$$k_2 = kl_{spring,0}/l_{spring,ext}^3 \quad (6.4)$$

These equations infer that in order for both a linear and a nonlinear response of the system to be observed the relation $l_{spring,0}/l_{spring,ext}$ should be less than one, lest the linear response be absent. As the ratio approaches zero, the nonlinear component of the response will also dwindle to zero. Thus, in order to observe both a linear and nonlinear response of the system, to determine the performance of the control system for both cases, the ratio has been set at $l_{spring,0}/l_{spring,ext} = 0.9891$.

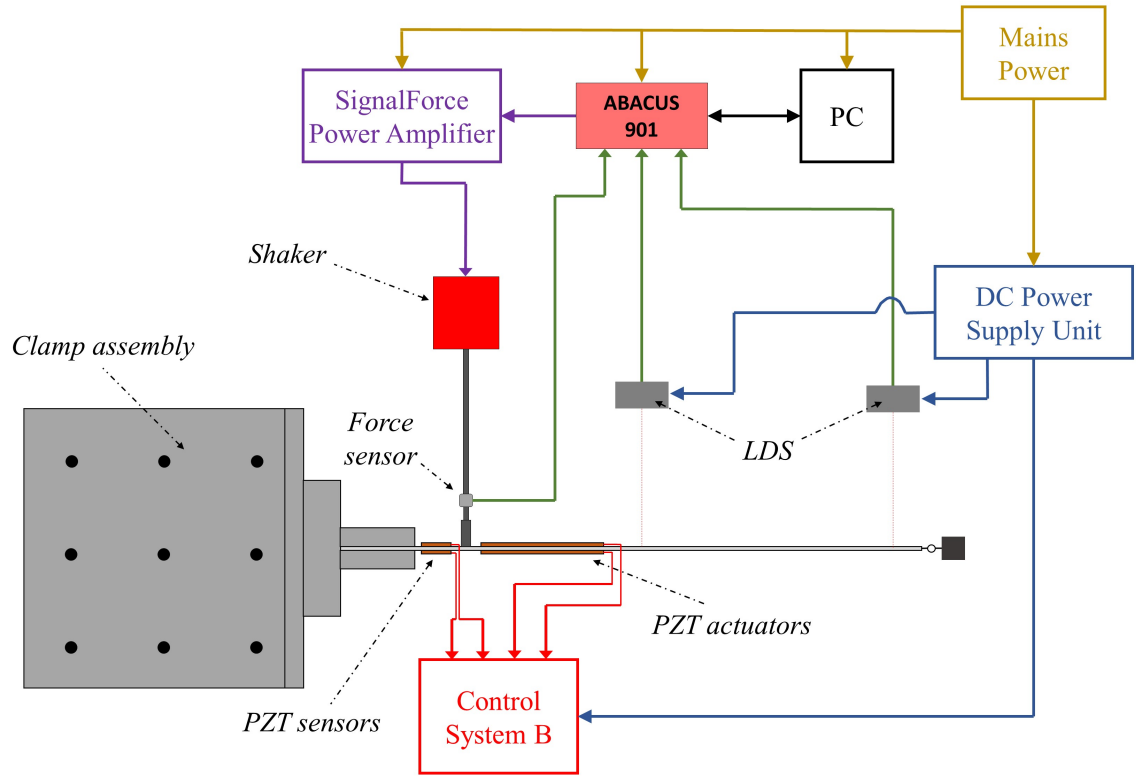


Figure 6.2.5: Illustration of the connections between the components and devices used throughout the nonlinear experiments.

Parameters	Link (Steel)	Piezoelectric Sensor (PZT-5A)	Piezoelectric Actuator (PZT-5A)
Overall length (m)	0.272	0.016	0.066
Overall width (m)	0.0397	0.016	0.031
Thickness (m)	0.0004	0.0003	0.0003
Active length (m)	-	0.007	0.056
Active width (m)	-	0.014	0.028
Density (kg/m ³)	7844	5440	5440
Young's Modulus (GPa)	204	60.48	60.48
Piezoelectric coefficient, \bar{e}_{31}	-	-11.6	-11.6
Electromechanical coupling term, k	-	0.34	0.34
Capacitance (nF)	-	7.89	113.06

Table 6.2.2: Geometric, mechanical and electric properties of link B and piezoelectric patches.

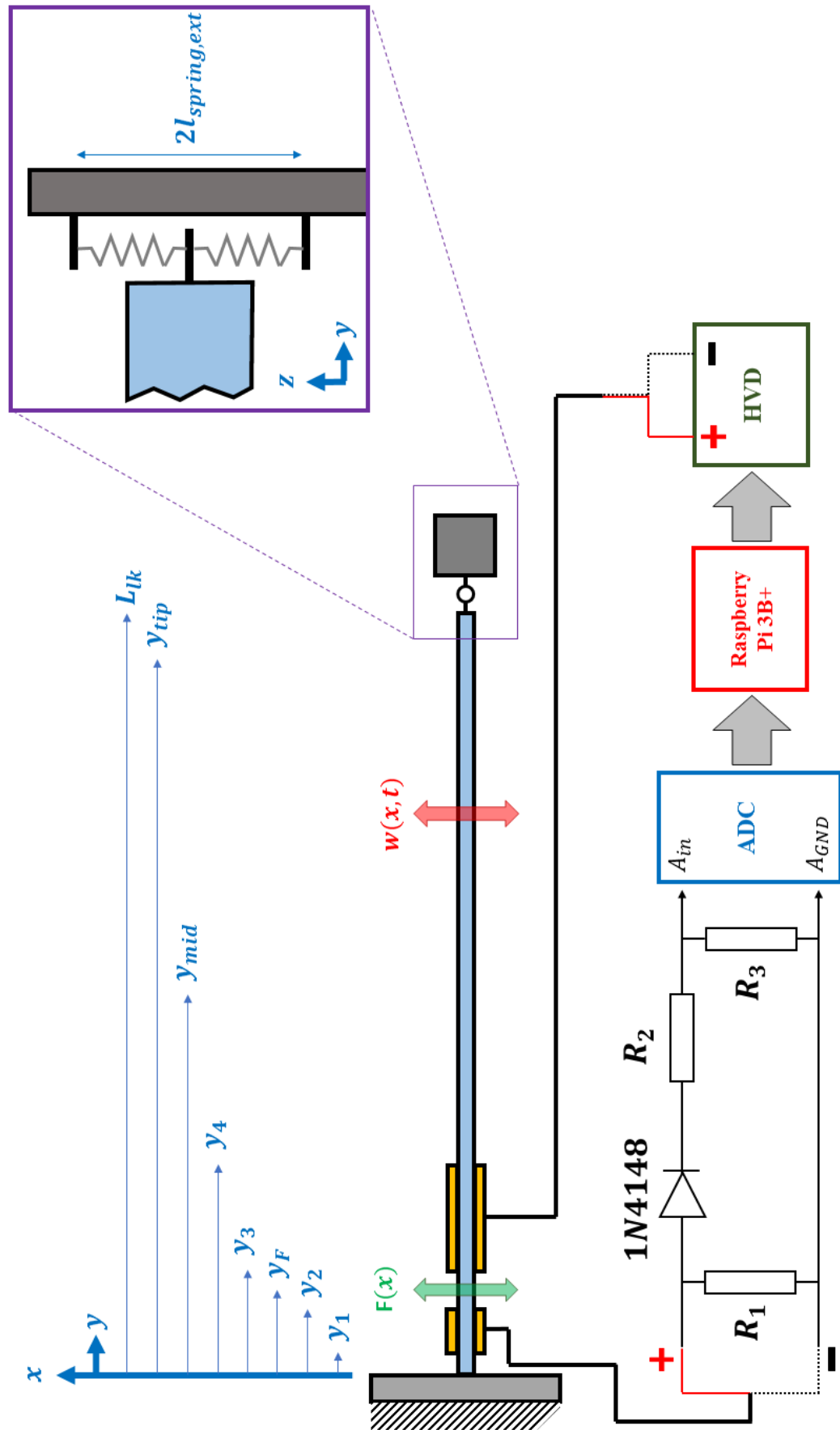


Figure 6.2.6: An illustration of the nonlinear experimental set-up, including the circuitry of the employed control system.

To obtain a better insight into the change of natural frequency with increasing force (as the random excitation method previously used linearised the FRFs), further studies were conducted utilising a harmonic excitation method. In these experiments, multiple excitation forces were considered (ranging from 1 N to 7 N), wherein each case saw the force remain constant as the frequency of the sinusoidal excitation was swept upwards from 12 Hz to 22 Hz (the frequency surrounding the first natural frequency). The results of these studies are shown in Figure 6.2.7, where it may be seen that nonlinear hardening is present at the higher forces. However, it is also noticeable that at around 3 N the response appears linear but the cases of lower forces than this are more indicative of a softening response. This experiment was repeated to ensure that the lower force cases shown in Figure 6.2.7 were not anomalous results, and similar responses were attained each time. This suggests that some softening is present in the system which only becomes apparent at lower levels of force. As this research is dedicated only to the control of a nonlinear response, and with a hardening nonlinearity present at higher force levels, the cases of lower forces were disregarded.

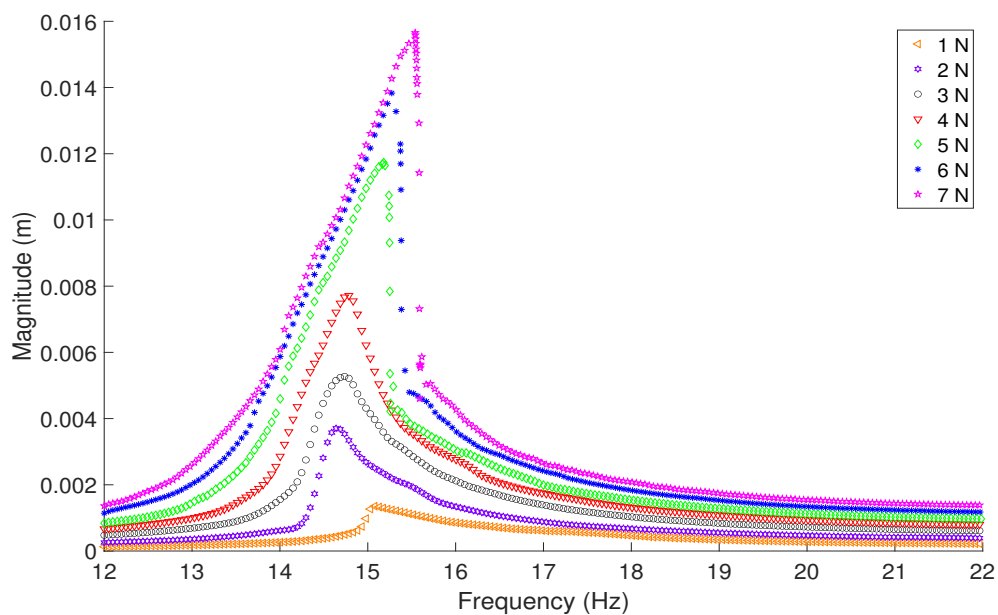


Figure 6.2.7: Response of the structure under increasing forces, sweeping upwards through frequencies surrounding the first natural frequency.

In addition to considering the influence on the force increase on the first natural frequency, it is also pertinent to observe the response of the system when excited at frequencies surrounding the second. The observation of this proves essential considering that the effects of the control system on the second natural frequency will also require surveillance so as to ensure that no undesirable spillover effects are present. Control spillover may be described for a control system as the effects that are present in higher

mode cases, when the control scheme is based on lower mode cases, this is most likely a result of dynamics that have not been modelled [167]. Some of these effects may be desirable, while others may not be. Responses related to control spillover may constitute any alteration of the modal parameters of the response with respect to a higher mode. In this research the main concern is whether the control system will excite the structure around its second mode as opposed to reducing the amplitude of the response, this situation is henceforth dubbed as a negative spillover effect.

Similar to the experiments which yielded the results shown in Figure 6.2.7, the system was excited at multiple cases of force which was kept constant throughout a swept sinusoidal excitation of increasing frequency. However, only forces previously shown to have induced a response indicative of nonlinear hardening have been presented (3 N to 7 N), and the frequencies were those surrounding the second natural frequency (25 Hz to 35 Hz). The results of these studies as shown in Figure 6.2.8 attest that there is no nonlinear response present, even for higher forces presented here. It may be possible to observe a nonlinear response of the system in the case of the second natural frequency through the application of a higher force level. However, the application of such a magnitude of force, especially in the frequency region surrounding a natural frequency is likely to cause structural damage and/or damage to the component connections to the link. This was actually proven in one test case during the investigations to obtain a nonlinear response, a higher force than presented here was applied, and the connection between the excitation source and the structure was compromised. The connection was replaced with a new structure as outlined in Table 6.2.1, however the concern over future damage remained, hence the apprehension regarding the application of higher force magnitudes.

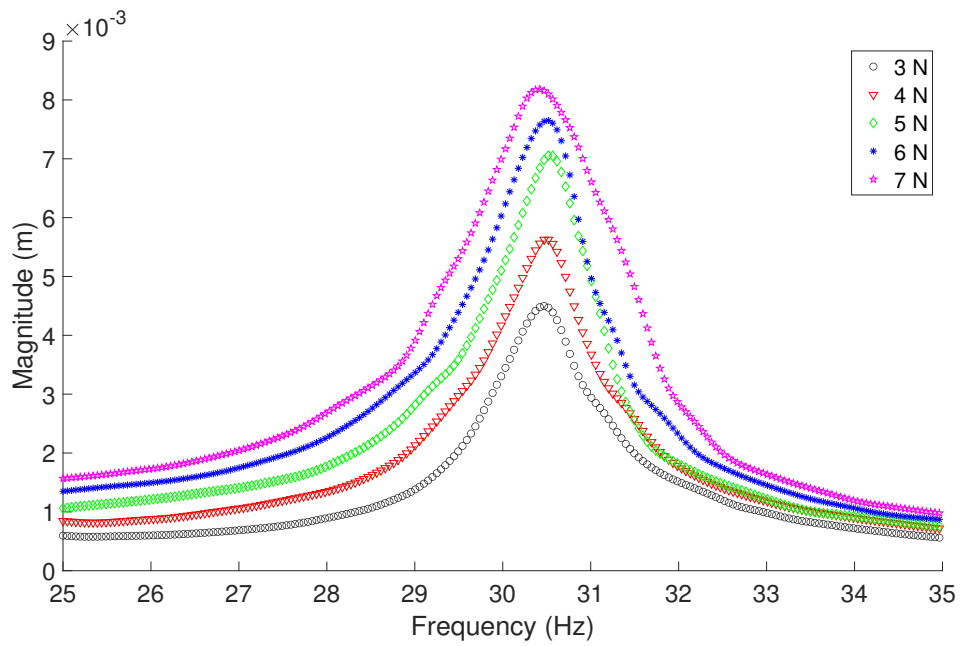


Figure 6.2.8: Response of the structure under increasing forces, sweeping upwards through frequencies surrounding the second natural frequency.

To further investigate the responses of the system with increased force, further studies were conducted. In these experiments the system was subject to the force levels at which the response of the system showed nonlinear hardening (3 N to 7 N). However, the sinusoidal excitation was applied in decreasing frequencies across the ranges (i.e. 22 Hz to 10 Hz and 35 Hz to 25 Hz). The results of these excitations of decreasing frequency or the ‘sweep down’ cases, were plotted alongside those of increasing frequency the ‘sweep up’ cases. Figure 6.2.9 contains these results for the first mode, and Figure 6.2.10 includes those for the second.

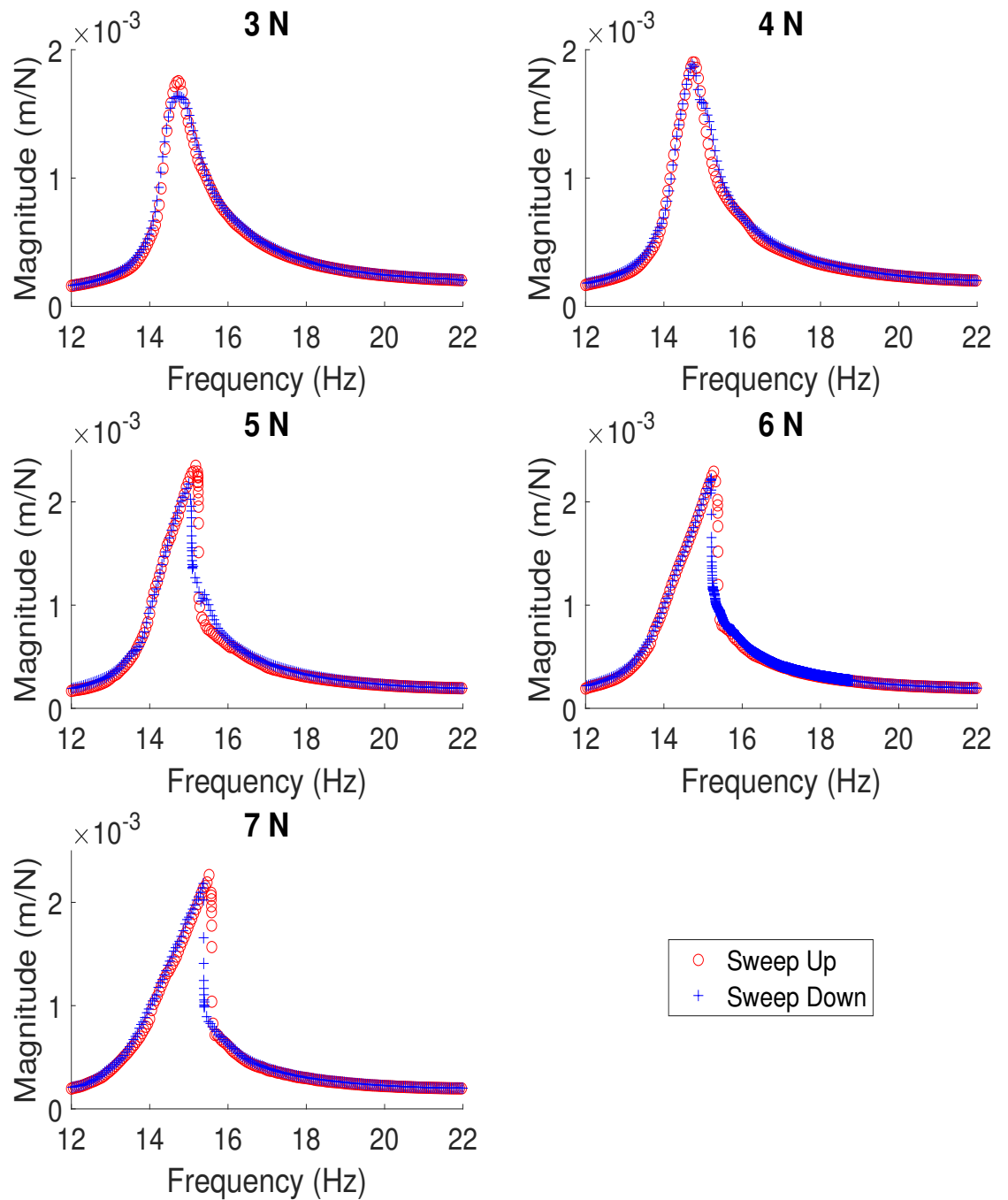


Figure 6.2.9: Results pertaining to the first natural frequency of the structure for five different excitation force magnitudes, sweeping both up and down the frequency range.

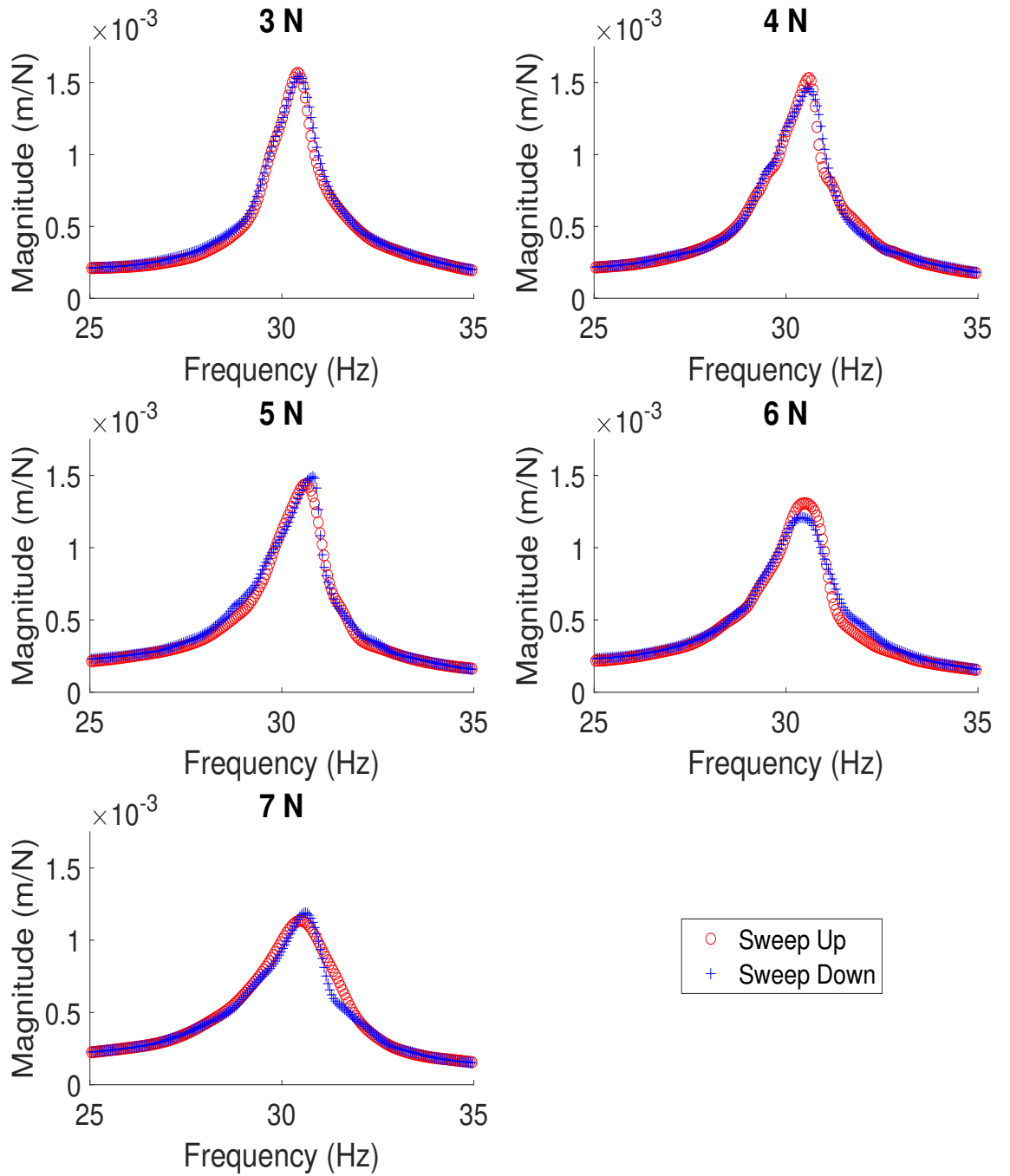


Figure 6.2.10: Results pertaining to the second natural frequency of the structure for five different excitation force magnitudes, sweeping both up and down the frequency range.

The results presented in Figure 6.2.9 are indicative of a system that contains a nonlinear element. The cases of lower force (3 N and 4 N) both show a close match between their respective data sets of increasing and decreasing frequency sweeps. There are some slight discrepancies i.e. in the 3 N case the amplitude of the ‘sweep up’ case is slightly larger than the ‘sweep down case’. However, both the 3 N and 4 N cases show very similar damping and natural frequencies between the increasing and decreasing frequency data sets. Thus, it can be assumed that the responses of these are both linear. Observing the 5 N force case, the two data sets yield slightly different responses immediately surrounding the natural frequency, whilst at frequencies outside of this region produce results that are fairly similar. Increasing the frequency whilst maintaining a force of 5 N yields a response of higher amplitude and a higher natural frequency, compared to the case in which the frequency is swept downwards. It is the difference between the natural frequencies of the two data sets that is characteristic of a nonlinear response, this may also be observed in the experiments wherein higher forces were applied to the system (6 N and 7 N). These higher force cases also contain the jump phenomena, which is indicative of a nonlinear response in that there is a discontinuity in the response near the two natural frequencies observed. Through the observation of these results it can be concluded that a nonlinearity has been successfully induced in the link structure through the inclusion of the spring arrangement for the first mode of the structure. From these findings the designed control system can be implemented to ascertain its performance with respect to a nonlinear response.

Figure 6.2.10 contains results from almost identical experiments to those presented in Figure 6.2.9, where the only difference lies in the frequency range. In order to observe the system’s response for frequencies surrounding the second natural frequency the link structure was excited between 25 Hz and 35 Hz, sweeping both up and down in this range. Five force cases were again considered to determine the response of the system (3 N to 7 N). Whilst it can be noticed that there are some discrepancies between the increasing and decreasing frequencies cases for each force investigation, none of the results are characteristic of a nonlinear response. The application of a higher force is likely to yield a nonlinear response of the second natural frequency, however it was deemed unnecessary to do so within this research. As previously mentioned the application of a higher force would most likely cause degradation of the connection between the components of the structure, presenting a risk. In addition a nonlinear response has been observed for the first natural frequency of the system which is sufficient to investigate the designed control system’s aptitude for the control of such a response. However, it would still be pertinent to observe the controlled response of the second natural frequency to ensure that no negative effects are present.

6.3 Application of control

This section presents the results from the experiments in which the control system was implemented on the modified system which yields a nonlinear response in the first mode. However, before presenting these results it is important to highlight that the control system has been slightly modified from previous experiments. Whilst the premise and the majority of the component connections have not been amended, the values of the resistors in the potential divider circuit have been adjusted. This is in accordance with the maximum voltage outputs from the PZT sensors in this scenario. These resistors are denoted as R_2 and R_3 in Figure 6.3.1 (a simplified version of Figure 6.2.6), where the values in these series of experiments are $R_2 = 470 \text{ k}\Omega$ and $R_3 = 1 \text{ M}\Omega$. This alteration still protects the analog to digital converter (ADC), whilst still allowing for an acceptable voltage range to reach it, based on the maximum voltages produced by the sensors at the natural frequencies. It was previously found that the noise within the readings was reduced when the values of these resistors were lower leading to a further justification for this amendment.

Another alteration was necessary, based on the changes made to the boundary conditions of the system. Consider the two experimental set-ups shown in Figure 6.3.2, the upper layout and excitation source position is true for the preceding experiments. The lower layout is that which applies to the experiments regarding the structure's nonlinear response, it should be noted that these images are exaggerated and not to scale. As can be seen from the illustration, the linear experiments excite the link at the base, which lends to the active actuator needing to be on the opposing side of the link to the sensor. However, in the nonlinear experiments the base is immovable and the excitation is applied between the sensors and actuators. Additionally, the latter case also has the boundary condition that arises from the spring structure, these facts led to the requirement that the active actuator is on the same side as the sensor. This required no physical alteration, as the designed control scheme could be adjusted on the RPi. As a change of the boundary conditions of the structure is unlikely to occur unintentionally in the suggested application (an other applications) further investigation into this matter was deemed irrelevant.

The results yielded from the implementation of the control system on the structure with it excited at a force magnitude of 3 N for the frequencies surrounding the first natural frequency are presented as Figure 6.3.3. It should be noted that the data has been presented using this plot style (a line with a marker denoting the gain value) as it is pertinent to observe the performance of the controller with different gain values for the particular force case. For this reason the results 3 N force case, along with the 5 N and 7 N cases (Figures 6.3.5 and 6.3.7 respectively) include only the swept

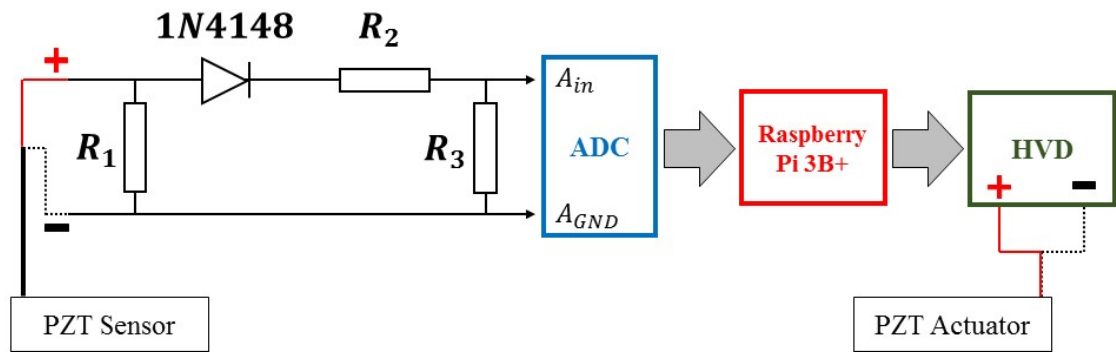


Figure 6.3.1: An illustration of the circuit used in the nonlinear experiments.

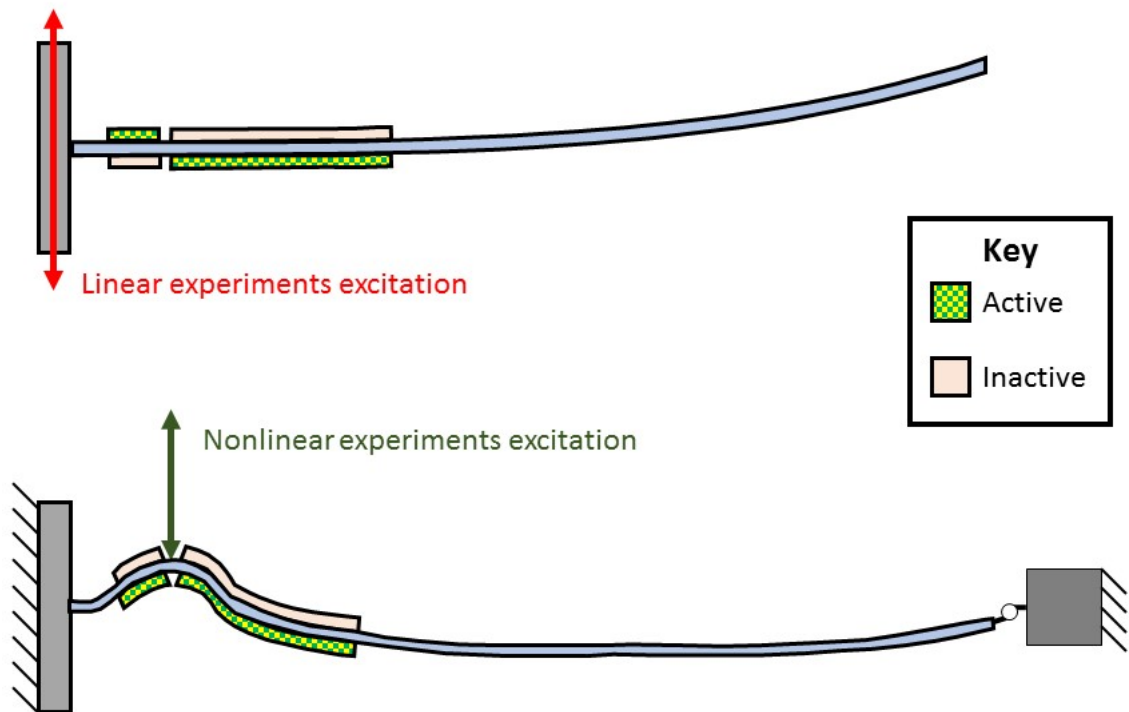


Figure 6.3.2: An illustration of the boundary conditions for the linear and nonlinear investigations.

upwards frequency scenario between 10 Hz and 20 Hz. The magnitude of these results is the tip displacement of the structure divided by the magnitude of the excitation force. Observations on the characteristics of the response with consideration to the nonlinear nature of the system will be presented afterwards. The proportional gain values (K_p) applied were: $K_p = 0$ (no control), $K_p = 50$, $K_p = 100$, and then increments of 100 up to and including $K_p = 700$.

For the first force case (3 N) the control system performed well as previously shown in other experiments where the response of the system was linear. The amplitude of the motion is reduced to almost a third of the uncontrolled response when the

control gain is set to $K_p = 500, 600$ or 700 . From the similar level of reduction of the response amplitude at these three gains it may be empirically realised that the optimum gain value lies in this region, with $K_p = 600$ producing a slightly better result. The explanation for this lies in the operating range of the PZT actuators, which is reached when the last three proportional control gains are employed, a concept explored when observing the results of previous experiments. Figure 6.3.4 contains the corresponding voltage output from the PZT sensors divided by the force input (sweeping upwards in frequency), which corroborates with the observations previously highlighted based on Figure 6.3.3. However it should be noted that the voltage output in the frequency domain was obtained through the application of the FFT on the data, as such the results are linearised, which is more noticeable in the cases relating to 5 N and 7 N excitation force magnitudes (Figures 6.3.6 and 6.3.8).

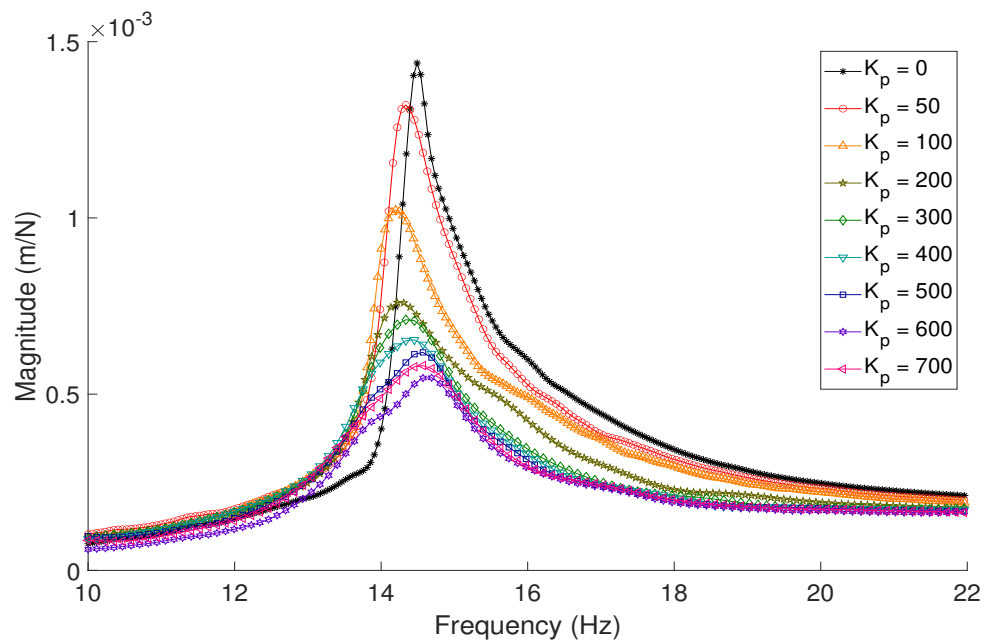


Figure 6.3.3: Controlled response of the structure excited at 3 N of force sweeping upwards through the frequency range surrounding the first natural frequency for varying gain values.

Figure 6.3.5 contains the response of the system 5 N case for the same range of gain values where the magnitude is the tip displacement divided by the magnitude of the force. The highest reductions in the amplitude of the response is again obtained when $K_p = 500, 600$ or 700 , and in this case the results converge. Whilst, unlike the 3 N force case, this reduction is smaller (most likely due to the increased magnitude of the excitation), it can be seen that the control system reduction in the nonlinear characteristics of the response. These characteristics pertain to the nonlinear ‘jump’ phenomenon and the ambiguity of the natural frequency between upwards and downwards sweep fre-

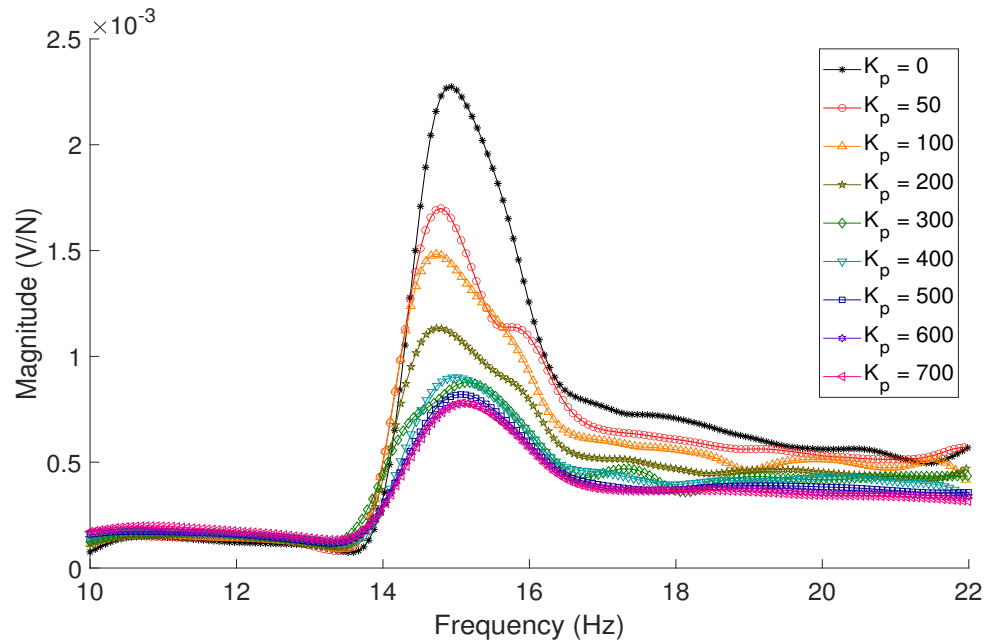


Figure 6.3.4: The voltage output from the PZT sensors divided by the magnitude of the force excitation (3 N) for multiple proportional gain values.

quencies, in this case the reduction of the former can be observed. The 7 N force case also shows some reduction of the nonlinear characteristics of the response as can be seen in Figure 6.3.5, however the relative reduction in the magnitude of the response is even less than the 5 N case, this further supports the hypothesis that it is due to the increased magnitude of the excitation force. As with the 3 N and 5 N cases, the control gain which obtains the highest reduction is in the region where $K_p = 500, 600$ or 700 . Figures 6.3.6 and 6.3.8 contain the voltage output from the sensors divided by the force magnitude for the cases of 5 N and 7 N, respectively. Both of the voltage responses of the system are reflective of their corresponding displacement response results in terms of the trends that may be observed.

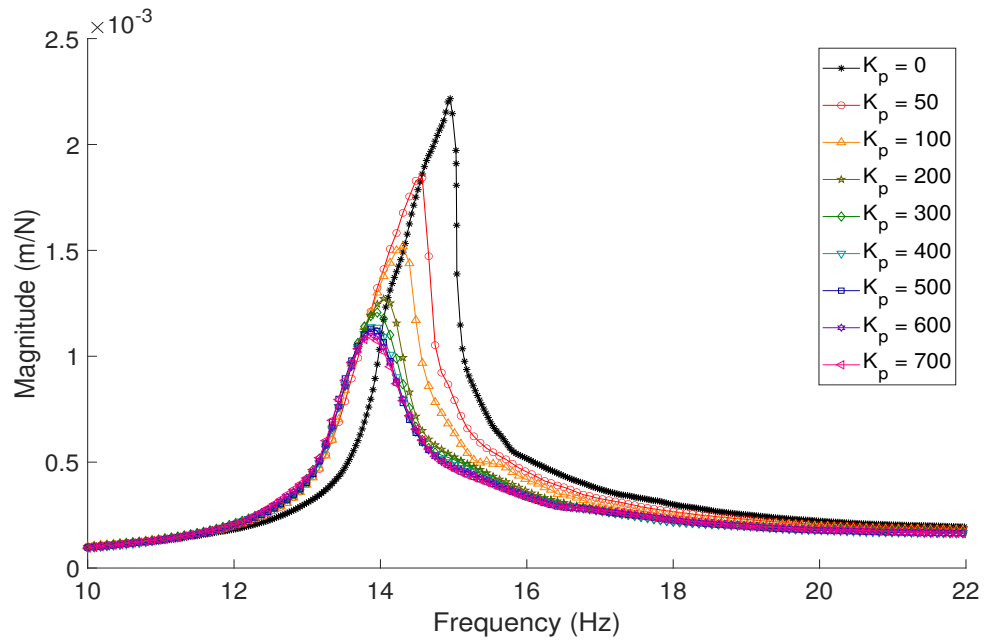


Figure 6.3.5: Controlled response of the structure excited at 5 N of force sweeping upwards through the frequency range surrounding the first natural frequency for varying gain values.

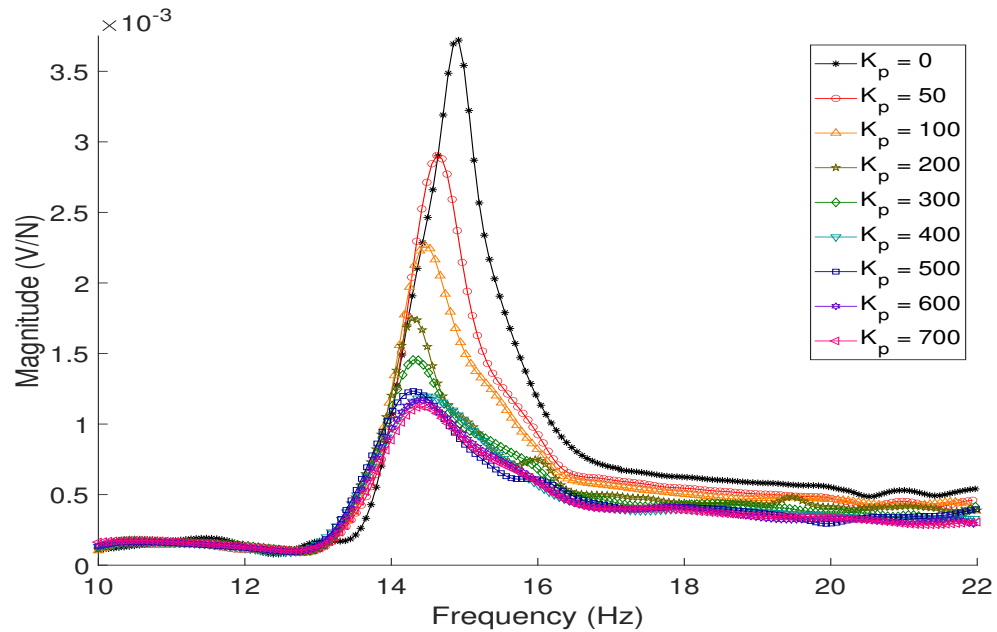


Figure 6.3.6: The voltage output from the PZT sensors divided by the magnitude of the force excitation (5 N) for multiple proportional gain values.

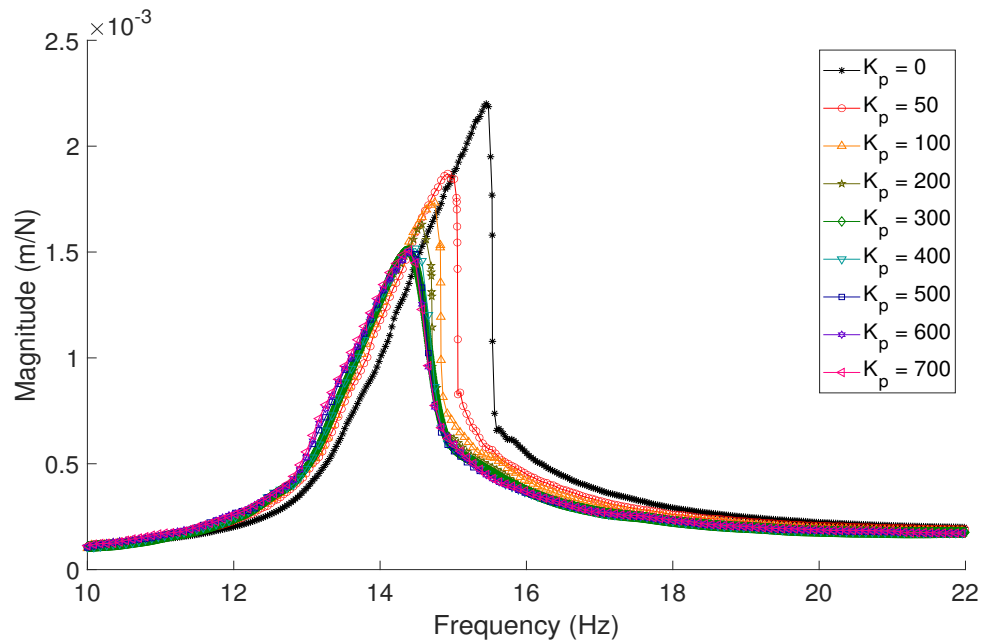


Figure 6.3.7: Controlled response of the structure excited at 7 N of force sweeping upwards through the frequency range surrounding the first natural frequency for varying gain values.

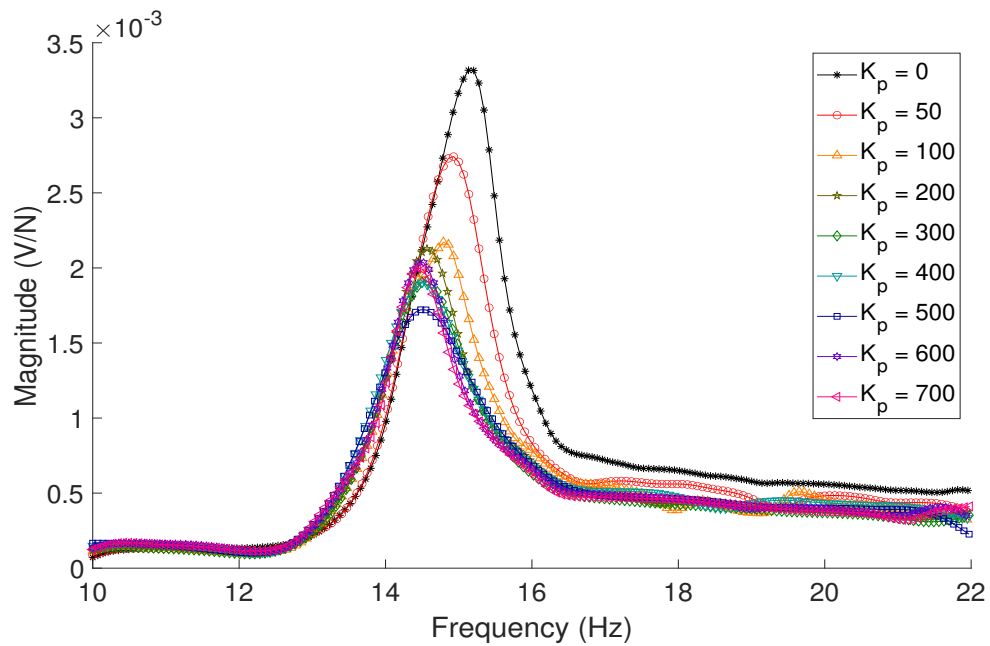


Figure 6.3.8: The voltage output from the PZT sensors divided by the magnitude of the force excitation (7 N) for multiple proportional gain values.

To further observe the capability of the control system to reduce the nonlinear characteristics of the response, three sets of data are presented. Each set relates to a particular magnitude of force (3 N, 5 N and 7 N, see Figures 6.3.9, 6.3.10 and 6.3.11, respectively), each containing three cases of proportional gain ($K_p = 0, 100$ and 600). For each case of proportional gain, the magnitude of the response is presented as the tip displacement divided by the excitation force, where the excitation is applied with both increasing and decreasing frequency. The application of a 3 N force to the structure has previously yielded no nonlinear characteristics in the response (as seen in Figure 6.2.9). The controlled response at this level of force does alter the natural frequency of the system alongside reducing the amplitude of the response, however this is attributed to the properties of the PZT sensors as previously explored. A concern for this 3 N force case would be that the alteration to the stiffness of the structure by the control system may yield some nonlinear characteristics of the response evidenced through the comparison of an upward and downward sweep of the excitation frequency. Contrarily to this concern the sweep up and sweep down data sets as shown in Figure 6.3.9, have very little discrepancies in the natural frequencies of the response for all proportional gain values included. There are, however, differences in the amplitudes of the response for the case in which $K_p = 600$, but this may not necessarily be due to the application of control as a discrepancy in the amplitudes can also be observed in the case of $K_p = 0$ i.e. no control is applied.

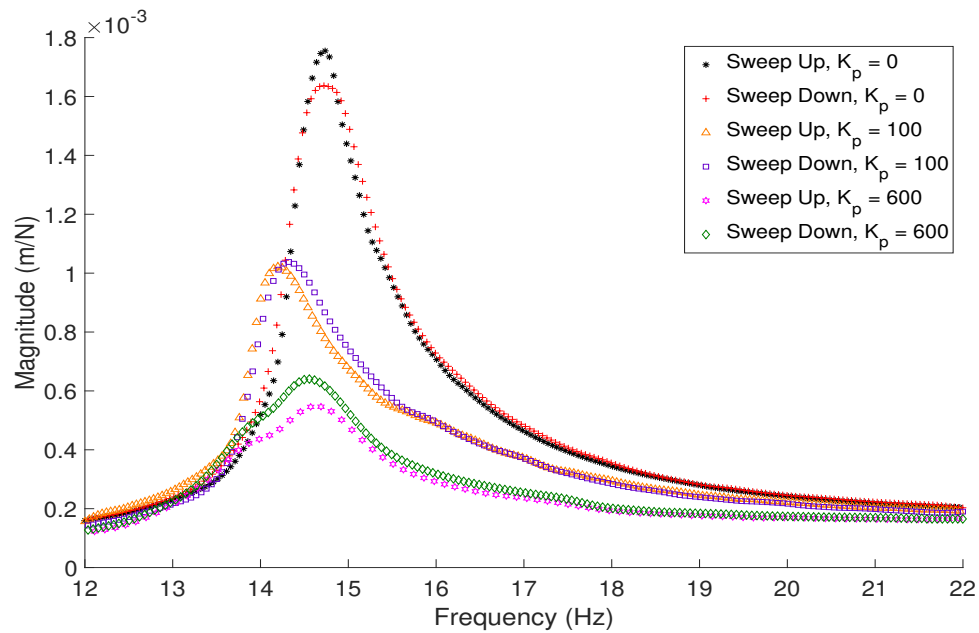


Figure 6.3.9: The response of the structure for an excitation force of 3 N, sweeping both upwards and downwards in frequency for selected cases of proportional gain values.

Figure 6.3.10, contains the results for the force level of 5N. The uncontrolled case ($K_p = 0$) contains two distinctive traits of a nonlinear response in the comparison the sweep up and sweep down frequency responses; the natural frequencies are noticeably different, and both show the jump phenomena. The controlled cases ($K_p = 100$ and $K_p = 600$) show a significant reduction of the difference in the respective natural frequencies, and the ‘jumps’ between the data points are reduced in the case where $K_p = 100$ and even more so in the case where $K_p = 600$. The results for the force level of 7 N are shown in Figure 6.3.11, where the same trends as the 5 N case can be observed. However, even in the case wherein the proportional gain is highest ($K_p = 600$) the nonlinear characteristics of the response are not reduced to the point where they may be considered absent. Whilst the control cases do reduce the discrepancy of the natural frequencies, the jumps between the data points can still be observed. This is most likely a consequence of the force applied by the control system being overwhelmed by the force applied to the structure. Even with the lessened reduction of the nonlinear characteristics of the response, the control system may still be deemed advantageous based on the reduction of the response amplitude.

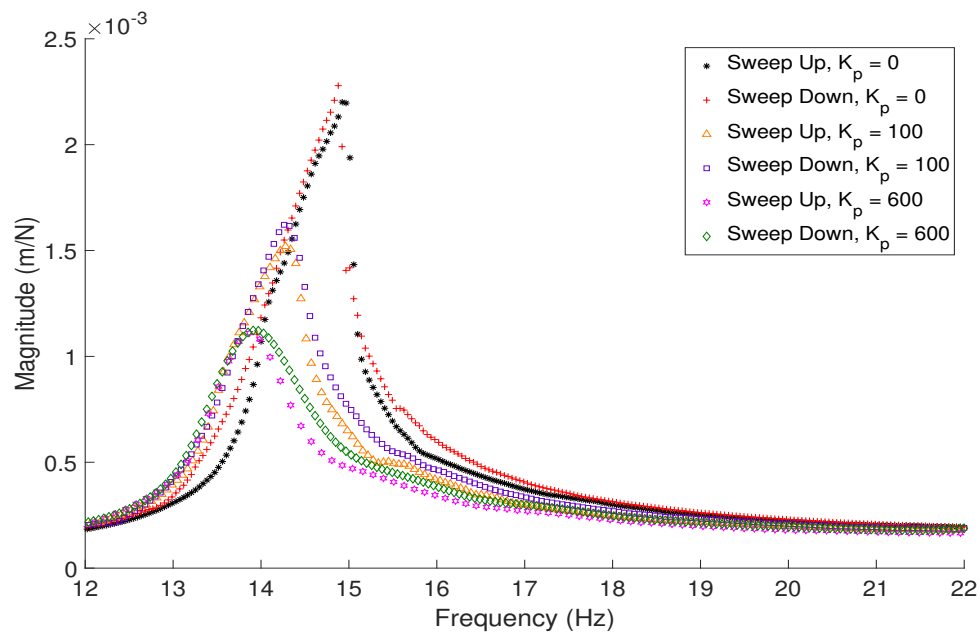


Figure 6.3.10: The response of the structure for an excitation force of 5 N, sweeping both upwards and downwards in frequency for selected cases of proportional gain values.

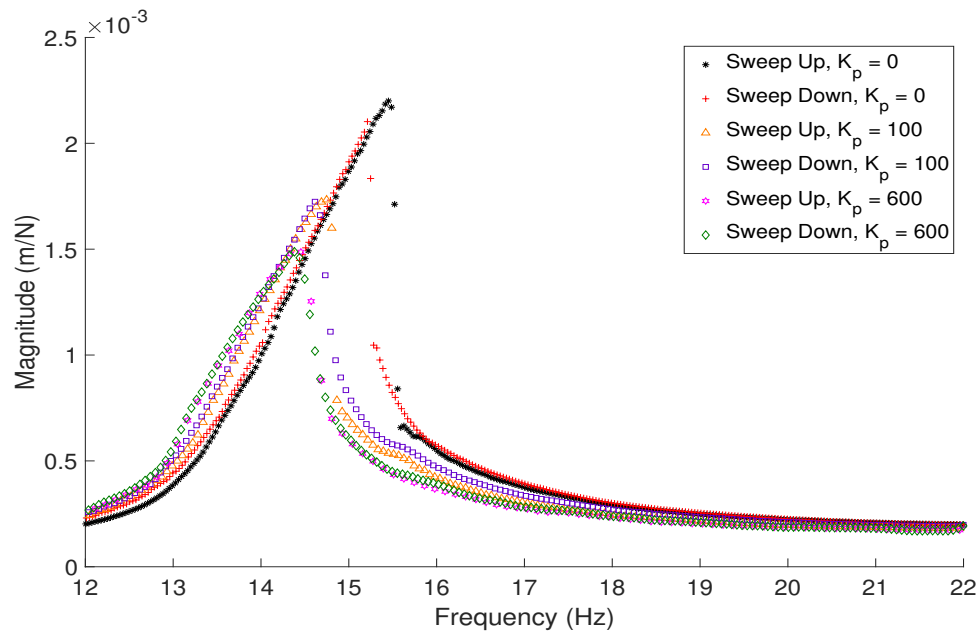


Figure 6.3.11: The response of the structure for an excitation force of 7 N, sweeping both upwards and downwards in frequency for selected cases of proportional gain values.

The final consideration with respect to the implementation of the control system to control a nonlinear response concerns the effect on the second natural frequency. Thus, presented here are Figures 6.3.12, 6.3.13 and 6.3.14, which contain the responses of the structure for three force cases 3 N, 5 N, and 7 N, respectively. In these cases the frequency was swept upwards from 10 Hz to 35 Hz, a range inclusive of the first and second natural frequencies. As previous observations of the structure showed that there were no nonlinear characteristics present in the second natural frequency, and that no nonlinear traits were induced by the application of control it is only the sweep up of the frequency cases that have been presented. The results of the 3 N force level case (Figure 6.3.12) have been plotted as solid lines as no nonlinear characteristics are present to observe. In this case the control system shows no negative spillover effects on the second natural frequency, conversely its effect on the response are advantageous. The amplitude of the response for the second natural frequency is reduced, which is also the outcome for the other force level cases. However, the level of reduction does decrease with increasing force, which again may be attributed to the force output of the control system being overwhelmed by the excitation force.

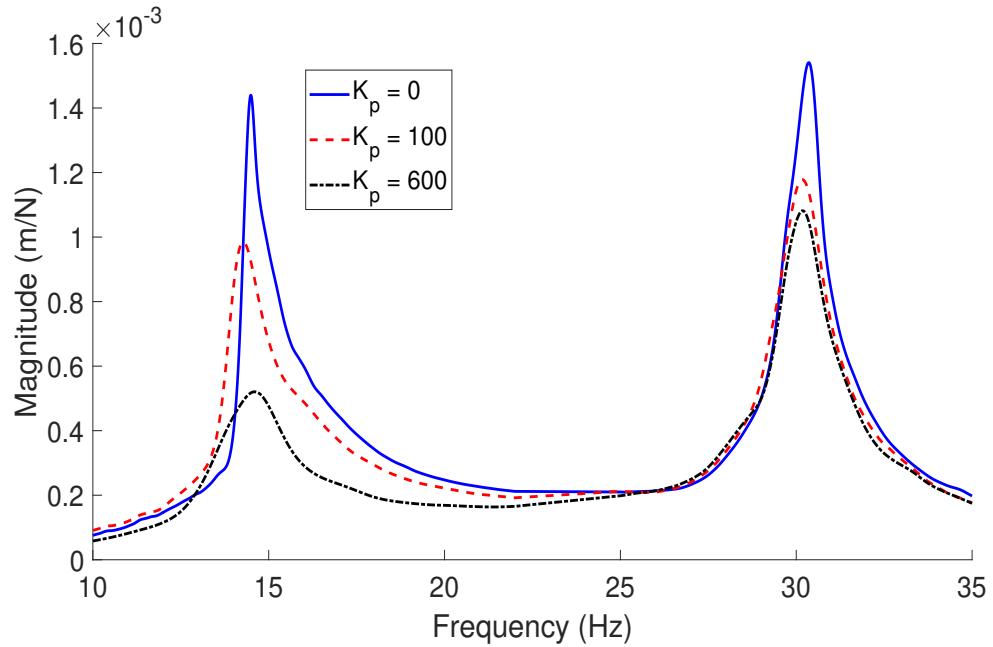


Figure 6.3.12: The response of the structure where the base excitation was swept upwards through the first and second natural frequencies at a force level of 3 N for three magnitudes of control gain.

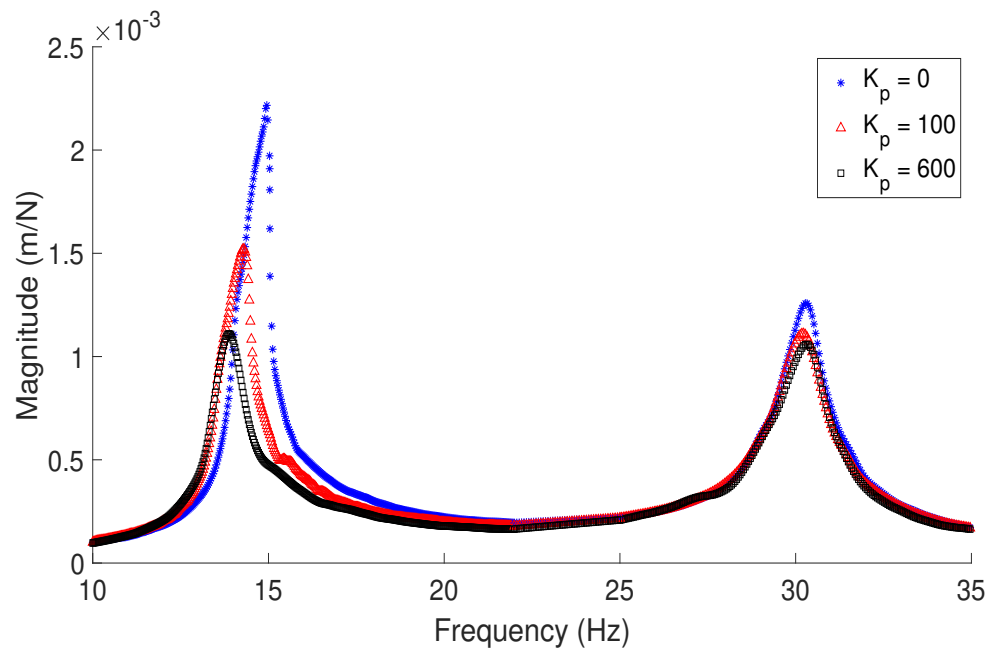


Figure 6.3.13: The response of the structure where the base excitation was swept upwards through the first and second natural frequencies at a force level of 5 N for three magnitudes of control gain.

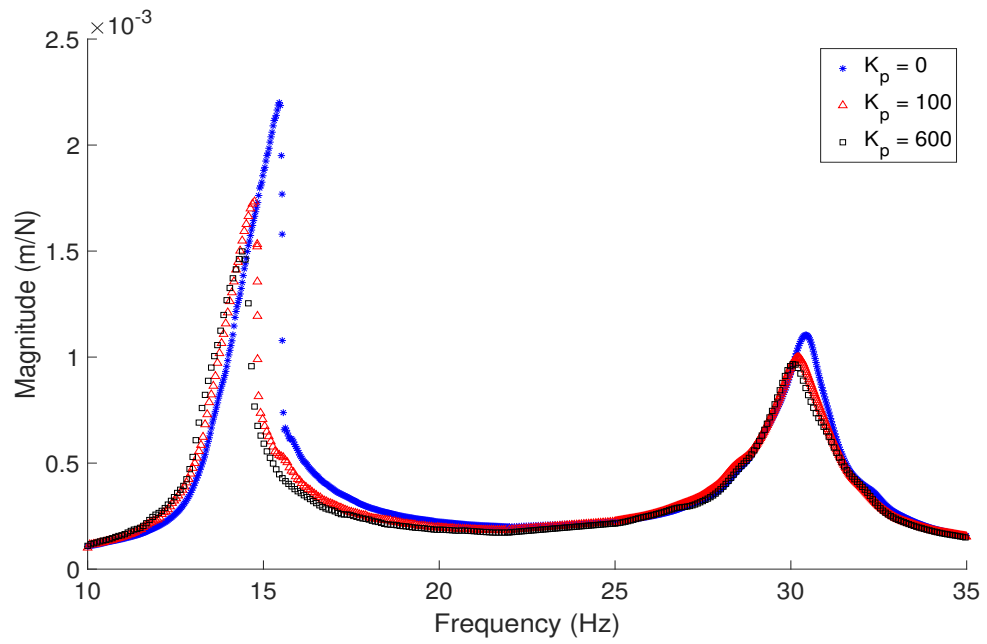


Figure 6.3.14: The response of the structure where the base excitation was swept upwards through the first and second natural frequencies at a force level of 7 N for three magnitudes of control gain.

6.4 Analytical model and optimisation

The equation of motion for the analytical model has been derived from Euler-Bernoulli Beam theory (EBT) as shown in Equation 6.5. The nomenclature used in this and the proceeding equations is described in Table 6.4.1. Figure 6.4.1 is an illustration of the experimental set-up and highlights the lengths along the link at which the components are positioned. It should be noted that the force (F) applied to and the resultant transverse displacement ($w(y, t)$) of the link are in the direction parallel to the x axis.

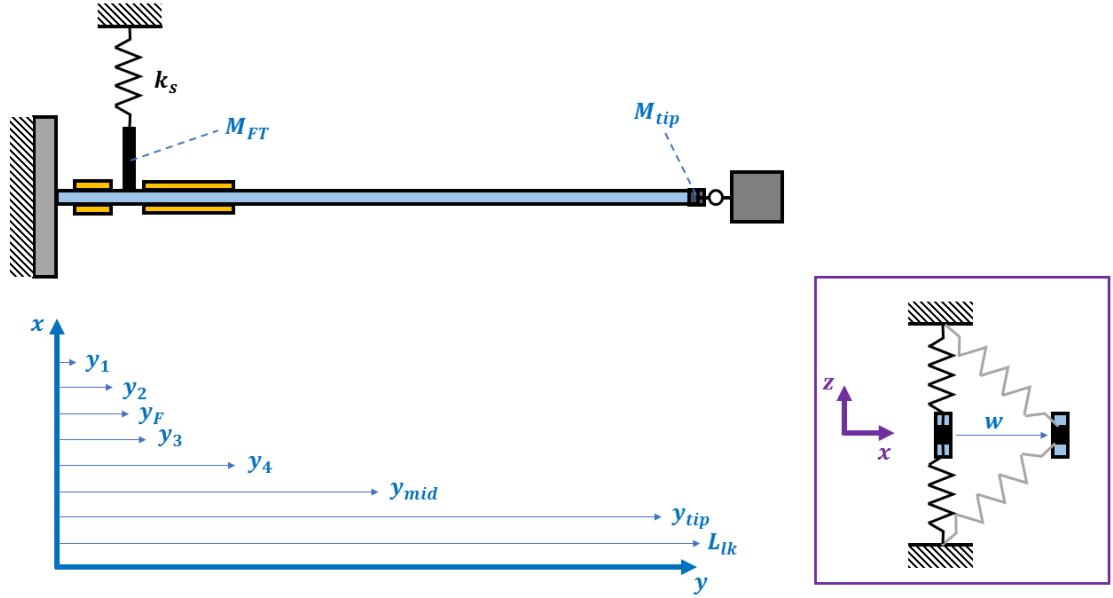


Figure 6.4.1: An illustration of the nonlinear analytical model.

$$\begin{aligned}
 & \frac{\partial^2 EI(y)}{\partial y^2} \frac{\partial^2 w(y, t)}{\partial y^2} + 2 \frac{\partial EI(y)}{\partial y} \frac{\partial^3 w(y, t)}{\partial y^3} + EI(y) \frac{\partial^4 w(y, t)}{\partial y^4} + \rho A(y) \frac{\partial^2 w(y, t)}{\partial t^2} \\
 & + \Upsilon \frac{\partial w(y, t)}{\partial t} + \varpi \frac{\partial}{\partial t} \left(\frac{\partial^4 w(y, t)}{\partial y^4} \right) + k_s w(y, t) \delta(y - y_F) \\
 & + M_{FT} \frac{\partial^2 w(y, t)}{\partial t^2} \delta(y - y_F) + M_{TM} \frac{\partial^2 w(y, t)}{\partial t^2} \delta(y - L_{lk}) \\
 & + k_l w(y, t) \delta(y - L_{lk}) + k_n w^3(y, t) \delta(y - L_{lk}) \\
 & - \vartheta_{ps} V_{in,ps}(t) \left[\frac{d\delta(y - y_1)}{dy} - \frac{d\delta(y - y_2)}{dy} \right] - \vartheta_{pa} V_{in,pa}(t) \left[\frac{d\delta(y - y_3)}{dy} - \frac{d\delta(y - y_4)}{dy} \right] \\
 & = F \sin(\Omega_F t) \delta(y - y_F)
 \end{aligned} \tag{6.5}$$

Variable	Definition
E	Young's modulus
I	Second moment of area
w	Transverse Displacement
ρ	Density
A	Area
Υ	Coefficient of proportional damping
ϖ	Coefficient of proportional damping
k_s	Stiffness of the stinger
δ	Dirac delta function
M_{FT}	Mass of force transducer
M_{TM}	Tip mass
L	Length
k_l	Linear spring stiffness
k_n	Nonlinear spring stiffness
V	Voltage (out from sensors, in from actuators)
ϑ	Piezoelectric coupling term
F	Amplitude of force applied to link
Ω_F	Frequency of force applied
H	Heaviside function
\bar{e}_{31}	Effective transverse piezoelectric coefficient
W	Width
h	Thickness

Table 6.4.1: Nomenclature used in the nonlinear analytical model (with some variables repeated for convenience).

Equations 6.6 and 6.7 describe the variation in stiffness and mass (respectively) along the length of the link due to the inclusion of the PZT elements. The piezoelectric coupling terms for the PZT sensors and actuators are shown in Equations 6.8. The subscripts lk , pa and ps denote terms relating to the link, PZT sensors and PZT actuators, respectively. The superscript Ψ denotes the active dimensions of the PZT elements.

$$EI(y) = E_{lk}I_{lk} + E_{ps}I_{ps} [H(y - y_1) - H(y - y_2)] \\ + E_{pa}I_{pa} [H(y - y_3) - H(y - y_4)] \quad (6.6)$$

$$\rho A(y) = \rho_{lk}A_{lk} + \rho_{ps}A_{ps} [H(y - y_1) - H(y - y_2)] \\ + \rho_{pa}A_{pa} [H(y - y_3) - H(y - y_4)] \quad (6.7)$$

$$\vartheta_{ps} = \frac{\bar{e}_{31}W_{ps}^{\Psi}}{h_{ps}} \left[\left(h_{ps} + \frac{h_{lk}}{2} \right)^2 - \frac{h_{lk}^2}{4} \right] \\ \vartheta_{pa} = \frac{\bar{e}_{31}W_{pa}^{\Psi}}{h_{pa}} \left[\left(h_{pa} + \frac{h_{lk}}{2} \right)^2 - \frac{h_{lk}^2}{4} \right] \quad (6.8)$$

As introduced in previous chapters the voltage to be applied to the PZT actuators ($V_{in,pa}$) is a product of the proportional gain (K_p) and the voltage output from the PZT sensors ($V_{out,ps}$), as shown in Equation 6.9. The voltage output from the PZT sensors may be obtained from Equation 6.10.

$$V_{in,pa} = K_p V_{out,ps} \quad (6.9)$$

$$C_{ps} \frac{dV_{out,ps}(t)}{dt} + \frac{V_{out,ps}(t)}{2R_{l_{ps}}} - i_{ps}(t) = 0 \quad (6.10)$$

where,

$$C_{ps} = \frac{\bar{\epsilon}_{33}W_{ps}^{\Psi}L_{ps}^{\Psi}}{h_{ps}} \quad (6.11)$$

$$i_{ps}(t) = - \sum_{n=1}^{\infty} \kappa_{nps} \frac{dP_n(t)}{dt} \quad (6.12)$$

where, $\bar{\epsilon}_{33}$ is the dielectric permittivity coefficient, and the modal coupling term (κ_{nps}) is defined as:

$$\kappa_{nps} = \bar{\epsilon}_{31} \frac{(h_{ps} + h_{lk}) AW_{ps}}{2} \int_0^{L_{lk}} \frac{d^2 \phi_n(y)}{dy^2} dy \quad (6.13)$$

As in the previous analytical model the resistive load across the PZT sensors (R_{lps}) and their capacitance (C_{ps}) are unknown values to be determined. It should be noted in this case that rather than obtaining the value of C_{ps} to be utilised, the unknown coefficient $\bar{\epsilon}_{33}$ (see Equation 6.11) is sought. The assumed-mode method is utilised along with the application of Galerkin decomposition to Equation 6.5 to yield the discretised equation of motion. The response of the link may be yielded through Equation 6.14, where $P_n(t)$ and $\phi_n(y)$ represent the n^{th} mode's generalised coordinate and the mode shape of the link structure, respectively.

$$w(y, t) = \sum_{n=0}^N P_n(t) \phi_n(y) \quad (6.14)$$

The steady state response of the system in the frequency domain is obtained through the use of the modified complex averaging technique (MCXA) alongside the arc-length continuation method. This technique was developed and or utilised in research by Taghipour [89, 168, 169] who assisted in the production of the results presented in the following section. To yield the steady state response of the link structure its generalised coordinates are assumed as harmonic functions as in Equation 6.15, where $Q_{n,i}$ is the complex amplitude of the i^{th} harmonic of the generalised coordinate $P_n(t)$.

$$P_n(t) = \sum_{i=0}^N Q_{n,i} e^{jn\omega t} \quad (6.15)$$

Within with equation of motion (see Equation 6.5) and the subsidiary equations which represent certain parameters (Equations 6.11 and 6.10) there are nine unknown variables: Υ , ϖ , M_{FT} , M_{TM} , k_s , k_l , k_m , $\bar{\epsilon}_{33}$ and R_{lps} . All of these unknown variables (bar the last two) can be optimised through an optimised-based identification method whilst employing the experimental data of the uncontrolled response. After the optimisation of said variables, those relating to the control of the structure ($\bar{\epsilon}_{33}$ and R_{lps}) may then be obtained through optimisation based on the experimental data of the controlled response(s). As in the technique developed by Taghipour et. al. [89], the objective function is defined as:

$$O = \min \left(\sum_{p=1}^{N_f} \left| \log (\| w_{exp}(\omega_p) \|_2) - \log (\| w_{ana}(\omega_p) \|_2) \right| \right) \quad (6.16)$$

where, $w_{exp}(\omega_p)$ and $w_{ana}(\omega_p)$ denote the experimental and analytical response at the excitation frequency ω_p in the frequency domain. The number of frequency points used within this optimisation process is denoted by N_f . To ensure that feasible optimised values for the unknown variables are obtained, and also improve the efficiency of the optimisation process the following should be considered:

- An appropriate selection of the upper and lower bounds of each parameter should be employed.
- To reduce the effect of noise, appropriate experimental data should be collected, and the analytical model should reflect this. For example, in this case, the response was obtained by sweeping up through the frequencies for a system with a hardening nonlinearity. As a result, the upper (stable) branch was obtained, and the model should then reflect this.
- The frequency range of the analytical response may be limited to that of the experimental data.
- Weights may be applied to the selected data based on the discrepancies between the experimental and analytical results.
- Where appropriate certain sets of data may be omitted from the optimisation process. For example, if the unstable branches are not of concern or have not been experimentally investigated then they may be disregarded.

6.5 Analytical model validation

The optimisation process previously outlined yielded the values of the unknown parameters as shown in Table 7.3.1. These optimised values are feasible when considering the components of the experimental set-up, and in some cases the experimental results. For example, the masses of the force transducer and tip mass are highly plausible, the force transducer weighs 0.026 kg, however some of this weight is supported by stinger/shaker, and the tip mass consisted of two small nails, and small plastic holders hence 0.00425 kg is very feasible. The capacitance of the PZT sensors (C_{ps}) as stated by the manufacturer is 7.89 nF, and the value of the dielectric permittivity coefficient ($\bar{\epsilon}_{33}$) obtained through optimisation renders $C_{ps} = 7.35$ nF. This can be considered as a relatively close match between the optimised value and that provided by the manufacturer.

Parameter	Value
Υ	0.0975 N.s/m ²
ϖ	5×10^{-6} N.s.m ²
k_s	7.25×10^3 N/m
M_{FT}	0.016 kg
M_{TM}	0.00425 kg
k_l	55 N/m
k_n	4×10^4 N/m ³
$\bar{\epsilon}_{33}$	2.25×10^{-8}
R_{lps}	600 Ω

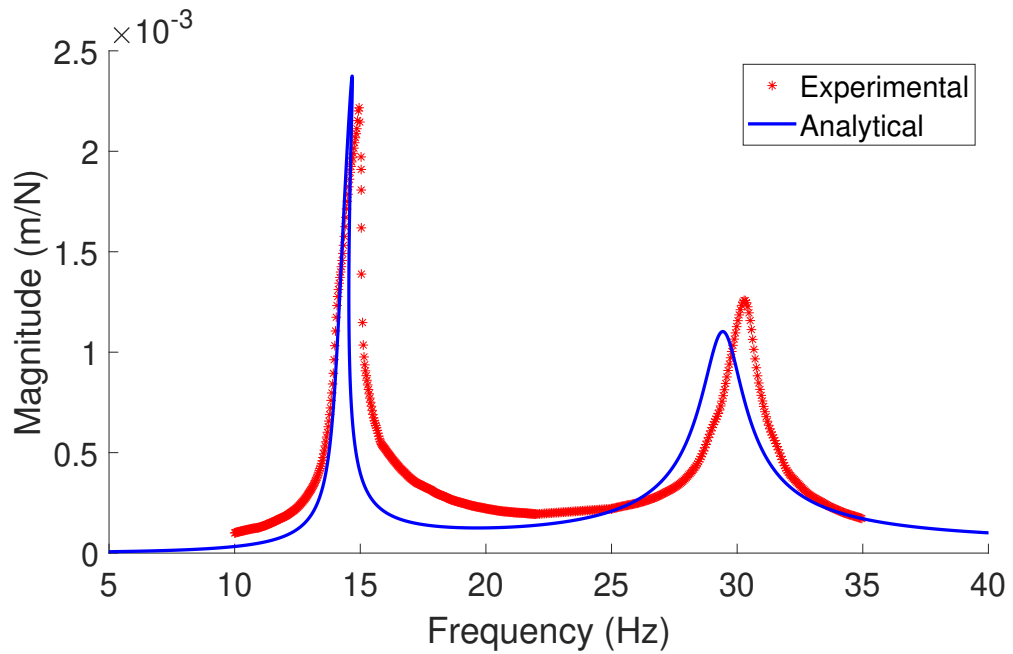
Table 6.5.1: Values of the unknown parameters obtained through optimisation.

Previously it was noted that the values of the resistors used in the circuitry between the PZT elements and the ADC need not be included in the analytical model as the RPi manipulates the readings to reflect the voltage output. In prior optimisations the value of R_{lps} was negligible in comparison to the total resistance of the resistors in the physical circuitry. Whilst the optimal resistive load found in this case is larger than those previously, the magnitude is still considerably smaller than the resistance in the experimental set-up. Hence, the aforementioned explanation that this resistance is from other components in the circuit is still valid, and the increase of R_{lps} compared to prior values attained may be attributed to the alteration of the resistors in the circuit. Whilst it is possible to comment on the plausibility of these values, the same cannot be

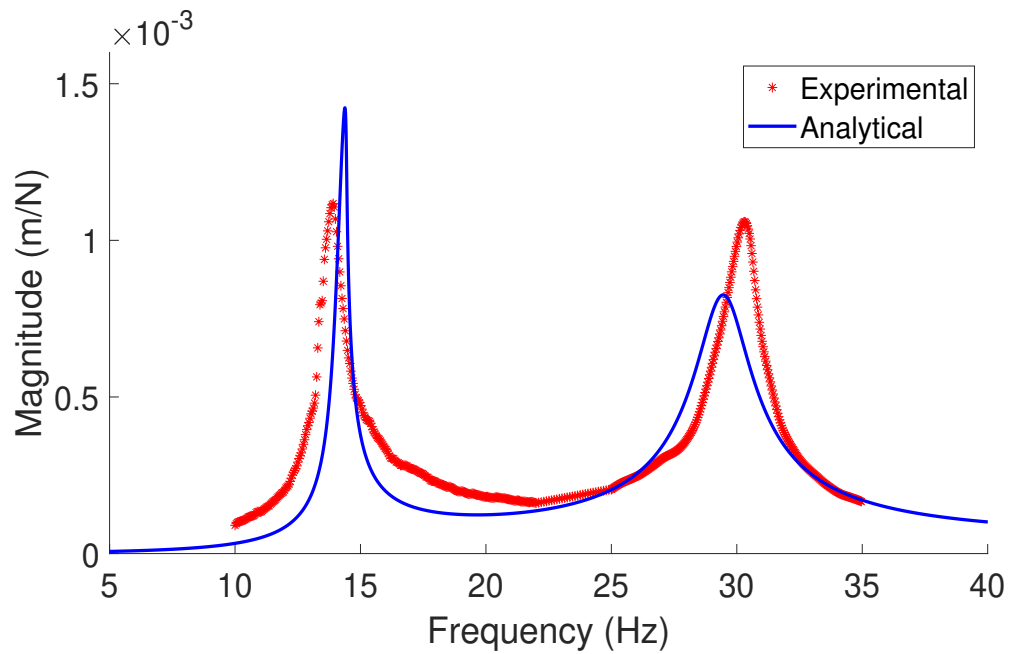
done for the stiffness and damping terms, as the former has a nonlinear element which is harder to predict, and the latter is commonly obtained through a comparison with experimental data. Hence, to obtain an insight into the feasibility of these values the experimental and analytical responses of the system should be compared.

The results obtained from the updated analytical model are shown in Figures 6.5.1 and 6.5.2, both of these concern the system excited through an increasing frequency range. It should be noted that the 3 N case has not been considered as an analytical model for such a response has been previously developed and verified. The former of the two figures considers the system with an excitation force of 5 N, where Figure 6.5.1a contains the uncontrolled response of the system ($K_p = 0$), and Figure 6.5.1b contains the controlled results where $K_p = 600$. Figures 6.5.2a and 6.5.2b, contain the uncontrolled and controlled results for the 7 N case, respectively. Again the proportional gain value was set to $K_p = 600$ as this was previously empirically determined to obtain the best level of attenuation of the response before this attenuation converged.

The analytical model can be considered as a relatively good representation of the experimental results when observing Figures 6.5.1a to 6.5.2b. For all cases bar the 5 N controlled case (Figure 6.5.1b) the amplitude of the response for the first mode corroborates with the experimental results to an acceptable degree. However, there is a larger discrepancy present in the amplitude of the response when observing each figure with respect to the second mode. The damping of the response is a fairly accurate representation, although not an exact match when observing both modes presented in the results. These discrepancies may be attributed to the fact that higher modes were not included in the analytical model, and so their influence on the response was excluded. Additionally when optimising the damping of a system which considers two (or indeed more) modes, then some degree of compensation of the damping of each mode is required. Hence an accurate representation of the damping of multiple modes is challenging. Acknowledging the omission of the higher modes and the challenges surrounding the representation of damping, the analytical model can be considered as a good representation of the experimental results.

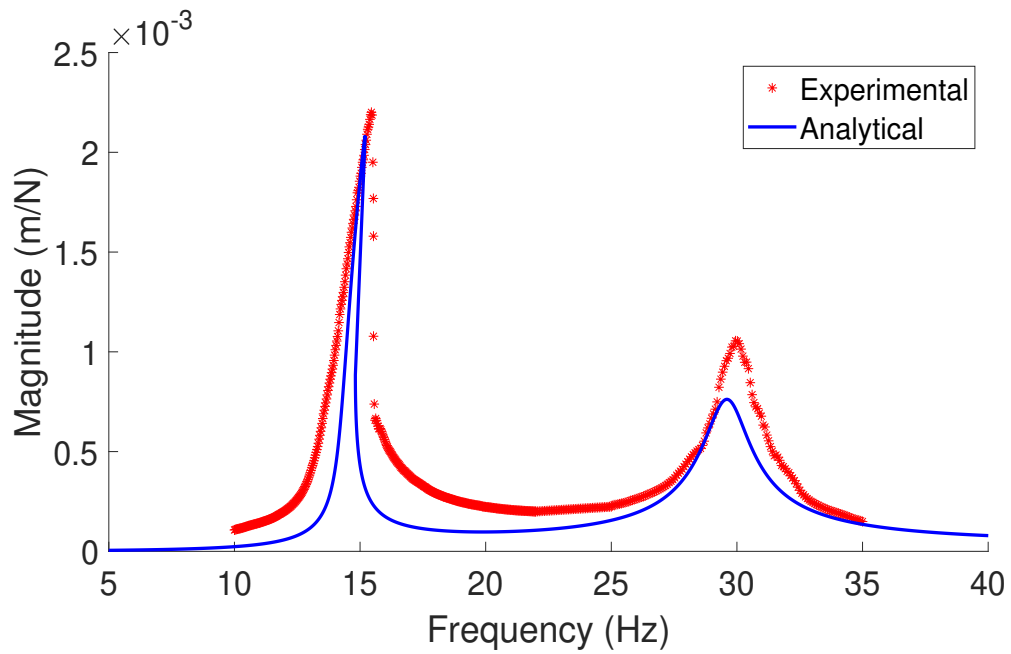


(a) Uncontrolled ($K_p = 0$).

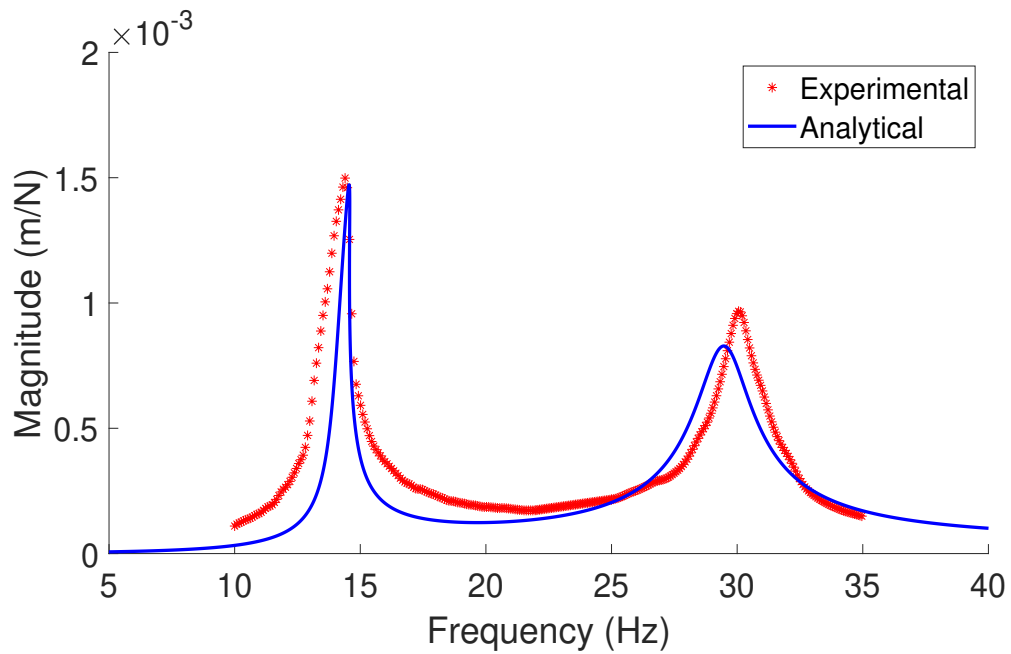


(b) Controlled ($K_p = 600$).

Figure 6.5.1: A comparison between the experimental data obtained across the first and second natural frequencies experimentally, and the data simulated by the analytical model at a force level of 5 N with a) no control applied, and b) control applied.



(a) Uncontrolled ($K_p = 0$).



(b) Controlled ($K_p = 600$).

Figure 6.5.2: A comparison between the experimental data obtained across the first and second natural frequencies experimentally, and the data simulated by the analytical model at a force level of 7 N with a) no control applied, and b) control applied.

6.6 Summary

This chapter included the induction of a nonlinear response on the link structure of the previous chapters. A geometric nonlinearity was introduced, which yielded a nonlinear response of the first mode, but not the second. With the nonlinearity present in the system the designed control system was employed to observe its effect and performance regarding the attenuation of the transverse motion of the link. Additionally the second mode of the structure was considered to observe any spillover effects present as a result of the application of the control system. The control system was found to effectively attenuate the amplitude of the response for both modes considered, and no undesirable control spillover effects were present. Additionally, the nonlinear characteristics of the response (natural frequency deviation and ‘jumps’ within the data) were seen to have been reduced by the control system. Finally, an analytical model was developed and the optimisation technique utilised to obtain the unknown parameter values was introduced. The analytical model was compared with selected sets of experimental results and was found to be a good representation of the response of the link structure.

Chapter 7

Optimal control of the system via the implementation of a more advanced control method

Throughout this research a priority was imposed upon the feasibility of the control system hardware, as opposed to the control scheme. Whilst the employment of a less complex control scheme allowed for the relevant investigations to take place without processing capacity being a concern, it did not allow for the optimisation of control system parameters nor more advanced control methods. This chapter aims to address this remaining question, modifying the previously validated analytical model to represent the link structure. The modified analytical model is presented and alongside further validation, which is then followed by the control system design and optimisation in the continuous-time domain. To represent the control system in a manner more representative of experimental implementation the Tustin transformation has been applied, and the results presented.

7.1 Modifications to analytical model

The analytical model of the closed loop system introduced in Chapter 4, has been modified to produce a transfer function model of the system. The governing equations previously introduced (Equations 4.5 and 4.6) are repeated here as Equations 7.1 and 7.2 for convenience. Note, as previously, there is no voltage applied to the PZT sensors hence $V_{in,ps} = 0$. These equations were utilised to obtain the transfer functions $G_1(s)$ and $G_2(s)$ utilised in the model, these are shown in Figure 7.1.2.

$$(-\omega^2 + 2\zeta\omega_n j\omega + \omega_n^2) P_0 - \chi_{ps} V_{in,ps} - \chi_{pa} V_{in,pa} = F_0 \quad (7.1)$$

$$V_{out,ps} = \frac{-j\omega\kappa_{nps}}{j\omega C_{ps} + \frac{1}{2R_{lps}}} P_0 \quad (7.2)$$

where, ω is the excitation frequency, ω_n denotes the natural (or resonance) frequency, and ζ is the damping ratio. P_0 is the generalised modal coordinate and χ and V are the electromechanical coupling term and voltage applied/generated, respectively. The subscripts pa and ps , denote the variable as being related to the PZT sensors and actuators, respectively. The amplitude of the force input is represented as F_0 , $j = \sqrt{-1}$, and the modal coupling of the PZT sensors is represented as κ_{nps} . The capacitance and resistive load across the PZT sensors are represented as C_{ps} and R_{lps} , respectively. The application of the Fourier transform ($s = j\omega$) to and the rearrangement of Equations 7.1 and 7.2 yields the transfer functions $G_1(s)$ and $G_2(s)$ (Equations 7.3 and 7.4). The former of these equations utilises the same variable for the reference signal for both the error in terms of the voltage output from the PZT sensors ($E_{V_{ps}}$), and the error in terms of the generalised coordinate (P_0). This is possible as $V_{out,ps}$ is proportional to P_0 , and the objective of the control in this case is to drive both variables to zero.

The transfer functions $G_1(s)$ and $G_2(s)$, alongside that of the control transfer function $G_c(s)$ (see Equation 7.5), can be utilised to provide the overall transfer function of the system relating the disturbance (F_0) and the reference ($REF(s)$) to the generalised coordinate (P_0). This relation is shown as Equation 7.6, which may be written as Equation 7.7 when utilising $REF(s) = 0$ and Equations 7.3 to 7.5.

$$G_1(s) = \frac{E_{V_{ps}}}{E_{P_0}} = \frac{REF(s) - V_{out,ps}(s)}{REF(s) - P_0(s)} = \frac{-s\kappa_{nps}}{sC_{ps} + \frac{1}{2R_{lps}}} \quad (7.3)$$

$$G_2(s) = \frac{P_0(s)}{F_0(s) + \chi_{pa} V_{in,pa}(s)} = \frac{1}{s^2 + 2\zeta\omega_n s + \omega_n^2} \quad (7.4)$$

$$G_c(s) = \frac{V_{in,pa}(s)}{E_{V_{ps}}} = K_p + K_i \frac{1}{s} + K_d s \quad (7.5)$$

$$P_0(s) = \frac{REF(s)G_1(s)G_c(s)\chi_{pa}G_2(s)}{1 + G_1(s)G_c(s)\chi_{pa}G_2(s)} + \frac{F_0(s)G_2(s)}{1 + G_1(s)G_c(s)\chi_{pa}G_2(s)} \quad (7.6)$$

$$\frac{P_0(s)}{F_0(s)} = \frac{1}{\left(1 + \frac{K_d \chi_{pa} \kappa_{nps}}{s C_{ps} + \frac{1}{2R_{lps}}}\right) s^2 + \left(2\zeta\omega_n + \frac{K_p \chi_{pa} \kappa_{nps}}{s C_{ps} + \frac{1}{2R_{lps}}}\right) s + \left(\omega_n^2 + \frac{K_i \chi_{pa} \kappa_{nps}}{s C_{ps} + \frac{1}{2R_{lps}}}\right)} \quad (7.7)$$

The analysis of Equation 7.7 yields an insight into the influence of the control gains on the response of the system. Previous investigations have proven that the application of a proportional gain renders a response containing traits of proportional-derivative (PD) control. This was attributed to the real and imaginary terms included in the system as a result of the resistance and capacitance of the PZT sensors (the second term in the denominator of Equation 7.7 should be considered here). As the capacitance of the sensors (C_{ps}) tends to zero the application of K_p will yield a response more akin to that expected of derivative control. In an opposing manner, as the resistive load of the sensors (R_{lps}) tends to infinity the application of K_p will render a response similar to proportional control. Hence, the application of K_p within this system will render a response between purely proportional and purely derivative control.

Similarly, the application of a derivative gain within the control of this system is unlikely to render a conventional response (see the first term of Equation 7.7), with $R_{lps} \rightarrow \infty$ resulting in pure derivative control, and $C_{ps} \rightarrow 0$ resulting in an inerter, or an ungrounded capacitor. This may be described as being analogous within a mechanical system (in a force-current analogy) as a mechanical device with one port and two nodes, that has the property that the relative acceleration between the nodes is proportional to the equal and opposite force applied at the nodes [170]. The effect of an inerter within a control system is similar to increasing the inertia of the sprung object, in this case the link structure. Thus, the application of K_d within this control system results in a response which lies between pure derivative control and the increase of inertia. Hence, it may be hypothesised that rather than a convergence of the minimisation of the attenuation of the response as previously seen when increasing values of K_p were employed, the result of increasing K_d will lead to a minima when an appropriate balance has been attained.

Finally, through the observation of the third term in the denominator of Equation 7.7 an insight into the influence of the integral gain may be obtained. Here, as $R_{lps} \rightarrow \infty$ the application of K_i would yield a response akin to purely integral control, whereas as $C_{ps} \rightarrow 0$ the result is more like pure proportional control. Thus, for this system the response will contain traits of proportional-integral (PI) control. As a final important note regarding the third term of the denominator of Equation 7.7, the integral gain is divided by the s term. To further investigate the influence of this relation on the response of the system (and the polarity of the gain), it was multiplied by the complex conjugate to yield its real and imaginary parts. This is shown as Equation 7.8 where it can be seen that the last term on the right-hand side is negative, but the second to last is positive. The real part of this term will increase the natural frequency of the system (added to ω_n^2), however, the imaginary part will reduce the damping. Plotting the transfer function (Equation 7.7) against K_i (shown in Figure 7.1.1) shows that the effect of a decrease in damping is much more significant than an increase in stiffness when only an integral controller is used ($K_p = K_d = 0$). Therefore, it may be inferred that for this particular system, and if only integral control is used, which is not a common practice in control systems engineering, a negative control gain will attenuate the steady-state response. However, it will be shown later that a positive integral gain will give the minimum response when PID control is utilised.

$$\omega_n^2 + \frac{K_i \chi_{pa} \kappa_{nps}}{s C_{ps} + \frac{1}{2R_{lps}}} \times \frac{s C_{ps} - \frac{1}{2R_{lps}}}{s C_{ps} - \frac{1}{2R_{lps}}} = \omega_n^2 + \frac{K_i \chi_{pa} \kappa_{nps} \frac{1}{2R_{lps}}}{\omega^2 C_{ps}^2 + \left(\frac{1}{2R_{lps}}\right)^2} - \frac{K_i \chi_{pa} \kappa_{nps} C_{ps}}{\omega^2 C_{ps}^2 + \left(\frac{1}{2R_{lps}}\right)^2} s \quad (7.8)$$

It should be noted that a second system, that omitted the transfer function relating to the PZT sensors ($G_1(s)$) and the associated gain (χ_{pa}), was created for the verification of this finding. This system also had a second-order plant ($G_2(s)$), with the coefficients set to one so that $G_2(s) = 1/(s^2 + s + 1)$. It was found that, as with the system within this research, the integral gain had to be negative in order to attenuate the response when using PI control. It may then be inferred that the necessity for a negative integral gain is attributed to the transfer function of the system as opposed to the inclusion of the PZT sensors. Whilst it is uncommon for negative gains to result in effective attenuation, it is not unheard of, as in some situations the system design may require this [171].

The two transfer functions $G_1(s)$ and $G_2(s)$ are included in the block diagram used to model the system as shown in Figure 7.1.2. The error in terms of the generalised coordinate is denoted as E_{P_0} , and in terms of the voltage output from the PZT sensors

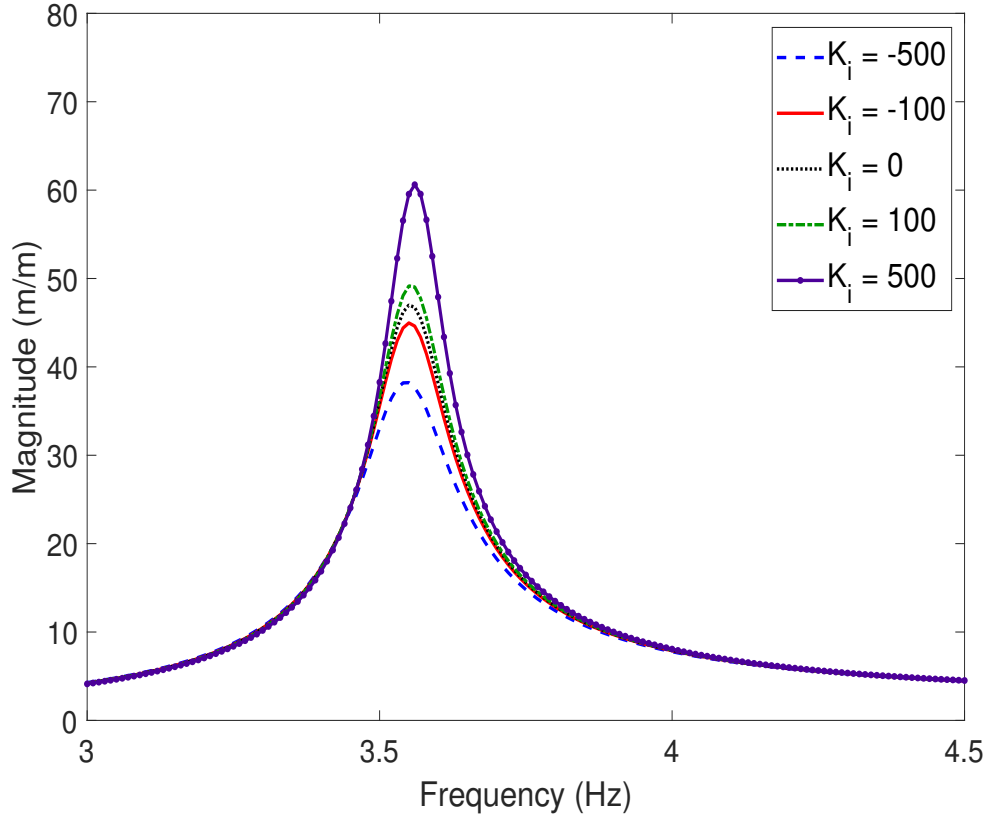


Figure 7.1.1: The response of the system (tip displacement divided by the base displacement) for varying values of integral gain ($K_p = K_d = 0$).

as $E_{V_{ps}}$. Also included in Figure 7.1.2 is a gain block labelled χ_{pa} that essentially utilises the electromechanical coupling term so that the voltage is rendered into a unit equivalent to that of P_0 . The block labelled as $G_c(s)$ represents the control block which, for the purpose of validating the model, only applies proportional control. This is akin to setting the integral and derivative gains (K_i and K_d) to zero in representation of $G_c(s)$ shown in Figure 7.1.2. The transfer function model was employed where the disturbance (shown as $F_0(s)$ in Figure 7.1.2) was harmonic and the reference ($REF(s)$) was set to zero. All other variables were of the same values as those obtained or calculated for the link first introduced in Chapter 3.5 (link B). The voltage to the PZT actuators was limited to 350 V in the transfer function model to reflect the limitations of the physical system. All of the blocks shown in Figure 7.1.2 were employed in a SIMULINK model [172], with the addition of a function block between $G_c(s)$ and χ_{pa} employed to limit the magnitude of the voltage to the actuators.

The results obtained from the transfer function model were compared to those obtained in previous experimental investigations, which were presented in Chapter 5 (Figures 5.2.4 and 5.2.5). This comparison is presented as Figures 7.1.3 a) and 7.1.3 b), for

the four proportional gain values previously used. The transfer function model yields a good representation of the experimental results for both the tip displacement and the voltage output from the PZT sensors, and although there are some discrepancies, they are on par with those of the analytical model. With the new model showing such a good representation of the system, it can be confidently utilised further to analyse the response and control of the system with a more advanced control scheme. One notable advantage of modelling the system in this way concerns the weighting values for the real and imaginary parts of the equation utilised in the analytical model to describe the voltage output from the PZT sensors (see Equation 5.4). These values were not necessary as the equation describing the output from the PZT sensors (Equation 7.2) was employed without the manipulation rendering its real and imaginary parts.

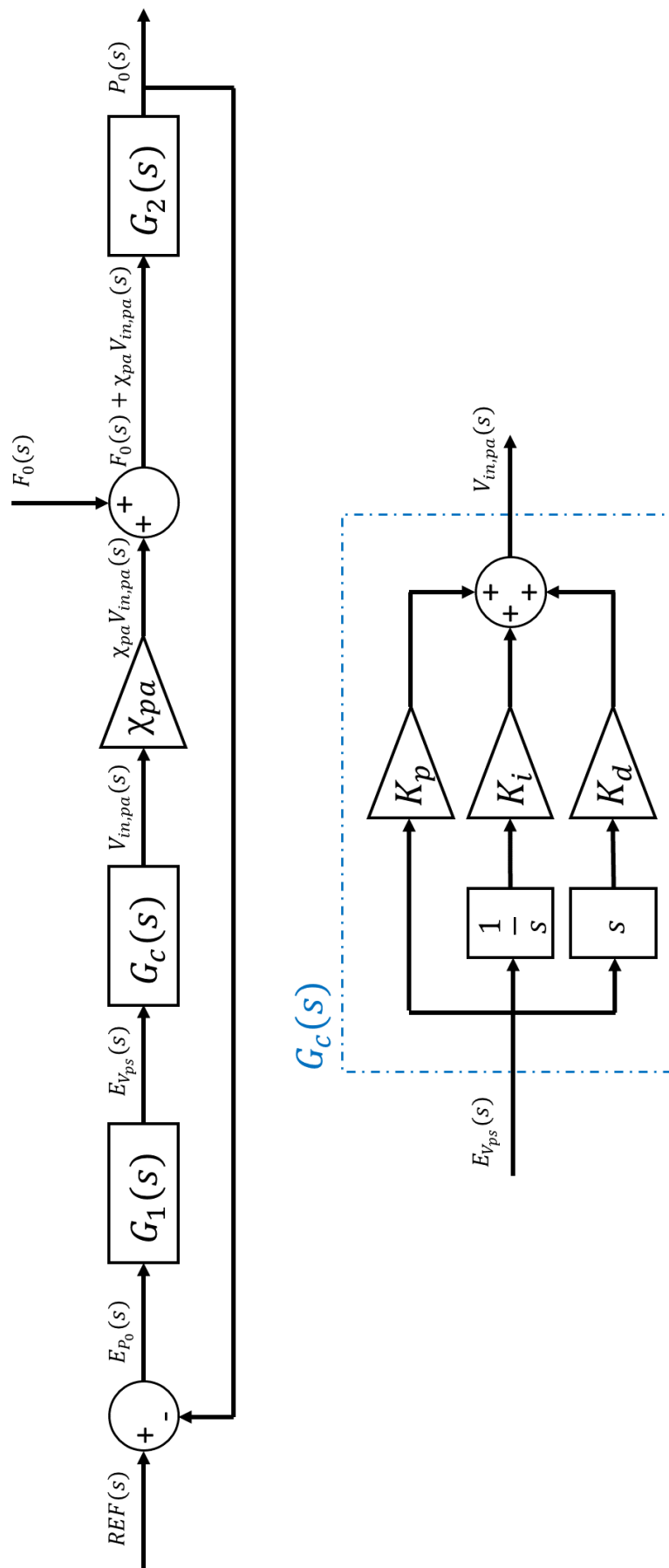
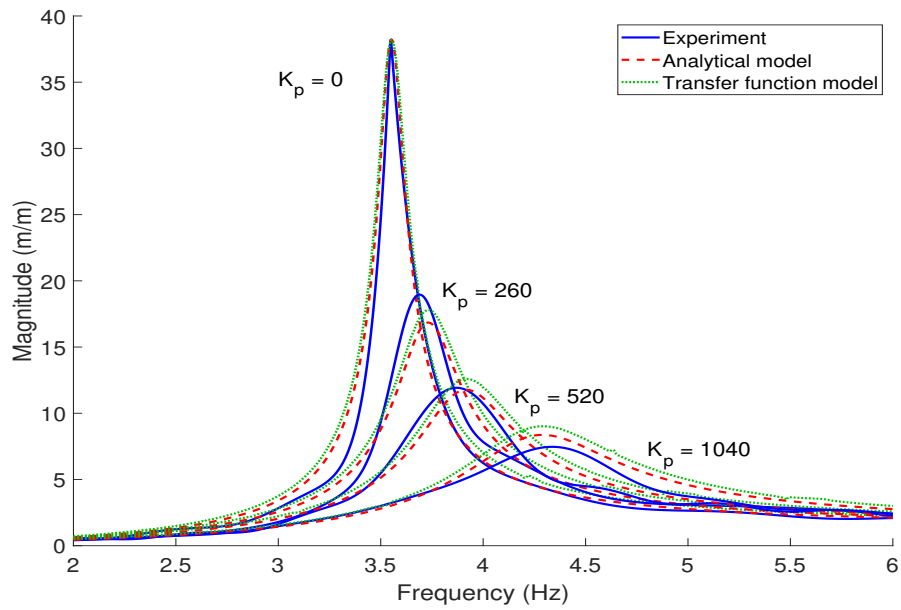
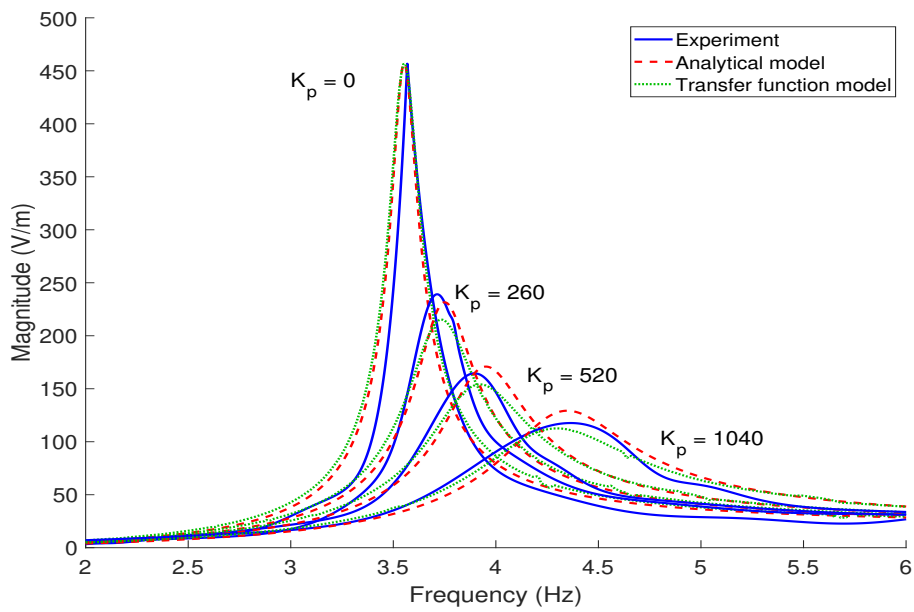


Figure 7.1.2: An illustration of the block diagram of the closed loop system, highlighting the control block.



(a) Tip displacement divided by the base displacement.



(b) Voltage output from sensors divided by the base displacement.

Figure 7.1.3: A comparison between the experimental (solid lines), analytical model (dashed lines), and transfer function model (dotted lines) results concerning a) the tip displacement, and b) the voltage output from the sensors.

7.2 Overview of PID control and associated tuning methods

A proportional-integral-derivative (PID) control scheme is widely employed within control systems engineering [57, 173, 174], however its employment in this case was not based on popularity. A PID controller may, in this case, be thought of as an extension of the previous investigations which only considered proportional control. However, even with this previously limited control scheme the response of the system contained traits of both proportional and derivative control affecting both the damping and natural frequency of the response. Often the derivative term of the classic PID control scheme is omitted to yield a proportional-integral (PI) control scheme. The reason for this lies in the effect this term has on a system in comparison to the other two terms; the proportional term decreases the response time of a closed loop system and has a major impact on the response of the system in terms of controlling the amplitude. However, the proportional term, reduces the steady state error but does not eliminate it entirely, leading to the employment of the integral term [175]. The derivative term provides phase lead, which offsets the phase lag that results from the use of the integral term. Although this term does affect the response of the system positively, the effect is often small in comparison to the proportional and integral terms, having a “more dramatic” effect on second-order systems [176].

Whilst it is important to acknowledge the omission of the derivative term in certain cases, in this research this will not be the case as it has been deemed highly relevant to the investigation of more advanced control. This is to observe its influence on a response that already contains traits of proportional-derivative control when only proportional control is utilised. The control system employed within the transfer function model is a common one, and has been included in Figure 7.1.2 labelled as ‘ $G_c(s)$ ’. The error that is the input into the controller is in terms of the voltage output from the PZT sensors ($E_{V_{ps}}(s)$) is also included in Figure 7.1.2, as is the output from the control block which is the voltage applied to the PZT actuators ($V_{in,pa}(s)$). This output is a summation of the error multiplied by the proportional gain, the integral of the error multiplied by the integral gain and the derivative of the error multiplied by the derivative gain, as shown in Equation 7.9.

$$V_{in,pa}(s) = E_{V_{ps}}(s) \left(K_p + \frac{1}{s}K_i + sK_d \right) \quad (7.9)$$

As with most control schemes a PID controller requires ‘tuning’, or the adjustment of the gain values (K_p , K_i and K_d) to obtain the required response (or as close to it as the system will allow). The Zeigler-Nichols (Z-N) method is a popular and relatively

simplistic method (no complex computer algorithms for optimisation), that has been employed in many a research endeavour [177, 178, 179]. Tan et al. [180] compare several “well-known” tuning methods for a PID control including, among others: the Z-N (based on the ultimate gain (K_{cr}) and the ultimate period (T_{cr})), the Cohen-Coon (C-C), the internal model control (IMC), the gain-phase (G-P) margin, and the integral of time-weighted absolute error (ITAE) methods. The reader is referred to [180] for the objective functions utilised by Tan et al. in their research. The responses of the system using the gains optimised by each of these methods were compared after a step input and a load disturbance were applied sequentially at $t = 0$ and $t = 10$ seconds. It should be noted that different tuning formulas for the ITAE method were used depending on whether there is a set-point or a load disturbance. Of the methods listed above, Z-N, C-C, and the ITAE-load methods are considered the load-based methods. The authors note from the results (see Figure 7.2.1) that the C-C method is too aggressive in comparison to the remaining two methods. In terms of the set point the approximate overshoot for the C-C method was 60%, the ITAE-load method was 55% and the Z-N method was 40%. When considering the response after the load disturbance, the ITAE method had the fastest, followed closely by the Z-N method with the C-C being a lot slower and the system showed a transient response (see Figure 7.2.1).

Of the set-point methods (IMC and G-P), the authors note that the G-P method is only slightly better than the IMC method. Again, considering the approximate percentage overshoot (for the set-point disturbance), the two set-point methods produce almost identical responses at around 17%. However, the responses take longer to return to the unit set-point than both the Z-N and ITAE-load methods, a similar observation can be made when considering the load disturbance where the responses of the IMC and the G-P methods are also slower than the Z-N and ITAE-load methods. The groupings of the methods as shown in Figure 7.2.1 are not arbitrary, with the authors labelling the grouped methods as ‘conservative’, ‘proper’ and ‘aggressive’ from the top to the bottom graphs. The results of the research lend to the authors concluding that the Z-N method offers the best compromise between the performance for the process in question and robustness.

It is important to acknowledge that whilst the results published by Tan et al. show the Z-N method to be the most suitable tuning method for a PID controller, this may only be true for the particular system and disturbances within their research. Hence, it was deemed necessary to investigate not only the Z-N method but also the use of the ITAE criterion as an objective function to be minimised via parametric sweeps of the gain values and the utilisation of MATLAB’s Optimisation Toolbox [181].

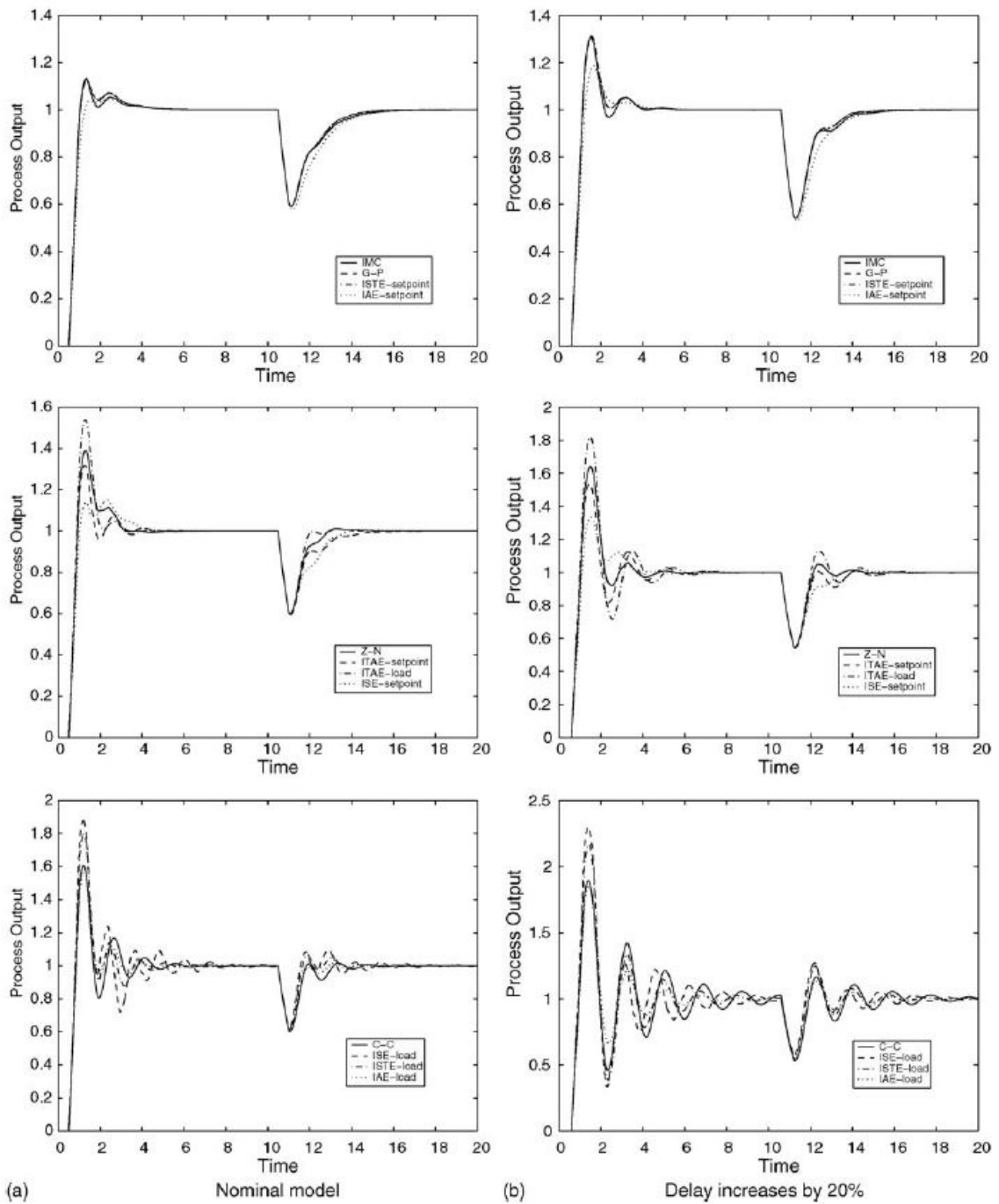


Figure 7.2.1: The results published by Tan et al. [180] showing the responses of the system for a) nominal model and b) delay increases by 20%.

7.3 An investigation of PID tuning methods

The Ziegler-Nichols (Z-N) tuning method requires that the critical gain value (K_{cr}) and the critical period (T_{cr}) be obtained. These may be identified when the system is subject to input (i.e., the disturbance in Figure 7.1.2), and the proportional gain value K_p is adjusted until a marginally stable response is obtained. This response will be of constant amplitude and period, which is taken to be T_{cr} , and the value of K_p is then said to be K_{cr} . These values are then utilised for a proportional (P), a proportional-integral (PI), a proportional-derivative (PD) and a proportional-integral-derivative (PID) controller as shown in Table 7.3.1 [182].

Control Type	K_p	K_i	K_d
P	$0.50K_{cr}$	-	-
PI	$0.45K_{cr}$	$0.54K_{cr}/T_{cr}$	-
PD	$0.8K_{cr}$	-	$0.10K_{cr}/T_{cr}$
PID	$0.60K_{cr}$	$1.2K_{cr}/T_{cr}$	$0.075K_{cr}/T_{cr}$

Table 7.3.1: The Ziegler-Nichols tuning method parameters for four control types (P, PI, PD and PID).

As previously identified, the employment of proportional control lends to a response that contains traits of both proportional and derivative control. Due to this, the conventional use of the Z-N is not suitable, and the control types denoted here as P, PI, PD and PID describe only the control gains applied within the controller and not necessarily the closed loop system as a whole. It should be noted that an investigation was conducted where the proportional gain value was increased, with the disturbance a unit impulse and the reference ($REF(s)$) set to zero. However, due to the derivative aspect of the response, a constant amplitude oscillation could not be attained. Thus, another value for use as the proportional gain was sought, which would lend to attaining the critical gain value. In a previous investigation an optimal proportional gain value was empirically obtained ($K_p = 1040$), this being the maximum gain value before the percentage decrease of the amplitude converged. However, this was deemed an inappropriate value to use within the Z-N tuning method for two reasons, the first being that this was based on a harmonic input and the second being that it was obtained under the circumstances of a discrete-time system whereas the transfer function model is in the continuous-time domain. Hence a unit impulse was applied as the disturbance within the model of the closed loop system, and a parametric sweep of the proportional

control gain (K_p) was conducted. The value of K_p that yielded the minimum of the integral of the time-weighted absolute error (ITAE) was taken to be the optimal value. The ITAE performance index may be mathematically described as Equation 7.10 [183].

$$ITAE = \int_0^{\infty} t | E_{P_0}(t) | dt \quad (7.10)$$

A multitude of research has utilised the ITAE criterion for the tuning of PID control parameters, including the work by Tan et al. [180] as previously discussed, [184, 185, 186]. The use of ITAE is often proven to result in smaller overshoots and oscillations than similar methods such as the integral of the absolute error (IAE) and the integral of the square error (ISE) [185]. The time-weighting is employed due to the initial error being large relative to the error at a later time in the response for a unit step or impulse excitation [187]. Hence, it is important to acknowledge that whilst the sampling frequency has an influence on the accuracy of the integral of a signal (more so when approximation methods are employed), this is small in comparison to the effect that the multiplication of the time has within the ITAE method. However, for a continuous-time model the sampling frequency for both the integration operation and the multiplication of the time can be set so as the resultant value is considered accurate, which is not the case in a discrete-time model and thus is addressed in the proceeding section.

Whilst conducting the parametric sweep of the proportional gain value (K_p) for use in the Z-N method, it was deemed pertinent that the sensitivities of the system to each of the gain values were investigated. For this system it was hypothesised based on similar systems that integral only control is likely to render large overshoots and/or oscillation, neither of which is desirable. Hence, for the parametric sweep of this control gain (K_i) the proportional control gain was held constant at the value previously indicated as the optimum from the parametric sweep. In a similar manner, the use of derivative control alone was hypothesised to render an undesirable response, hence the parametric sweep of the derivative gain was also conducted with the proportional gain held at a value previously indicated as the optimum. The results of these investigations are shown in Figures 7.3.1 and 7.3.2, and the empirically obtained optimum gain values are presented in Table 7.3.2 alongside the corresponding values of the ITAE for each case.

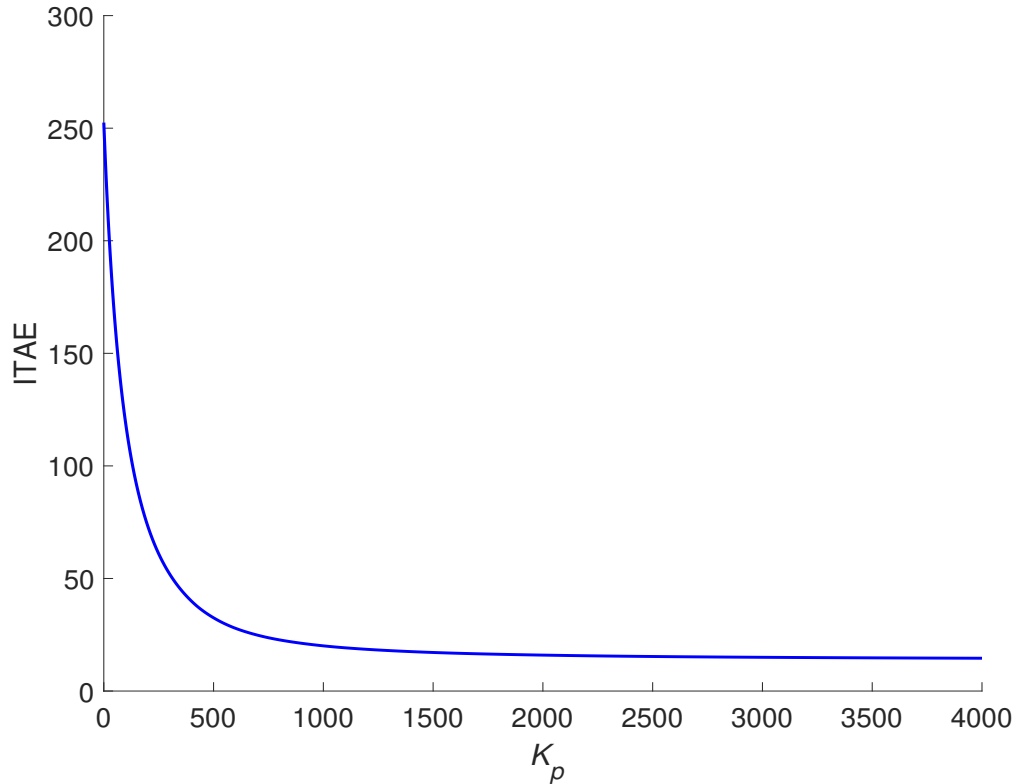
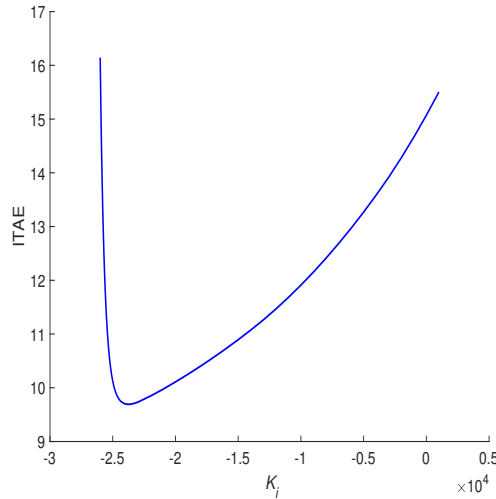
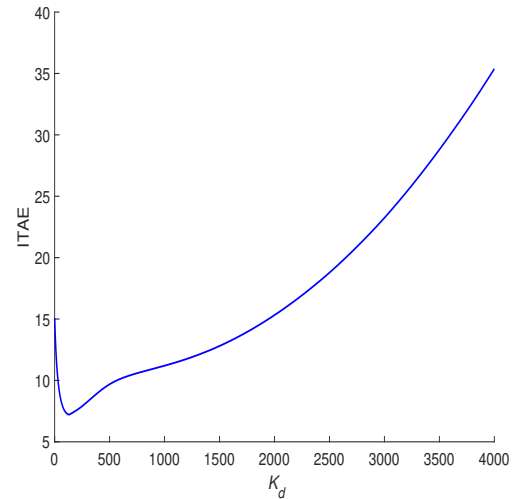


Figure 7.3.1: The value of the ITAE for the case of the parametric sweep of the proportional gain (K_p), with the integral and derivative gains set to zero ($K_d = K_i = 0$)

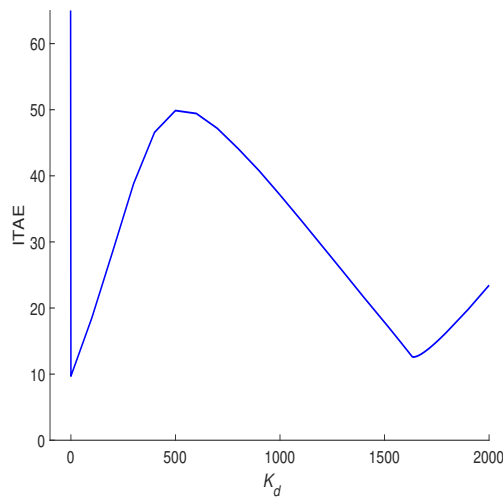
Figure 7.3.1 contains the result of the parametric sweep of the proportional gain (increased in steps of one), which enables an insight into the most appropriate value of proportional gain to employ in the Z-N tuning method. The ITAE reaches a minimum and converges at a value of 15.0706 at $K_p = 2860$, which was then utilised in the Z-N tuning method ($0.50K_{cr} = 2860$). Figure 7.3.2 contains the results from multiple parametric sweep investigations, with Figure 7.3.2a containing the resultant values of the ITAE in the case where the integral gain is swept from $K_i = -26000$ to $K_i = 1000$, and the proportional gain is held constant ($K_p = 2860$). Whilst it is not conventional to utilise a negative integral gain value as this often leads to instability, it was in this case necessary (see Section 7.1). For this system decreasing the value of K_i from zero decreases the value of the ITAE, until a certain point at which the lower values (higher magnitudes of negative gain) lead to the system becoming unstable. In a similar manner, increasing K_i from zero leads to an increase in the ITAE. In the case shown in Figure 7.3.2a the ITAE value is increased beyond that of the case where only K_p is used. However, it was found that regardless of the value of K_p , a positive K_i will lead to an increase in the ITAE. Thus, a proportional gain must be employed when using a positive integral gain, however this will not lead to an optimal set of gains



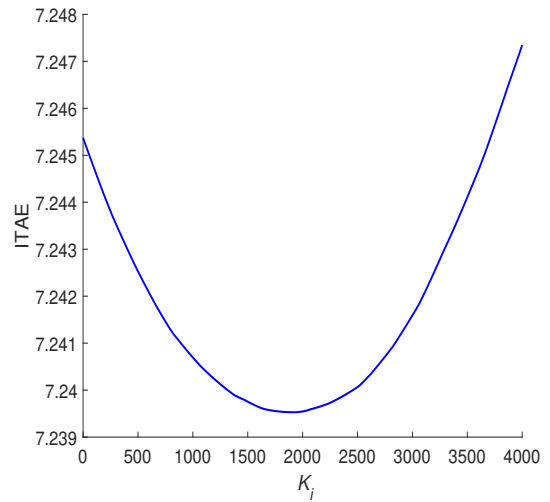
(a) K_i sweep ($K_p = 2860$).



(b) K_d sweep ($K_p = 2860$).



(c) K_d sweep ($K_p = 2860$ and $K_i = -23745$).



(d) K_i sweep ($K_p = 2860$ and $K_d = 120$).

Figure 7.3.2: The value of the ITAE for the case of a) the parametric sweep of the integral gain when $K_p = 2860$, b) the parametric sweep of the derivative gain when $K_p = 2860$, c) the parametric sweep of the derivative gain when $K_p = 2860$ and $K_i = -23745$, and d) the parametric sweep of the integral gain when $K_p = 2860$ and $K_d = 120$.

within a PI control scheme. As can be seen from the results of Figure 7.3.2a, the gain values of $K_p = 2860$ and $K_i = -23745$ yield a minimum of the ITAE value at 9.6928.

It was hypothesised that, after the analysis of the transfer function of the system, the maximum attenuation of the system when increasing the value of K_d would be found as a minima as opposed to a convergence (as in the case of the parametric sweep of K_p). As can be seen from Figure 7.3.2b, where the results were obtained through the utilisation of $K_p = 2860$ and a parametric sweep of K_d was conducted, this is the case. A minimum value of the ITAE in this investigation was found to be 7.2454, where

Parametric sweep of:	Gain Value			ITAE
	K_p	K_i	K_d	
K_p	2860	0	0	15.0706
K_i (with K_p held)	2860	-23745	0	9.6928
K_d (with K_p held)	2860	0	120	7.2454
K_d (with K_p and K_i held)	2860	-23745	0	9.6928
K_i (with K_p and K_d held)	2860	1917	120	7.2395
both K_p and K_i	1500	-20813	0	9.6090
both K_p and K_d	1775	0	100	7.1509

Table 7.3.2: Gain values obtained based on the parametric sweeps, alongside the corresponding ITAE value for each of the investigations.

$K_d = 120$. It should be noted that negative values of K_d were employed, but this led to an increase in the value of the ITAE. A second investigation involving the parametric sweep of K_d was conducted, and in this case both the proportional and integral gains were held constant ($K_p = 2860$ and $K_i = -23745$). The results of this are presented as Figure 7.3.2c, where it can be seen that again minima are present. The minima with the lowest value of the ITAE (9.6928) occurs when $K_d = 0$, with the second minima having an ITAE value of 12.5959 when $K_d = 1640$. The lowered effectiveness of the derivative gain may in this case be attributed to the large magnitude of the integral gain leading to the system being in a situation where it is closer to instability. This is supported further when noting that values lower than $K_d = 0$ and higher than $K_d = 1640$ lead to an increase of the ITAE (partially shown in Figure 7.3.2c).

The final parametric sweep of a single control gain involved holding the proportional and derivative gains constant ($K_p = 2860$ and $K_d = 120$), and increasing the value of the integral gain (K_i). The results of this investigation are presented as Figure 7.3.2d, from which a few observations may be made. Firstly, there is a minima present when $K_i = 1917$, which yields an ITAE value of 7.2395. This reduction is relatively small in comparison to the other parametric sweeps as when $K_i = 0$ the value of the ITAE was 7.2454, which, in comparison to the reduction achieved by K_p alone (252.4734 to 15.0706) is negligible. Secondly, the K_i value utilised to obtain the minimum value of the ITAE is positive in this case. The change in sign of the integral gain may be attributed to the inclusion of the derivative gain, which adjusts the dynamics of the system in terms of damping and inertia. The system is more sensitive to the derivative gain in comparison to the integral gain, allowing for the implementation of a positive integral gain with little effect on the ITAE value. Increasing K_d while holding K_p constant, and conducting a sweep of K_i would yield a minimum value of the ITAE at

a higher value of K_i . However, as the reduction in the ITAE is minimal with the set values of K_p and K_d for this system, it was not deemed pertinent to investigate this further.

From the results shown in Figure 7.3.2 it can be seen that the system is most sensitive to the proportional gain, less sensitive to derivative gain and the least sensitive to the integral gain. This last statement is based on the results from Figures 7.3.2a and 7.3.2d. The level of decrease of the ITAE attained in the first of these cases (i.e., PI control) may be attained with PD control (Figure 7.3.2b) with a gain of significantly lower magnitude. In the second case relating to the integral gain (Figure 7.3.2d), as previously mentioned the reduction of the ITAE value is negligible. Considering the method in which these results were obtained, holding certain gain values constant whilst altering others, the optimum combination is unlikely to have been obtained. Prior to conducting an optimisation of the three gain values, two studies were conducted in which the proportional and integral gains were swept parametrically simultaneously and the proportional and derivative gains were also swept parametrically simultaneously. These results are shown in Figure 7.3.3a and Figure 7.3.3b, respectively. The minimum values of the ITAE obtained in these investigations and the corresponding control gains are noted in Table 7.3.2.

Although these investigations have maximum gain values and step sizes set intuitively and conservatively based on the previous investigations and the reduction of computation time, they do provide a better insight into the influence of the combinations of gain values on the ITAE. The first investigation involving K_p and K_i , reveals that even with a varying value of proportional gain the integral gain must be negative to have a positive impact on the minimisation of ITAE. It can also be seen that at higher values of K_i the ITAE converges at a value higher than the case with no control. The minimum value obtained in this parametric sweep is $\text{ITAE} = 9.6090$ when $K_p = 1500$ and $K_i = -20813$. From previous results these are not the most effective of values or the most effective combination of control parameters. However, this does enforce the hypothesis that the system is less sensitive to the integral gain, as the magnitude of the integral gain is still relatively large. The second case (shown in Figure 7.3.3b), pertains to the simultaneous parametric sweep of the proportional and derivative gains. Here a minimum ITAE value of 7.1509 is achieved when $K_p = 1775$ and $K_d = 100$, and shows a similar trend to the previous results (see Figure 7.3.2b). This further supports the observations stated previously regarding the influence of the resistance and capacitance of the PZT sensors. Whilst it is acknowledged that with larger steps between gains these gain values may not be considered accurate, they do provide a set of values that may be used as initial estimates within the optimisation.

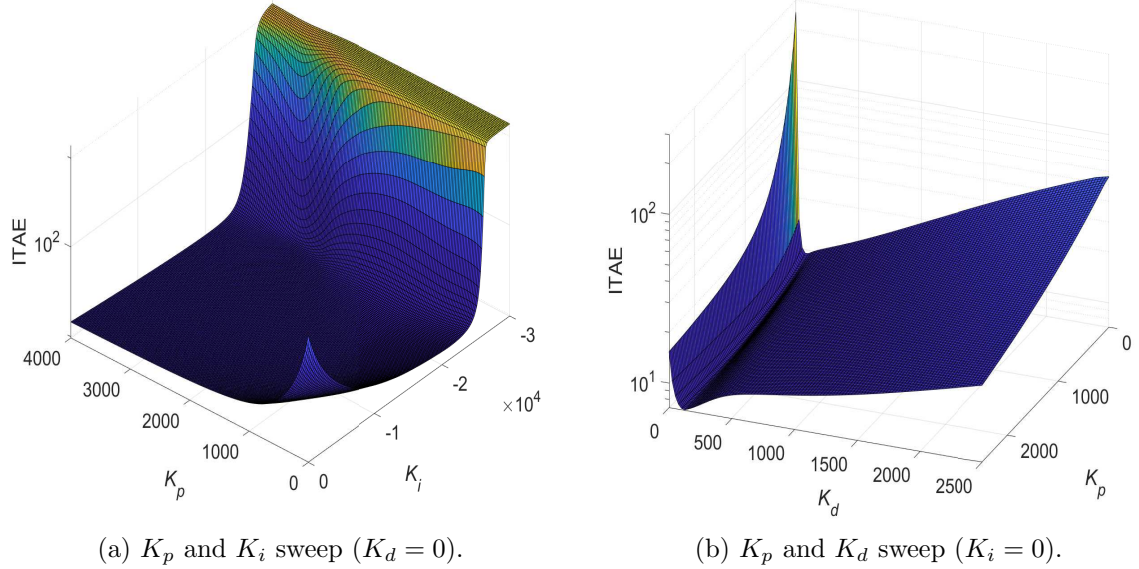


Figure 7.3.3: The value of the ITAE for the case of a) the parametric sweep of the proportional and integral gains ($K_d = 0$), and b) the parametric sweep of the proportional and derivative gains ($K_i = 0$).

An optimisation of the gain values was then conducted, employing MATLAB’s ‘fmincon’ function [188] for each of the four control schemes (P, PI, PD and PID). The objective function within this optimisation was the minimum of the ITAE (see Equation 7.10), with the initial values being those suggested as the optimum by the parametric sweeps. The lower and upper bounds were 0 and 10^6 for the proportional and derivative gains, the lower bound of the integral gain was -10^6 , and its upper bound was 10^6 . The gain values obtained from the parametric sweep, the optimisation and the Z-N tuning method are presented in Table 7.3.3, alongside the resultant ITAE value for each case. It should be noted that the Z-N values were obtained using the relations shown in Table 7.3.1, where the critical period was taken to be the average period of the response ($T_{cr} = 0.1953$ s).

The ITAE values presented in Table 7.3.3, reveal the effectiveness of each of the sets of gains in the reduction of the ITAE value. Noting that for the case with no control $ITAE = 252.5$, all of the gain sets provide a significant reduction. For each set of gain values (by the manner in which they were obtained), the values produced by the optimisation yield the lowest values of the ITAE for all of the control schemes investigated, whereas the Z-N method yields the highest. The latter statement is with the exception of the proportional only control scheme where the gain value is the same for both the parametric sweep and the Z-N method.

		Control Type			
		P	PI	PD	PID
Optimised values from parametric sweeps	K_p	2860	1500	1775	2860
	K_i	0	-20813	0	1917
	K_d	0	0	100	120
	ITAE	15.0706	9.6090	7.1509	7.2395
Optimised values from the minimum of the ITAE	K_p	47238	1221	1830	2744
	K_i	0	-18699	0	8708
	K_d	0	0	104	143
	ITAE	13.6420	9.6088	7.1468	7.1167
Z-N values	K_p	2860	2574	4576	3432
	K_i	0	15813	0	35140
	K_d	0	0	2928.3	2196.2
	ITAE	15.0706	30.049	16.263	14.888

Table 7.3.3: Gain values obtained based on the parametric sweeps, the optimisation and the Z-N tuning method, alongside the corresponding ITAE value for each of the control schemes (P, PI, PD and PID).

The responses of the system following the excitation by a unit impulse for each of the twelve cases shown in Table 7.3.3 are included in Figure 7.3.4. The results are presented so that the gain values obtained through the three different methods are shown for the cases that utilise P (Figure 7.3.4a), PI (Figure 7.3.4b), PD (Figure 7.3.4c) and PID control (Figure 7.3.4d). These results show the same trend as the ITAE values included in Table 7.3.3, with the Z-N method showing a less desirable response in terms of both the settling time and the response amplitude (with the exception of the proportional control). The response of the system when employing the control gains obtained using optimisation is shown to be the most desirable for all control schemes, although for the cases that involve derivative control the gains obtained through the parametric sweeps show similar results. This may be further supported through the comparison of the ITAE values shown for these cases in Table 7.3.3, as well as the set of results for the optimisation based gain values for the different control schemes as shown in Figure 7.3.5.

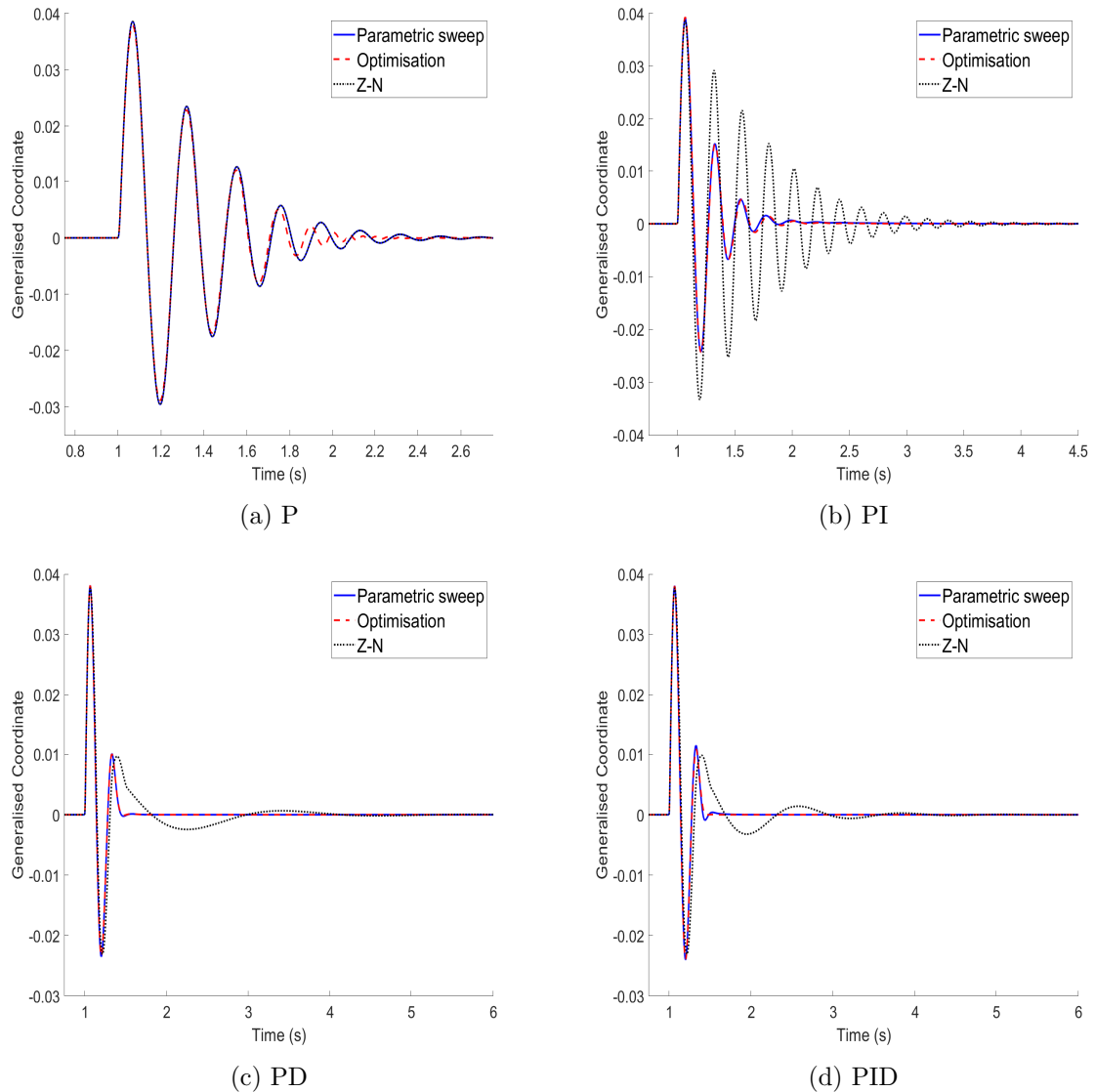


Figure 7.3.4: The response of the system subjected to a unit impulse with the application of the values from the parametric sweep, the optimisation and the Z-N method for a) P, b) PI, c) PD, and d) PID control.

The results shown in Figure 7.3.5, provide further insight into the sensitivity of the system to the different gain values, focussing on only those values obtained through the optimisation method. All four control schemes show a good level of attenuation of the response, however their effectiveness varies between them. In general terms, the P control scheme is the least effective, followed by the PI control scheme, and both the PD and PID are the most effective with few discrepancies between them. From Table 7.3.3 it can be seen that K_p for the P control scheme is almost fifty times larger than that used in the PI control scheme, and the PI control scheme utilises an integral gain of relatively high magnitude. Large values of gains may lead to instability, however as the parametric sweep of K_p showed that lower values of proportional gain still provide

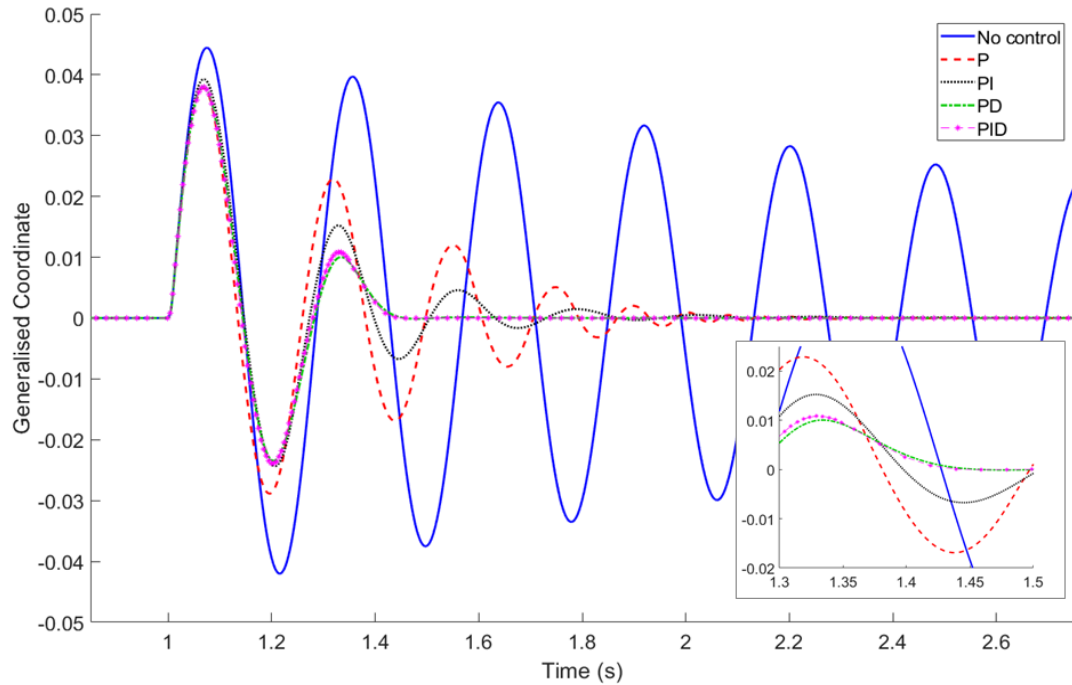


Figure 7.3.5: The response of the system subjected to a unit impulse with the application of the values from the optimisation for the four cases of control P, PI, PD and PID, alongside the case where no control was applied.

relatively good attenuation for P only control, this not of concern. However, large values of K_i are required for a similar level of attenuation, which is a concern as the parametric sweeps indicated an approach to instability. The PD control scheme utilises a proportional gain of much lower magnitude than the other control schemes, and has a higher level of attenuation than both the P and the PI control schemes. The PID control scheme results in an almost identical response to the PD control scheme, yet uses larger values of K_p and K_d by comparison. It may be inferred that the increase in K_p and K_d is a result of the inclusion of integral control.

Within the frequency response functions (FRFs) previously presented, the amplitude of the response was reduced and the natural frequency was increased (see Figure 7.1.3). This response was attributed to the resistance and capacitance of the PZT sensors, and the analysis of the transfer function of the system suggested that unconventional responses may be obtained with the employment of K_i and K_d . Hence, it is relevant to observe the response of the system whilst employing the four control schemes. Additionally, as the optimal gain values were obtained based on an unit impulse excitation it is also pertinent to observe the FRFs (i.e., harmonic excitation) for the cases where the gains values were based on the parametric sweeps, the optimisation and the Z-N method. These results are presented as Figure 7.3.6, where 7.3.6a shows the results from P only control, 7.3.6b from PI control, 7.3.6c from PD control, and 7.3.6d from

PID control. It should be noted that in this set of results the voltage to the actuators was limited to a magnitude of 350 V, as previously discussed, and the amplitude of the response at each frequency was obtained from the steady-state response in the time-domain at the corresponding frequency.

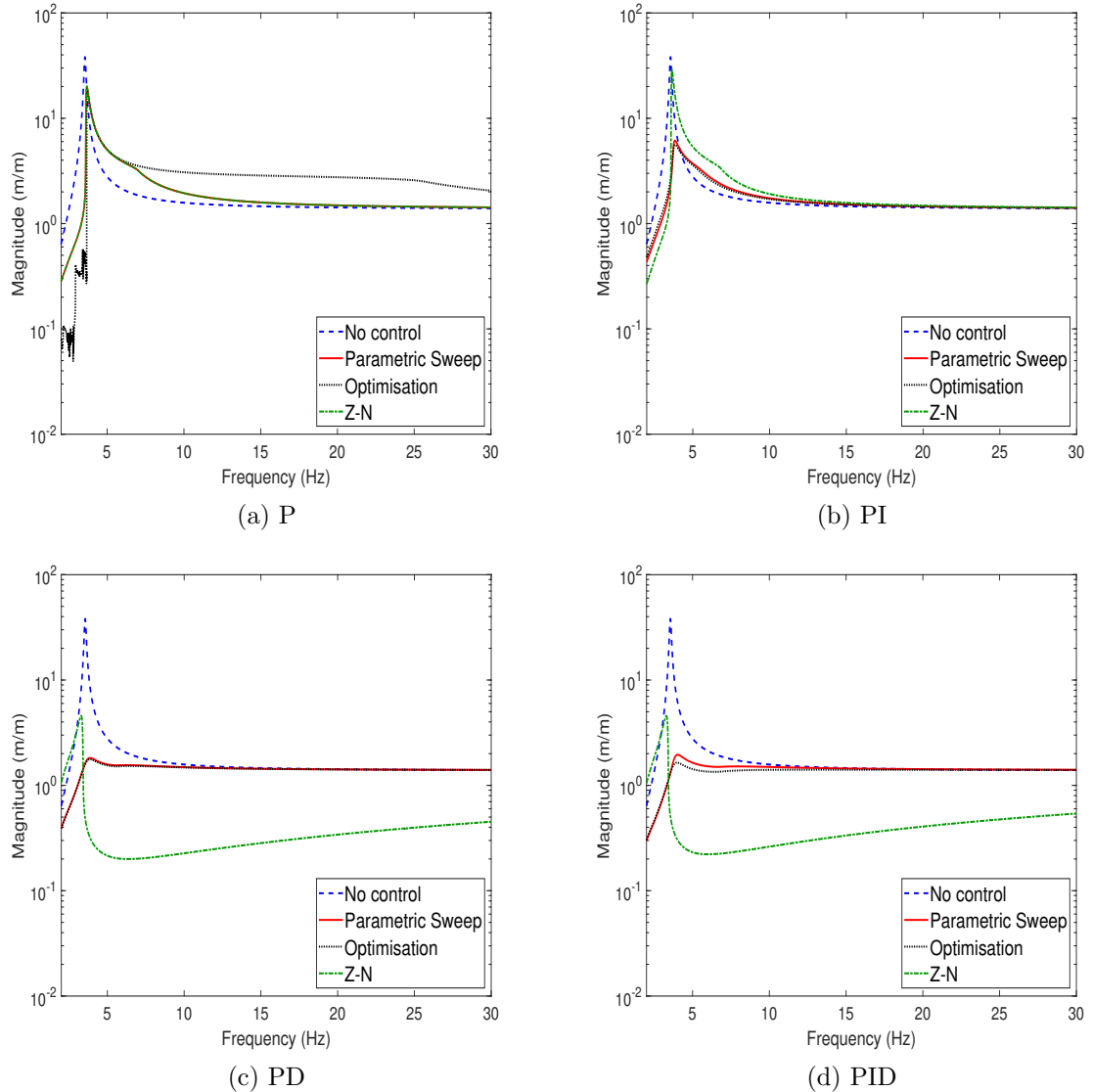


Figure 7.3.6: The response of the system subjected to a harmonic disturbance with the application of the values from the parametric sweep, ITAE method and the Z-N method compared with the case where no control was applied for a) P, b) PI, c) PD, and d) PID control.

Considering the first set of these results, the P control (Figure 7.3.6a) it is clear that an abnormal response is present when the gain values from the optimisation are utilised. Whilst this result does follow the general trend of an FRF, at frequencies below the natural frequency the response appears to contain noise followed by a jump in the response not dissimilar to a nonlinear response. This jump (but not the noise)

can also be seen (to a lesser extent) for the gains for the other two methods used to obtain the gains when P control was utilised, and again for all three methods when using PI control. It was hypothesised that the abnormalities were the result of the inclusion of the voltage limit in the control, which then introduced a nonlinear term. Considering the same control scheme (P) but in this case focussing on the response where the gain values were obtained from the parametric sweep and the Z-N method, both have identical responses. This can be explained through the analysis of the gain values employed (see Table 7.3.3) where the proportional gain utilised for both cases is identical ($K_p = 2860$). Neither of the other two methods contain the abnormal results (noise) that are present at the lower frequencies for the gains from the optimisation, which implies that they are only present at large values of K_p . It should be noted that the noise was present for all of the control schemes when a large value of proportional gain was employed (i.e., $K_p > 10^4$), which further supported the hypothesis that the voltage limitation was the cause.

Additionally, for the cases using the values obtained from the parametric sweep and the Z-N method (P and PI control), it can be seen that there is also a section of the results that have an abnormal response (between 5 Hz to 10 Hz). Again, it is hypothesised that the inclusion of the voltage limitation in the control is the cause of this response. Regardless of the values of the gains employed for the P control scheme there is a reduction in the peak amplitude of the response of approximately 50%. This suggests that the voltage limitation prevented the control system from reducing the amplitude of the response any further. This is especially noticeable when comparing the proportional gain value obtained from the optimisation ($K_p = 47238$) with those identified through the parametric sweep ($K_p = 2860$) and the Z-N method ($K_p = 2860$). Were it not for the voltage limitation a better performance would be expected from the first of these gain values, in comparison to the latter two.

The PI control scheme attains a variation in the percentage decrease of the peak amplitude of the FRFs, these values are outlined in Table 7.3.4. In the case of the PI control, the gains obtained using the Z-N method do not attenuate the response in terms of the amplitude of the peak as well as the other two methods used to attain the gains. Noting the gain values used in the PI control scheme shown in Table 7.3.4, and considering that a higher value of K_p should yield a greater reduction in the amplitude of the peak, the remaining discrepancy lies in the value of K_i . Both the parametric sweep method and the optimisation method yield values of similar magnitudes and are both negative, whereas the Z-N method yields a slightly lower magnitude and positive. The parametric sweep of K_i with $K_p = 2860$ revealed that positive values of K_i increased the ITAE beyond that of when only proportional control was applied (see Figure 7.3.2a). This lends an explanation as to why the gain values obtained using the Z-N method

lend to a less effective control scheme even though a higher value of K_p was utilised.

Figures 7.3.6c and 7.3.6d present the FRFs of the system when PD and PID control were employed, respectively. Both PD and PID control yield results similar with respect to the gain values obtained in the same manner, this may also be deduced from the respective percentage decrease values presented in Table 7.3.4. As previously identified the system is not as sensitive to the integral gain in comparison to the others, hence the similarities that may be seen between the PD and PID control schemes. Both control schemes have a response where the natural frequency has been reduced in the case of the Z-N method, and increased in the other two cases. Previously the application of control has seen an increase in the natural frequency, this difference may also be attributed to the inclusion of the voltage limitation and its introduction of a nonlinear term into the system model. Alternatively, but less likely, this may be attributed to the inclusion of the derivative term, with the decrease only being present for the gains of the Z-N method as the magnitudes of the gains are larger (See Table 7.3.3).

Method used to obtain gain values	Location	Control Type			
		P	PI	PD	PID
Parametric sweep	ω_n	95.24%	95.79%	95.75%	96.56%
	peak	47.53%	83.95%	95.24%	94.89%
Optimisation	ω_n	98.62%	92.96%	95.86%	96.59%
	peak	49.63%	85.32%	95.37%	95.70%
Z-N	ω_n	95.24%	94.27%	98.73%	98.66%
	peak	47.54%	23.19%	88.03%	88.04%

Table 7.3.4: The percentage decrease of the response amplitude based on the uncontrolled response amplitude when the voltage limit is imposed.

The gain values obtained from both the parametric sweep and the optimisation employed in the PD and PID control schemes (see Figures 7.3.6c and 7.3.6d) both show a considerable amount of control across the frequency range surrounding the first natural frequency. For the PD and PID control cases, the gain values obtained from the parametric sweep and the optimisation both yield a similar percentage decrease of around 95% of the peak amplitude of the FRF, and in a similar comparison a percentage decrease of 96% at the natural frequency (ω_n). In comparison, the Z-N method's gain values used in the PD and PID control schemes yield a higher percentage decrease at the natural frequency of the response ($\sim 99\%$), but a lower percentage decrease at the peak of the response ($\sim 88\%$). All of the aforementioned discrepancies in the decreases attained may be attributed to the magnitudes of the gain values utilised as presented in Table 7.3.3 (acknowledging that the integral gain has less impact on the response).

Even with the voltage limitation imposed the attenuation of the response by the four control schemes considered and the employment of gain values dictated by one of the three methods discussed, is greater than that shown in previous investigations. Hence, it was deemed necessary to investigate the cause of this discrepancy by modelling the system in the discrete-time domain (presented in a later section). Preceding this, given the hypotheses mentioned regarding the voltage limitation applied to the control system, it was deemed pertinent to remove this voltage limit and analyse the resultant responses with respect to the different control schemes and the manner in which the gain values were obtained. As the P control scheme where the gains were obtained from optimisation contains abnormal results, an investigation was conducted at the lower frequencies (namely 2 Hz, 2.5 Hz and 3 Hz) and at 10 Hz for comparison, for said control case. This was with the aim to discern the differences between the voltage applied to the actuators with and without the limitation. The results of this investigation are shown in Figure 7.3.7, and the corresponding responses are presented in Figure 7.3.8.

Figures 7.3.7a to 7.3.7c present the voltage applied to the actuator at the excitation frequencies 2 Hz, 2.5 Hz and 3 Hz, respectively. Comparing the voltage applied to the actuators when the voltage limitation is imposed against the case where it is not, it can be seen that the inclusion of the voltage limitation changes the form of the voltage applied at the lower frequencies considered, and introduces more frequencies into the signal. The response of the system at these lower frequencies shown in Figures 7.3.8a to 7.3.8c, confirm that the additional frequencies introduced into the voltage applied to the actuator are projected into the response. At an excitation frequency of 10 Hz these changes are not present (see Figures 7.3.7d and 7.3.8), suggesting that; this effect is dependent on the excitation frequency and is not caused by either the integral or the derivative gain as only the proportional gain was employed.

The results shown in Figure 7.3.6 may suggest that the derivative control corrects the abnormalities. However, a more reasonable explanation lies in the order of magnitude of the proportional gain used in the P and PI control schemes compared to the PD and PID control schemes (see Table 7.3.3). This leads to the voltage limitation having more of an influence on the response for the P and PI control schemes. As well as supporting the hypothesis that the inclusion of the voltage limitation caused the abnormal results shown in Figures 7.3.6a and 7.3.6b at the lower frequencies, it also offers an explanation of the shape of the FRFs at frequencies higher than the natural frequency. The voltage limitation does not allow the control scheme to reach its full potential and introduces a nonlinear term into the system. This may be addressed by utilising PZT actuators that are able to operate at higher voltages such as those shown in Figure 7.3.7 (i.e., > 600 V).

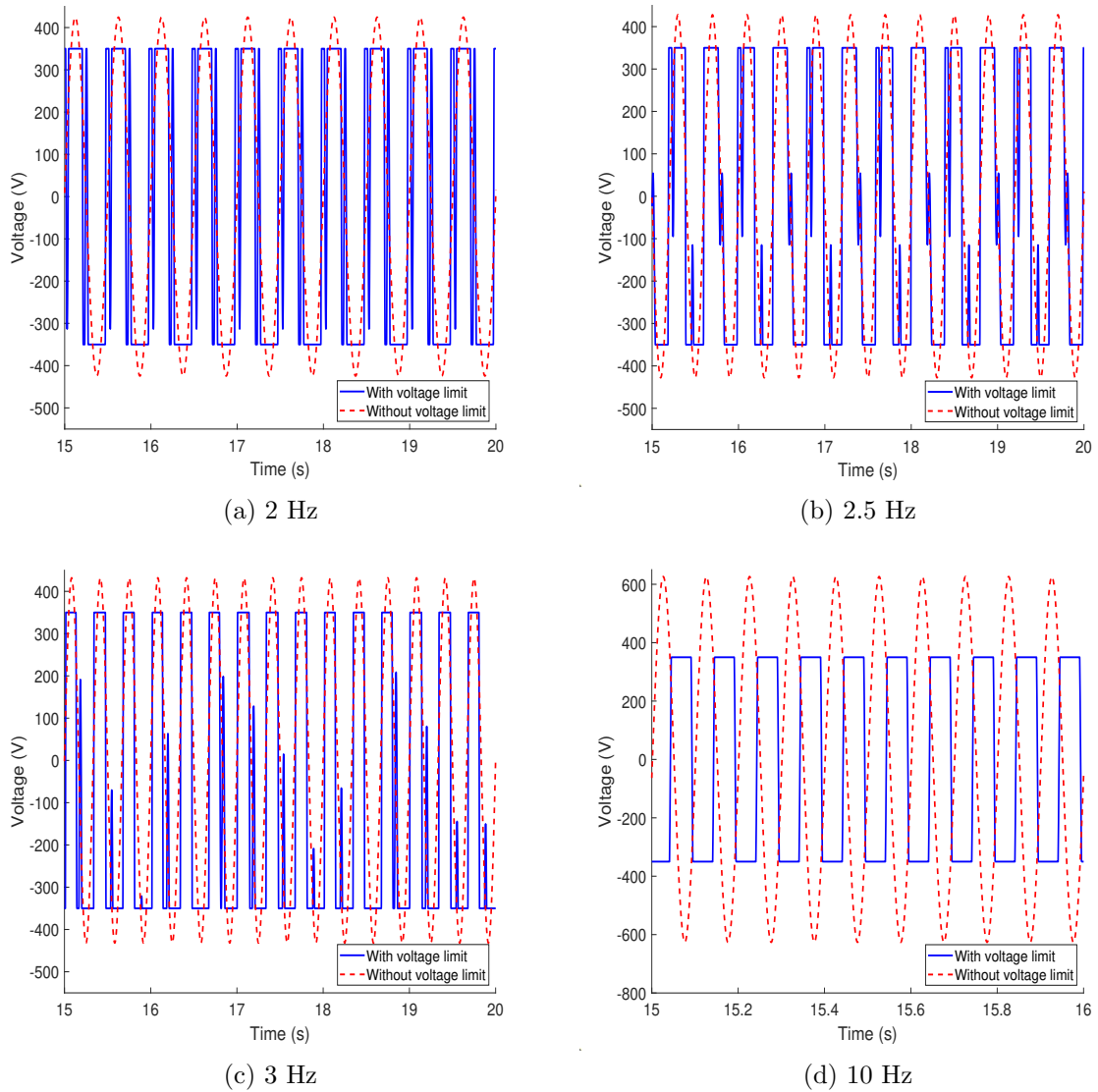


Figure 7.3.7: The voltage applied to the PZT actuators when utilising P control with the gain value obtained from the optimisation in the case of a harmonic disturbance of the frequencies a) 2 Hz, b) 2.5 Hz, c) 3 Hz, and 10 Hz.

To further investigate the effect of the removal of the voltage limitation, the FRFs of the response for the different control schemes and subsequently the different methods of obtaining the gain values are presented in Figure 7.3.9. The corresponding percentage decreases at the peaks of the response and the natural frequency of the structure are presented in Table 7.3.5. With the removal of the voltage limitation, the abnormalities within the results are dissipated as can be seen from the results presented for the four control schemes P, PI, PD and PID shown in Figures 7.3.9a, 7.3.9b, 7.3.9c, and 7.3.9d, respectively. The FRFs relating to the P and PI control contain more discrepancies between them in comparison to the same control schemes for the case where the voltage limit was employed. This may be attributed to the different magnitudes of the propor-

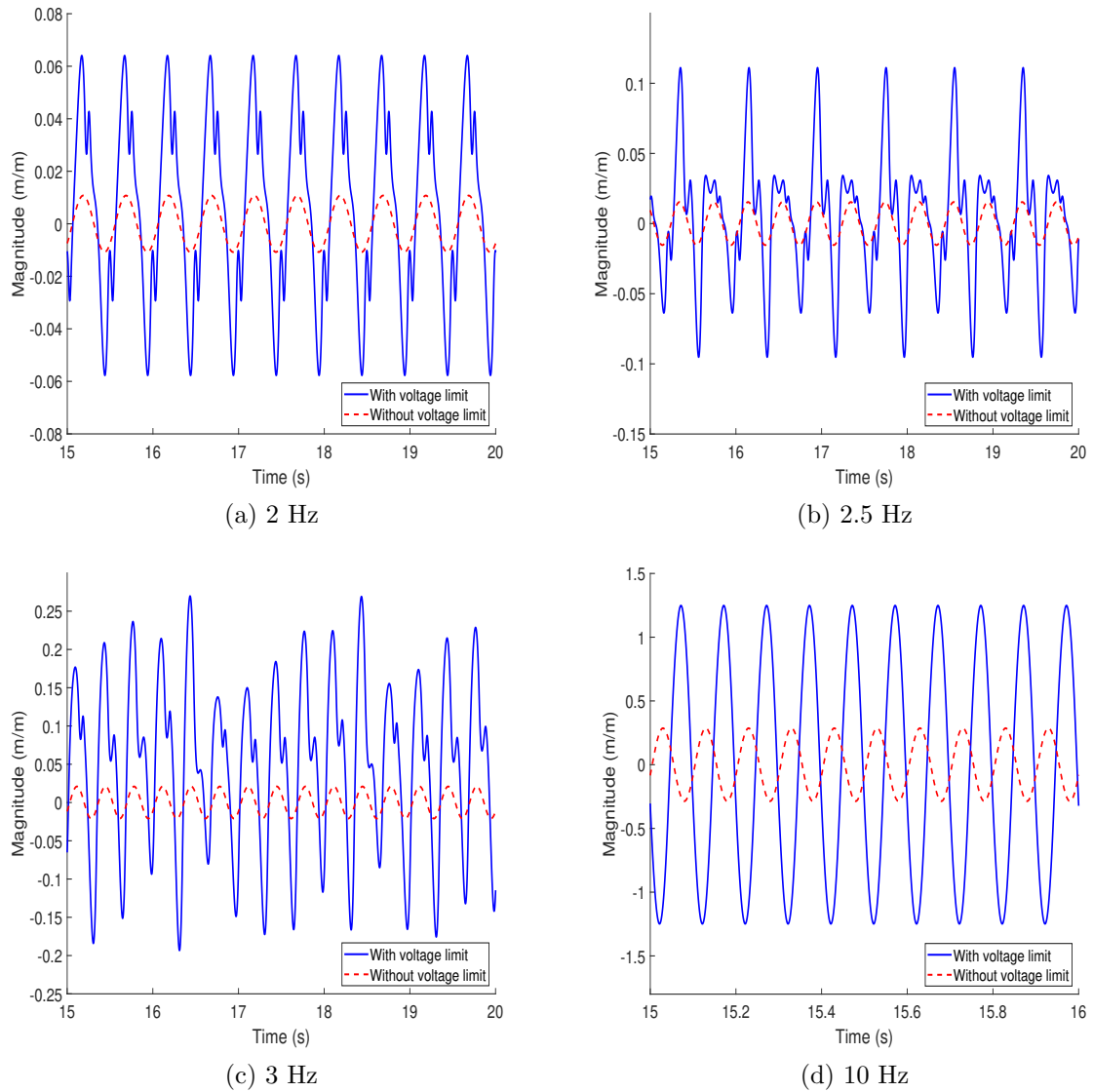


Figure 7.3.8: The response of the system when utilising P control with the gain value obtained from the optimisation in the case of a harmonic disturbance of the frequencies a) 2 Hz, b) 2.5 Hz, c) 3 Hz, and 10 Hz.

tional gain used in the P and PI control schemes, not noticeable in the results shown in Figure 7.3.6 due to the voltage limitation.

Another noticeable difference when the voltage limitation is removed is that all sets of gain values used within the two control schemes (P and PI) show an increase in the natural frequency of the response, an increase not present to such an extent when the voltage input was limited. As noted in Section 7.1 (and in other previous chapters), the application of K_p will increase the stiffness of the link structure. Thus, the increase in the natural frequency may be attributed to the application of K_p . This is further supported by the results of the P and PI control scheme shown in Figures 7.3.9a and 7.3.9b as the higher values of K_p lead to higher natural frequencies. The

frequency values at the peaks of the responses are presented in Table 7.3.6, for the case with voltage limitation (WVL) and without voltage limitation (WOVL). Acknowledging that the uncontrolled natural frequency is 3.59 Hz, the voltage limited P and PI control both achieve an increase in the natural frequency of just over 100% for nearly all of the methods used to obtain the optimal gain values. Whereas without the voltage limitation the increase of the natural frequency varies between cases with the maximum being 488%. Such an increase, whilst not impossible, is improbable in a physical system, hence to gain a better understanding of what increase would be possible, experimental investigations would be necessary. However, as the inclusion of the case wherein the voltage applied to the actuators was not limited was only to discern the cause of the abnormal results with the voltage limitation, further investigations were deemed beyond the scope of this research.

Method used to obtain gain values	Location	Control Type			
		P	PI	PD	PID
Parametric sweep	ω_n	97.02%	95.30%	97.07%	97.81%
	peak	83.65%	90.21%	95.93%	96.04%
Optimisation	ω_n	99.82%	94.45%	97.17%	97.85%
	peak	69.25%	89.93%	96.00%	96.31%
Z-N	ω_n	97.02%	96.79%	99.87%	99.82%
	peak	83.65%	70.23%	99.06%	98.78%

Table 7.3.5: The percentage decrease of the response amplitude based on the uncontrolled response amplitude when the voltage limit is not imposed.

Method used to obtain gain values	Case	Control Type			
		P	PI	PD	PID
Parametric sweep	WVL	3.68 Hz	3.84 Hz	3.87 Hz	4.03 Hz
	WOVL	5.47 Hz	4.81 Hz	6.25 Hz	8.00 Hz
Optimisation	WVL	3.71 Hz	3.85 Hz	3.87 Hz	3.99 Hz
	WOVL	17.35 Hz	4.59 Hz	6.50 Hz	12.50 Hz
Z-N	WVL	3.68 Hz	3.65 Hz	3.29 Hz	3.29 Hz
	WOVL	5.47 Hz	5.27 Hz	> 30 Hz	> 30 Hz

Table 7.3.6: The natural frequencies of the link for the cases where P, PI, PD and PID were employed, for the three methods of obtaining the optimal gains both with and without the voltage limitation.

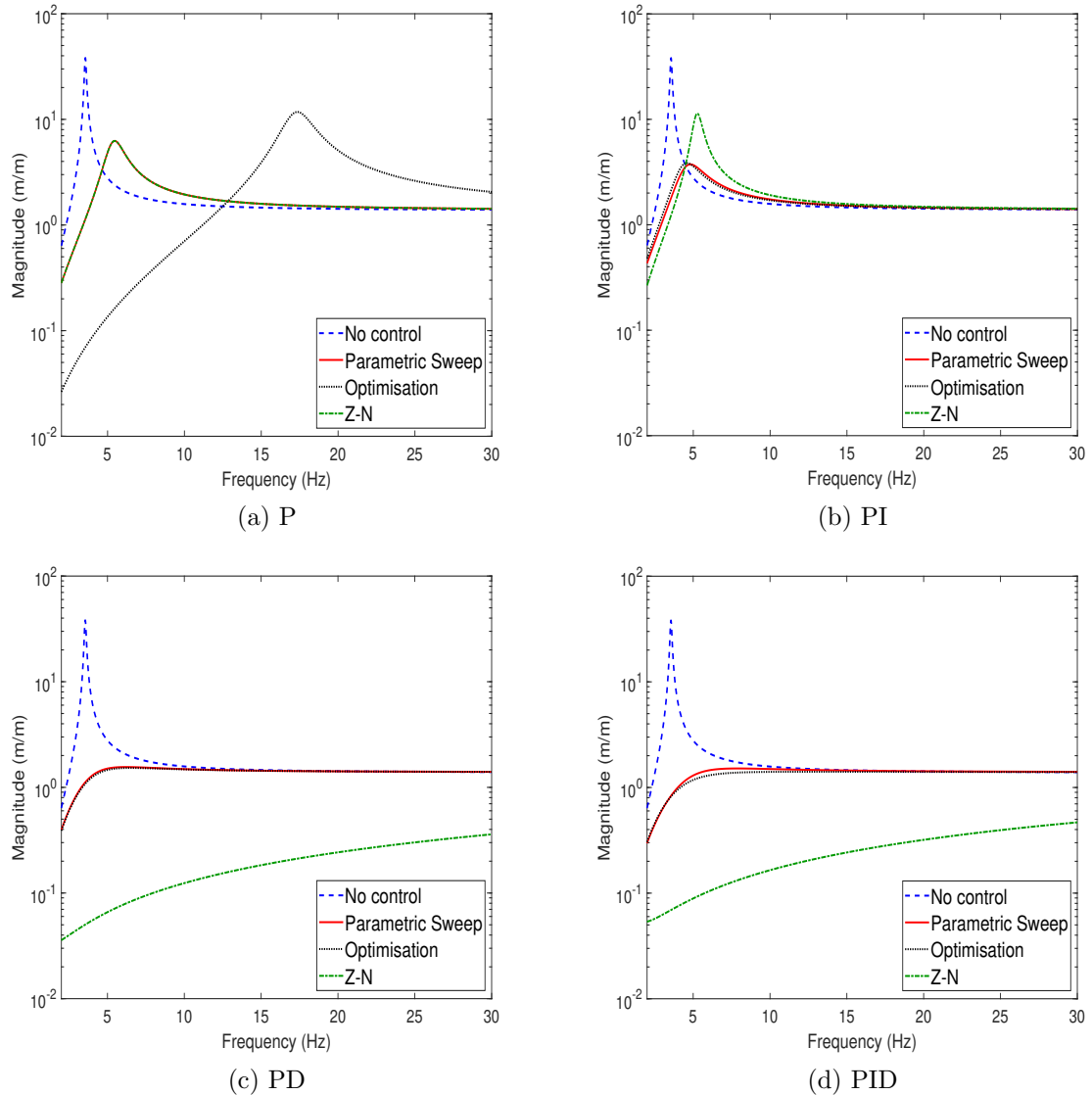


Figure 7.3.9: The response of the system subjected to a harmonic disturbance with the application of the control values from the parametric sweep, ITAE method and the Z-N method with the voltage limit removed. These cases were compared with the case where no control was applied for a) P, b) PI, c) PD, and d) PID control.

The attenuation of the magnitude of the response by the P and PI control schemes is greater when the voltage limitation is removed, for both the peak of the response and the response at the natural frequency. Additionally, without the voltage limitation there are discrepancies between the P and PI control schemes, with the exception of where the gain values were obtained using the parametric sweep and the Z-N method for the P control case, as $K_p = 2860$ in both cases. When considering both the P and PI control schemes (Figures 7.3.9a and 7.3.9b) the introduction of an integral gain into the control scheme has a positive influence on the response when the gain values were obtained through optimisation or the parametric sweeps. However, there is a slight

discrepancy between the set of results from the optimisation and the parametric sweep. This can be explained through the consideration of the gain values obtained from the optimisation ($K_p = 1221$ and $K_i = -18699$) and the parametric sweep ($K_p = 1500$ and $K_i = -20813$). The discrepancy between the K_i values is large in comparison to that of the K_p values, but it has been previously identified that the system is less sensitive to the integral gain. As this is the case, the discrepancy seen in Figure 7.3.9b is most likely due to the difference in the K_p values. In these cases the K_i value was negative, however, in the case where the Z-N method was used, the K_i value was positive. The gains from the Z-N method are less effective in the case of the PI control when compared to P control. Given the sensitivity of the system to the proportional gain, the difference of K_p between the P and PI control schemes would be unlikely to yield such a discrepancy in the responses that have been presented. Hence, the discrepancies in the results may be attributed to the positive K_i value utilised.

With the introduction of the derivative term in the control scheme (the PD and PID control schemes) a greater attenuation of the response is achieved (see Figures 7.3.9c and 7.3.9d). This increase in attenuation is with respect to a comparison with the P and PI control, and the corresponding FRFs in the case where the voltage limit was employed (PD and PID control). Acknowledging that the system is less sensitive to the integral gain in comparison to the derivative gain, the similarity in the reduction of the response magnitude between the PD and PID cases can be understood. Regardless of the method used to obtain the gain values for the control the first mode becomes overdamped, and as with the increase in the natural frequency this scenario is improbable. When the gain values are based on the Z-N method for the latter two of the control schemes, the natural frequency is increased beyond the range of frequencies considered in this study (> 30 Hz).

It should be noted that alongside the proposed experimental investigation to determine the realistic increase of the natural frequency when PZT actuators of higher operating voltage are employed, there are several other investigations which were deemed beyond the scope of this research. These include answering the following questions:

- Would the abnormal results occur as shown when the voltage limitation was imposed in the physical system when utilising the relevant gain values?
- What level of damping can be achieved when employing PD and PID control if using PZT actuators of a higher operating voltage?
- When employing the Z-N method, to what frequency would the natural frequency be increased to when utilising PD and PID control (assuming different PZT actuators)?

These questions have been deemed as such, as it is assumed that the results shown in Figure 7.3.9 may be achieved if utilising PZT actuators with a higher operating voltage. Additionally, as previously mentioned, the results obtained without the voltage limitation were only obtained to verify that the voltage limitation was the cause of the abnormal results.

7.4 The discrete-time Fourier transform

The Tustin transform (also known as the bilinear transform or the z transform) may be used to transform a continuous-time domain model (CTDM) to a discrete-time domain model (DTDM) [147]. DTDMs have been utilised in a wide range of research including, but not limited to, control applications [189, 190, 191]. Where the CTDM is in the s -plane (Laplace), i.e., having some transfer function $G(s)$, the system may be modelled in the discrete-time domain through the application of the z transform (i.e., $Z\{G(s)\} = G(z)$). The CTDM has been proven throughout this research to provide a fairly good representation of the physical system, but does not account for the sampling rate of the Raspberry Pi and the delay in the application of the voltage to the actuators following the reading of the voltage from the sensors.

As the model in this research is time-invariant, the real part of the complex variable z may be set to zero so that $z = j\omega$, effectively reducing the z transform to the discrete-time Fourier transform (DTFT). The z term may be considered to be a “shift operator”, such that within the z domain multiplication by z corresponds to shifting forward by one time sample (Δt). This is analogous to the multiplication by s within the Laplace/frequency domain corresponding to differentiation in the time domain.

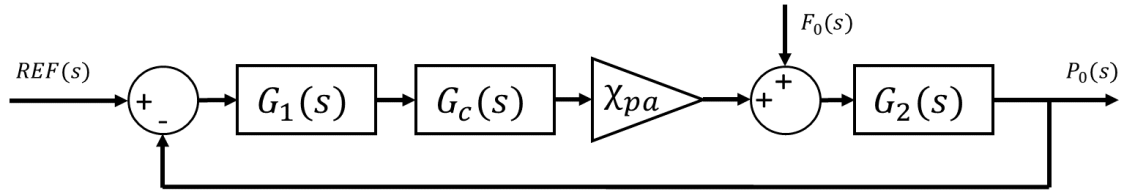


Figure 7.4.1: A simplified version of the block diagram of the system.

To apply the DTFT, an expression for the generalised coordinate (P_0) must be obtained. The blocks denoted as $G_1(s)$, $G_c(s)$ and $G_2(s)$ have been previously defined as Equations 7.3, 7.5 and 7.4, respectively. Utilising the block diagram (Figure 7.4.1) and the known transfer functions ($G_1(s)$, $G_c(s)$ and $G_2(s)$), an expression for the generalised coordinate may be obtained as previously introduced (Equation 7.6), repeated here as Equation 7.11 [192].

$$P_0(s) = \frac{REF(s)G_1(s)G_c(s)\chi_{pa}G_2(s)}{1 + G_1(s)G_c(s)\chi_{pa}G_2(s)} + \frac{F_0(s)G_2(s)}{1 + G_1(s)G_c(s)\chi_{pa}G_2(s)} \quad (7.11)$$

The Tustin transform of s for system involving a compensator (a closed loop system with a controller) may be written as Equation 7.12 where T is the sampling interval, and setting $z = j\omega$ reduces the Tustin transform to DTFT.

$$s = \frac{2(z - 1)}{T_t(z + 1)} \quad (7.12)$$

Equation 7.12 may then be substituted into Equation 7.11 to yield the DTFT of the generalised coordinate (P_0). To observe the system in the discrete-time domain a unit impulse was employed as the disturbance ($F_0(s)$) in Figure 7.4.1), and the sampling interval was set to $T_t = 0.01$ s (a sampling rate of 100 Hz). Control System B (CSB) was found to have a sampling rate of 1.558 kHz, which as previously stated is more than sufficient for the corresponding link structure with a natural frequency of 3.59 Hz. However, it was deemed more appropriate to employ a lower sampling rate within the discrete model so as to account for a situation where the sampling rate of the physical system is lower (i.e., CSA). Figure 7.4.2 contains the response of the system in both the continuous-time domain (s) and the discrete-time domain (z) with no control applied. From the results the discrete-time response appears to have a shifted in phase in comparison to the continuous-time response, however this shift is very minor and there is negligible difference in terms of the amplitude, frequency and damping of the response.

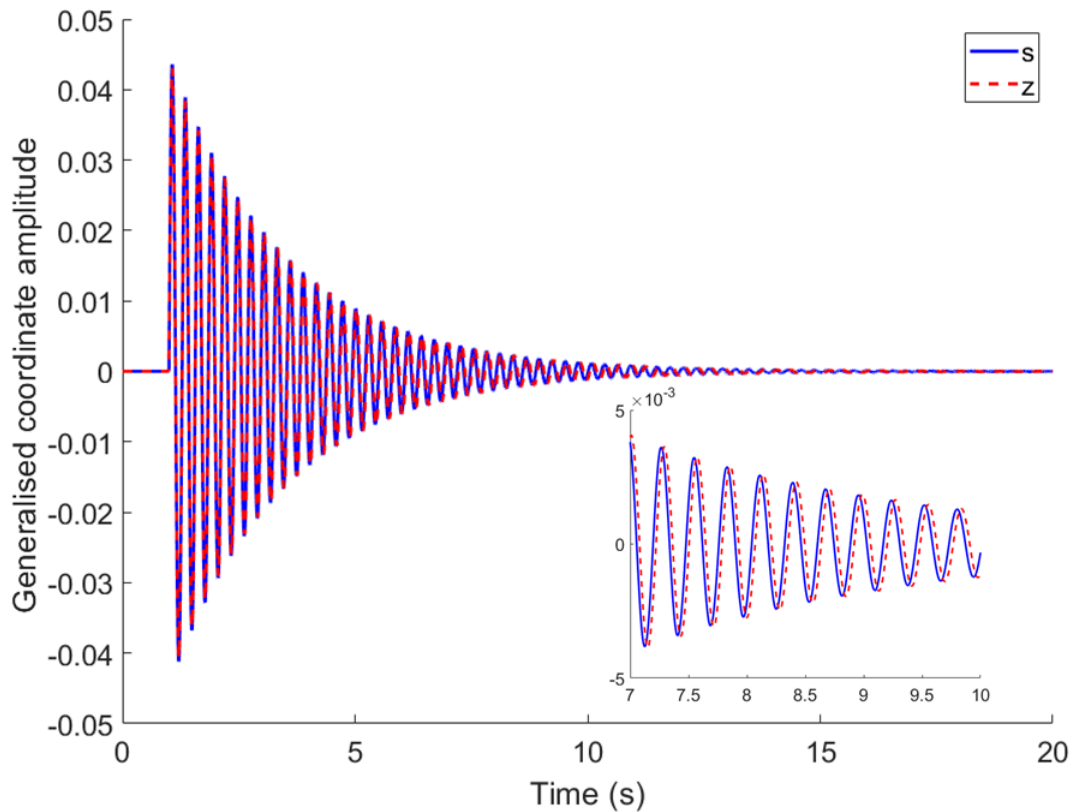


Figure 7.4.2: The transient response of the link for both the CTDM and the DTDM.

With the shift in the phase of the response between the continuous-time and discrete-time models present, it was pertinent to investigate the effect of this shift on the attenuation of the response, and subsequently investigate any discrepancy in the optimum gain values. A parametric sweep of the proportional gain was performed, and as with the parametric sweeps conducted on the continuous-time model the value of the integral of the time-weighted absolute error (ITAE) was recorded. The ITAE values across the range of proportional gain values considered ($K_p = 0$ to $K_p = 4000$) are shown in Figure 7.4.3 along with the results pertaining to CTDM. However, due to the time-weighting of the ITAE, its magnitude is dependent on the sampling interval. It can be seen that in the case where the ITAE was calculated using the sampling interval identical to that used in the definition of s (Equation 7.12) the magnitude of the ITAE is significantly smaller than that obtained from the CTDM. To avoid the dependence of the ITAE value on the sampling interval the calculation of the ITAE was performed with the sampling interval of the CTDM, where the error was obtained through interpolation at the respective time steps. This modified version of the ITAE of the discrete-time response yields a highly similar result to the ITAE of the continuous-time response, with only a minor discrepancy in magnitude which can be explained by the shift in phase shown in Figure 7.4.2. This suggests that the gain values obtained for use in the PID control scheme are the same regardless of whether the model is in the continuous-time domain or the discrete-time domain.

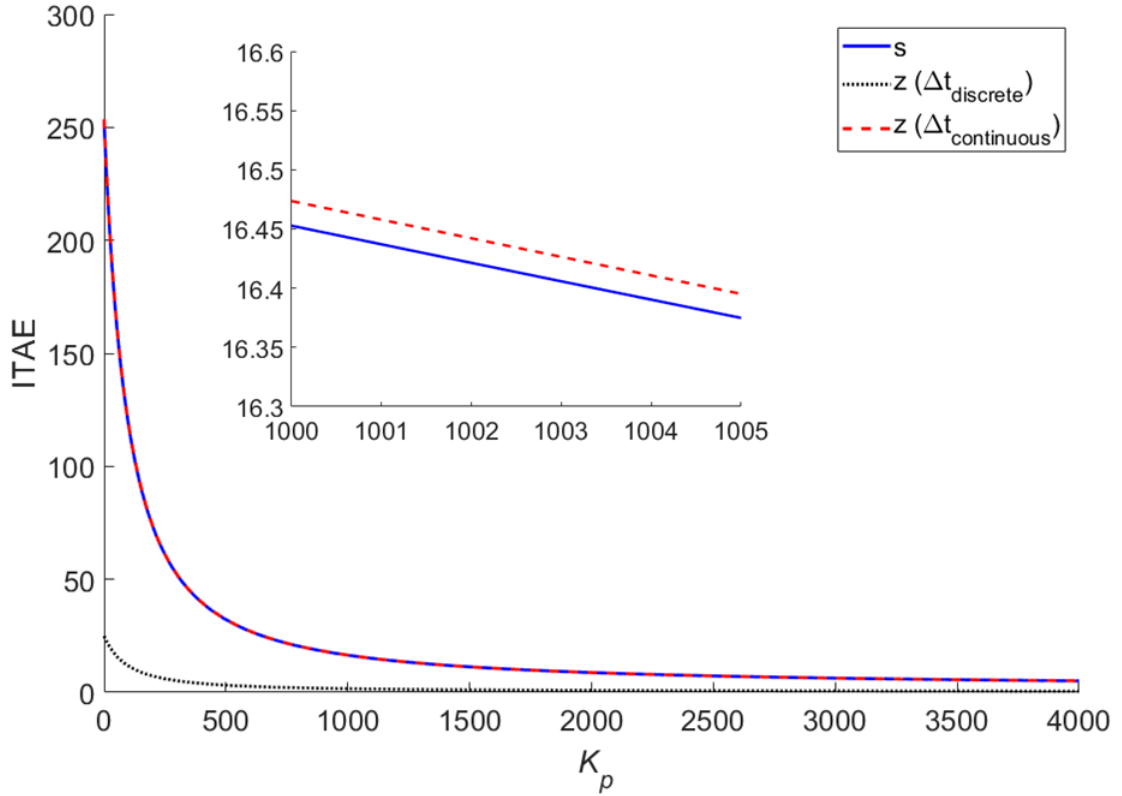


Figure 7.4.3: ITAE values across a parametric sweep of the proportional gain for the CTDM, the DTDM and the DTDM where the integral was performed using the sampling interval of the CTDM.

Whilst the modification of the ITAE for the discrete-time model yields a good representation of the continuous-time model, it does require additional computation and a prior knowledge of both the continuous-time result (to verify the trend or realise the discrepancy in the magnitudes) and the sampling rate. Thus rendering the modification unsuitable in the scenario where the system is only modelled in the discrete-time domain. In order to ensure that the optimum gain values may be obtained from either parametric sweeps of the gain values, an optimisation or the Z-N method when modelling in the discrete-time domain, all three sets of results shown in Figure 7.4.3 were normalised to unity. Figure 7.4.4 presents these normalised results, where it can be seen that the gradient of the curve of the discrete-time model with its respective sampling interval is identical to that of the modified version and the CTDM. With the gradient being identical, the resultant optimal proportional gain value is also identical to that previously identified for the CTDM when employing the parametric sweep method ($K_p = 2860$). With the system being less sensitive to the integral gain as proven previously, only a parametric sweep of the derivative gain was considered in addition to the proportional gain sweep. The ITAE value normalised to unity is shown for increasing

values of derivative gain ($K_d = 0$ to $K_d = 4000$) with the proportional gain held constant ($K_p = 2860$) in Figure 7.4.5. Whilst the results are different to those shown in Figure 7.3.2c due to the voltage limit not included as the governing equations are closed form, the differences between the CTDM, the DTDM and the modified DTDM are negligible. Hence the DTDM may be utilised to obtain the optimum values for use in a PID control scheme (or more aptly in this case the PD control scheme).

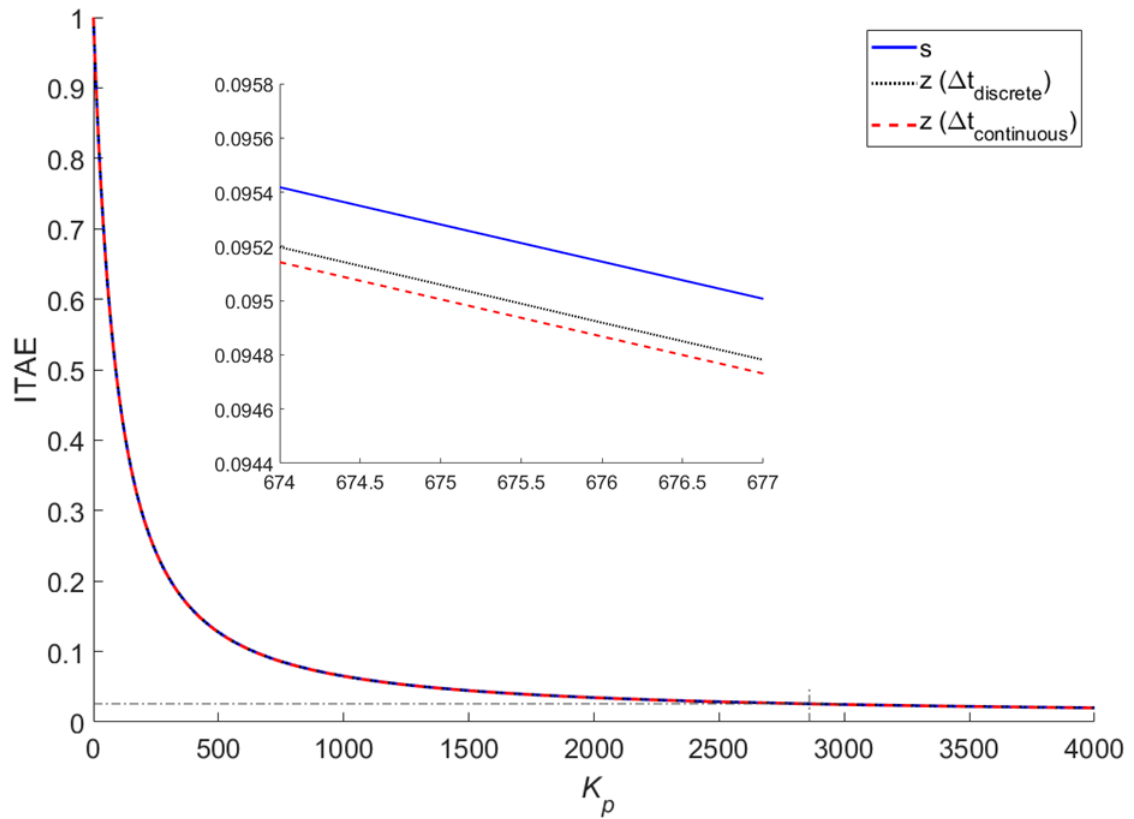


Figure 7.4.4: ITAE values normalised to unity across a parametric sweep of the proportional gain for the CTDM, the DTDM and the DTDM where the integral was performed using the sampling interval of the CTDM.

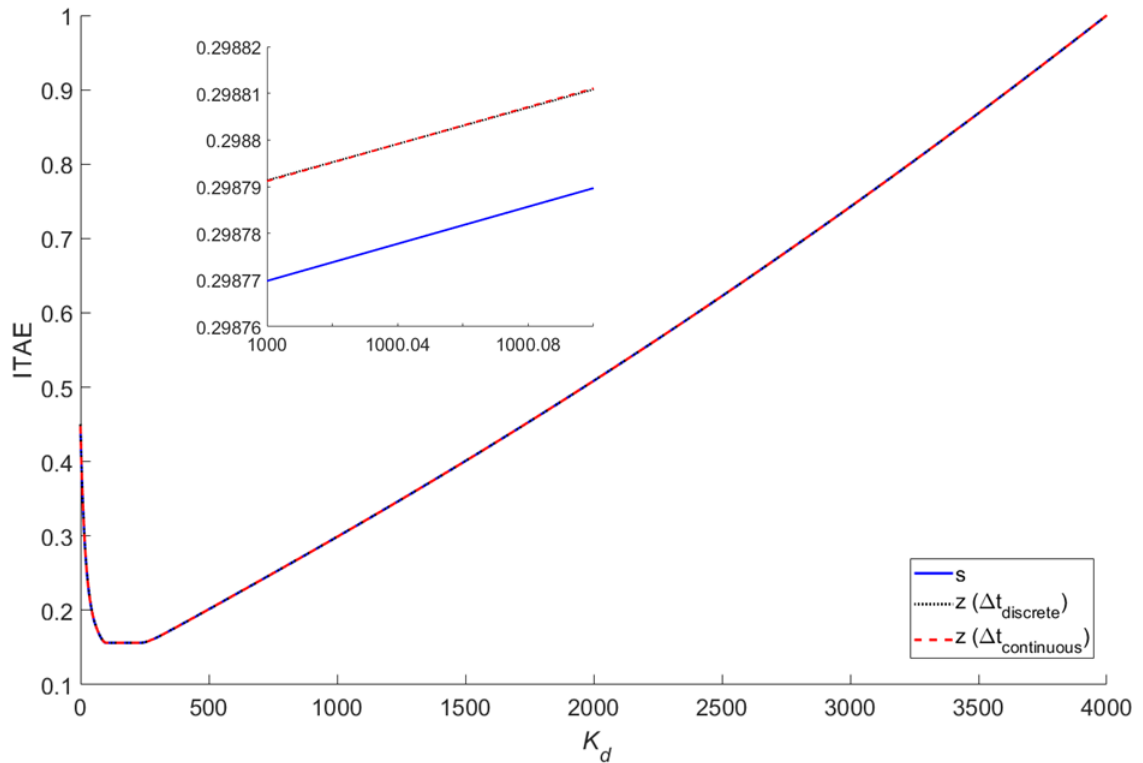


Figure 7.4.5: ITAE values normalised to unity across a parametric sweep of the derivative gain whilst holding the proportional gain constant ($K_p = 2860$) for the CTDM, the DTDM and the DTDM where the integral was performed using the sampling interval of the CTDM.

Within a PID control scheme, the integral and derivative control are dependent on the sampling interval, whereas the proportional control scheme is not dependent on the sampling interval. However, due to the lag of the response as shown in Figure 7.4.2 it was pertinent to observe the response of the DTDM with proportional control employed. Figures 7.4.6a through 7.4.6d present the responses of both the DTDM and the CTDM for the P, PI, PD and PID control schemes, respectively. The gain values utilised in these control schemes were those obtained through optimisation, and a unit impulse was utilised as the disturbance to the system. In the cases of PI, PD and PID control there is negligible difference between the DTDM and the CTDM as shown in Figures 7.4.6c and 7.4.6d. Conversely, in the case of P control (Figure 7.4.6a) the DTDM has a response with noticeable differences from its continuous-time counterpart. For this control scheme, the amplitude of the response is decreased, as is the damping, resulting in a higher discrepancies between the CTDM and the DTDM than the uncontrolled case. These discrepancies may be attributed to the magnitude of the proportional gain values used within the P control, $K_p = 47238$. This large value exaggerates the

lag shown in the uncontrolled case (Figure 7.4.2), affecting the response. The PI, PD and PID control schemes both utilise lower values of proportional gain by comparison ($K_p = 1221$, $K_p = 1830$ and $K_p = 2744$), and hence have few discrepancies between the CTDM and the DTDM.

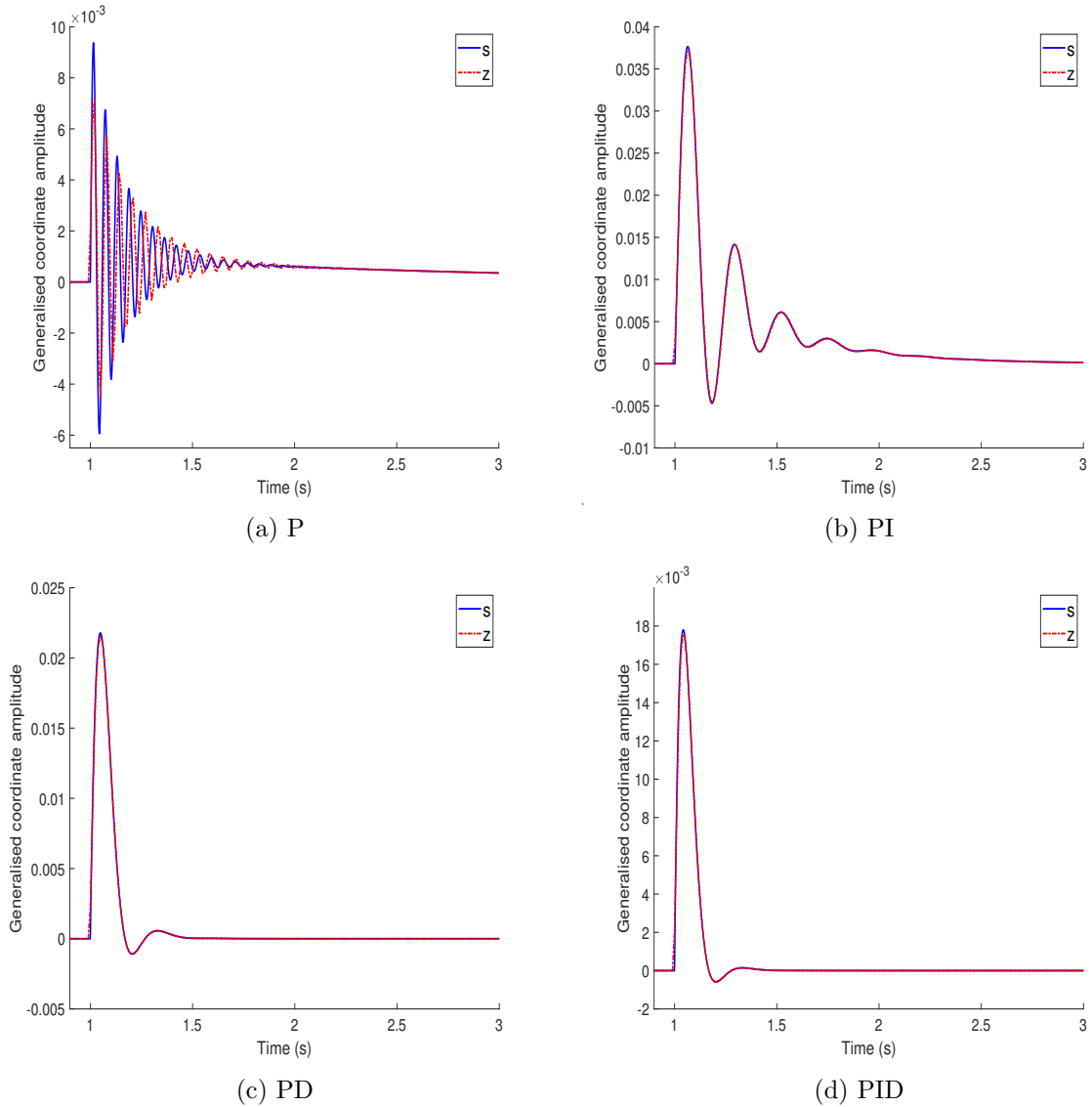


Figure 7.4.6: The transient response of the system as a result of a unit impulse disturbance for both the CTDM and the DTDM, where the control gain values were obtained through optimisation for use within a) P, b) PI, c) PD, and d) PID control.

To further confirm that the aforementioned discrepancies between the CTDM and the DTDM are dependent on the magnitude of the proportional gain, four proportional gains were utilised ($K_p = 100$, 1000 , 10000 and 100000), utilising $K_d = K_i = 0$. Again, a unit impulse was used as the disturbance to the system and the resultant responses of the link for the control gains of $K_p = 100$, $K_p = 1000$, $K_p = 10000$ and $K_p = 100000$ are presented as Figures 7.4.7a, 7.4.7b, 7.4.7c and 7.4.7d, respectively. It can be observed

from these results that there are few discrepancies between the CTDM and the DTDM for the first two cases where the proportional gain has a lower magnitude. The third case does show some discrepancies, but these are minor in comparison to the fourth case which contains noticeable discrepancies in terms of damping and the settling time. Thus, it may be concluded from these results that at higher magnitudes of proportional gain the phase shift is amplified leading to discrepancies between the CTDM and the DTDM.

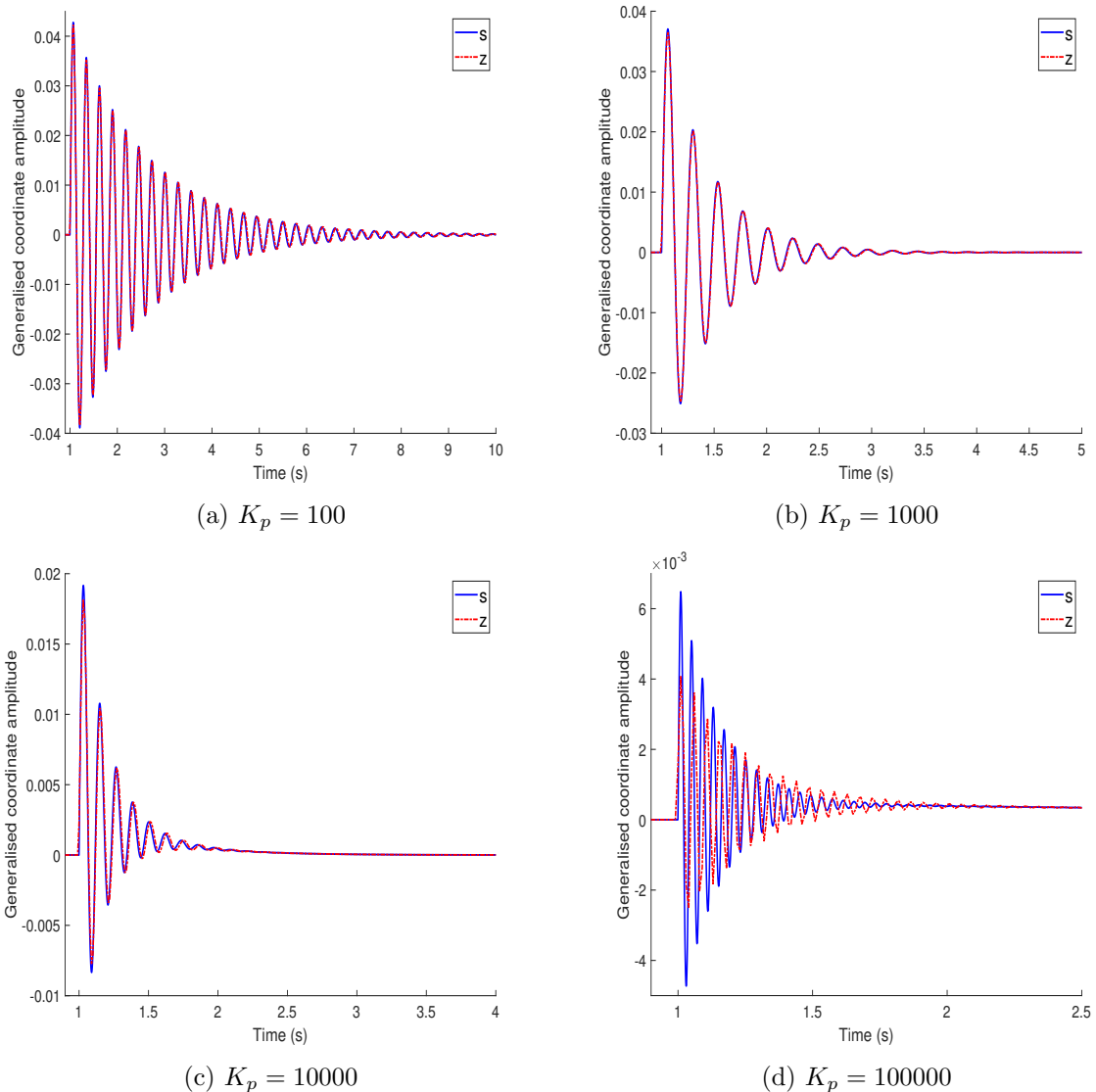


Figure 7.4.7: The transient response of the system as a result of a unit impulse disturbance for both the CTDM and the DTDM using P control for a) $K_p = 100$, b) $K_p = 1000$, c) $K_p = 10000$ and d) $K_p = 100000$.

The cases of gain values shown in Figure 7.4.7 do not consider the effect of the magnitude of the integral or derivative gains independent of the proportional gain. Whilst the system was proven to be less sensitive to the integral gain, it was still deemed

pertinent to investigate varying values of K_i and the resultant response. The derivative gain has been proven to influence the response and provides phase lead as previously stated a further investigation was deemed appropriate. The first investigation involves the increase of the magnitude of K_i (using negative values) whilst holding the other gain values constant ($K_p = 2860$ and $K_d = 0$). The K_i values utilised were $K_i = -100$, $K_i = -1000$, $K_i = -10000$ and $K_i = -25000$, and the results are shown in Figure 7.4.8. It should be noted that lower gain values were tested, however, as shown previously, these higher values led to an increase in the ITAE and the instability of the system. For the cases shown in Figure 7.4.8, the discrepancies between the CTDM and the DTDM are negligible, this infers that higher magnitudes of K_i are not the cause of the discrepancies within the control schemes. In the second case the proportional gain value was held constant at $K_p = 2860$, and the derivative gain value was adjusted to create four cases ($K_d = 100$, $K_d = 1000$, $K_d = 10000$, and $K_d = 100000$). The results of these cases are shown in Figures 7.4.9a, 7.4.9b, 7.4.9c, and 7.4.9d, respectively. From these results it can be seen that even at a relatively high value of the derivative gain the response of the system is practically identical between the CTDM and the DTDM in comparison to the scenario where the proportional gain value is of a large magnitude. Inferring that the derivative gain has negligible influence on the response of DTDM in comparison to the proportional gain.

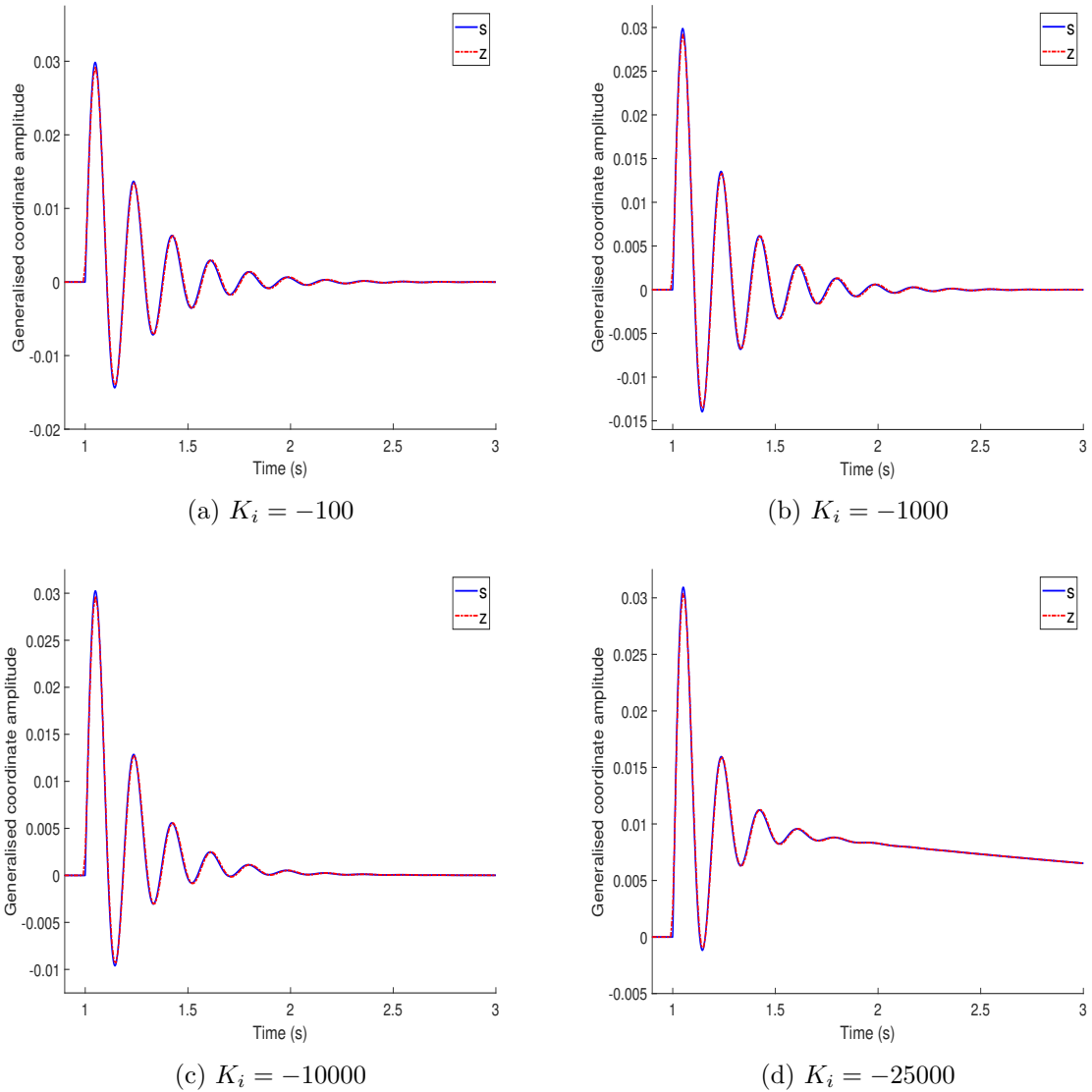


Figure 7.4.8: The transient response of the system as a result of a unit impulse disturbance for both the CTDM and the DTDM using PI control ($K_p = 2860$) for a) $K_i = -100$, b) $K_i = -1000$, c) $K_i = -10000$ and d) $K_i = -25000$.

A final consideration regarding the employment of the DTDM is to observe its accuracy in modelling an experimental investigation. To do so, only proportional control was employed to replicate the experimental results previously obtained utilising $K_p = 260$, $K_p = 520$ and $K_p = 1040$ (alongside an uncontrolled case). Figure 7.4.10 contains the FRFs from the experimental results, the CTDM and the DTDM. Both models are a good representation of the experimental results for the control gains considered, and the discrepancies between the CTDM and the DTDM are few. However, in comparison to the proportional gain values obtained through the optimisation, those used in the experiment are relatively small, hence the lag present in previous results between the CTDM and the DTDM has not been amplified to an extent where there are notable dis-

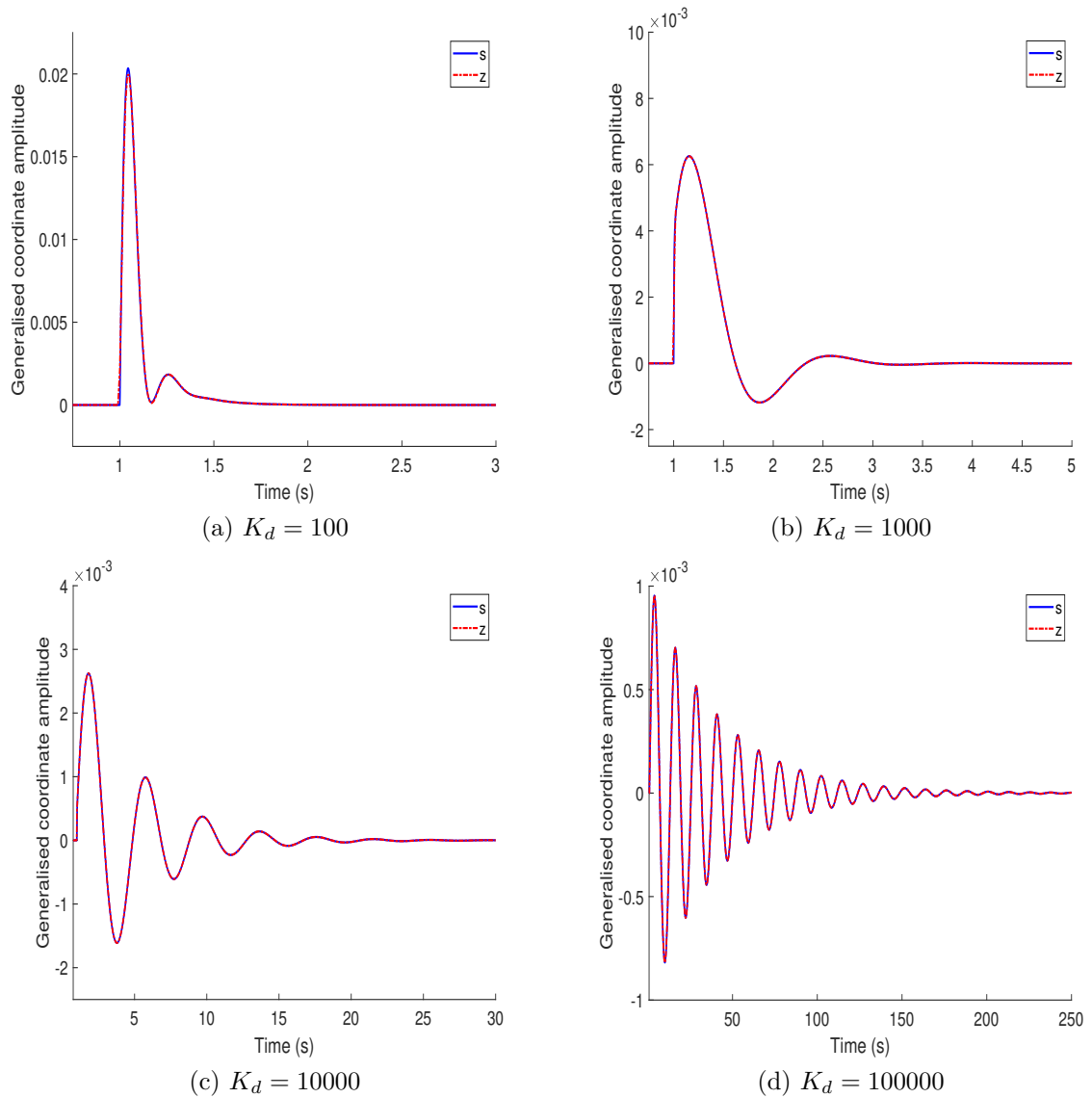


Figure 7.4.9: The transient response of the system as a result of a unit impulse disturbance for both the CTDM and the DTDM using PD control ($K_p = 2860$) for a) $K_d = 100$, b) $K_d = 1000$, c) $K_d = 10000$, and d) $K_d = 100000$.

crepancies between the two models. If the proportional gain values used were increased then there would likely be a higher discrepancy between the CTDM and the DTDM. To determine which is a better representation of the experimental response in this scenario, an experimental investigation would need to be conducted with PZT actuators of a higher operating voltage. This research focusses only on the attenuation attained by the PZT actuators previously introduced, and so carrying out such an experimental investigation was deemed beyond the scope of this research.

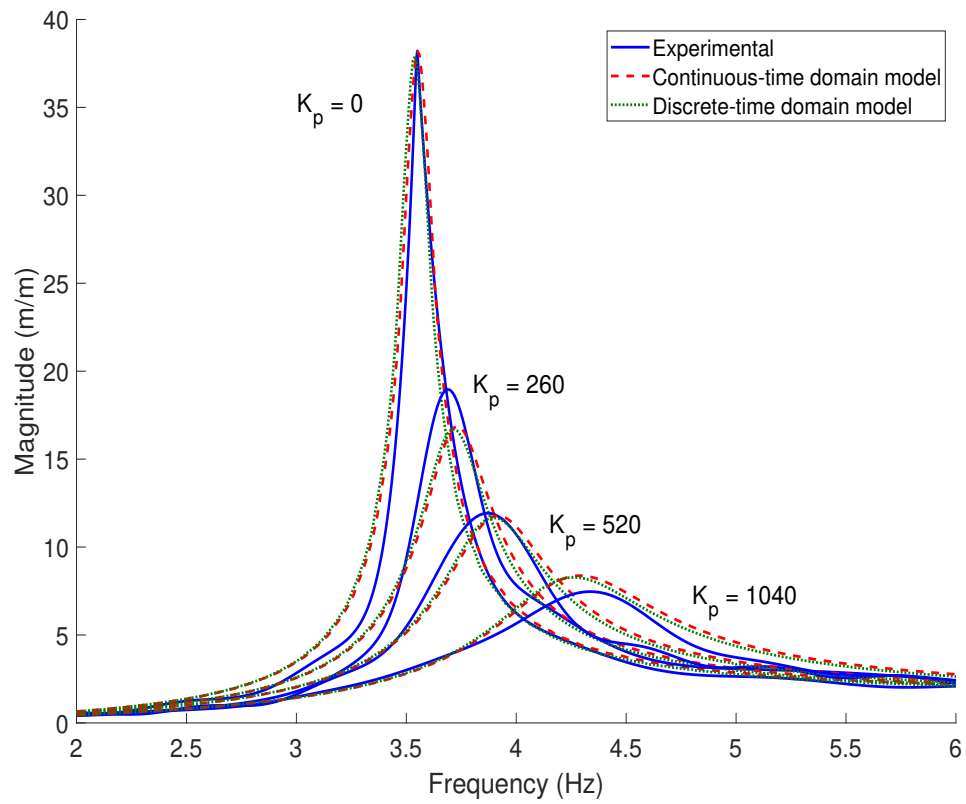


Figure 7.4.10: A comparison between the experimental (solid lines), the CTDM (dashed lines), and the DTDM (dotted lines) results.

7.5 Summary

This chapter introduced a modified model of the link and the control system so that a more advanced control method could be included and subsequently investigated. These modifications were verified through a comparison with experimental results presented in a previous chapter. Following this validation of the model three different methods were employed to determine the optimal gain values utilised to be utilised in a P, PI, PD and PID control scheme. It was concluded that the system was less sensitive to the integral gain and hence the most appropriate control scheme was PD, and the gain values that yielded the largest attenuation of the response were obtained through optimisation. This attenuation was an improvement on that seen previously within this research where only proportional control was employed. Another discovery related to the voltage limitation employed in the model to reflect the operating voltage of the PZT actuators, is that abnormal results were yielded due to the voltage limitation introducing a nonlinear term into the model.

The last section of this chapter saw the link and the control system modelled in the discrete-time domain so as to offer a better representation of the physical system which has a finite sampling rate. The DTDM was found have a small shift in the phase of the response when compared to the CTDM, but few other discrepancies. The shift in the phase was amplified by larger proportional gain values, resulting in larger discrepancies between the CTDM and the DTDM in terms of the frequency and damping of the response. A comparison of the DTDM and the experimental data showed that the DTDM was a good representation of the physical system at relatively low values of proportional gain. Both the more advanced control system and DTDM investigations lend to the conclusion that in the case where the PZT actuators have a higher operating voltage, the abnormal results that are attributed to the voltage limit imposed on the system may be avoided, and the DTDM may be validated through experimental results.

Chapter 8

Conclusions

This research sought a solution to the problem of nuisance vibrations that occur in long slender structures, in this case the structure was envisioned as a robot manipulator link. Upon the review of current works a potential contribution to the field was identified; a lightweight, inexpensive control system suitable for an array of applications wherein unwanted vibrations are to be attenuated. Focussing on these specifications suitable components were selected, including a Raspberry Pi 3 B+ (RPi) and Lead Zirconate Titanate (PZT) actuators, which led to two sensor options. Of these options PZT elements as sensors were deemed more suitable based on the higher sampling rate that could be employed, and that they exhibited less interference on the functionality of the link. A multitude of experiments were conducted to investigate the performance of the control system in multiple situations, ultimately proving its suitability for the suggested application including in the case where a nonlinear response is present. This suggested application would see the flexible link acting as an equipment armature as part of a drone system for purposes such as search and rescue. An analytical model was created and was developed alongside the experiments, with alterations and additions to reflect the experimental investigations. These analytical models not only aided in the proof of the underlying theory but also answered some hypotheses that arose in this research, further adding to the contribution of the research. Here six main conclusions have been discussed and summarised, before a discussion regarding potential future work.

Summary of conclusions from this research

The control system with a RPi, PZT sensors and PZT actuators as its primary components was employed in a situation where the link structure was excited in a sinusoidal manner at its base. A purpose-built system, the dSPACE MicroLabBox, was also tasked to attenuate the transverse displacement on the link in the same scenario, and with the same sensors and actuators. The same level of performance was observed for both systems in terms of the settling time reduction for an impact like excitation, and the reduction of the amplitude of the response for a harmonic excitation. Naturally it was concluded that the RPi, even with some of its specifications less favourable in comparison to the dSPACE, was more than suitable for this task. Drawing on the versatility of the RPi in terms of the methods of communication it is capable of and referring to the suggested application a further advantage to the RPi's employment may be realised. Should the flight control of the drone be conducted by a RPi, then the main component of the designed control system is already part of the system. Hence adding the peripheral components, perhaps as a modular camera armature, would add less weight to the existing system, an important consideration in drone design.

Conclusion: *The designed control system offers a lightweight, inexpensive solution to the attenuation of unwanted vibrations in long slender structures, with its performance comparable to pre-existing control systems.*

The utilisation of proportional control with the voltage output from the PZT sensors was found to produce a response more indicative of proportional-derivative control. An observation of the governing electromechanical equation of the PZT sensors supplied an explanation to this phenomenon. Within this equation lay two coefficients, relating to the real and the imaginary components of the PZT element output voltage. The coefficients are both positive, and their magnitudes are dependent on the resistance and capacitance of the control system and influence the stiffening and damping characteristics of the control system. This was further evidenced in the comparison between the RPi and the dSPACE systems, which had different values of resistance and capacitance. Both systems yielded a response indicative of proportional-derivative control, showing both an increase in the natural frequency and a decrease in the amplitude of the response. However, the dSPACE system achieved a higher reduction in the magnitude of the response, and contrastingly the RPi system yielded a higher increase in the natural frequency (at the same level of proportional gain). In certain applications one of these responses may be more favourable over the other, which can be achieved simply by altering the resistance and capacitance values, and so this finding is advantageous.

Conclusion: *The inclination for the control system to behave more towards either proportional or derivative control can be advantageously influenced through the adjustment of the capacitance/resistance of the control system.*

A KUKA iiwa 7 R800 manipulator was employed with the intention to observe the control system's performance in a more realistic scenario, and certainly one more akin to the suggested application. As with previous experiments the link was subjected to two different types of excitation, impact and harmonic, whilst it was mounted on the end effector of the robot. The results from these experiments exhibited a good level of performance from the designed control system for both types of excitation. Additionally, the mounting of the additional link and control system appeared to have no influence on the functionality of the manipulator. This was further supported through a comparison of the end effector position measured during the experiments, and that predicted by the kinematic model of the manipulator. The experimental results were obtained when the flexible link was mounted and excited, and the control was employed, whereas the kinematic model omitted the link. The joint angles related to the motion were obtained from the software of the manipulator and used as an input into the kinematic model. Very little error was observed between the resultant prediction of the end effector positions and the experimentally measured positions. Additionally, the voltage output from the PZT sensors obtained experimentally with the control employed was compared with that predicted by the analytical model of the link structure. It was perceived from this comparison that the model is a good prediction of the response of the link. Combining the conclusions drawn from these two comparisons it may be concluded that the models of the manipulator and link need not be coupled to provide a good prediction of the response of the link structure.

Conclusion: *The suitability for the designed control system to be employed in a scenario such as that of the suggested application has been proven.*

This research has seen the development of an open and closed loop analytical model to represent the link structure with the intention of both validating the underlying theory and providing a fast and accurate method of predicting the response of the link. Earlier chapters presented a link structure with no bonded PZT elements, from this the structure was altered as the control system was developed and improved, and the analytical model was adjusted accordingly. The amendments to the structure were made to include the addition of a pair and two pairs of collocated PZT elements, different tip masses and sensors, an alteration of the boundary conditions, and even a different link

altogether. Even with the added complexity of the induction of a nonlinear response, the relevant version of the analytical model was able to provide a good prediction of the response of the link. The underlying theory of the model rendered the answers to hypotheses posed and phenomena discovered in this research. As previously mentioned, the model was key in the explanation of the controlled response being indicative of both proportional and derivative control and providing an answer to the hypothesis relating to the coupling of the robot and link models. The analytical model also corroborated with the hypothesis that the resistance values of the control system need not be included in the model as the RPi accounts for their inclusion. It also played an important role in the explanation of the poor performance of the control system where inertial measurement units were used as sensors. In this case the analytical model was used to observe the effect of varying delay times on the performance of the control system. This removed the necessity to conduct a series of time consuming experiments, which was also the case when considering the placement of the PZT actuators along the length of the link.

Conclusion: *The analytical models developed in this research provide a good representation of the link structure, which can reduce time costs associated with experimentation, and assist in the understanding of the response of a link structure.*

An investigation was conducted in this research to determine the performance of the control system when the response of the link structure was nonlinear. The control system was found to attenuate the response for different levels of force, even those in which the characteristics of the response were significantly indicative of nonlinearity. The nonlinear characteristics in these cases were also reduced, the indicative ‘jump’ of the data was less blatant, and the discrepancy in the natural frequency between the swept upwards and swept downwards data was smaller. Additionally these experimental investigations considered the control system’s effect on the second mode, with the concern that an excitation of this mode would be present. This was not the case, and the control system was even shown to reduce the amplitude of the response at the second natural frequency for all of the instances of force considered. Thus proving the suitability of the control system in a scenario wherein the response is nonlinear and/or is excited at frequencies that concern the second mode.

Conclusion: *The designed control system has been proven to be effective in situations where the response of the link structure is nonlinear, and the control system has no negative spillover effects when considering the second mode.*

Dynamic control was introduced and utilised in the system in the form of proportional-integral-derivative control. It was identified that the system was insensitive to integral control, but a higher attenuation of the response may be yielded by employing proportional-derivative (PD) control. Three tuning methods were utilised and of these an optimisation of the control gains using the objective function of the minimum of the integral of the time-weighted error (ITAE) yielded the most desirable response from the system. However, it was also found that the voltage limitation employed to replicate the operating voltage of the actuators used in the physical system introduced a nonlinear term into the system resulting in abnormal results. The system was modelled in the discrete-time domain, and discrepancies between this model and its continuous-time domain counterpart were found in that a small phase lag was present. This small shift in the phase of the response was amplified at higher values of proportional gain, resulting in larger discrepancies between the discrete-time domain model (DTDM) and the continuous-time domain model (CTDM). However, the optimum gain values obtained through the use of the DTDM were the same as those from the use of the CTDM. Additionally, when the DTDM was compared with the experimental results, where the proportional gain values were relatively low, the DTDM yielded a good representation of the response of the physical system. This research focusses only on the suggested application, the host link, and the control system and subsequent hardware introduced and utilised throughout. Hence the relevant conclusions to be made are that a higher level of attenuation of the response may be attained through the employment of PD control, and that a DTDM may be utilised to represent the system and thus attain appropriate gain values for the control.

Conclusion: *Of the control schemes investigated, PD control has been shown to provide the best attenuation of the link, where optimisation may be used to obtain appropriate gain values, and a DTDM may be employed to represent the system at lower control gain values.*

Future work

Throughout this research there has been a few topics which have been deemed as being beyond the scope of this research. Ultimately this research has focussed on the design and investigation of a control system which has been subject to certain constraints to increase its suitability for use in an array of applications. Some of these topics include the further investigation as to why the nonlinear response of the link exhibited both softening and hardening nonlinearities, attaining a more in-depth insight into the influence of the resistance and capacitance values on the controlled response, and exciting the link at higher force levels (in both the robot manipulator and nonlinear investigations). Additionally, future work may focus on improving the effectiveness of the control system with its current hardware through the validation of the results concerning the dynamic control investigation in experimental investigations. Alternatively this improvement may be found through utilising PZT actuators of a higher operating voltage, and subsequently the discrepancies found when modelling the system in the discrete-time domain may be validated experimentally.

Whilst further investigations would have provided a better insight into the structural response and the control system, they would have removed focus on the main goal of this research, and in some cases risked the integrity of the control system and structure. Acknowledging this, and considering that the control system has been proven to be effective in a variety of situations, it would be pertinent to investigate these topics further in future to add to the overall contribution of this work, and provide a better understanding.

Such topics fall under one branch of the potential future work, whereas another could be the evolution of the structure and control system to the point where it is applied in a manner more befitting of the suggested application. A drone could be designed which utilises a RPi as its flight control and aims to answer the hypothesis previously mentioned. This may also answer questions such as: ‘Would the processing capacity of the RPi be sufficient to control both the drone and the designed control system?’, ‘Would mounting a camera on the end of the link cause a spurious mode to be present given the wiring?’, and ‘Would the implementation of the control system during flight affect the performance or stability of the drone?’. Of course, whilst answering these questions it is also possible to address the other topics that were deemed beyond the scope of this research. Ultimately a further evolution of this research has the potential to produce a search and rescue system which would significantly assist in such missions, while contributing further to the fields of robotics and control.

Bibliography

- [1] *Raspberry Pi 3 Model B+*. n.d. URL: <https://www.raspberrypi.org/products/raspberry-pi-3-model-b-plus/> (visited on 20th July 2021).
- [2] *dSPACE MicroLabBox*. 2020. URL: [https://www.dspace.com/shared/data/pdf/2020/dSPACE-MicroLabBox_Product-Brochure_2020-01_EN.pdf](https://www.dsspace.com/shared/data/pdf/2020/dSPACE-MicroLabBox_Product-Brochure_2020-01_EN.pdf) (visited on 3rd Feb. 2020).
- [3] *LBR iiwa*. 2016. URL: <https://www.kuka.com/en-gb/products/robotics-systems/industrial-robots/lbr-iiwa> (visited on 11th May 2020).
- [4] Steven H Strogatz et al. “Crowd synchrony on the Millennium Bridge”. *Nature* 438.7064 (2005), pp. 43–44.
- [5] Daniel J Inman. *Vibration with control*. John Wiley & Sons, 2017.
- [6] RA Ibrahim. “Recent advances in nonlinear passive vibration isolators”. *Journal of sound and vibration* 314.3-5 (2008), pp. 371–452.
- [7] Rabih Alkhatib and MF Golnaraghi. “Active structural vibration control: a review”. *Shock and Vibration Digest* 35.5 (2003), p. 367.
- [8] *Vibration damping: what’s the difference between passive and active methods?* 2019. URL: <https://www.motioncontroltips.com/vibration-damping-whats-the-difference-between-passive-and-active-methods/> (visited on 23rd July 2021).
- [9] *Active Vs. Passive Vibration Isolation Technology*. 2016. URL: <https://www.azom.com/article.aspx?ArticleID=12898> (visited on 23rd July 2021).
- [10] John C Dixon. *Suspension geometry and computation*. John Wiley & Sons, 2009.
- [11] George B Seldon. *Road Engine*. US Patent 549,160. 1895.
- [12] Edward F Crawley and Javier De Luis. “Use of piezoelectric actuators as elements of intelligent structures”. *AIAA journal* 25.10 (1987), pp. 1373–1385.
- [13] Edward F Crawley et al. “Development of piezoelectric technology for applications in control of intelligent structures”. *1988 American Control Conference*. IEEE. 1988, pp. 1890–1896.

- [14] Nesbitt W Hagood and Andreas von Flotow. “Damping of structural vibrations with piezoelectric materials and passive electrical networks”. *Journal of sound and vibration* 146.2 (1991), pp. 243–268.
- [15] Francesco dell’Isola, Corrado Maurini and Maurizio Porfiri. “Passive damping of beam vibrations through distributed electric networks and piezoelectric transducers: prototype design and experimental validation”. *Smart Materials and Structures* 13.2 (2004), p. 299.
- [16] Ugur Aridogan and Ipek Basdogan. “A review of active vibration and noise suppression of plate-like structures with piezoelectric transducers”. *Journal of Intelligent Material Systems and Structures* 26.12 (2015), pp. 1455–1476.
- [17] Vivek Gupta, Manu Sharma and Nagesh Thakur. “Mathematical modeling of actively controlled piezo smart structures: a review”. *Smart Structures and Systems* 8.3 (2011), pp. 275–302.
- [18] Gangbing Song, Vineet Sethi and H-N Li. “Vibration control of civil structures using piezoceramic smart materials: A review”. *Engineering Structures* 28.11 (2006), pp. 1513–1524.
- [19] Olek C Zienkiewicz and Robert L Taylor. *The finite element method for solid and structural mechanics*. Elsevier, 2005.
- [20] Longfei Sun et al. “Active vibration control of a conical shell using piezoelectric ceramics”. *Journal of Low Frequency Noise, Vibration and Active Control* 36.4 (2017), pp. 366–375.
- [21] Lotfi A Zadeh. “Fuzzy sets”. *Information and control* 8.3 (1965), pp. 338–353.
- [22] Francis Jeffry et al. “Review of Metamathematics of fuzzy logics”. *The Bulletin of Symbolic Logic* 6.3 (2000), pp. 342–346.
- [23] MC Ray and JN Reddy. “Active damping of laminated cylindrical shells conveying fluid using 1–3 piezoelectric composites”. *Composite Structures* 98 (2013), pp. 261–271.
- [24] Zhi-cheng Qiu et al. “Optimal placement and active vibration control for piezoelectric smart flexible cantilever plate”. *Journal of Sound and Vibration* 301.3-5 (2007), pp. 521–543.
- [25] Thomas Bailey and James E Hubbard Jr. “Distributed piezoelectric-polymer active vibration control of a cantilever beam”. *Journal of Guidance, Control, and Dynamics* 8.5 (1985), pp. 605–611.
- [26] Seyed Kamaleddin Yadavar Nikravesh. *Nonlinear systems stability analysis: Lyapunov- based approach*. CRC Press, 2018.

- [27] Gianluca Gatti, Michael J Brennan and Paolo Gardonio. “Active damping of a beam using a physically collocated accelerometer and piezoelectric patch actuator”. *Journal of Sound and Vibration* 303.3-5 (2007), pp. 798–813.
- [28] SY Wang, ST Quek and KK Ang. “Vibration control of smart piezoelectric composite plates”. *Smart materials and Structures* 10.4 (2001), p. 637.
- [29] KB Waghulde et al. “Vibration Control of Cantilever Smart Beam by using Piezoelectric Actuators and Sensors 1” (2010).
- [30] Jeffrey J Dosch, Daniel J Inman and Ephrahim Garcia. “A self-sensing piezoelectric actuator for collocated control”. *Journal of Intelligent material systems and Structures* 3.1 (1992), pp. 166–185.
- [31] Joël Bafumba Liseli et al. “An overview of piezoelectric self-sensing actuation for nanopositioning applications: Electrical circuits, displacement, and force estimation”. *IEEE Transactions on Instrumentation and Measurement* 69.1 (2019), pp. 2–14.
- [32] C Miclea et al. “Effect of temperature on the main piezoelectric parameters of a soft PZT ceramic”. *Rom. J. Inf. Sci. Technol* 10.3 (2007), pp. 243–250.
- [33] Niall J Donnelly and Clive A Randall. “Refined model of electromigration of Ag/Pd electrodes in multilayer PZT ceramics under extreme humidity”. *Journal of the American Ceramic Society* 92.2 (2009), pp. 405–410.
- [34] K Ramesh Kumar and S Narayanan. “Active vibration control of beams with optimal placement of piezoelectric sensor/actuator pairs”. *Smart Materials and Structures* 17.5 (2008), p. 055008.
- [35] JC Bruch Jr et al. “Optimal piezo-actuator locations/lengths and applied voltage for shape control of beams”. *Smart Materials and Structures* 9.2 (2000), p. 205.
- [36] Q Wang and Chien Ming Wang. “Optimal placement and size of piezoelectric patches on beams from the controllability perspective”. *Smart Materials and Structures* 9.4 (2000), p. 558.
- [37] Baptiste Chomette and Adrien Mamou-Mani. “Modal control based on direct modal parameters estimation”. *Journal of Vibration and Control* 24.12 (2018), pp. 2389–2399.
- [38] Marguerite Jossic et al. “Modal active control of Chinese gongs”. *The Journal of the Acoustical Society of America* 141.6 (2017), pp. 4567–4578.
- [39] Ameer Hamza Khan and Shuai Li. “Sliding mode control with PID sliding surface for active vibration damping of pneumatically actuated soft robots”. *IEEE Access* 8 (2020), pp. 88793–88800.

- [40] Xavier Weber, Loic Cuvillon and Jacques Gangloff. “Active vibration canceling of a cable-driven parallel robot using reaction wheels”. *2014 IEEE/RSJ International Conference on Intelligent Robots and Systems*. IEEE. 2014, pp. 1724–1729.
- [41] Mohammad Abdollahpouri, Gergely Takács and Boris Rohal’-Ilkiv. “Real-time moving horizon estimation for a vibrating active cantilever”. *Mechanical Systems and Signal Processing* 86 (2017), pp. 1–15.
- [42] Marek Iwaniec et al. “Development of vibration spectrum analyzer using the Raspberry Pi microcomputer and 3-axis digital MEMS accelerometer ADXL345”. *2017 XIIIth International Conference on Perspective Technologies and Methods in MEMS Design (MEMSTECH)*. IEEE. 2017, pp. 25–29.
- [43] Siwakorn Jindarat and Pongpisitt Wuttidittachotti. “Smart farm monitoring using Raspberry Pi and Arduino”. *2015 International Conference on Computer, Communications, and Control Technology (I⁴CT)*. IEEE. 2015, pp. 284–288.
- [44] Md Anam Mahmud et al. “A complete internet of things (IoT) platform for structural health monitoring (shm)”. *2018 IEEE 4th World Forum on Internet of Things (WF-IoT)*. IEEE. 2018, pp. 275–279.
- [45] Leonhard Euler. *The Rational Mechanics of Flexible Or Elastic Bodies 1638-1788: Introduction to Vol. X and XI*. Springer Science & Business Media, 1960.
- [46] Stephen P Timoshenko. “LXVI. On the correction for shear of the differential equation for transverse vibrations of prismatic bars”. *The London, Edinburgh, and Dublin Philosophical Magazine and Journal of Science* 41.245 (1921), pp. 744–746.
- [47] Isaac Elishakoff. “Who developed the so-called Timoshenko beam theory?” *Mathematics and Mechanics of Solids* 25.1 (2020), pp. 97–116.
- [48] André Teófilo Beck and Cláudio RA da Silva Jr. “Timoshenko versus Euler beam theory: Pitfalls of a deterministic approach”. *Structural Safety* 33.1 (2011), pp. 19–25.
- [49] Daniel J Inman and Ramesh Chandra Singh. *Engineering vibration*. Vol. 3. Prentice Hall Englewood Cliffs, NJ, 1994.
- [50] OJ Aldraihem, RC Wetherhold and T Singh. “Intelligent beam structures: Timoshenko theory vs. Euler-Bernoulli theory”. *Proceeding of the 1996 IEEE International Conference on Control Applications IEEE International Conference on Control Applications held together with IEEE International Symposium on Intelligent Contro*. IEEE. 1996, pp. 976–981.

- [51] Mana Afshari and Daniel J Inman. “Continuous crack modeling in piezoelectrically driven vibrations of an Euler–Bernoulli beam”. *Journal of Vibration and Control* 19.3 (2013), pp. 341–355.
- [52] Saurabh Kumar, Rajeev Srivastava and R Srivastava. “Active vibration control of smart piezo cantilever beam using pid controller”. *International Journal of Research in Engineering and Technology* 3.1 (2014), pp. 392–399.
- [53] Wei-Jiun Su and Jean W Zu. “Design and development of a novel bi-directional piezoelectric energy harvester”. *Smart materials and structures* 23.9 (2014), p. 095012.
- [54] Alper Erturk and Daniel J Inman. “An experimentally validated bimorph cantilever model for piezoelectric energy harvesting from base excitations”. *Smart materials and structures* 18.2 (2009), p. 025009.
- [55] Mohsen Dadfarnia et al. “A Lyapunov-based piezoelectric controller for flexible Cartesian robot manipulators”. *J. Dyn. Sys., Meas., Control* 126.2 (2004), pp. 347–358.
- [56] Jae-Hung Han, Keun-Ho Rew and In Lee. “An experimental study of active vibration control of composite structures with a piezo-ceramic actuator and a piezo-film sensor”. *Smart Materials and Structures* 6.5 (1997), p. 549.
- [57] M Naushad Alam et al. “Active vibration control of a piezoelectric beam using PID controller: Experimental study”. *Latin American Journal of Solids and Structures* 9.6 (2012), pp. 657–673.
- [58] Jinjun Shan, Hong-Tao Liu and Dong Sun. “Slewing and vibration control of a single-link flexible manipulator by positive position feedback (PPF)”. *Mechatronics* 15.4 (2005), pp. 487–503.
- [59] OA Garcia-Perez, G Silva-Navarro and JF Peza-Solis. “Flexible-link robots with combined trajectory tracking and vibration control”. *Applied Mathematical Modelling* 70 (2019), pp. 285–298.
- [60] Ho-Cheol Shin and Seung-Bok Choi. “Position control of a two-link flexible manipulator featuring piezoelectric actuators and sensors”. *Mechatronics* 11.6 (2001), pp. 707–729.
- [61] SK Tso et al. “Vibration control for a flexible-link robot arm with deflection feedback”. *International journal of non-linear mechanics* 38.1 (2003), pp. 51–62.

- [62] Amor Jnifene and William Andrews. “Experimental study on active vibration control of a single-link flexible manipulator using tools of fuzzy logic and neural networks”. *IEEE transactions on instrumentation and measurement* 54.3 (2005), pp. 1200–1208.
- [63] M Hassan et al. “Active vibration control of a flexible one-link manipulator using a multivariable predictive controller”. *Mechatronics* 17.6 (2007), pp. 311–323.
- [64] Vinh Nguyen, Joshua Johnson and Shreyes Melkote. “Active vibration suppression in robotic milling using optimal control”. *International Journal of Machine Tools and Manufacture* 152 (2020), p. 103541.
- [65] Olof Sörnmo et al. “Increasing the milling accuracy for industrial robots using a piezo-actuated high-dynamic micro manipulator”. *2012 IEEE/ASME international conference on advanced intelligent mechatronics (AIM)*. IEEE. 2012, pp. 104–110.
- [66] Alexandra Ast et al. “An adaptronic approach to active vibration control of machine tools with parallel kinematics”. *Production Engineering* 3.2 (2009), pp. 207–215.
- [67] Fan Chen et al. “Contact force control and vibration suppression in robotic polishing with a smart end effector”. *Robotics and Computer-Integrated Manufacturing* 57 (2019), pp. 391–403.
- [68] Yingjie Guo et al. “Vibration analysis and suppression in robotic boring process”. *International Journal of Machine Tools and Manufacture* 101 (2016), pp. 102–110.
- [69] J Denavit et al. “54 KINEMATIC PARAMETER”. *Journal of applied mechanics* 77.2 (1955), pp. 215–221.
- [70] Peter I Corke. “A simple and systematic approach to assigning Denavit – Hartenberg parameters”. *IEEE transactions on robotics* 23.3 (2007), pp. 590–594.
- [71] Alireza Izadbakhsh. “Closed-form dynamic model of PUMA 560 robot arm”. *2009 4th International Conference on Autonomous Robots and Agents*. IEEE. 2009, pp. 675–680.
- [72] Guanbin Gao et al. “Structural parameter identification for 6 DOF industrial robots”. *Mechanical Systems and Signal Processing* 113 (2018), pp. 145–155.
- [73] Carlos Faria et al. “Position-based kinematics for 7-DoF serial manipulators with global configuration control, joint limit and singularity avoidance”. *Mechanism and Machine Theory* 121 (2018), pp. 317–334.

- [74] Shangpei Li et al. “Solving inverse kinematics model for 7-DoF robot arms based on space vector”. *2018 International Conference on Control and Robots (ICCR)*. IEEE. 2018, pp. 1–5.
- [75] Jingguo Wang, Yangmin Li and Xinhua Zhao. “Inverse kinematics and control of a 7-DOF redundant manipulator based on the closed-loop algorithm”. *International Journal of Advanced Robotic Systems* 7.4 (2010), p. 37.
- [76] Dominik Bertram et al. “An integrated approach to inverse kinematics and path planning for redundant manipulators”. *Proceedings 2006 IEEE International Conference on Robotics and Automation, 2006. ICRA 2006*. IEEE. 2006, pp. 1874–1879.
- [77] David Wagg and SA Neild. *Nonlinear vibration with control*. Springer, 2016.
- [78] George Platanitis and Thomas W Strganac. “Control of a nonlinear wing section using leading-and trailing-edge surfaces”. *Journal of Guidance, Control, and Dynamics* 27.1 (2004), pp. 52–58.
- [79] Farshad Khorrami, Sandeep Jain and Anthony Tzes. “Experimental results on adaptive nonlinear control and input preshaping for multi-link flexible manipulators”. *Automatica* 31.1 (1995), pp. 83–97.
- [80] Bor-Sen Chen, Chung-Shi Tseng and Huey-Jian Uang. “Robustness design of nonlinear dynamic systems via fuzzy linear control”. *IEEE Transactions on fuzzy systems* 7.5 (1999), pp. 571–585.
- [81] Marios M Polycarpou and Petros A Ioannou. “A robust adaptive nonlinear control design”. *1993 American control conference*. IEEE. 1993, pp. 1365–1369.
- [82] Dong Sun et al. “Hybrid control of a rotational flexible beam using enhanced PD feedback with a nonlinear differentiator and PZT actuators”. *Smart materials and structures* 14.1 (2004), p. 69.
- [83] Tobias Schweickhardt and Frank Allgöwer. “Linear control of nonlinear systems based on nonlinearity measures”. *Journal of Process Control* 17.3 (2007), pp. 273–284.
- [84] C Desoer and Yung-Terng Wang. “Foundations of feedback theory for nonlinear dynamical systems”. *IEEE Transactions on Circuits and Systems* 27.2 (1980), pp. 104–123.
- [85] OV Rudenko and CM Hedberg. “Strong and weak nonlinear dynamics: models, classification, examples”. *Acoustical Physics* 59.6 (2013), pp. 644–650.
- [86] Hassan K Khalil and Jessy W Grizzle. *Nonlinear systems*. Vol. 3. Prentice hall Upper Saddle River, NJ, 2002.

- [87] M. Y. Harmin and J. E. Cooper. “Aeroelastic behaviour of a wing including geometric nonlinearities”. *The Aeronautical Journal (1968)* 115.1174 (2011), 767–777.
- [88] Javad Taghipour et al. “On the sensitivity of the equivalent dynamic stiffness mapping technique to measurement noise and modelling error”. *Applied Mathematical Modelling* 89 (2021), pp. 225–248.
- [89] Javad Taghipour et al. “An Optimization-Based Framework for Nonlinear Model Selection and Identification”. *Vibration* 2.4 (2019), pp. 311–331.
- [90] *PRODRONE Unveils the World’s First Dual Robot Arm Large-Format Drone*. 2016. URL: <https://www.prodrone.com/archives/1420/> (visited on 11th May 2020).
- [91] Johanna Wallén. *The history of the industrial robot*. Linköping University Electronic Press, 2008.
- [92] Mordechai Ben-Ari and Francesco Mondada. “Robots and their applications”. *Elements of robotics*. Springer, 2018, pp. 1–20.
- [93] Isaac Asimov. “Runaround”. *Astounding Science Fiction* 29.1 (1942), pp. 94–103.
- [94] Isaac Asimov. *Robots and Empire*. 1985. 1996.
- [95] NyTechnik. “NyTechnik Automation”. 29 (2007), pp. 94–103.
- [96] *The First Industrial Robot*. 2015. URL: <https://www.robotics.org/joseph-engelberger/unimate.cfm> (visited on 3rd Sept. 2019).
- [97] *Executive Summary World Robotics 2020 Industrial Robots*. 2019. URL: https://ifr.org/img/worldrobotics/Executive_Summary_WR_2020_Industrial_Robots_1.pdf (visited on 11th May 2020).
- [98] *Powering tomorrow’s bomb disposal robots*. 2018. URL: <https://www.theengineer.co.uk/powering-tomorrows-bomb-disposal-robots/> (visited on 26th Feb. 2021).
- [99] *Canadarm2*. 2019. URL: https://www.nasa.gov/mission_pages/station/research/news/b4h-3rd/hh-robotic-arms-reach (visited on 2nd Nov. 2019).
- [100] *Puma 560*. 2016. URL: <https://www.britannica.com/technology/PUMA-560> (visited on 18th Oct. 2019).
- [101] Robert A Manning. *Rising robotics and the third industrial revolution*. 2013.
- [102] *About da Vinci Systems*. 2015. URL: <https://www.davincisurgery.com/da-vinci-systems/about-da-vinci-systems> (visited on 18th Oct. 2019).

- [103] *KUKA Coaster*. 2017. URL: <https://www.kuka.com/en-gb/industries/other-industries/entertainment/amusement-rides/kuka-coaster> (visited on 11th May 2020).
- [104] *Press and Events*. 2019. URL: <https://www.kuka.com/en-gb/press> (visited on 11th May 2020).
- [105] *Robotic Arc Welding*. 2019. URL: <https://www.motoman.com/en-us/applications/arc-welding> (visited on 11th May 2020).
- [106] *Strongest robot arm*. 2016. URL: <https://www.guinnessworldrecords.com/world-records/strongest-robot-arm> (visited on 11th May 2020).
- [107] *This Is the Most Powerful Robot Arm Ever Installed on a Mars Rover*. 2019. URL: <https://spectrum.ieee.org/automaton/robotics/space-robots/robot-arm-mars-2020-rover> (visited on 11th May 2020).
- [108] *Flexible Gripper for UR Cobots*. 2019. URL: <https://www.assemblymag.com/articles/95318-soft-robotics-introduces-modular-flexible-gripper-for-ur-cobots> (visited on 11th Jan. 2021).
- [109] *Get a Glimpse of the Next-generation Innovations on Display at Samsung's Technology Showcase*. 2019. URL: <https://news.samsung.com/global/get-a-glimpse-of-the-next-generation-innovations-on-display-at-samsungs-technology-showcase> (visited on 2nd Nov. 2019).
- [110] *War comes to Salisbury*. 2019. URL: <https://www.thetimes.co.uk/article/gallery-war-comes-to-salisbury-h5x9kqjisp> (visited on 1st Nov. 2019).
- [111] *About Dextre*. 2018. URL: <https://asc-csa.gc.ca/eng/iss/dextre/about.asp> (visited on 2nd Nov. 2019).
- [112] *da Vinci Robotic Assisted Surgery*. 2012. URL: <https://www.amitahealth.org/services/surgical-services/surgical-technology/robotic-surgery/da-vinci> (visited on 2nd Nov. 2019).
- [113] *About da Vinci Systems*. 2019. URL: <https://www.davincisurgery.com/davinci-systems/about-da-vinci-systems> (visited on 2nd Nov. 2019).
- [114] *Modular Prosthetic Limb*. 2018. URL: <https://robots.ieee.org/robots/mpl/> (visited on 2nd Nov. 2019).
- [115] *Modular Prosthetic Limb*. 2012. URL: <https://www.jhuapl.edu/Prosthetics/ResearchMPL> (visited on 2nd Nov. 2019).

- [116] *Man moves his robotic arms with his MIND*. 2016. URL: <https://www.dailymail.co.uk/sciencetech/article-3397823/Man-moves-robotic-arms-MIND-brain-controlled-prosthetic-attaches-implant-patient-s-bone.html> (visited on 2nd Nov. 2019).
- [117] Matthew S Fifer et al. “Simultaneous neural control of simple reaching and grasping with the modular prosthetic limb using intracranial EEG”. *IEEE transactions on neural systems and rehabilitation engineering* 22.3 (2013), pp. 695–705.
- [118] *Samsung CES 2020: the best thing at the booth is this salad-making Chef Bot*. 2020. URL: <https://www.techradar.com/news/samsungs-bot-chef-made-me-a-salad-at-ces-2020-and-i-ate-it> (visited on 20th Jan. 2020).
- [119] Antoni Grau et al. “Industrial robotics in factory automation: From the early stage to the Internet of Things”. *IECON 2017-43rd Annual Conference of the IEEE Industrial Electronics Society*. IEEE. 2017, pp. 6159–6164.
- [120] *Research cooperation projects*. 2017. URL: <https://www.kuka.com/en-us/future-production/research-and-development/research-collaborations> (visited on 2nd Nov. 2019).
- [121] *KMR iiwa*. 2016. URL: <https://www.kuka.com/en-gb/products/mobility/mobile-robots/kmr-iiwa> (visited on 2nd Nov. 2019).
- [122] *Car manufacturing in the automotive industry done by robots*. 2015. URL: <https://www.universal-robots.com/industries/automotive-and-subcontractors/> (visited on 2nd Nov. 2019).
- [123] *Nissan Motor Company*. 2017. URL: <https://www.universal-robots.com/case-stories/nissan-motor-company/> (visited on 2nd Nov. 2019).
- [124] *The mGrip System*. 2019. URL: <https://www.softroboticsinc.com/products/mgrip/> (visited on 11th Jan. 2021).
- [125] *Opinion: The incredible potential of soft robotics*. 2020. URL: <https://roboticsandautomationnews.com/2020/03/09/opinion-the-incredible-potential-of-soft-robotics/31146/> (visited on 11th Jan. 2021).
- [126] *Wearable Soft Robotics for Independent Living*. 2016. URL: <https://therighttrousers.com/> (visited on 11th Jan. 2021).
- [127] Johann Berger et al. “Evaluation of an IEEE 11073 SDC Connection of two KUKA Robots towards the Application of Focused Ultrasound in Radiation Therapy”. *Current Directions in Biomedical Engineering* 5.1 (2019), pp. 149–152.

- [128] Paul Tucan et al. “Ankle Rehabilitation of Stroke Survivors Using Kuka LBR Iiwa”. *International Workshop on Medical and Service Robots*. Springer. 2020, pp. 29–36.
- [129] Javad Fotouhi et al. “Reflective-ar display: An interaction methodology for virtual-to-real alignment in medical robotics”. *IEEE Robotics and Automation Letters* 5.2 (2020), pp. 2722–2729.
- [130] Alexander Beyer et al. “Caesar: Space robotics technology for assembly, maintenance, and repair”. *Proceedings of the International Astronautical Congress, IAC*. 2018.
- [131] Andrew Price, Linyi Jin and Dmitry Berenson. “Inferring occluded geometry improves performance when retrieving an object from dense clutter”. *arXiv preprint arXiv:1907.08770* (2019).
- [132] *Sensitive robotics LBR iiwa*. 2016. URL: https://www.kuka.com/-/media/kuka-downloads/imported/9cb8e311bfd744b4b0eab25ca883f6d3/kuka_lbr_iiwa_brochure_en.pdf?rev=4f549f7d92824ccdb462ae25a96c1d61 (visited on 3rd Dec. 2016).
- [133] Peter Corke. *Robotics, vision and control: fundamental algorithms In MATLAB® second, completely revised*. Vol. 118. Springer, 2017.
- [134] Carlos Faria et al. “Position-based kinematics for 7-DoF serial manipulators with global configuration control, joint limit and singularity avoidance”. *Mechanism and Machine Theory* 121 (2018), pp. 317–334.
- [135] *Structural Materials for Robots*. 2014. URL: https://www.cs.rochester.edu/~nelson/courses/csc_robocon/robot_manual/materials.html (visited on 11th Sept. 2019).
- [136] Minhang Bao. *Analysis and design principles of MEMS devices*. Elsevier, 2005.
- [137] Edward Ramsden. *Hall-effect sensors: theory and application*. Elsevier, 2011.
- [138] Stefano Brenna et al. “A low-noise sub-500 μ W lorentz force based integrated magnetic field sensing system”. *2015 28th IEEE International Conference on Micro Electro Mechanical Systems (MEMS)*. IEEE. 2015, pp. 932–935.
- [139] SO Reza Moheimani and Andrew J Fleming. *Piezoelectric transducers for vibration control and damping*. Springer Science & Business Media, 2006.
- [140] *What is “PZT”?* 2011. URL: <https://www.americanpiezo.com/piezo-theory/pzt.html> (visited on 3rd May 2017).
- [141] *The COMSOL Software Product Suite*. 2018. URL: <https://uk.comsol.com/products> (visited on 17th Aug. 2018).

- [142] *Media Flange*. 2016. URL: http://www.oir.caltech.edu/twiki_oir/pub/Palomar/ZTF/KUKARoboticArmMaterial/Option_Media_Flange_en.pdf (visited on 14th Feb. 2017).
- [143] PCB Piezotronics. *PCB Piezotronics ICP Accelerometer 352C03 (datasheet)*. 2006.
- [144] *Macro Fibre Composite - MFC*. 2017. URL: https://www.smart-material.com/media/Datasheets/MFC_V2.3-Web-full-brochure.pdf (visited on 3rd Oct. 2019).
- [145] *The Online Materials Information Resource*. 2007. URL: <http://www.matweb.com> (visited on 3rd Oct. 2019).
- [146] *Raspberry Pi Camera Module*. 2016. URL: <https://docs.rs-online.com/3b9b/0900766b814db308.pdf> (visited on 14th Jan. 2021).
- [147] Alan V Oppenheim. *Discrete-time signal processing*. Pearson Education India, 1999.
- [148] Richard C Dorf and Robert H Bishop. *Modern control systems*. Pearson, 2011.
- [149] *MFC P2 and P3 types (d31 effect), Contractor*. 2017. URL: <https://www.smart-material.com/MFC-product-P2.html> (visited on 10th May 2019).
- [150] *MACRO FIBER COMPOSITE - MFC*. 2017. URL: https://www.smart-material.com/media/Datasheets/MFC_V2.3-Web-full-brochure.pdf (visited on 10th May 2019).
- [151] *DRV2700EVM-HV500 - Flyback High Voltage Evaluation Module*. 2015. URL: <http://www.ti.com/tool/DRV2700EVM-HV500> (visited on 10th May 2019).
- [152] *DRV2700EVM-HV500 High Voltage Piezo Driver Evaluation Kit*. 2015. URL: <http://www.ti.com/lit/ug/slou407a/slou407a.pdf> (visited on 10th May 2019).
- [153] *MCP3004/3008, 2.7V 4-Channel/8-Channel 10-Bit A/D Converters with SPI Serial Interface*. 2008. URL: <https://cdn-shop.adafruit.com/datasheets/MCP3008.pdf> (visited on 10th May 2019).
- [154] *I2C*. 2013. URL: <https://learn.sparkfun.com/tutorials/i2c/all> (visited on 22nd Apr. 2019).
- [155] *MPU-9250 Product Specification*. 2016. URL: <https://invensense.tdk.com/wp-content/uploads/2015/02/PS-MPU-9250A-01-v1.1.pdf> (visited on 10th Mar. 2018).

- [156] *Serial Peripheral Interface (SPI)*. 2013. URL: <https://learn.sparkfun.com/tutorials/serial-peripheral-interface-spi/all> (visited on 10th May 2019).
- [157] Amor Jnifene. “Active vibration control of flexible structures using delayed position feedback”. *Systems & control letters* 56.3 (2007), pp. 215–222.
- [158] *modalfit*. n.d. URL: <https://uk.mathworks.com/help/signal/ref/modalfit.html> (visited on 27th July 2021).
- [159] *Explained: Linear and nonlinear systems*. 2010. URL: <https://news.mit.edu/2010/explained-linear-0226> (visited on 10th Jan. 2020).
- [160] Philip G Drazin and Philip Drazin Drazin. *Nonlinear systems*. Vol. 10. Cambridge University Press, 1992.
- [161] Ali H Nayfeh and Dean T Mook. *Nonlinear oscillations*. John Wiley & Sons, 2008.
- [162] James Gleick. *Chaos: Making a new science*. Open Road Media, 2011.
- [163] Steven H Strogatz. “Nonlinear dynamics and chaos. 1994”. *Reading: Perseus Books* (1996).
- [164] Eduardo D Sontag and Yuan Wang. “On characterizations of the input-to-state stability property”. *Systems & Control Letters* 24.5 (1995), pp. 351–359.
- [165] Alberto Isidori. *Nonlinear control systems*. Springer Science & Business Media, 2013.
- [166] Alexander D Shaw et al. “Periodic responses of a structure with 3: 1 internal resonance”. *Mechanical Systems and Signal Processing* 81 (2016), pp. 19–34.
- [167] Xingjian Dong et al. “Research on spillover effects for vibration control of piezoelectric smart structures by ANSYS”. *Mathematical Problems in Engineering* 2014 (2014).
- [168] Javad Taghipour and Morteza Dardel. “Steady state dynamics and robustness of a harmonically excited essentially nonlinear oscillator coupled with a two-DOF nonlinear energy sink”. *Mechanical Systems and Signal Processing* 62 (2015), pp. 164–182.
- [169] Javad Taghipour, Morteza Dardel and Mohammad Hadi Pashaei. “Vibration mitigation of a nonlinear rotor system with linear and nonlinear vibration absorbers”. *Mechanism and Machine Theory* 128 (2018), pp. 586–615.
- [170] Malcolm C Smith. “Synthesis of mechanical networks: the inerter”. *IEEE Transactions on automatic control* 47.10 (2002), pp. 1648–1662.

- [171] *When Tuning the PID Controller, the D Gain Has a Different Sign from the I Gain*. n.d. URL: <https://uk.mathworks.com/help/slcontrol/ug/when-tuning-the-pid-controller-the-d-gain-has-a-different-sign-from-the-i-gain.html> (visited on 16th Dec. 2021).
- [172] *Simulink*. n.d. URL: <https://uk.mathworks.com/products/simulink.html> (visited on 17th Nov. 2021).
- [173] Shunqi Zhang, Rüdiger Schmidt and Xiansheng Qin. “Active vibration control of piezoelectric bonded smart structures using PID algorithm”. *Chinese journal of aeronautics* 28.1 (2015), pp. 305–313.
- [174] Juntao Fei. “Active vibration control of flexible steel cantilever beam using piezoelectric actuators”. *Proceedings of the Thirty-Seventh Southeastern Symposium on System Theory, 2005. SSST'05*. IEEE. 2005, pp. 35–39.
- [175] Hari Om Bansal, Rajamayyoor Sharma and PR Shreeraman. “PID controller tuning techniques: a review”. *Journal of control engineering and technology* 2.4 (2012), pp. 168–176.
- [176] Yun Li, Kiam Heong Ang and Gregory CY Chong. “PID control system analysis and design”. *IEEE Control Systems Magazine* 26.1 (2006), pp. 32–41.
- [177] PM Meshram and Rohit G Kanojiya. “Tuning of PID controller using Ziegler-Nichols method for speed control of DC motor”. *IEEE-international conference on advances in engineering, science and management (ICAESM-2012)*. IEEE. 2012, pp. 117–122.
- [178] Duarte Valério and José Sá Da Costa. “Tuning of fractional PID controllers with Ziegler–Nichols-type rules”. *Signal processing* 86.10 (2006), pp. 2771–2784.
- [179] Chang C Hang, Karl Johan Åström and Weng Khuen Ho. “Refinements of the Ziegler–Nichols tuning formula”. *IEE Proceedings D (Control Theory and Applications)*. Vol. 138. 2. IET. 1991, pp. 111–118.
- [180] Wen Tan et al. “Comparison of some well-known PID tuning formulas”. *Computers & chemical engineering* 30.9 (2006), pp. 1416–1423.
- [181] *Optimization Toolbox*. n.d. URL: <https://uk.mathworks.com/products/optimization.html> (visited on 29th Sept. 2016).
- [182] B Wayne Bequette. *Process control: modeling, design, and simulation*. Prentice Hall Professional, 2003.
- [183] Fernando G Martins. “Tuning PID controllers using the ITAE criterion”. *International Journal of Engineering Education* 21.5 (2005), p. 867.

- [184] Ala Eldin Abdallah Awouda and Rosbi Bin Mamat. “Refine PID tuning rule using ITAE criteria”. *2010 The 2nd International Conference on Computer and Automation Engineering (ICCAE)*. Vol. 5. IEEE. 2010, pp. 171–176.
- [185] Deepyaman Maiti et al. “Tuning PID and PI/ λ D δ controllers using the integral time absolute error criterion”. *2008 4th International Conference on Information and Automation for Sustainability*. IEEE. 2008, pp. 457–462.
- [186] Lucas M Argentim et al. “PID, LQR and LQR-PID on a quadcopter platform”. *2013 International Conference on Informatics, Electronics and Vision (ICIEV)*. IEEE. 2013, pp. 1–6.
- [187] *A stepwise method for tuning PI controllers using ITAE criteria*. 2012. URL: <https://www.embedded.com/a-stepwise-method-for-tuning-pi-controllers-using-itae-criteria/> (visited on 17th Nov. 2021).
- [188] *fmincon*. n.d. URL: <https://uk.mathworks.com/help/optim/ug/fmincon.html> (visited on 17th Nov. 2021).
- [189] L Magni et al. “Robust model predictive control for nonlinear discrete-time systems”. *International Journal of Robust and Nonlinear Control: IFAC-Affiliated Journal* 13.3-4 (2003), pp. 229–246.
- [190] Silviu Folea et al. “Discrete-time implementation and experimental validation of a fractional order PD controller for vibration suppression in airplane wings”. *Acta Polytechnica Hungarica* 14.1 (2017), pp. 191–206.
- [191] J Yuh. “Application of discrete-time model reference adaptive control to a flexible single-link robot”. *Journal of Robotic Systems* 4.5 (1987), pp. 621–630.
- [192] Norman S Nise. *Control systems engineering*. John Wiley & Sons, 2020.